NORTHWESTERN UNIVERSITY

Assembly and Optical Properties of Colloidal Metacrystals Engineered with DNA

A DISSERTATION

SUBMITTED TO THE GRADUATE SCHOOL
IN PARTIAL FULLFILLMENT OF THE REQUIREMENTS

for the degree

DOCTOR OF PHILOSOPHY

Field of Chemistry

By

Cindy Yizhe Zheng

EVANSTON, ILLINOIS

December 2021

ABSTRACT

Realizing electromagnetic metamaterials which operate in the optical regime requires creating precise arrangements of sub-100 nm building blocks. As such, fabricating these materials using conventional lithographic methods is extremely costly. On the other hand, bottom-up assembly of nanoparticles into crystalline superlattices offers opportunities to explore the scalable fabrication of 2- (2D) and 3-dimensional (3D) metamaterials. Of various nanoparticle assembly methods, colloidal crystal engineering with DNA is unique in that the specificity of DNA binding allows one to deliberately prepare materials with predesigned structures. This thesis takes a *materials-by-design* approach towards using DNA to assemble nanoparticles into optical metamaterials with targeted properties. Throughout the thesis, metamaterials on multiple dimensionalities are explored. Chapter 2 describes the template-mediated assembly of individual nanocube-on-mirror anntenas into 2D photonic lattices, and the interaction of these antennas with precisely embedded emitter molecules. Chapter 3 explores using DNA to assemble *high volume fraction*, 3D metacrystals which give rise to tunable, mid-IR Mie resonances. In Chapters 4 and 5, methods to assemble 2D metasurfaces from anisotropic nanoparticles on the wafer-scale are discussed. Furthermore, the metasurfaces are designed to exhibit actively tunable near-IR resonances and epsilon-near-zero (ENZ) conditions. Expanding on the results in Chapter 3, Chapter 6 reports the preparation of uniform arrays of 3D metacrystals, by confining superlattice growth inside microscale trenches. First, the growth mechanism and outcomes are probed using a combination of electron microscopy and synchrotron X-ray based techniques. Next, the efficacy of the method towards large-scale fabrication of uniform 3D metacrystals is explored. Finally, an additional degree of hierarchy is introduced by arranging 3D metacrystals into periodic lattices, which give rise to diffractive modes. Taken together, these discoveries significantly advance the

scalable assembly of 2D and 3D optical metamaterials, which could find use in numerous applications including sensing, telecommunications, and optical computing.

Thesis Co-Advisor: Prof. Chad A. Mirkin

Thesis Co-Advisor: Prof. George C. Schatz

ACKNOWLEDGEMENTS

I am extremely indebted to my advisors, Professors Chad Mirkin and George Schatz. I feel incredibly grateful to have been mentored by two advisors who pushed me to reach my potential and supported me in every possible way. Thank you to Chad for encouraging me when I did not believe in myself and George for always being available to discuss research.

Next, I thank the other members of my thesis committee – Professors Todd Gingrich and Koray Aydin. Koray introduced me to the fields of plasmonics and metamaterials in a course during my first quarter here and was an especially important collaborator throughout my PhD. I also thank the Mirkin group office staff for creating an environment where I could focus on research and NUANCE for its amazing facilities and even more amazing staff.

I am very fortunate to have crossed paths with Dr. Byeongdu Lee in the latter half of my PhD. He was a role model for me and a great resource for wisdom in research and life. Thank you, also, to my other collaborators at Argonne: Dr. Ralu Divan, Dr. Seonke Seinfert, Dr. Xiaobing Zuo, Dr. Yudong Yao, and Dr. Junjing Deng. You made working on these projects exciting.

This work would not have been possible without the help of my collaborators and guidance from mentors. Dr. Edgar Palacios and Wenjie Zhou played a pivotal role in my first project. I thank them for trusting me as a project lead when I was a first year and teaching me many experimental techniques. Wisnu Hadibrata was a consistent collaborator throughout my PhD journey as well as a great friend. I enjoyed discussing anything and everything with him, and he contributed significantly to much of the work in this thesis. Thank you to Dr. Seungkyu Lee for being a fun collaborator and friend and to Dr. Seokhyoung Kim, who became an important collaborator and mentor during my third year. Seokhyoung taught me so much about optics, and more importantly, how to critique myself as a scientist.

The highlight of my PhD was meeting a surplus of friends who brightened my days here. Many group members also served as role models to me. Thank you to Heather Calcaterra, Yushang Chou, Dr. Sasha Ebrahimi, Jungsoo Park, Liban Jibril, Dr. Minliang Lai, Dr. Xinpeng Zhang, Dr. Bo Shen, Henry Han, Dr. Shengshuang Zhu, Ziyi Miao, Dr. Dia Das, Yuan Liu, Dr. Taegon Oh and many others. Thanks to Alexa Wong, my mentee, for her contributions to this work.

Most importantly, I thank God for providing me with the health, perseverance, and opportunities that brought me to where I am today. I am also thankful for my parents and younger brother, David, who are all scientists/engineers themselves and shaped my interests. And thank you to my other friends within and outside of NU for keeping me company throughout the years. Finally, I would like to thank my husband, Liliang. His dedication to research is inspirational, and he has pushed me to become the best person I can be.

Cindy Y. Zheng

Evanston, IL

December 2021

TABLE OF CONTENTS

LIST OF FIGURES

CHAPTER 1

CHAPTER 2

CHAPTER 3

CHAPTER 4

CHAPTER 5

CHAPTER 6

LIST OF TABLES

CHAPTER 2

CHAPTER 3

CHAPTER 4

CHAPTER 5

CHAPTER 1: INTRODUCTION

Colloidal Metamaterials for Unusual Optical Refractions

1.1 Colloidal Metamaterials

1.1.1 Historical perspective on metamaterials and metasurfaces
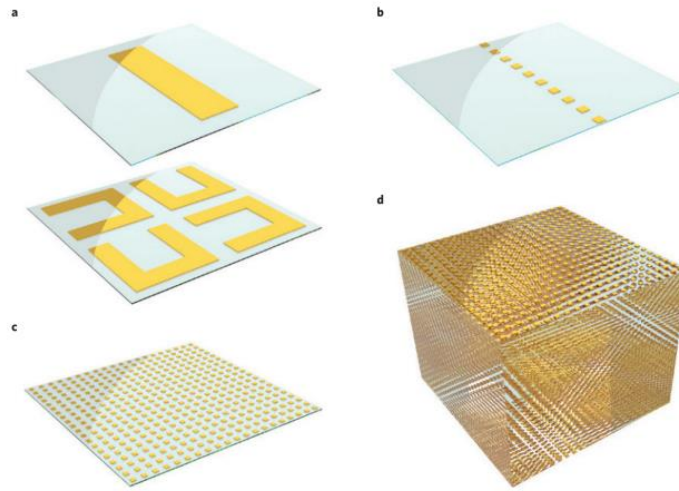
Figure 1-1. Schematic representation of the meta-atom concept. (a) Two types of lithographically fabricated metaatoms. (b-d) Representation of (b) a 1D meta-atom chain, (c) a 2D metasurface, and (d) a 3D metamaterial. Adapted from ref. 1.

Optical metamaterials[2–7] are man-made materials, engineered to interact with light in novel or unusual ways. Typically, they consist of sub-wavelength ("meta-atom") building blocks[8,9] arranged in rationally designed periodic structures (Figure 1-1). Analogous to natural materials, which interact with incident electric fields *via* materials parameters such as electric permittivity (ε), magnetic permeability (μ), and refractive index (n), light-matter interactions in metamaterials can be described using the effective parameters, ε_{eff}, μ_{eff}, and n_{eff}.[9] In order for metamaterials to behave as homogeneous media which can be described by effective medium theories, the structural scale of meta-atoms should be much smaller than the operational wavelengths ($<< \lambda/5$).[8,10] From years 2000 to 2010, progress in metasurfaces research was mainly focused in the terahertz regime.[11–15] Advances in micro- and nano-lithography enabled the fabrication of 2-dimensional
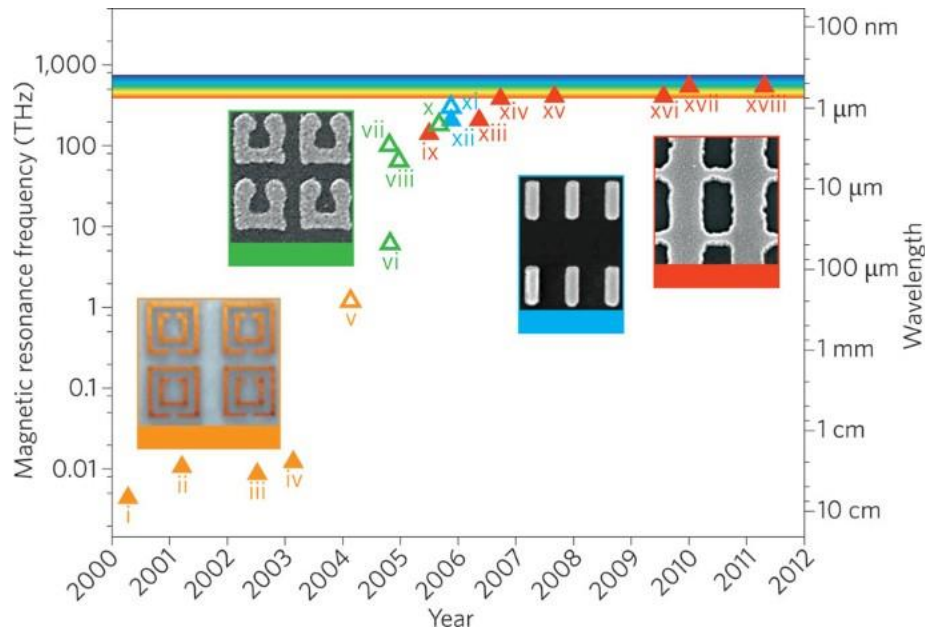
Figure 1-2. The operating frequency of metamaterials with negative permeability (empty triangles) and negative refractive index (solid triangles) shown on a logarithmic scale. Orange: structures based on double SRRs; green: U-shaped SRRs; blue: metallic cut-wire pairs; red: negative-index double-fishnet structures. Figure adapted from ref. 2.

metasurfaces comprised of novel meta-atom structures, such as the split-ring resonator[16–18] and metallic cut wires.[19] These metasurfaces exhibit a wide range of unnatural optical phenomenon, one of the most notable being optical magnetism and, by extension, negative refractive index,[20–22] which was first experimentally shown by David Smith's group in 2001.[23] By the latter half of the decade, state-of-the-art nanolithography techniques could produce features smaller than 100 nm, enabling the exploration of metasurfaces which operate at optical (visible and IR) frequencies (Figure 1-2).[2] Still, there inevitably exists a trade-off between resolution and throughput especially when patterning sub-100 nm features which requires extremely precise lithography using complicated optical systems.[24,25] Nevertheless, the expansion to optical frequencies opened up a myriad of opportunities for the metamaterials community and over the next decade, metasurface research enabled realization of previously unimaginable optical phenomena including cloaking,[26–28] perfect absorption,[29–31] optical chirality,[4,32,33] and superlensing[34].
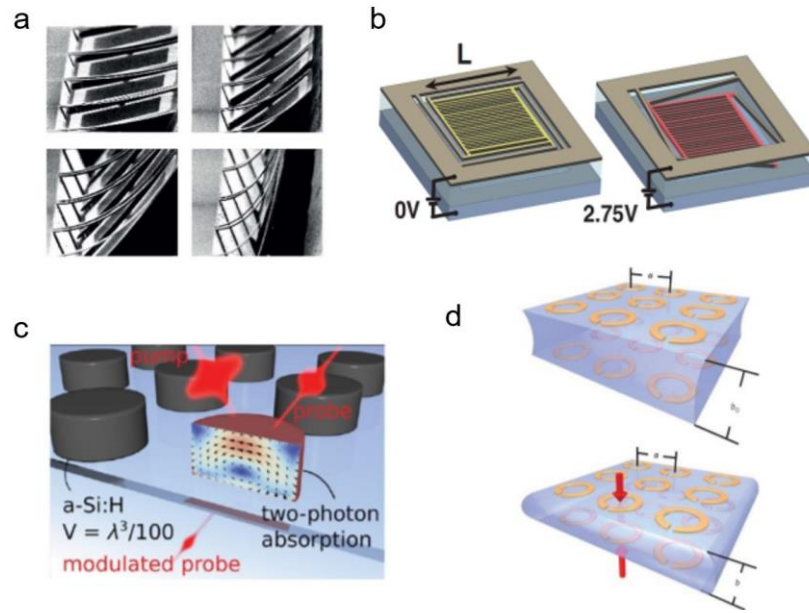
Figure 1-3. Methods to actively tune metadevices. (a) Thermal tuning (b) Electromechanical tuning (c) Incorporating active materials such as semiconductors (d) Opto-mechanical tuning. Figure adapted from Ref. 34.

As metasurface research approached a relatively mature stage, the focus began to shift from fundamental discovery towards devising methods to integrate metasurfaces into devices, known as *metadevices*.[35,36] Due to their subwavelength size, metadevices provide a means to achieve highly efficient, flat alternatives to conventional bulky optical components. In addition, researchers have devised creative methods to actively tune the optical response of metadevices. These tuning strategies can be classified into two categories. First, structural parameters such as lattice constant, resonator shape, or spatial arrangements, can be tuned through mechanical reconfiguration. For instance, thermal tuning takes advantage of the expansion of materials with increased temperatures.[37,38] By arranging two materials with different thermal expansion coefficients into a single resonant unit cell, a change in temperature will result in thermal bending. On the other hand, electro-mechanical tuning utilizes an electrostatic force from an electric field. Specifically, when a DC bias is applied between a movable and stationary electrode, actuation occurs. Electro-mechanical tuning thus far has been the most popular method to mechanically

actuate metamaterials. On this front, micro-electromechanical (MEMS) and nano-electromechanical system (NEMS) technologies are well established for fabricating complicated micro- and nano-mechanical systems, enabling reconfigurable functionalities in metamaterials operating at various frequency ranges.[39–41] Second, incorporating active materials such as semiconductors, phase change materials, or liquid crystals enables tuning of optical response due to the sensitivity of these materials to external stimuli. For example, band structures of semiconductors can be tuned with stimuli including an external electric field, optical pumping, magnetic biasing, and temperature change, which in turn changes their optical properties.[42]

1.1.2 Effective medium description for metamaterials

As previously mentioned, n, ε, and μ are the parameters commonly used to describe light-matter interactions in optical materials. n is defined by $n = \sqrt{\varepsilon\mu}$, where ε and μ are related to electric polarization (P) and magnetic diamagnetization (M), respectively. Specifically,

$$\varepsilon = 1 + \frac{P}{\varepsilon_0 E}$$

and

$$\mu = 1 + \frac{M}{H}$$

where ε_0, E, and H are the vacuum permittivity, incident electric field, and incident magnetic field, respectively. The effective optical behavior of many metamaterials is well described by the Maxwell-Garnett equation, $\frac{\varepsilon_{eff} - \varepsilon_{host}}{\varepsilon_{eff} + 2\varepsilon_{host}} = FF \frac{\varepsilon_{inc} - \varepsilon_{host}}{\varepsilon_{inc} + 2\varepsilon_{host}}$, where FF is the inclusion volume fraction, and ε_{eff}, and ε_{host}, and ε_{inc} are the dielectric constants of the effective metamaterial, host material, and inclusion, respectively.[43] For metasurfaces, inclusions are the lithographically patterned features, and the host is the substrate material. The Maxwell-Garnett theory essentially describes the effective metamaterials parameters as weighted averages of the host and inclusion

parameters. It holds true when there are no interactions between inclusion particles, usually at volume fractions below 20% and disordered arrangements of nanoparticles. For metamaterials with higher volume fractions of inclusions, where interactions between inclusion particles become significant, the s-parameter retrieval method can be used instead. Pioneered by Smith et al.,[44] the s-parameter retrieval method allowed for the generalization of the metamaterials concept and has had a significant impact on the field, being used to determine effective optical parameters in numerous papers.[45–49] In short, reflection, transmission, and their relevant phase change, collectively denoted as s-parameters, are calculated using simulation or retrieved from experimental measurements. Next, the resultant effective parameters are retrieved from the s-parameters. As the work in this dissertation focuses on metamaterials in the high volume fraction regime, the s-parameter retrieval method is employed to calculate effective materials parameters (Chapters 3, 4, 5).

1.1.3 Colloidal metamaterials

Until very recently, research on lithographically fabricated metamaterials was mainly limited in 2 dimensions. In order to be considered "materials", however, the structures must have several layers in the third dimension.[2] In fact, operation of 2D metasurfaces is typically limited to certain angles and polarizations due to their planar nature, limiting applicability in practical devices. As such, fabrication of three-dimensional (3D) metamaterials is currently one of the major goals for the metamaterials community. Towards this end, one way to fabricate 3D metamaterials is to stack several metasurfaces on top of one another.[2] However, as each layer is fabricated using lithography, which is already time-consuming, the cost of 3D metamaterials prepared using this method greatly limits their widespread application.
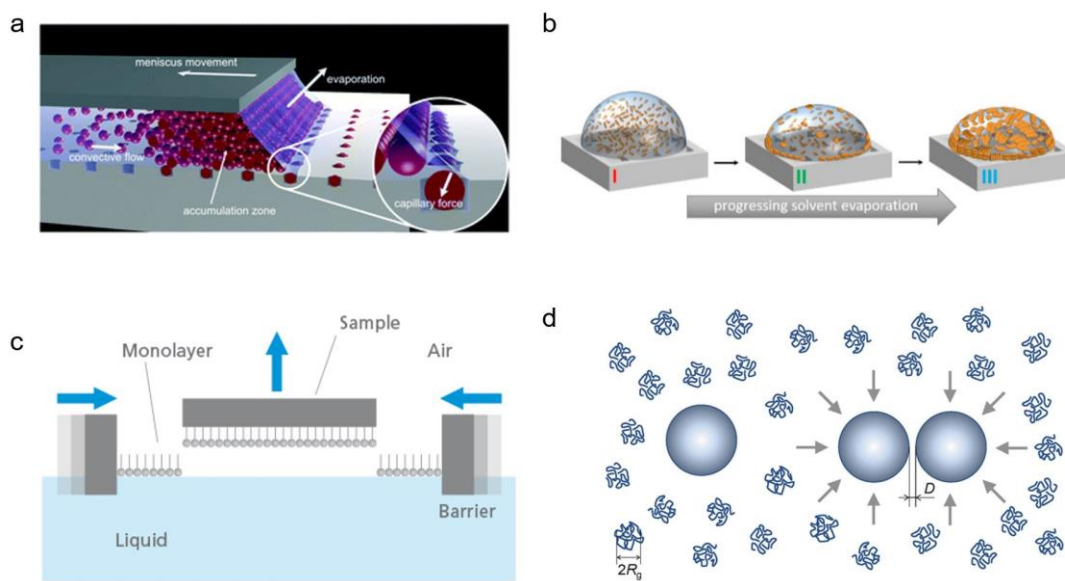
Figure 1-4. Methods to assemble colloidal nanoparticles. (a) Capillary force method. (b) Evaporative self-assembly. (c) Langmuir-Blodgett method. (d) Depletion force assembly.

On the other hand, bottom-up assembly of nanoparticles into 3D colloidal crystals has opened the possibility of exploring 3D metamaterials with engineered optical responses. Methods to assemble crystalline nanoparticle superlattices include convective self-assembly (Figure 1-4a),[50] depletion force assembly (Figure 1-4d),[51–53] enthalpic methods such as DNA-mediated assembly[54], and interfacial assembly methods such as the Langmuir-Blodgett technique (Figure 1-4c).[55] In all of these methods, achieving highly crystalline colloidal assemblies, or superlattices, requires nanoparticles to be synthesized in high purity and uniformity. Fortunately, numerous synthesis techniques have been developed to synthesize highly uniform nanoparticles with various sizes, shapes, and compositions.[56–60] Most notably, seed mediated synthesis,[61,62] which separates nucleation and growth stages into a 2-step synthesis, results in exceptionally uniform nanoparticles. Here, very small nanoparticles are prepared in a rapid nucleation step, using high concentrations of both metal ion precursor and reducing agent. Next, the small nanoparticles are used as "seeds" to template the growth of larger nanoparticles through the epitaxial deposition of
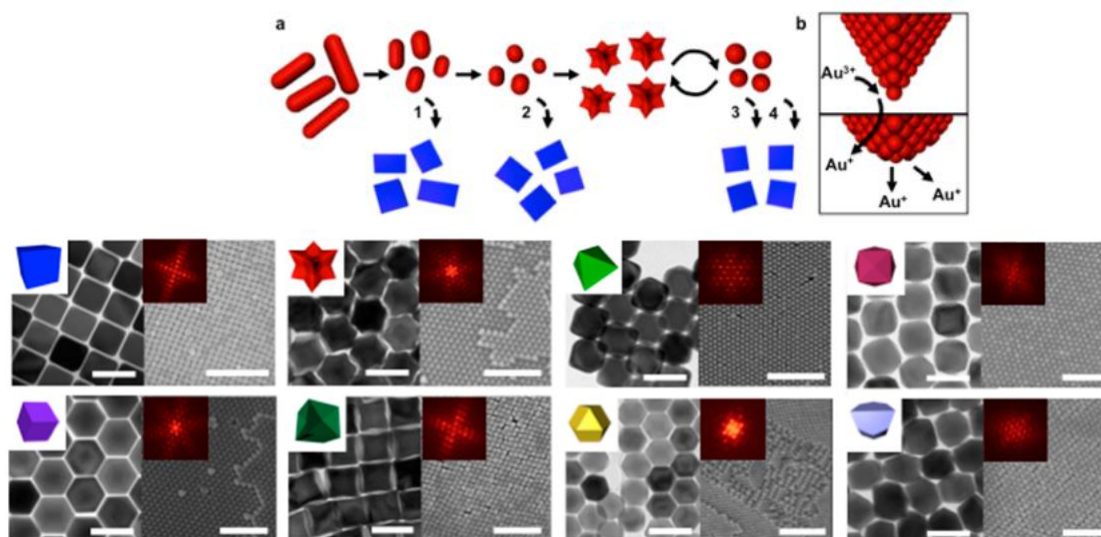
Figure 1-5. Seed-mediated synthesis of Au nanoparticles. (top) Uniform, spherical nanoparticles are synthesized using an iterative growth and etching process. (bottom) The nanoparticles are then used as seeds to template the growth of uniform anisotropic nanoparticles of various shapes and sizes. Figure adapted from Ref. 62.

reduced metal ions. Because the seeds were grown via rapid nucleation, their size dispersity is very small. As a result, subsequent overgrowth results in highly uniform nanoparticles. Notably, the Mirkin group developed a general Au seed synthesis procedure (Figure 1-5) which can be used to grow uniform anisotropic, Au nanoparticles of various shapes including the cubes (Chapters 2-6), octahedra (Chapter 4-6), and rhombic dodecahedra (Chapter 4) used in this work.[63] The procedure involves first growing single-crystalline Au nanorods and etching them into small, spherical Au nanoparticles. Next, the spherical nanoparticles are overgrown into concave rhombic dodecahedron particles and etched again into spheres, increasing their uniformity.

1.1.4 Plasmonic metamaterials

Plasmonic nanoparticles, made of noble metals such as Au or Ag, are the most commonly used building blocks for optical metamaterials due to their extraordinarily strong interactions with light.[9,64] Two types of plasmon resonances exist, localized surface plasmon resonances (LSPRs) and surface plasmon polaritons (SPPs). SPPs are electromagnetic waves which travel along a

metal-dielectric or metal-air interface. On the other hand, LSPRs, are excited when light of a specific frequency hits a plasmonic nanoparticle, causing a collective oscillation of its conduction electrons. The nanoparticle absorbs or scatters light extremely intensely at this resonance frequency, leading to vivid colors in their colloidal suspensions. Another useful feature of LSPR is that it is highly sensitive to nanoparticle size and shape.[64] For example, the LSPR of Au nanorods can be tuned between 600 nm and 2 µm by increasing their aspect ratio, allowing them to be used for both visible and IR applications.[65] To harvest these properties, researchers have devised methods to synthesize plasmonic nanoparticles, especially those of Au and Ag, with a wide variety of sizes and shapes.[57,66] In addition, when two plasmonic nanoparticles are placed close enough that they can interact in the near field, the resonances of individual particles hybridize, resulting in a shift in their LSPR wavelength as well as an immense field concentration in the gap between the two particles.[5,67] This coupling is extremely sensitive to structure, adding another design parameter to tune the properties of colloidal metamaterials. Indeed, the metamaterials community has devoted significant effort towards designing ordered arrangements of plasmonic nanoparticles that give rise to various effective behavior and developing methods to experimentally realize 2- and 3-dimensional arrays (or superlattices) of plasmonic nanoparticles using both lithography and colloidal assembly.[51,68,69] Additionally, all of the work in this thesis involves studies of crystalline assemblies of Au nanoparticles.

The strong absorbing and scattering ability of plasmonic nanoparticles also enables them to interact with excitonic media placed in their vicinity.[70–72] Depending on the position and emission wavelength of the excitonic material, its emission can either be quenched or enhanced by the plasmon resonance, modifying both emission lifetime and intensity.[73] This property is useful for preparing ultrabright or ultrafast light sources such as lasers,[74,75] as well as for detection

applications, where a molecule is quenched or enhanced near a plasmonic surface.[76] The broad spectral tunability of plasmon resonances enables these structures to interact with a virtually any excitonic wavelength in the visible and near-IR. Chapter 2 of this thesis studies the interaction of Au nanocube arrays with dye molecules placed in plasmonic hotspots.

1.2 Assembling Nanoparticles into Crystalline Metamaterials using DNA

1.2.1 Colloidal crystal engineering with DNA

The Mirkin group first introduced the idea of using DNA as a surface ligand to direct nanoparticle assembly in 1996.[77] This technique repurposes the genetic code as a synthetic material, utilizing the specificity of DNA binding (adenine (A) binds with thymine (T) and guanine (G) binds with cytosine (C)) to direct nanoparticles into predesigned structures. Due to their similarity to atoms, DNA-functionalized nanoparticles are termed "programmable atom equivalents (PAEs)".[78] By exploiting various surface chemistries, a wide variety of nanoparticles can be functionalized with dense shells of oligonucleotides.[79,80] To date, PAEs have been synthesized using nanoparticles of sizes ranging from 2 to 250 nm in diameter, a wide range of shapes, and diverse compositions including gold, silver, iron oxide, platinum, semiconductor quantum dots, and proteins.[81–84] To attach DNA to Au nanoparticles, such as those used in this work, DNA is synthesized with a thiol functional group on its 3' end, such that it can be easily attached to Au nanoparticles through ligand exchange, by exploiting Au-thiol bonding.[85] DNA sequences are then designed such that they direct nanoparticles to bind with one another through complementary base pairing, forming extended networks of nanoparticle aggregates.

Crystallization of DNA-functionalized nanoparticles into structures with long-range order was first reported in 2008, independently by Mirkin and Gang.[81,86] To form ordered crystals, researchers utilized weak DNA bonds (4-6 bases instead of 10-30), which allowed particles to

reversibly attach and reorganize when annealed just below the melting temperature (the point at which assemblies fully dehybridize into discrete nanoparticles). During this process, particles in unstable, disordered states reordered into the thermodynamically favored crystalline state. These studies also showed the use of DNA design to direct superlattice symmetry. Specifically, using self-complementary DNA resulted in the formation of closest-packed face-centered cubic (FCC) structures because PAEs could hybridize to every other particle in solution. On the other hand, when a binary non-self-complementary system of particles was used, particles functionalized with complementary DNA exhibited attractive interactions through DNA binding while particles functionalized with the same DNA exhibited only repulsive interactions due to the electrostatic repulsion between the negatively charged DNA backbones. As a result, non-close-packed body centered cubic (BCC) lattices were formed. Motivated by these initial studies, researchers have
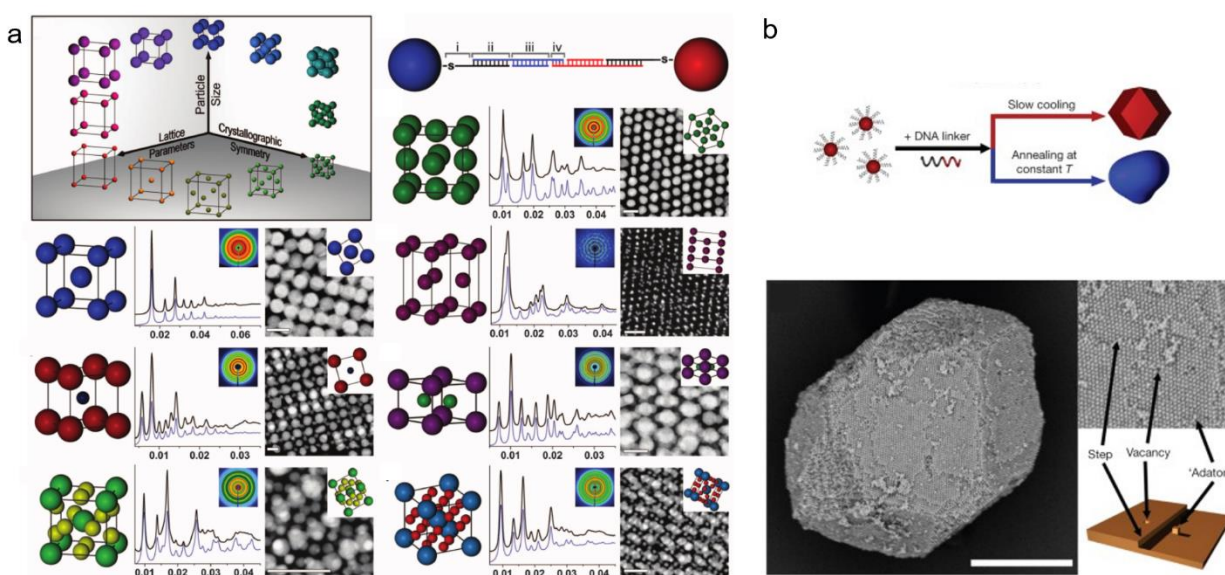
Figure 1-6. Assembling nanoparticle superlattices with DNA. (a) A few examples from a large library of nanoparticle superlattices which can achieved using this technique. Adapted from Ref. 2 (b) Slowly cooling DNA-functionalized colloids through their melting temperature results in faceted single-crystalline superlattices. Adapted from Ref. 86.

utilized colloidal crystal engineering with DNA to assemble ordered superlattices with over 50 structures (Figure 1-6a).[54,87]

Design rules were developed to predict and explain the formation of DNA-assembled superlattices, following the principle of maximizing hybridization events between commentary DNA strands. These rules are summarized into a "complementary contact model (CCM)", which was developed to predict lattice symmetry through the geometric overlap between neighboring complementary particles.[78] Initially, the model was based solely on enthalpic considerations, and ignored repulsive interactions between DNA strands. Later, the model was expanded to account for entropic considerations as well as a variety of repulsive interactions to predict assembly outcomes even more accurately.[88,89]

Finally, superlattices assembled with DNA can form discrete, well-defined microscale crystal habits. To grow these, instead of annealing below the melting temperature of a PAE system, PAEs are slowly cooled from above the melting temperature, through the entire melting transition, resulting in the thermodynamic Wulff polyhedron (Figure 1-6b).[90] Colloidal crystal assembly with DNA uniquely enables the preparation of 3D metamaterials with well-defined habits, which can be used to dictate their mesoscale photonic response, enabling shape-dependent resonances and directional light scattering.

1.2.2 Optical Properties of DNA-Assembled Superlattices

In Mirkin's 1996 paper, when DNA-functionalized Au nanoparticles were combined with complementary linker strands, the color of the solution changed from red to purple, indicating coupling between the nanoparticle LSPRs.[77] Crystalline SLs contain thousands of nanoparticles, which can exhibit complex coupling with one another. This coupling depends on the composition, size, and shape of nanoparticles, the distance between them, and the lattice symmetry, creating a

vast design space for engineering the SLs' optical response (Figure 1-7b).[91–94] In addition, the 3D crystal habit can be used to dictate the SLs' collective photonic responses. For example, Ag nanoparticle superlattices with Ag volume fractions between 5 and 25 % exhibited epsilon-near-zero (ENZ) response.[93] In another study, superlattices of high aspect ratio nanorods were shown, using electromagnetics simulation, to give rise to a variety of useful optical properties such as
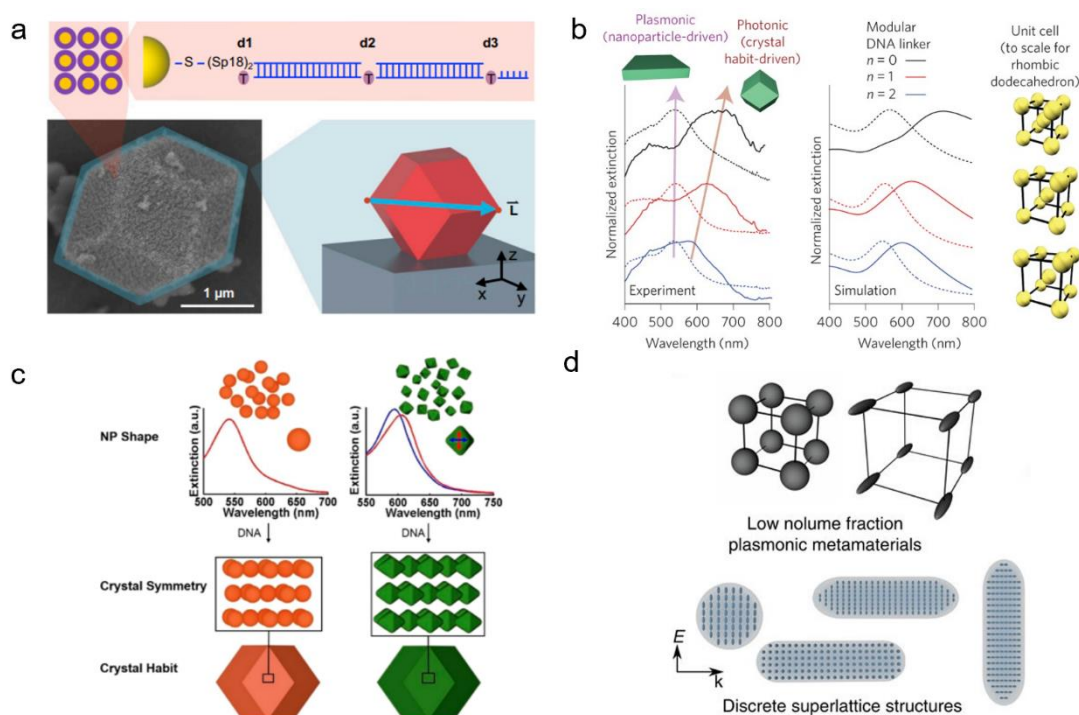
Figure 1-7. Emergent optical properties in DNA-assembled plasmonic nanoparticle superlattices. (a) Coupling dye-molecules to DNA strands holding together plasmonic nanoparticle superlattices results in enhanced emission lifetimes and intensities. Adapted from Ref. 94. (b) Design parameters for DNA-assembled nanoparticle metamaterials include nanoparticle size, DNA length, and crystal habit size and shape. Adapted from Ref. 93. (c) Superlattices assembled from anisotropic nanoparticles give rise to polarization-dependent responses. Adapted from Ref. 91. (d) Nanorod superlattices can be designed to exhibit novel optical properties that cannot be achieved using spherical nanoparticles. Adapted from Ref. 90.

birefringence and waveguiding (Figure 1-7d).[91] Finally, rhombic dodecahedron-shaped 3D superlattices were shown to behave as microcavities, exhibiting waveguiding behavior.[95]

Incorporating excitonic materials into DNA-assembled superlattices enables fabrication of light-emitting devices and studies of plasmon-exciton coupling. There are several ways to modify DNA-assembled Au nanoparticle superlattices with excitonic materials. First, dye molecules can be covalently attached to specific DNA sequences (Figure 1-7a), as utilized in Chapter 2 of this thesis. Alternatively, excitonic nanoparticles such as quantum dots can be made into PAEs and co-assembled with Au nanoparticles into crystalline superlattices. As an example of the first method, 3D BCC superlattices with rhombic dodecahedral crystal habits were used as microcavities for studying light emission from dye molecules coupled to the DNA strands that link the particles together.[96] The study showed that at the mesoscale, the rhombic dodecahedron crystal habit couples with photonic modes, resulting in directional light emission, while at the nanoscale, the dye dipoles interact with the nanoparticle LSPR in a distance-dependent manner to modify the emission intensity and lifetime. As an example of the second method, Gang et al. co-assembled quantum dots and Au nanoparticles into superlattices and showed that the quantum dots' fluorescence intensity and lifetime can be modulated with DNA bond distance between the Au nanoparticle and the quantum dot.[79]

1.2.3 Dynamic Superlattices

Another property of DNA that makes it especially useful for metamaterials preparation is its responsiveness to variety of chemical and physical cues. Specifically, DNA bonds can reversibly shrink and expand, or even break, in response to external triggers such as heat, solution polarity,[97] light,[98] and pH.[99] Actuation using these methods is not only reversible but also occurs on a relatively quick timescale, within seconds in many cases, making it especially promising for use in active metamaterials.[100] In this thesis (Chapters 2 and 5), solution polarity is used as the stimulus for actuating DNA. Using solution polarity to change the lattice constant between

nanoparticles in a DNA-assembled superlattice was developed by Mason et al.[97] In this work, ethanol was added in varying percentages to the aqueous saline buffer that DNA-assembled superlattices are usually crystallized and stored in. Ethanol has a much lower dielectric constant (~25) than water (~80), so it cannot solvate charged species as effectively. Because DNA is highly charged, it undergoes structural changes upon experiencing changes in solution dielectric constant. Small angle X-ray scattering (SAXS) results showed that as ethanol concentration was gradually increased from 0 to 80%, nanoparticle bond length in a BCC superlattice assembled from 20 nm particles decreased from 16 to 3 nm, for a total of 80% reduction in length.[97] This actuation technique was subsequently successfully used to change the length of DNA holding together a stack of plasmonic nanoparticles, thereby changing the interparticle distance. Because plasmon coupling depends sensitively on interparticle distance, the metasurfaces' absorption wavelength could be tuned between 400 and 700 nm.[100]

1.3 Dissertation Overview

As discussed, colloidal crystal engineering with DNA provides immense opportunity for the scalable fabrication of crystalline metamaterials, especially in 3D. The work of this dissertation explores this opportunity across multiple dimensionalities.

In Chapter 2, colloidal crystal engineering with DNA on template-confined surfaces is used to prepare arrays of nanocube-based plasmonic antennas and deliberately place dyes with sub-nm precision into their hotspots, on the DNA bonds that confine the cubes to the underlying gold substrate. This combined top-down, and bottom-up approach provides independent control over both the plasmonic gap and photonic lattice modes of the surface-confined particle assemblies and allows for the tuning of the interactions between the excited dyes and plasmonically active antennas. Furthermore, the gap mode of the antennas can be modified in situ by utilizing the

solvent-dependent structure of the DNA bonds. This is studied by placing two dyes, with different emission wavelengths, under the nanocubes and recording their solvent-dependent emission. It is shown that dye emission not only depends upon the in-plane structure of the antennas but also the size of the gap, which is regulated with solvent. Importantly, this approach allows for the systematic understanding of the relationship between nanoscale architecture and plasmonically coupled dye emission, and points towards the use of colloidal crystal engineering with DNA to create stimuli responsive architectures, which can find use in chemical sensing and tunable light sources.

Chapters 3 describes the DNA-mediated assembly and optical response of closely packed, 3D superlattices assembled from Au nanocubes. We show that such structures can exhibit refractive indices as large as ~8 in the mid-infrared, far greater than that of common high-index dielectrics. Additionally, we report the first observation of multipolar Mie resonances in metacrystals with well-formed habits, occurring in the mid-infrared for submicrometer metacrystals which we measured using synchrotron infrared microspectroscopy. Finally, we predict that arrays of metacrystals could exhibit negative refraction. These results present a promising platform for engineering devices with unnatural optical properties. A major synthetic advance in this work is the assembly of high volume fraction (>70%) superlattices, which enabled large capacitive coupling between neighboring nanocubes, resulting in the observed high refractive indices. To achieve this, we incorporated flexible spacer units into both the anchor and linker DNA strands, which allowed the cube PAEs to form crystals rather than the amorphous kinetic traps formed in previous studies of a similar system (large anisotropic NPs with short DNA bonds).

Chapter 4 explores the assembly and reorganization of a complementary system of anisotropic PAEs on substrates. Specifically, DNA was used to assemble polyhedral nanoparticles of three shapes – cubes, octahedra, and rhombic dodecahedra – on substrates. Subsequent thermal annealing induced reorganization of the amorphous assemblies into 2D crystalline films. Here, two new low-density 2D structures, including a honeycomb lattice based on octahedral nanoparticles were reported. The low-density lattices favored here are not usually seen when particles are crystallized via other bottom-up assembly techniques. Furthermore, consistent with the complementary contact model, it was shown that a primary driving force for crystallization is the formation of directional, face-to-face DNA bonds between neighboring nanoparticles and between nanoparticles and the substrate. This work shows how colloidal crystal engineering with DNA can be used to deliberately prepare crystalline superlattices with novel structures, which can potentially be used as optical metasurfaces.

In Chapter 5, we develop a high temperature crystallization technique to prepare highly crystalline 2D metamaterials comprised of colloidal gold nanocubes, over macroscopic areas. Using an effective medium description, the metasurfaces are shown to behave as dielectric media with high refractive indices that can be dynamically tuned by tuning DNA length. Furthermore, when coupled with an underlying thin gold film, the real permittivity of these metasurfaces exhibits a crossover region between positive and negative values, known as the epsilon-near-zero (ENZ) condition, which can be tuned between 1.5 – 2.6 µm by changing DNA length. Optical characterization performed on the DNA-assembled metasurfaces reveals that the predicted optical properties agree well with measured response. Overall, this work introduces an efficient method for realizing large-area plasmonic metasurfaces that enable dynamic control over unique optical characteristics.

In Chapter 6, uniform arrays of faceted, 3D superlattices are assembled inside micron-sized trenches. First, their assembly outcomes are explored using a combination of X-ray based techniques and electron microscopy. The results indicate that nanocubes form simple-cubic SLs with square-prism morphology and (100) out-of-plane orientation to maximize DNA bonding. In-plane, SLs align with the template, exposing their {100} side facets, and degree of alignment depends on trench size. Interestingly, the distribution of in-plane orientations determined from SAXS and SEM do not agree, indicating that the internal and external structures of SLs differ. To understand this discrepancy, X-ray ptychography was employed to image the SLs' internal structure and discover that SLs which appear as single crystals in SEM may have subsurface grain boundaries, depending on trench size. By tracing the growth process using SEM, we discover that SLs grow *via* nucleation and growth of randomly oriented domains, followed by their coalescence, explaining the observed size-dependence in alignment and defect structure. Interestingly, we discovered that crystallization occurs *via* an unusual growth mode, whereby continuous SL layers grow on top of several misoriented islands.

Next, the emergent optical properties of the superlattice arrays are examined. Specifically, we found that the templated superlattices preserve the mid-IR Mie resonances described as in Chapter 3, with resonant wavelength tunable through trench (superlattice) size. Importantly, the superlattice arrays exhibit uniform optical response in the mid-IR, enabling measurement of their ensemble properties using laboratory FTIR instruments.

Finally, Chapter 7 summarizes the work in this thesis and describes some of the future outlooks for using colloidal crystal engineering with DNA to scalably fabricate 3D optical metamaterials and metadevices with emergent properties and applications.

CHAPTER 2

Tunable Fluorescence from Dye-Modified DNA-Assembled Plasmonic Nanocube Arrays

This chapter is based on published work:

C.Y. Zheng*, E. Palacios*, W. Zhou, G. C. Schatz, K. Aydin, C. A. Mirkin, et al., "Tunable Fluorescence from Dye-Modified DNA-Assembled Plasmonic Nanocube Arrays" *Adv. Mater.*, **2019**, 31, 1904448. (*indicates equal contribution)

2.1. Background

Plasmonic nanoparticles[101] (NPs) give rise to strong electric field (E-field) confinements, and therefore, when coupled with nearby emitters such as dye molecules or quantum dots, act as antennas to enhance their emission rates and intensities.[102,103] These so-called plasmonic nanoantennas can be used in lasing,[104] molecular sensing,[64] and quantum information processing.[105] Although single NPs can function as plasmonic nanoantennas,[70] typically researchers exploit dimers of NPs,[106,107] particles coupled with a metallic surface,[108–110] or arrays of particles lithographically placed into configurations that lead to optimum plasmonic coupling effects.[107] The nanoscale patch antenna geometry,[108–110] where a nanoparticle is positioned a short distance above a metallic film with a dielectric spacer, gives rise to a plasmonic gap mode that enhances light absorption and subsequent fluorescence. When plasmonic NPs are placed in an array with a periodicity comparable to the wavelength of light, long-range radiative coupling between localized surface plasmons (LSPs) of single NPs give rise to diffraction modes in the plane of the array known as surface lattice resonances (SLRs, or lattice plasmons), producing even stronger field enhancements and higher quality resonances.[74,111] Consequently, particle arrays have found use in both lasing[75] and sensing.[112,113]

Colloidal crystal engineering with DNA is emerging as a robust method for controlling crystal composition, lattice parameter, and habit.[79,81,84,87,90,114] In addition to being useful for preparing 3-dimensional assemblies, the technique can be combined with top-down lithography (e.g. e-beam, EBL) to position nanoparticles on substrates, which allows one to synthesize 2-dimensional structures not attainable through conventional lithographic techniques.[100,115] For example, arrays of single crystalline nanocubes that display strong coupling between plasmonic gap modes and photonic lattice modes[116] have been assembled on gold-coated silicon substrates. Here, we explore how such structures, combined with DNA structural sensitivity to solvent,[97,100] can be used to modify the emission properties of dyes strategically placed into the E-field hotspots of the particle array structure. These studies reveal four novel and attractive characteristics of such assemblies which enable precise control over structural parameters that affect the plasmonic resonances, coupling strength, and emission enhancement. First, the emission of the dye can be controlled through lattice spacing, which controls the lattice mode resonance. Second, the gap mode resonance, tunable through DNA length and solvent,[97] can be used to control dye emission. This is important because it allows one to do so without irreversibly changing lattice structure. Third, the position of the dye, which can be controlled through chemical attachment to specific bases, can be fine-tuned with sub-nm precision and used to influence and optimize emission.[73,117] Finally, using multiple different dyes, emission of each can be regulated through an understanding of these effects and coupling to specific structures. Exploration of active tunability in plasmonic patch antennas is preliminary and typically involves employing thermoresponsive polymers as gap materials,[118,119] which does not enable precise emitter coupling. Methods to couple dye molecules into antennas include using macrocyclic molecules[120] or DNA origami[121] to position the dye molecules inside the gap. These are neither scalable nor allow for active tuning. Our method

enables not only precise positioning of the dye molecules in a repeatable and scalable manner, but also controllable and reversible tuning using solvent-responsive DNA.

2.2. Results and Discussion
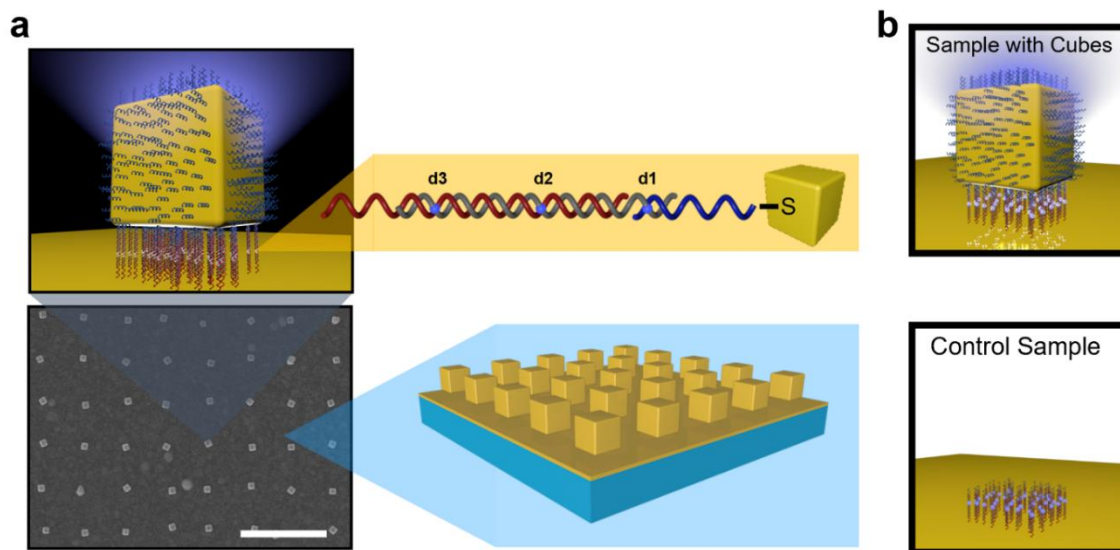
Figure 2-1. a) Schematic showing dye-functionalized nanocube arrays. Scale bar is 1 µm. Thiolated DNA is functionalized onto the substrate (red) and the nanocube (blue), a complementary linker strand (grey) is hybridized to the substrate DNA, which leaves a single-stranded binding region that is complementary to the nanocube binding region. The dye is attached to the linker strand at one of three binding sites (blue dots, denoted d1, d2, and d3) on the linker strand. b) Schematic of the samples with cubes and a control sample (DNA modified with dye without cubes).

To explore these structure-function relationships, dye-functionalized gold nanocube arrays were assembled using template-confined DNA-mediated assembly[100,115,116] (Figure 2-1a). First, EBL was used to pattern poly(methyl methacrylate) (PMMA) pores at desired lattice positions on gold-coated Si substrates, with the bottom of each pore consisting of exposed gold. Both the nanocubes and the exposed gold in the pores were densely functionalized with specific sequences of propylthiolated DNA. Dye-labeled linker strands complementary to the substrate strand were then hybridized to the substrates. Note that these DNA strands were synthesized with amino-modified dT groups at the desired base, where dye-labeled NHS esters can be covalently linked.

80 nm cubes were assembled in the pores by designing their single-stranded binding region to be complementary to the binding region of the linkers. Previous work using this technique hybridizes linker strands to both the gold substrate and the NPs and then assembles the NPs within the pores using complementary binding regions on the two linkers. However, in this approach, only a single linker was attached to the substrate, which was directly hybridized to the binding region of the thiolated DNA on the cube to allow one to position the dye near the cube (Figure 2-1a, top). Cube-functionalized DNA were not directly labeled with dyes because only dyes underneath the cube are inside the plasmonic hotspots. Due to the short length of the DNA strands on the cube (15 bases compared to conventionally used 28 bases[115,116,122]), assembly was done in aqueous 0.3 M NaCl, rather than 0.5 M, and at lower temperatures, in order to keep the cubes from aggregating. The successful implementation of this new 3-strand DNA design, which asymmetrically incorporates dye molecules underneath the nanocubes, highlights that we can change DNA design and assembly conditions to create structures required for a desired optical response not achievable with previously studied designs. After assembly, the PMMA template was removed, and the samples were transferred to 0.5 M NaCl buffer for optical characterization.

Dye-labeled nanocube arrays with periodicities from 400 to 880 nm in 20 nm increments were assembled onto the same substrate (Figure 2-2). ATTO 680 was chosen as the dye since it emits at 702 nm, within the range of experimentally accessible lattice and gap modes. A control sample was made by hybridizing dye-labeled linker DNA to the substrate DNA without the final step of assembling nanocubes in order to quantify the enhancement in dye photoluminescence (PL) from the nanocube arrays (Figure 2-1b). The control sample can also account for differences in dye density between different array periodicities and slight variation of dye emission in different

solvents. PL measurements were taken by illuminating the samples with a 633 nm HeNe laser coupled to an inverted microscope and spectrometer. PL maps were collected at 700 nm, near the dye emission maximum (Figure 2-2c,d). To obtain fluorescence enhancement factors, the fluorescence of the sample was normalized to that of the control (Figure 2-9). A significant enhancement was observed (maximum of ~20), with certain periodicities having larger enhancements due to the presence of lattice or gap modes. Importantly, the unique ability to place dyes only in plasmonic hotspots allowed for large-area characterization, whereas other work on similar geometries only measured PL from under individual nanocubes.[109,110]
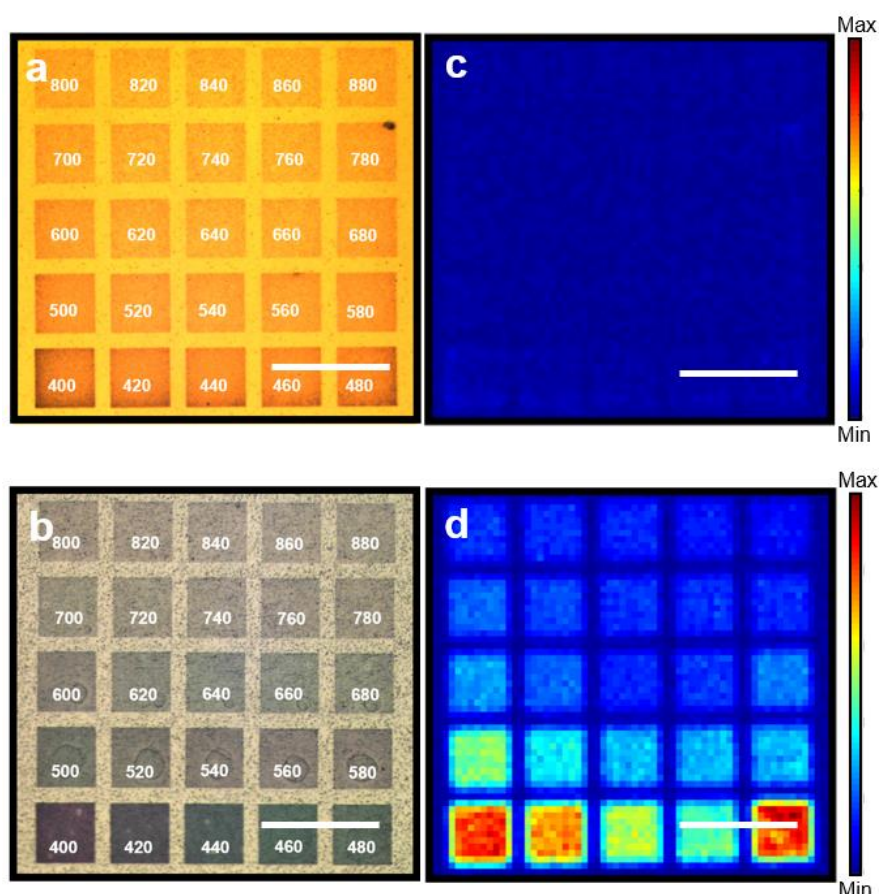
Figure 2-2 a,b) Optical images of the control sample (DNA modified with ATTO 680 without cubes) and sample with cubes, respectively. The periods are labeled on each corresponding array. c,d) Corresponding PL maps. Scale bars are 200 µm.
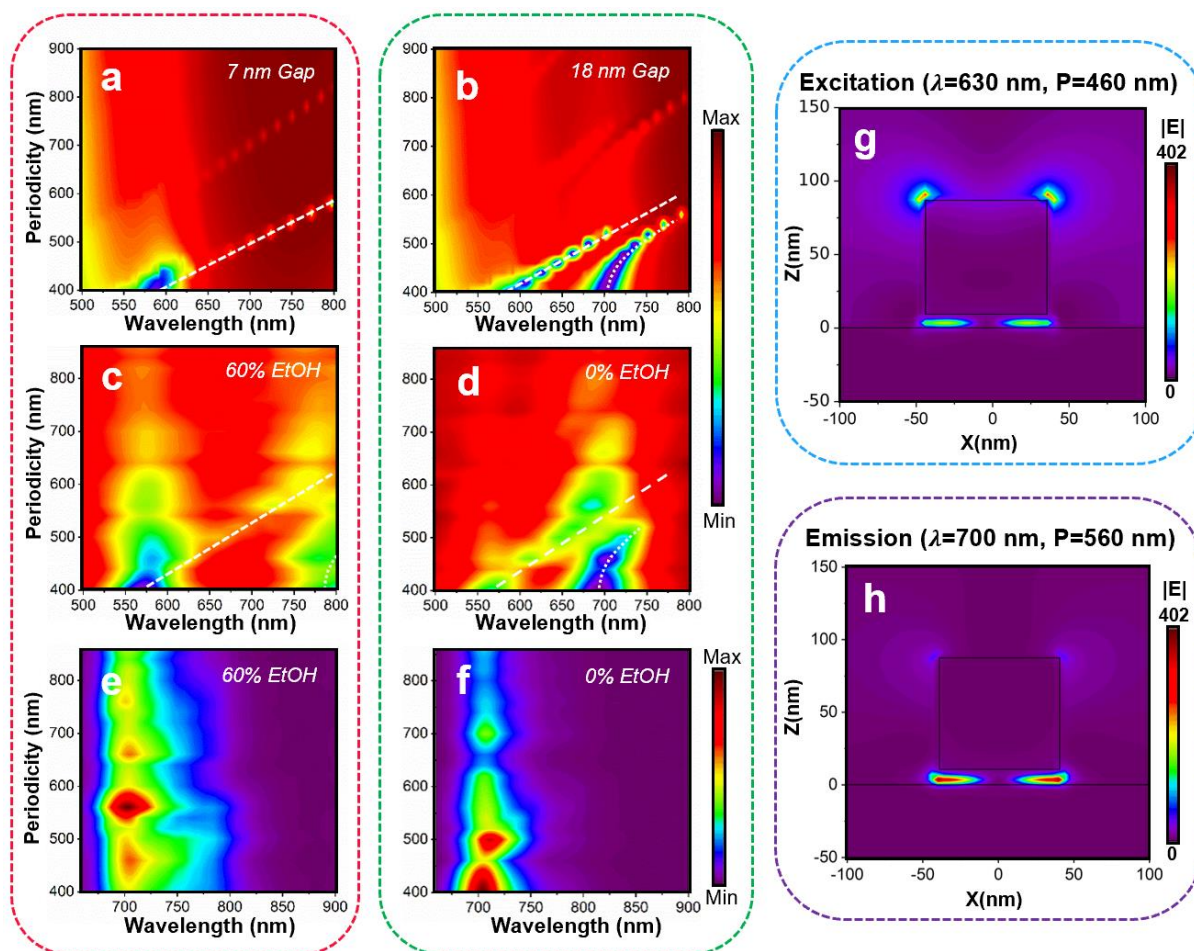
Figure 2-3. a,b) FDTD simulation of reflection spectra for 7 and 18 nm gap arrays. The white, dashed lines indicate lattice modes and dotted lines indicate gap modes. c,d) Corresponding experimental reflection spectra at 60% and 0% ethanol, respectively. The reflection minima near 570 nm in all spectra a-d are from individual nanocube resonances. e,f) Experimental PL spectra at 60% and 0% ethanol, respectively. g) E-field plot of the excitation enhancement at a 7 nm gap h) E-field plot of the emission enhancement at a 7 nm gap.

To explain the trends in PL at different periodicities, lattice and gap mode dispersions were measured experimentally at 0 and 60% ethanol in water at constant 0.5 M NaCl and calculated using finite-difference time-domain (FDTD) simulations. To experimentally characterize the interaction of nanocube arrays with dye emission and laser excitation, optical and PL measurements were performed between 500 and 800 nm wavelengths using an inverted optical microscope in reflection mode. In order to correlate ethanol concentrations to gap distances, experimental reflectivity spectra were compared to FDTD spectra at different gap distances. From

this comparison, 0% ethanol correlates with an 18 nm gap and 60% ethanol with a 7 nm gap, falling within the range of expected gap sizes[97] (Figure 2-3a-d). The lattice modes can be recognized through their dispersive nature, whereas gap modes depend on gap size, which changes with solvent.

PL intensity was examined as a function of lattice periodicity (Figure 2-3e,f). At 60% ethanol, the dye emission and laser excitation only overlap with lattice modes, which depend on periodicity. The PL maximum occurs at a periodicity of 560 nm, where the strong enhancement is attributed to coupling between the dye emission and lattice mode around 700 nm. A smaller PL peak occurs for a periodicity of 460 nm and, in this case, is due to coupling between the laser and the lattice mode around 630 nm. These peaks occur at periodicities for which the lattice mode overlaps with either the incident laser or dye emission wavelengths and are known as excitation and emission enhancement, respectively. Although in both cases coupling with lattice modes occur, enhancement is dependent on the E-field inside the gap, shown in simulations to be higher at the emission energy for 560 nm periodicity than at the excitation energy for 460 nm periodicity (Figure 2-3g,h). At other periodicities the lattice mode does not cross with either the laser excitation or dye emission, yet still produce increased PL relative to the reference sample, attributed to non-resonant E-field enhancements inside the gap. At 0% ethanol, PL maxima occur for 400 and 500 nm periodicities. In both cases, emission enhancements are observed, but this time, in the presence of the gap mode occurring near 700 nm. Only a gap mode exists for 400 nm periodicity, but for 500 nm periodicity the dye emission is in the regime of lattice-gap coupling and could be interacting with both modes simultaneously. The ability for two spectrally separate, yet spatially overlapping, tunable modes, to interact with the dye could be used to simultaneously

produce excitation and emission enhancements. Furthermore, the gap mode can be tuned in situ

by changing solvent polarity (Figure 10).
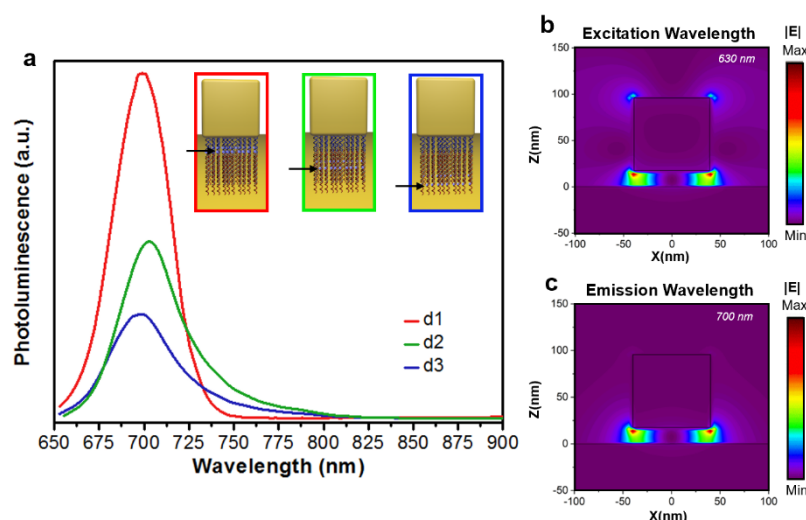
Figure 2-4. a) PL for three locations of the dye. In all cases, nanocubes are assembled in a 400 nm lattice and measurements are performed in buffer with 40% ethanol. b) Calculated E-field intensity profile at the dye excitation wavelength (630 nm) for a nanocube separated from a gold film by a 16 nm gap. c) The same calculation done at the dye emission wavelength (700 nm).

To study the distance dependence of the plasmon-exciton interactions, PL was measured

at three dye-to-cube distances between the bottom of the cube and the film (5, 10, and 15 nm,

termed d1, d2, and d3) in 40% ethanol (~16 nm DNA length) and a 400 nm period array. Here, the

dye experiences emission enhancement from a gap mode at 700 nm. We found that the PL intensity

decreased from d1 to d2 to d3 (Figure 4a). This trend can be explained by the calculated E-field

intensities at the excitation and emission wavelengths (Figure 2-4b,c). In both cases, the E-field is

strongly localized in the gap near the nanocube edges, characteristic of a gap mode, explaining

why d1 has the highest PL. When the dye is too close to either the cube or the substrate, the PL

intensity could be diminished, due to non-radiative quenching.[70]
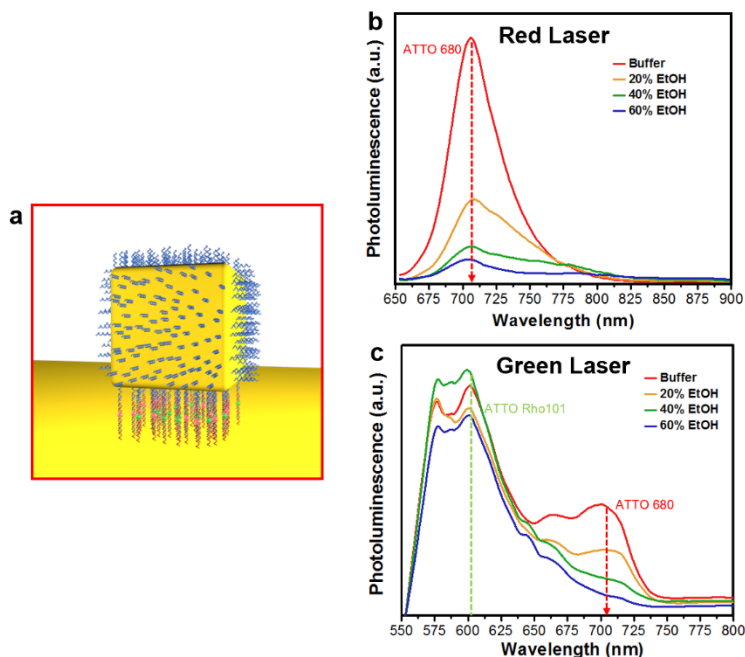
Figure 2-5. Samples prepared with and two dyes (Atto Rho 101 and Atto 680) under the cubes randomly dispersed in the d1 plane a) Schematic. b,c) PL measurement at varying ethanol concentrations when the sample is excited with a b) red and c) green laser.

Finally, to explore the potential for such lattices in tunable optics, 400 nm period array samples with two dyes under the nanocubes were prepared. These assemblies contained one dye that emits at 609 nm (ATTO Rho101) in the d1 position in addition to the original dye; both dyes are physically in the same proximity to the cubes but randomly mixed within the d1 plane (Figure 2-5a). Since the dyes have different excitation wavelengths, they can be addressed in a wavelength-dependent manner. Irradiation with 635 nm light (red laser, Figure 2-5b), leads to single dye emission, while exciting with 543 nm light (green laser, Figure 2-5c) leads to emission from both dyes. In both cases one can clearly see that ethanol can contract the DNA and shorten the gap distance, which in turn diminishes the ATTO 680 emission with little effect on that of ATTO Rho101. Indeed, at 0% ethanol, the gap mode is spectrally matched with the emission maximum of ATTO 680 (Figure 2-10a), causing enhanced emission near 700 nm, while at 60% ethanol, the gap mode moves away from the dye emission, resulting in little fluorescence. In contrast, the

emission of ATTO Rho101, is relatively unaffected by ethanol since it is spectrally mismatched with the gap mode at all ethanol concentrations. It has a large peak near 609 nm, at all ethanol concentrations, because of its inherently high quantum yield coupled to off-resonant enhancement. Therefore, by changing the concentration of ethanol, the intensity ratio of the two dyes can be tuned, yielding a tunable light source.

2.3. Conclusions

In conclusion, we have shown that template-confined colloidal crystal engineering with DNA can be used to construct plasmonic nanoantennas with individual control over in situ tunable plasmonic gap modes and in-plane photonic lattice modes, both capable of enhancing the emission behavior of fluorophores strategically placed into the antenna hotspots. Additionally, the molecular-level control over the placement of dye molecules afforded by using DNA as linkers allows for fine-tuning of plasmon-exciton interactions. The geometry of the nanoantennas can be optimized in the future for different emission responses by using other anisotropic nanoparticles such as elongated rods and flat disks, or by arranging the nanoparticles in arrays of oligomers. In principle, this novel technique will allow for the fabrication of tunable plasmonic nanoantennas that can be tailored to achieve the desired emission responses in chemical sensing, lasers, and other forms of tunable light sources.

2.4. Experimental Details

Materials. Au nanoparticles were purchased from BBI via Ted Pella, Inc., and reagents for DNA synthesis were purchased from Glen Research. Chemicals were purchased from Sigma-Aldrich. Milli-Q® water was used in all aqueous solutions.

Nanoparticle Synthesis. Single crystalline gold cubes were synthesized via a seed-mediated method described in detail by O'Brien et al.[63] Briefly, uniform single crystalline spherical gold nanoparticles were synthesized via an iterative chemical growth and etching process. These nanoparticles were then used as seeds for the growth of anisotropic nanoparticles, including these cubes. This synthetic procedure results in structurally uniform anisotropic nanoparticles synthesized with high yield, which makes them ideal for use in optical property measurements that rely on long-range order. In this work, the average edge length of cubes was determined to be 80 $\pm$ 3 nm as measured by scanning transmission electron microscopy (STEM, Hitachi HD-2300).
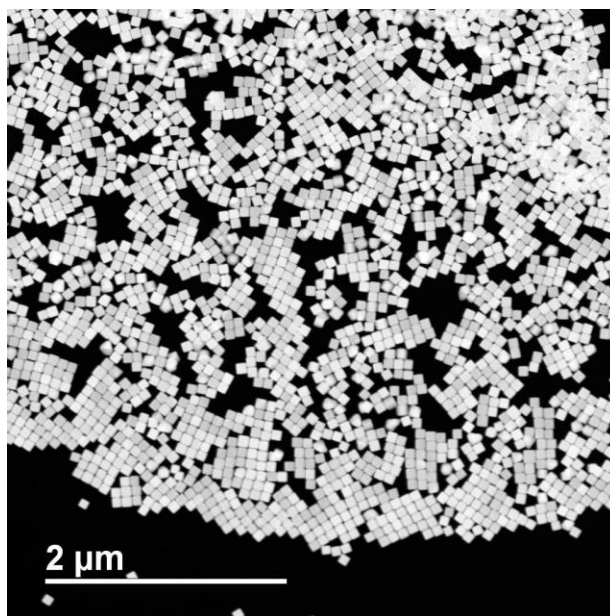
Figure 2-6. STEM images of gold nanocubes with edge length 80 ± 3 nm

Substrate Fabrication. PMMA pores were fabricated on Au-coated Si substrates with electron beam lithography (EBL). First, a Si wafer was cleaned via an O_2 plasma at 50 W for 5 min. Following plasma cleaning, electron beam evaporation (Kurt J. Lesker Company) was used to deposit a 5 nm Cr adhesion layer, followed by a 100 nm Au layer onto the Si substrate. The wafer was then cut into pieces (1.5×1.5 cm^2) and stored in a vacuum desiccator. Substrates were then spin-coated with positive e-beam resist (poly(methyl methacrylate), PMMA, 495 A2, MicroChem) at 4000 rpm, resulting in a ~50 nm thick PMMA layer. The PMMA was then baked at 200 °C for 60 s, followed by EBL using a FEI Quanta ESEM to define the trenches. Specifically, we used an accelerating voltage of 30 kV with a dosage of 150-250 µC/cm^2 to pattern squares with 120 nm edge length over a 100×100 µm^2 area for each periodicity. The substrates were then developed in a methyl isobutyl ketone (MIBK) / isopropyl alcohol (IPA) 1:3 solution for 60 s, rinsed with IPA, and blown dry with N_2. After development, each substrate was cleaned using O_2 plasma at 50 W for 1 min (O_2 pressure: ~200 mBar) to remove potential PMMA residue at the bottom of pores and cut into four smaller pieces to fit in 2 mL Eppendorf tubes, which was necessary for surface functionalization with DNA.

DNA Synthesis and Purification. All oligonucleotides used in this work were synthesized on a BioAutomation MerMade 12 (MM12) automated oligonucleotide synthesizer using reagents purchased from Glen Research. After synthesis, all DNA was purified with reverse-phase high-performance liquid chromatography (HPLC, Agilent) followed by standard deprotection procedures. Matrix-assisted laser desorption ionization time-of-flight mass spectrometry (MALDI-TOF-MS) was used to characterize the purified oligonucleotides and confirm their molecular weight.

Dye Labeling of Linker Strands. Purified DNA linker strands were labeled with ATTO 680 or ATTO Rho101 NHS Ester. The dye-labeled DNA was characterized again with MALDI-TOF-MS. Separation of free dyes was not necessary because they are washed away along with any unhybridized DNA strands in subsequent steps.

DNA Functionalization. The DNA sequences used in this work are listed in Table S1 and functionalization procedures are modified from the literature.[123] Briefly, we functionalized particles with 5' propylthiolated DNA and substrates with 3' propylthiolated DNA sequences. Then, a complementary linker DNA strand was hybridized the substrate DNA. The linker strand possessed a short 5-base single-stranded region complementary to the 5-base single-stranded region on the particle DNA, in order to link the particles to the substrates through complementary DNA hybridization events.

Table S1. DNA Sequences used in this work

Description	DNA Sequences (5' to 3')
Particle DNA	SH (CH$_2$)$_3$ - AAA AAA AAA A TCTCT
Substrate Anchor DNA	TTT TTT TTA CTG AGC AGC ACT GAT TTT TTA AAA AAA AAA A - (CH$_2$)$_3$ SH
Substrate Linker DNA d1	TAA AAA ATC AGT GCT GCT CAG TAA AAA AAA (A-dT) AGAGA
Substrate Linker DNA d2	TAA AAA ATC AGT GC (A-dT) GCT CAG TAA AAA AAA A AGAGA
Substrate Linker DNA d3	(A-dT) AA AAA ATC AGT GCT GCT CAG TAA AAA AAA A AGAGA

- "A-dT" refers to Amino-Modifier C6 dT manufactured by Glen Research

Cubes were functionalized using a procedure modified from that described by Jones et al.[124] and O'Brien et al.[125] Briefly, 3' propylthiol-modified oligonucleotides were first treated with a 100 mM solution of dithiothreitol (DTT) in 170 mM sodium phosphate buffer (pH = 7.4), followed by purification on a Nap-5 size exclusion column (GE Life Sciences) to remove DTT. During this time, 1 mL aliquots of the cube solutions were centrifuged for 8 min at 5,800 rpm, the supernatant was removed, and the nanoparticles were resuspended in water. The cubes were then centrifuged a second time for 8 min at 5,800 rpm, the supernatant was removed, and then the purified DNA and water was added to the pellet immediately. 5 µmol of thiolated DNA were added per 1 mL of particles. The particle solution was then brought to 0.01 M sodium phosphate buffer (pH = 7.4) and 0.01 wt. % sodium dodecyl sulfate (SDS) in water. Stepwise addition of 2 M NaCl was then carried out every half hour, such that the NaCl concentration was increased to 0.05 M, 0.1 M, 0.2 M, 0.3 M, respectively. Following this process, the nanoparticles were placed on a shaker at 1,000 rpm and left overnight to ensure a dense loading of oligonucleotides. After functionalization, the nanoparticle solutions were centrifuged three times to remove excess DNA. After each of the first two round of centrifugation, nanoparticles were resuspended in 0.01 wt. % SDS, and after the last centrifugation step, the particles were resuspended in 0.3 M NaCl, 0.01 M sodium phosphate buffer (pH = 7.4), and 0.01 wt. % SDS. For DNA functionalization of the substrate, the procedure was similar as describe above. Specifically, 1 µmol of DTT-treated DNA in water was added to each substrate. However, instead of stepwise addition of NaCl, the substrates were brought to 1 M NaCl in one addition, and then shaken overnight at 1,000 rpm. Substrates were then rinsed three times with water and placed in a 0.5 M NaCl, 0.01 M sodium phosphate buffer (pH = 7.4), and 0.01 wt. % SDS solution. After functionalization with thiolated DNA strands, linker strands were hybridized to the substrate. Substrates were incubated in a solution containing 0.5 µM linker and

subsequently heated to 55 ºC for 30 min, then allowed to slowly cool to room temperature to ensure full hybridization between anchor and linker DNA sequences.

Nanocube Array Assembly. Following linker hybridization, the substrates were rinsed in a 0.5 M NaCl, 0.01 M sodium phosphate buffer, and 0.01 wt. % SDS solution three times. Substrates were then placed in a small cube solution and shaken at 1,000 rpm for 6 hours at room temperature. During this time, cubes assembled preferentially into the trenches functionalized with DNA at the bottom. After assembly, the substrate was then vigorously rinsed three times in 0.5 M NaCl, 0.01 M sodium phosphate buffer, and 0.01 wt. % SDS solutions. Then they were immersed in 80% IPA in water (by volume) with 0.2 M ammonium acetate (AA) at 45 ºC for 30 minutes to remove the PMMA. Next, the substrates were transferred back into the buffer for optical characterization. For SEM, substrates were rinsed three times with a solution of 80% IPA (by volume) and 0.2 M AA and blown dry with N_2. in addition to removing the PMMA, alcohol reduces the solvent polarity around the DNA-assembled nanocube arrays, which condenses the DNA bonds between nanoparticles and allows the structures to be transferred with little disturbance from the solution phase to the solid state. Figure S2 and S3 show SEM images of assembled nanocube arrays.
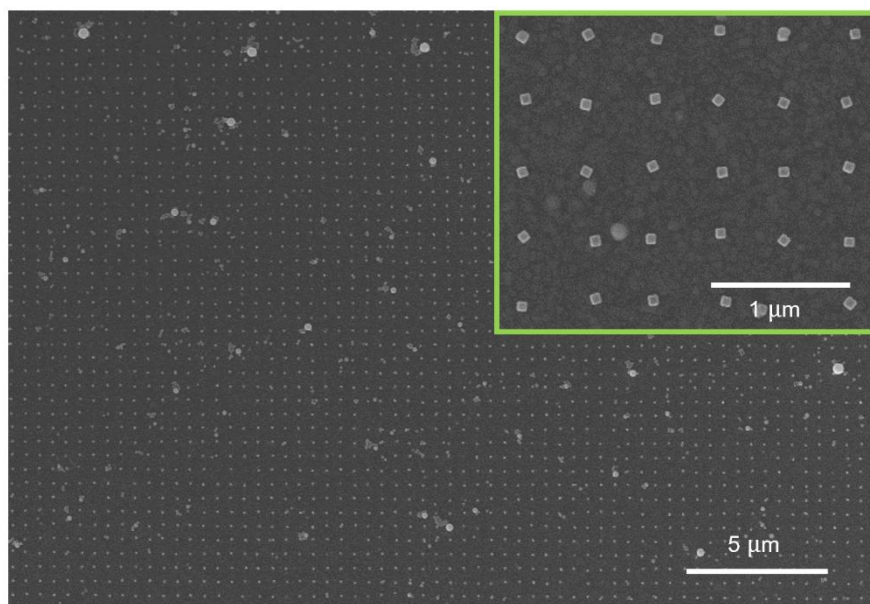
Figure 2-7. Large scale SEM images of assembled nanocube arrays with 500 nm periodicity. The large circular particles are salt crystals that were dried from the saline buffer.
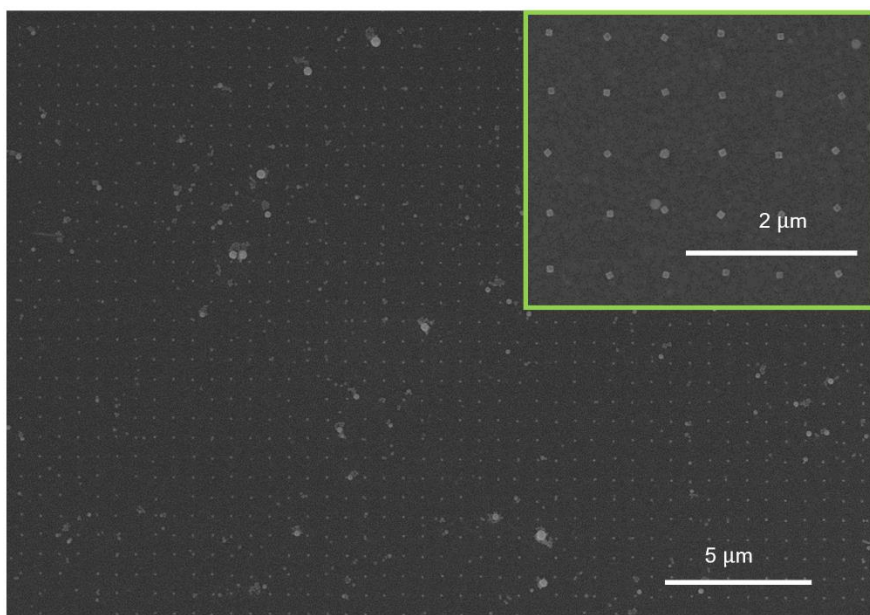
Figure 2-8. Large scale SEM images of assembled nanocube arrays with 700 nm periodicity

Reflection Measurements. An inverted microscope equipped with a spectrometer consisting of a 303-mm-focallength monochromator and Andor Newton electron multiplication charge-coupled device (EM-CCD) camera was utilized for optical measurements. A broadband halogen light source was used. Reflected light was collected from a $32 \times 32 \ \mu m^2$ area using a 5x Nikon microscope objective with a numerical aperture of 0.15. An optically thick (100 nm) planar gold film was used as a reference to calibrate the reflection of gold cube samples.

Photoluminescence Measurements. Measurement was carried out in a homemade photoluminescence setup. HeNe laser (Thorlabs) with wavelength of 633 nm was used as excitation source. The focused laser beam was coupled into an upright microscope (Nikon Eclipse Ti-U) with a computer controlled x-y piezo stage (Thorlabs MLS203). Emitted and reflected beam from the sample is then filtered through a 650 nm long pass filter and coupled into a spectrometer (Andor Technology) containing multiplication charge-coupled device (EM-CCD) (Andor Newton). Single photoluminescence measurement was performed from an exposed area of $\sim 25 \times 25 \ \mu m^{2.}$ Meanwhile, the mapping was carried out by measuring photoluminescence from an exposed area of $\sim 13 \times 13 \ \mu m^2$ then scanning throughout the sample with a step length of 10 um in both x and y direction.

FDTD Simulations. Electromagnetic wave numerical calculations were performed using the finite-difference time-domain simulation software package Lumerical™. A unit cell of the structure was simulated using periodic boundary conditions along the x and y axes and perfectly matched layers (PML) along the propagation of electromagnetic waves (z-axis). Plane waves were launched incident to the unit cell along the +z direction. A mesh override was set over the Au cubes to 1 nm x 1 nm x 1 nm with a variable length buffer representing the gap distance. Refractive

indices were taken from literature[4] for Si and Au while the DNA and background indices were set to a constant 1.35.

Fluorescence Enhancement Factors
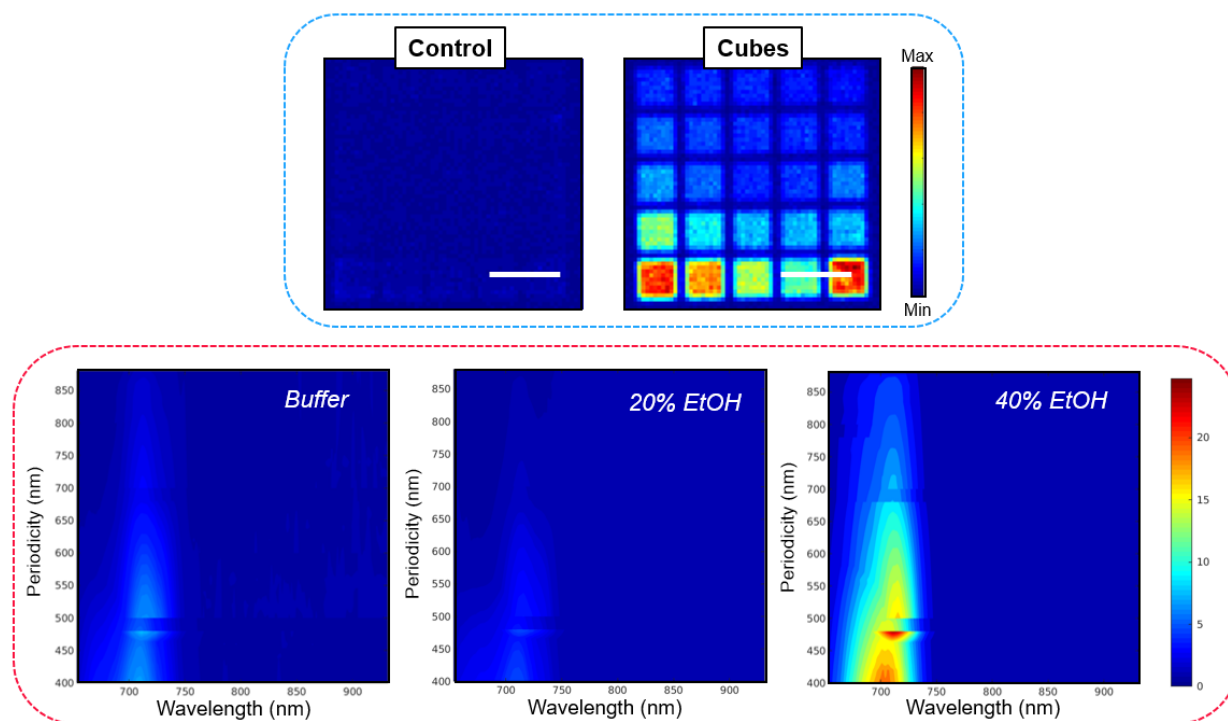
Figure 2-9. PL mapping of the control sample and the sample with cubes arrays. (top) PL enhancement factors for 0%, 20%, and 40% ethanol concentration. (bottom) Enhancement factors calculated by dividing the PL of the sample with cube arrays by the PL of the control sample at each periodicity.

Effect of Gap Length on PL
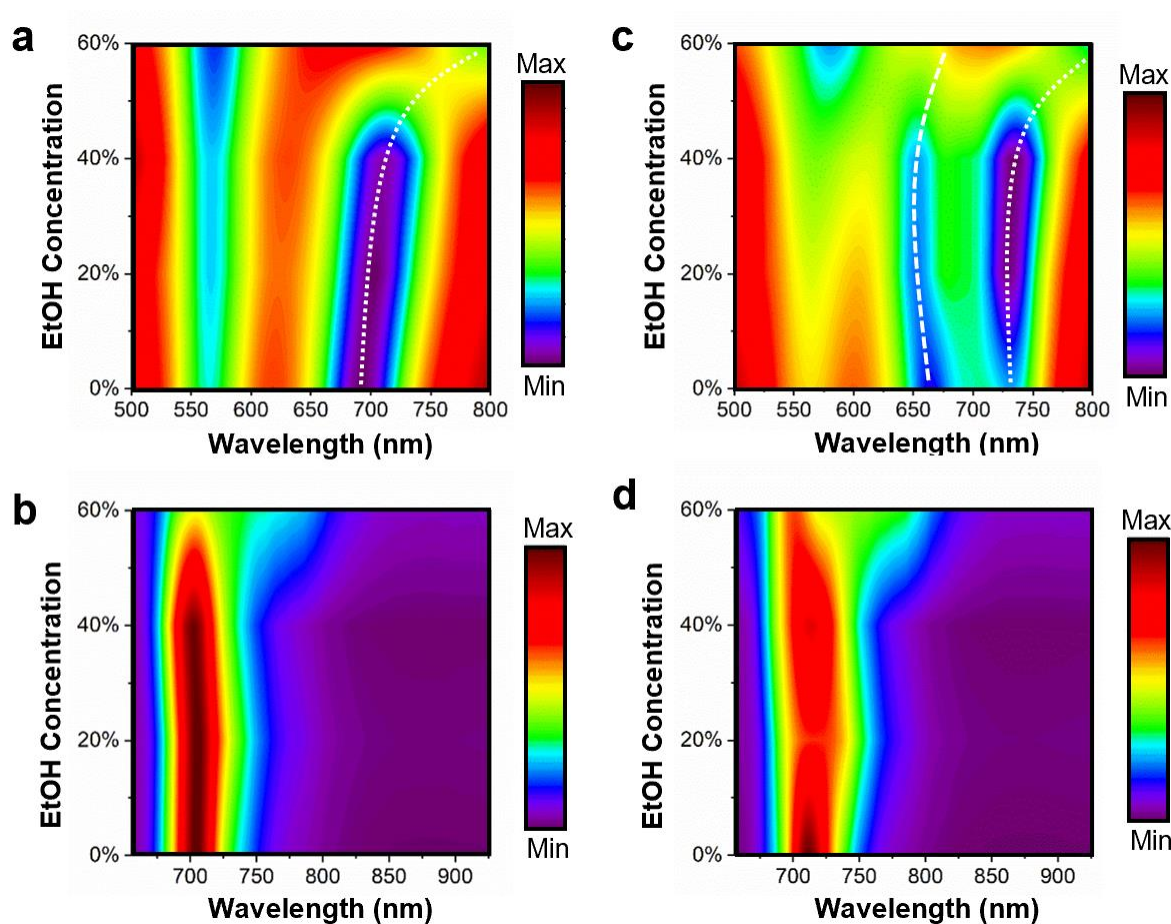
Figure 2-10. a) Reflection measurements for a 400 nm periodicity array at various ethanol concentrations. b) The corresponding PL measurements. c) Reflection measurements for a 500 nm periodicity array at various ethanol concentrations. d) The corresponding PL measurements.

Discussion. In order to study the effect of changing gap distance on PL, we studied PL at various

gap distances for 400 nm and 500 nm periodicities. To accomplish this, we collected reflection

and PL measurements at 20% intervals of ethanol concentrations between 0 and 60%. For a 400

nm period array a gap mode occurs near 700 nm (Figure S5a). As seen in the figure, the gap mode

resonance begins at 698 nm when at 0% ethanol and continually redshifts to 710 nm when at 40%

ethanol. The source of the shift is understood to be a cause of the continuous contraction of the DNA, which is estimated to yield a 2 nm reduction in gap size by correlating experimental and simulated reflection dips. During this small contraction the PL is not significantly affected and retains a similar PL intensity and spectral shape up to 40% ethanol concentration as is shown in Figure S5b. After increasing the ethanol concentation past 40%, however, the gap resonance redshifts above 800 nm, which broadens the PL spectrum as it follows the resonance and suggests an estimated gap distance of 7 nm. A second reflection peak is present for the 500 nm periodicity array where there exists both a lattice and gap mode near the dye emission wavelength (Figure S5c). PL maps shown in Figure S5d show a similar negligible effect on PL shape and intensity up to 40% and broadening at higher ethanol concentrations. Here, PL is likely enhanced by both the lattice and gap modes simultaneously.

CHAPTER 3

Mie-Resonant Three-Dimensional Metacrystals

This chapter is based on published work:

S. Kim*, **C.Y. Zheng***, G.C. Schatz, C.A. Mirkin, et al., "Mie-Resonant Three-Dimensional Optical Metacrystals" *Nano Letters*, **2020**, *20*, 11, 8096. (*indicates equal contribution).

3.1. Introduction

The notion of *meta-atoms*[9] – that refer to resonant or non-resonant nanoparticles (NPs) comprising optical metamaterials[2,9,69] – has become a tool for understanding how metamaterial properties evolve from their primitive building blocks. It has enabled the rational design of *meta-molecules*[126] based on clusters of NPs in distinct geometries that exhibit novel properties such as chiroptical activity and optical magnetism.[127] On a larger scale, lithographically patterned 2D metasurfaces[9] have enabled the development of *material* analogues that have unusual properties including near-zero[128] or negative[129] refractive indices, very large electric permittivities,[130] and negative permeabilities,[131] which have led to applications in optical sensing,[132] metatronic nanocircuitry,[133] and achromatic flat metalens development.[134] In contrast, bottom-up colloidal crystal engineering with DNA[54,77,81] has yielded 3D metamaterials that cannot be prepared by lithographic methods. Characterization of these 3D metamaterials has uncovered epsilon-near-zero (ENZ) properties,[93] photonic band gaps,[92] and unusual optical metallic scattering capabilities.[91] In these studies, the meta-atom or NP concentration was in the dilute regime, where NPs do not interact with their neighbors. However, closely packed 3D *metacrystals*, where the constituent meta-atoms strongly couple to each other, should have optical properties substantially enhanced from those of the constituent materials.[1,135] Here, we use DNA-mediated programmable assembly

to prepare superlattices (SLs) of Au nanocubes closely packed with controlled, sub-10 nm gap distances in simple cubic geometries. Indeed, these isotropic 3D metacrystals exhibit unnaturally high refractive indices due to the strong capacitive coupling of neighboring metallic nanocubes, giving rise to tunable mid-infrared Mie resonances in sub-micron SL habits, a novel property heretofore never observed.

3.2. Results and Discussion

To explain the working principle underpinning these novel metacrystals, we compare them with atomic crystals, an analogy commonly used to describe the mechanistic origins of meta-optical properties. When a NP comprised of an atomic crystalline material resonates with an external time-varying electric field, the microscopic descriptions of the Lorentzian resonances differ according to the dielectric properties of the material. The determining parameters assume several forms
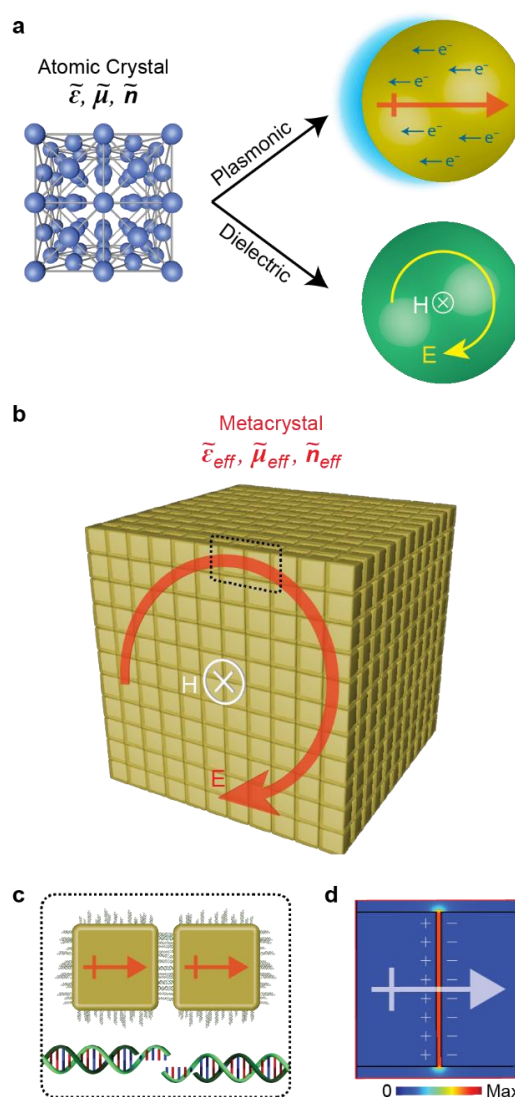
Figure 3-1. Depiction of the working principle of a metacrystal. **a)** Atomic crystal with complex (real and imaginary components) dielectric functions can support either plasmonic or dielectric resonances. **b)** A metacrystal composed of Au nanocube meta-atoms that exhibits a dielectric Mie resonance. **c)** Microscopic picture of the boxed region from panel **b** showing DNA programmable bonding of two polarized Au nanocubes through hybridization. The molecules shown at the bottom are the DNA with sticky ends that are immobilized on the cubes. **d)** Finite-element model showing a capacitively enhanced dipole moment in a small nanogap.

including complex electric permittivity ($\tilde{\varepsilon}$), magnetic permeability ($\tilde{u}$), and refractive index ($\tilde{n}$). The two most common resonant modes in NPs are plasmonic and dielectric Mie resonances[136] (Fig. 3-1a). In a plasmonic NP, an incoming electric field will displace the free carriers in a direction opposing the driving field, creating a linearly polarized dipole moment. In contrast, in a dielectric NP, each bound charge will be polarized by an electric (magnetic) field, producing a circular displacement current loop, which in turn induces a penetrating magnetic (electric) dipole.

From finite-element modeling (FEM), we predict a hybrid behavior from these metacrystals, which are micron-sized, cube-shaped SLs consisting of Au nanocubes equally spaced in 3D arrays (Fig. 3-1b): each *plasmonic* nanocube meta-atom should experience a linear polarization under an electric field (Fig. 3-1c) leading to a collective electric displacement current loop inside the metacrystal, which induces a *dielectric* magnetic dipole Mie resonance (Fig. 3-1b). This unique behavior arises because the highly polarizable metallic nanocubes are separated by insulating gaps, DNA duplex bonds in these experiments (Fig. 3-1c). This structure is analogous to the internal structure of dielectric materials where the polarizable atoms are interconnected by covalent bonds. The optical properties of the metacrystal can thus be described by effective optical constants including $\tilde{\varepsilon}_{eff}$, $\tilde{\mu}_{eff}$, and $\tilde{n}_{eff}$. Furthermore, the electric response of each meta-atom is significantly enhanced when the interparticle distances are under 10 nm because the large gap capacitance between neighboring nanocubes induces an even stronger polarizability (Fig. 3-1d).

The FEM of a cube-shaped metacrystal with a cubic symmetry and edge length, $L = (a+g) \times N$, where a is the edge length of the constituent nanocubes, g is the gap distance, and N is the number of nanocubes in each dimension sheds light on properties of this novel system (Fig. 3-2a). To accurately analyze it, we employed full-structure calculations in 2D and an effective medium
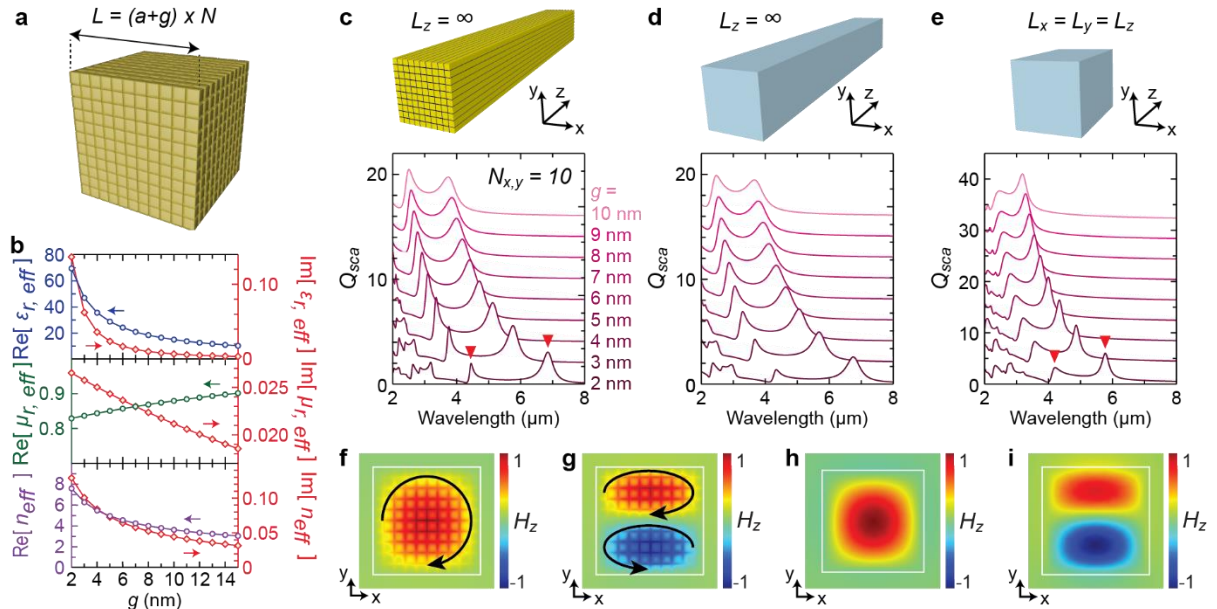
Figure 3-2. FEM analysis of metacrystals. a) Model SL with an edge length L, determined by the cube size a, gap distance g, and number of particles in each dimension N. b) $\tilde{\varepsilon}_{r,eff}$ (top), $\tilde{\mu}_{r,eff}$ (middle), and $\tilde{n}_{eff}$ (bottom) as a function of g for a SL with $a = 60$ nm. c) Simulation geometry (top) and Q_{sca} spectra with varying gap distance (bottom) of a two-dimensional SL of infinite Au bars with $a = 60$ nm and $N_{x,y} = 10$. Red triangles denote the two lowest-order modes for $g = 2$ nm. d-e) Effective medium equivalents of panel c in two- (d) and three-dimensions (e). f-i, Field patterns of the first (f, h) and second (g, i) lowest modes from panels c (f,g) and e (h,i), respectively. Colors and black arrows represent normalized H_z and the electric field vector, respectively.

approach in 3D since full-structure 3D modeling is nearly impossible due to the required large computation size. The effective medium description combines a rigorous analytical model from the literature with a parameter retrieval method from FEM to accurately determine both the real and imaginary parts of the effective constants (see Experimental Details).

Effective parameters were calculated in the long wavelength quasi-static regime (2-12.4 µm) as a function of gap distance. The calculations were performed away from geometry-dependent resonances such as a Fabry-Pérot (FP) etalon to accurately account only for bulk properties (Fig. 3-2b, 3-9). Importantly, the size of the nanocubes (60 nm) and gaps (2-15 nm) were chosen in the experimentally accessible range,[63] as opposed to the hypothetical ones used to

establish records based upon calculations.[1,135,137] The plot shows that the real parts of the effective permittivity and permeability increase and decrease, respectively, with increasing gap distance. Due to the close similarity in curve shapes, the effective refractive index is clearly dominated by the permittivity. Both diverge as gap distance decreases, which is attributed to the inverse dependence of gap capacitance on gap distance. At 2 nm, the smallest gap currently achievable through DNA-mediated assembly,[138] the off-resonance permittivity and refractive index reach ~70 and ~8, respectively, much higher than those of common high-index materials in nature (Ge, GaAs, or SiC).[139] With gap distances much larger than the values investigated in this work, capacitive coupling vanishes, and the overall volume fraction of the dielectric gap material significantly increases. In this case, the SLs start to behave as Maxwell-Garnett-type effective media in which the photonic and plasmonic characteristics are mainly dictated by the dielectric material and Au nanoparticles, respectively.[140]

Figs. 2c-e show a progression of simulation geometries from a 2D full-structure, to its 2D effective medium analog, and finally to the isotropic 3D geometry. In the 2D model, the scattering efficiency (Q_{sca}) was calculated for a 10×10 square array of infinitely-long Au bars with $a = 60$ nm and varying gap distances. We observe two Mie scattering peaks that shift to longer wavelengths when the gap distance is reduced from 10 to 2 nm (Fig. 3-2c), as expected due to the increasing effective refractive index (Fig. 3-2b). Notably, a 10-fold mode volume reduction is observed at the fundamental mode at 6.86 µm for $g = 2$ nm, where the metacrystal edge length is only 0.62 µm.

When the array of Au bars is replaced by a single block of the effective medium of the same metacrystal size (Fig. 3-2d), with parameters extracted from Fig. 2b, the Q_{sca} spectra are

reproduced with near perfect agreement in peak positions and linewidths, validating the accuracy of the calculated effective parameters. Therefore, this effective medium approach should provide accurate modeling of a single cubic 3D metacrystal (Fig. 3-2e). Indeed, most features are maintained in the spectra of 3D effective medium metacrystals, with only slight blue-shifts of the peaks caused by truncation in the z-direction.

The field patterns of the two lowest-order Mie modes from the 2D full-structure calculation, denoted with red triangles in Fig. 3-2c, are shown in Fig. 3-2f-g. Black arrows represent one and two electric displacement current loops formed in the TE_{01} (Fig. 3-2f) and TE_{11} (Fig. 3-2g) modes, respectively, and the red-to-blue color scale represents induced magnetic fields oriented along the infinitely-extended z-direction (see 3-10 for electric field patterns). The grid lines arise from the highly concentrated fields inside the dielectric gap regions. Identical magnetic field profiles are observed from the two lowest modes of the 3D effective medium calculation (Fig. 3-2h-i), indicating that the resonance patterns are well preserved with an additional truncation in the z direction. These two modes are the magnetic dipolar (MD, Fig. 3-2h) and electric dipolar (ED, Fig. 3-2i) Mie resonances, respectively (Detailed electric and magnetic field patterns shown in Fig. 3-11). These Mie resonances are tolerant to various types of lattice defects (Fig. 3-12).

To experimentally realize these unusual metacrystals, colloidal crystal engineering with DNA was used to assemble Au nanocube SLs. In order to observe strong capacitive coupling between individual nanocubes, it was critical to synthesize SLs from sufficiently large particles ($>$ 60 nm) but with small interparticle spacings (< 10 nm). The assembly of such high volume-fraction ($>$70 %) SLs, previously elusive due to the formation of amorphous, kinetic structures,[141] was enabled by the addition of flexible spacer units in both the anchor and linker sequences. In a typical

experiment, we synthesized Au nanocubes with an average edge length of 67 nm (Figs 3-6, 3-7)

and densely functionalized their surfaces with 3' propylthiolated anchor DNA. Upon adding linker

DNA complementary to the anchor strand, but with a self-complementary binding region (Table

3-1), the DNA-functionalized nanocubes rapidly assembled. Next, the solution was slowly cooled

through the DNA melting temperature, forming single crystals with a simple-cubic geometry. The

SLs were transferred to the solid state by embedding in SiO_2 matrix, yielding a lattice parameter
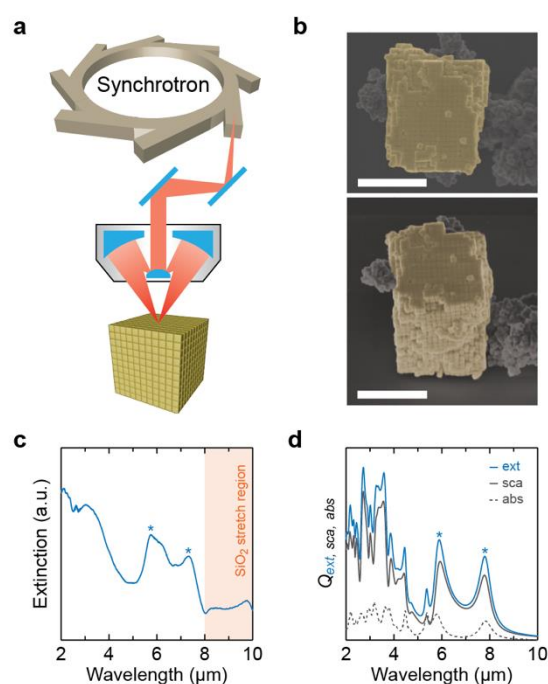
of ~73 nm, and cube-shaped crystal habits (Fig. 3-8). With these lattice parameters, we estimate

an effective refractive index of 4.7.

Figure 3-3. Single-SL extinction measurement with synchrotron infrared radiation. a) Illumination geometry of the measurement. The spot size of the diffraction-limited beam is on the order of $\lambda/2$. The size of the SL is exaggerated for visualization. b) False-color SEM images of a SL from the top (top) and at a 40˚ tilt angle (bottom); scale bar, 1 µm. c-d) Measured (c) and calculated (d) optical spectra of the SL from panel b. The two lowest-order modes are denoted with asterisks. The SiO_2 stretching region is highlighted in orange. False color is used to guide the reader to the portion of the sample responsible for the observed effects.

We performed far-field Fourier-transform infrared (FTIR) extinction measurements using

a synchrotron infrared beamline with sufficient radiation output to collect the scattering response

from single metacrystals (Fig. 3-3a). An intense, coherent infrared beam was focused by a Cassegrain objective to a diffraction-limited spot size (on the order of l/2) and directed to the target metacrystal on a double-side-polished Si substrate. The experimental extinction spectrum for the metacrystal in Fig. 3b shows two clear peaks at ~7.3 and ~5.7 µm (Fig. 3c, Fig. 13 for size analysis). Calculated extinction spectra show good agreement with the experiment (Fig. 3-3d). Higher-order peaks appearing in the short wavelength region of the calculated extinction spectra are not clearly resolved in the measurement due to low coupling efficiencies and inevitable spectral

Figure 3-4. Size-dependent tunability of Mie resonances. a) Spectral tuning of Mie resonances of an effective metacrystal with increasing habit size in increments of 144 nm. b) False-color SEM images of SLs with varying habit sizes at a 40° tilt angle; scale bar, 1 µm. c) Normalized experimental extinction spectra of SLs from panel b. Each curve vertically offset by 0.5. The SiO_2 stretching region is highlighted in orange.

broadening. It is worth noting that absorption contributions are substantially lower than scattering contributions (Fig. 3-3d) because most of the electric field is concentrated inside the gap regions (Fig. 3-10). This low-loss characteristic, analogous to that of metal-insulator-metal (MIM) waveguides, distinguishes these metacrystals from infrared surface plasmon nanoantennas,[142] and should enable various technologies that have previously been limited by the high Ohmic losses of

plasmons. Additionally, the highly concentrated electric fields distributed throughout the interior of the Mie-resonant metacrystals can enable applications such as cavity-enhanced catalysis through the infusion of molecules into the gaps.[143]

The wavelengths of NP Mie resonances are tunable through resonator size. Similarly, Fig. 3-4a shows a smooth tuning of the metacrystal Mie resonances spanning the mid-infrared spectrum, as the metacrystal size (a = 66 nm and g = 6 nm) increases from 720 (N = 10) to 1584 nm (N = 22). This size-dependent tunability is experimentally validated through FTIR measurements of metacrystals with the same lattice parameters and varying habit sizes (sub-micron to 2 µm). A clear trend, of the resonance peaks moving toward longer wavelengths as crystal size increases, is observed (Fig. 3-4b,c). However, detailed spectral features vary for different samples, likely caused by defects in the metacrystals as well as their non-unity aspect ratios. Nevertheless, this measurement clearly demonstrates the ability of these programmably-assembled 3D metacrystals to give rise to tunable mid-infrared Mie resonances.
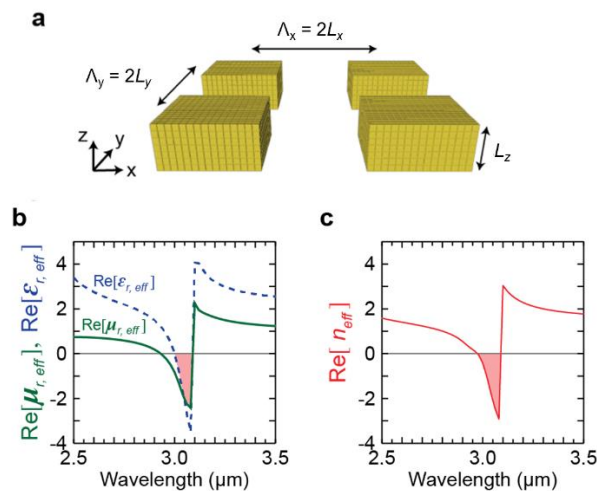
Figure 3-5. Left-handed array of cuboidal metacrystals. a) Illustration of an array of cuboidal metacrystals where a = 60 nm; g = 10 nm; $N_x = N_y = 15$, $N_z = 7$; and array periods $\Lambda_x = \Lambda_y = 2L_x = 2L_y$. b) Simulated real parts of the $\varepsilon_{r,eff}$ (dashed blue) and $\mu_{r,eff}$ (solid green) of the array from panel a simultaneously exhibit a negative region (red shade). c) Simulated real part of the n_{eff} of the array.

To apply Mie resonant particles to practical applications, researchers have engineered them to support MD and ED in a close spectral range and arranged them into arrays to allow the modes to overlap. This overlap of modes induces a variety of complex interference effects such as optical bound states in the continuum[144] and complete scattering suppression.[145] It can also lead to simultaneous negative permittivity and permeability, known as optical left-handedness, or negative refractive index,[45] and we therefore hypothesize that a rationally designed array of our 3D metacrystals could exhibit this effect. Indeed, we designed a periodic array of cuboidal metacrystals which have overlapping MD and ED at ~3.1 µm (Fig. 3-5a). Both permittivity and permeability (Fig. 3-5b) show Lorentz oscillation features with negative values around 3 µm, giving rise to a doubly negative region (red shade in Fig. 3-5b) and a spectral band of negative refraction in this range (Fig. 3-5c). Interestingly, we also observe completely suppressed reflection here (Fig. 3-14), which is caused by matched values of permittivity and permeability. The ability to engineer left-handed metacrystal arrays will inspire future studies of invisibility. Additionally, further development of metacrystal assembly on surfaces should allow for the fabrication of functional devices, including active metasurfaces through the reversible tuning of stimuli-responsive DNA.

3.3. Conclusions

In conclusion, we have realized a new class of isotropic 3D optical metacrystals by precisely assembling Au nanocubes into closely packed SLs with well-defined crystal habits through DNA-mediated assembly. The metacrystals exhibit unnaturally high refractive indices and low losses, and their well-formed habits (cube-shaped, in this case) give rise to multipolar Mie resonances, which we experimentally observed using synchrotron FTIR. Notably, we have reduced

to practice a generalizable approach to *meta-photonics,* where individual metallic nanocubes are arranged by the sequence-specific binding properties of DNA and behave as meta-atoms to produce unnatural optical behavior. Finally, as a proof-of-concept of the cloaking potential of such structures, we simulated arrays that exhibit negative refractive indices. Therefore, this system for engineering new metacrystal geometries will allow for the systematic study of structures not attainable by conventional methods but ones likely to exhibit unexplored metaphotonic properties.

3.4. Experimental Details

Materials and Methods

Nanocube synthesis and characterization. All precursors were purchased from Sigma-Aldrich and used without further purification. Uniform Au nanocubes were synthesized using a seed-mediated method developed by O'Brien *et al.*[63] which yields >95% of the desired shape with <5% variation in size. In brief, single-crystalline spherical Au nanoparticles were synthesized and chemically refined through iterative reductive growth and oxidative dissolution reactions leading to uniform spherical nanoparticles, which were subsequently used as seeds to template the growth of anisotropic nanoparticles, including these nanocubes.
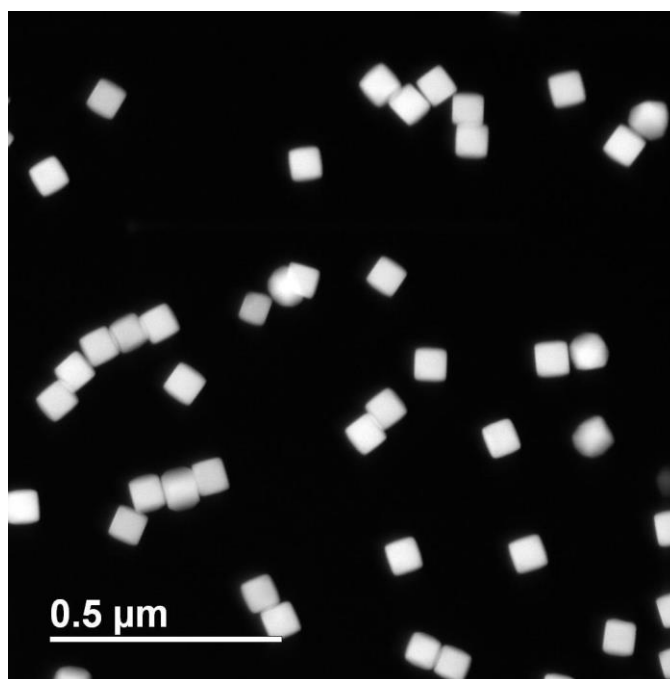
Figure 3-6. STEM image of Au nanocubes with an average edge length of 67 ± 2 nm.
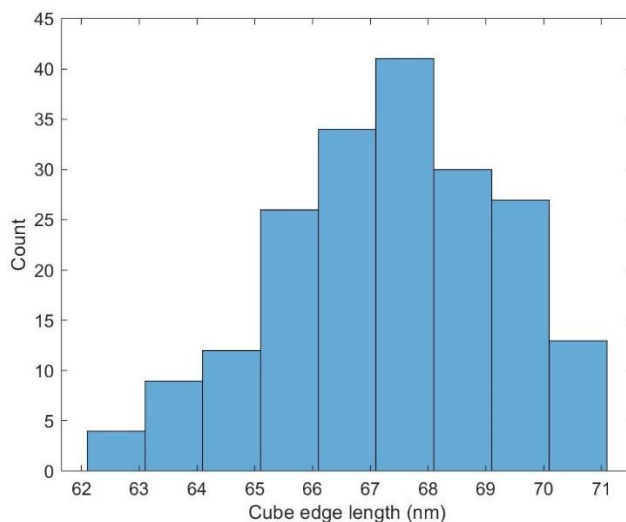
Figure 3-7. Distribution of edge lengths measured from 200 nanocubes.

Nanocubes were imaged on a Hitachi HD2300 STEM with an accelerating voltage of 200 kV in Z-contrast mode and the edge lengths of 200 nanocubes were measured using ImageJ. The average edge length of the cubes was determined to be 67 ± 2 nm.

DNA synthesis, purification, and design. All oligonucleotides used in this work were synthesized on a BioAutomation MerMade 12 (MM12) automated oligonucleotide synthesizer using reagents purchased from Glen Research. After synthesis, all DNA was purified with reverse-phase high-performance liquid chromatography (HPLC, Agilent) followed by standard deprotection procedures. Matrix-assisted laser desorption ionization time-of-flight mass spectrometry (MALDI-TOF-MS) was used to characterize the purified oligonucleotides and confirm their molecular weight.

The DNA sequences used in this work are listed in Table 1 and are taken from the literature. Black denotes spacer regions, purple denotes thiols, blue denotes complementary regions in the anchor and linker strands, and red denotes the self-complementary *sticky end* binding region. Sp18

is a hexaethylene glycol spacer unit used to increase flexibility of the DNA. The sequences were modified such that the single-stranded spacer regions in both the anchor and linker were replaced with more flexible sp18 spacer units. The extra flexibility was needed so that large nanocubes functionalized with short DNA ligands could form well-defined single crystals instead of the amorphous, kinetic structures that otherwise form.

Table 3-1. DNA sequences used in this work

Name	Sequence (5' to 3')
Anchor	TCA ACT ATT CCT ACC TAC (sp18)$_2$ SH
Self-Complementary Linker	GTA GGT AGG AAT AGT TGA (sp18) GCGC
Self-Complementary Linker for Control in Fig. S3	GTA GGT AGG AAT AGT TGA A GCGC

Nanocube functionalization and assembly. Nanocubes were functionalized using a procedure modified from that described by Jones *et al.*[124] and O'Brien *et al.* Briefly, 3' propyl-modified oligonucleotides were first treated with a 100 mM solution of dithiotreitol (DTT) in 170 mM sodium phosphate buffer (pH = 7.4), followed by purification on a Nap-5 size exclusion column (GE Life Sciences) to remove excess DTT. During this time, 1 mL aliquots of the as-synthesized cube solutions (~ 1 OD) were centrifuged for 8 min at 5,800 rpm, the supernatant was removed, and the nanoparticles were resuspended in water. The cubes were then centrifuged a second time for 8 min and 5,800 rpm, the supernatant was removed, and then purified DNA was added to the pellet. 1 OD of DNA was added per each 1 mL of particles. The particle solution was then brought to 0.01 M sodium phosphate buffer (pH = 7.4) and 0.01 wt. % sodium dodecyl sulfate (SDS) in water. Stepwise addition of 2 M NaCl was carried out every half hour, such that the NaCl

concentration was increased to 0.05 M, 0.1 M, 0.2 M, 0.3 M, 0.5 M respectively. Following this process, the nanoparticles were placed on a shaker at 1,000 rpm and left overnight to ensure a dense loading of oligonucleotides. After functionalization, the nanoparticle solutions were centrifuged three times to remove excess DNA. After each of the first two rounds of centrifugation, the nanoparticles were resuspended in 0.01 wt. % SDS, and after the last centrifugation step, the particles were resuspended in 0.3 M NaCl, 0.01 M sodium phosphate buffer (pH = 7.4), and 0.01 wt. % SDS. To the nanoparticle solution, 25,000 linker strands were added per nanoparticle (in excess of the number of thiolated strands). Nanoparticle solutions were prepared such that the final concentration was 8 OD in a total volume of 100 µL. Each solution was then pipetted into 200-µL PCR eight-tube strips (Life Technologies) and placed into a thermal cycler (Life Technologies). The temperature of the thermal cycler was slowly cooled from 70 ˚C (where the particles are fully discrete) to 20 ˚C (where the particles are fully associated) for all samples at a rate of 0.1 ˚C/10 min. The slow speed of this temperature change ensures that the system has enough time to reach equilibrium at each temperature.

Silica embedding of SLs. Nanocube SLs were encapsulated in silica according to literature precedent. This method largely preserves the crystal symmetry and lattice parameters of the lattice in the solid state. Slow-cooled samples were transferred to a 1.5 mL Eppendorf tube, and the volume was brought up to 1 mL with an overall NaCl concentration of 0.5 M. To this solution, 2 µL of the quaternary silane salt, N, trimethoxysilylpropyl-N,N,N-trimethylammonium chloride (TMSPA), was added and the tube was mixed at room temperature on a thermomixer (Eppendorf) at a rate of 700 rpm for 30 min. Then, 4 µL of triethoxysilane (TES) was added to the solution and allowed to form a silica network around the entire lattice. The mixture was left on the thermomixer at 700 rpm for four days, followed by three rounds of centrifugation, removal of supernatant, and

resuspension in Nanopure water. Note, in the case of successful silica embedding, the addition of water does not result in lattice dissolution (i.e., the solution does not turn pink).

SL characterization. SLs were imaged on a Hitachi SEM SU8030 instrument at an accelerating voltage of 5 or 30 kV. Silica-embedded SLs were redispersed in 100 μL of ethanol and the solution was vortexed to break up aggregates. Next a 5 μL droplet of the solution was drop-cast onto a small piece of silicon wafer.

SLs assembled with a sp18 unit in the linker formed crystals with larger domain sizes, and a higher proportion of well-formed crystal habits (Fig. 3-8a,c,d) compared to those assembled without one (Fig. 3-8b). High-magnification images were taken of the SLs surfaces using an accelerating voltage of 30 kV (Fig. 3-8e) to quantify the periodicity of the SLs and deduce their gap distance by subtracting the average cube size measured from STEM images (67 nm). Periodicity was measured using ImageJ. Specifically, the distance across 3 periods was measured for higher precision, and then this value was divided by 3 to obtain the periodicity. This measurement was done for 50 different regions and averaged. The average periodicity was determined to be 73 nm giving an average gap of 6 nm.
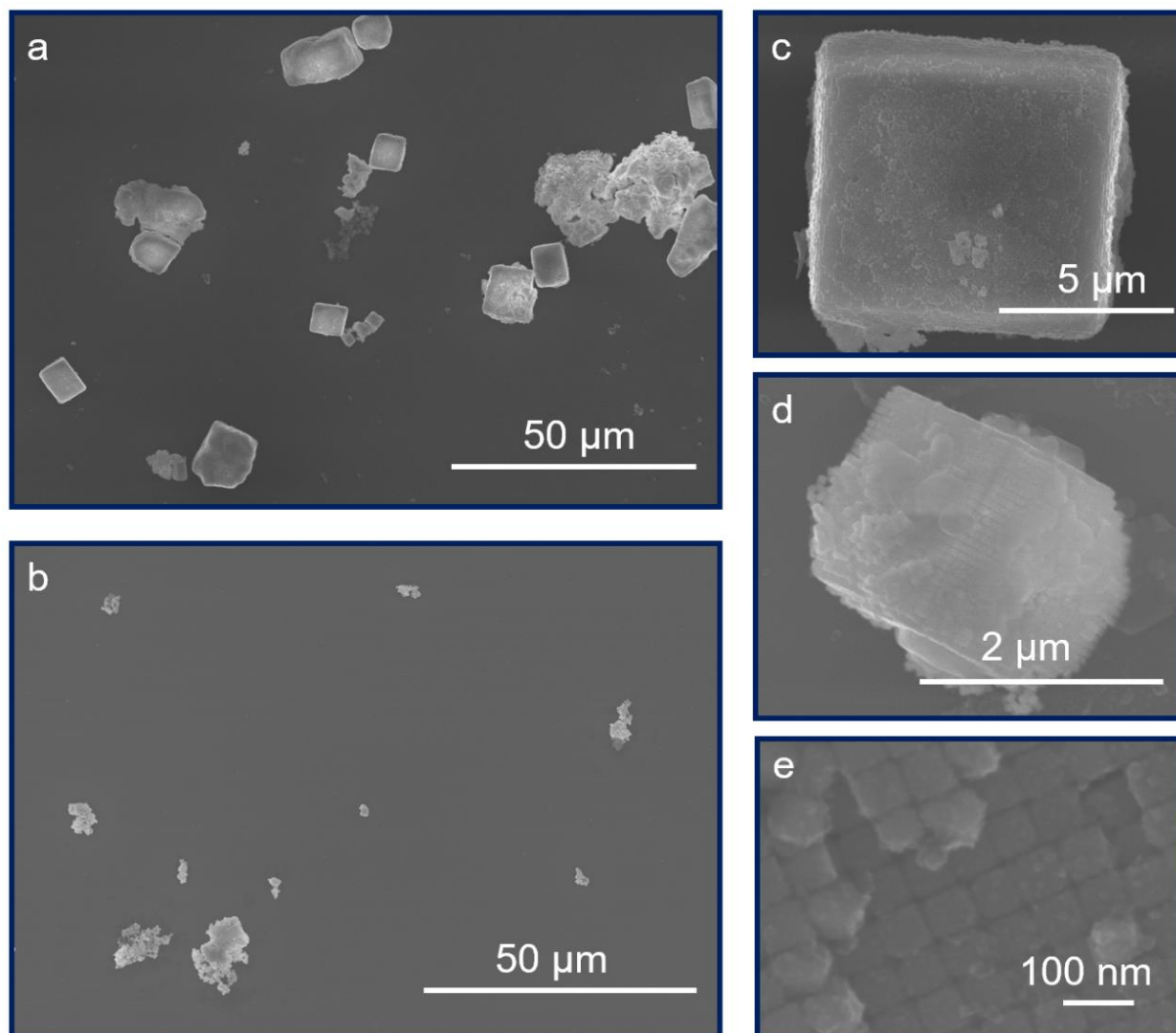
Figure 3-8. a) Large-area SEM images showing SLs formed with our modified DNA design. b) SEM image of SLs formed with the same DNA design except with the sp18 unit in the linker replaced by a single-stranded A base. c-d) Magnified SEM images of representative SLs in a. e) High-magnification SEM image of a SL surface used to quantify gap size.

Removal of excess silica. Because silica exhibits strong absorption in the mid-IR region, excess silica formed during the embedding process had to be removed before optical characterization. To do this, a density gradient separation method was employed. 50 µL of sodium metatungstate solution was pipetted to the bottom of a 1.5 mL Eppendorf tube and 30 µL of the silica embedded SLs in water was added to the top of the sodium metatungstate solution, forming two layers. After 12 h, all the SLs fell into the bottom layer because of their heavier density, while the excess silica remained in the top layer. The top layer was carefully removed with a pipette. To remove the sodium metatungstate, the SLs were washed 5x with water, centrifuging each time at 12,000 rpm for 10 s and subsequently removing the supernatant. The SLs were redispersed in 100 µL of water.

Sample preparation for synchrotron measurements. Double-side-polished silicon wafers were cut into ~1.5 x 1.5 cm^2 pieces and cleaned by sonicating in acetone and IPA and then blown dry using N_2. Next, the wafers were plasma cleaned with an O_2 plasma at 50 W for 5 min. Immediately following plasma cleaning, 10 µL of the SL solutions were dropped onto the wafer and the wafer was placed in a desiccator to dry. Isolated SLs of desired sizes for synchrotron FTIR measurements were found using SEM and their positions on the substrate were tracked with a series of SEM images at different magnifications and corresponding optical microscopy images.

Finite-Element Modeling. Numerical modeling was performed using *COMSOL Multiphysics* with the wave optics module. The effective parameters were extracted by a modified Nicholson-Ross-Weir (NRW) method from full-field calculations using infinite slabs of SLs. A refractive index of 1.5 was used for silica and DNA. Scattering calculations in 2D and 3D geometries were performed with SL structures under a plane wave surrounded by a large air domain terminated by perfectly matched layers. The calculation for Fig. 5 was performed using an effective crystal with

optical constants derived from Fig. 3-2b with an in-plane periodic boundary condition. The mesh size in the Au bars and gap region was set to no larger than the gap distance, and a predefined extra fine mesh size was used for the rest of the simulation region. The calculations were done in the frequency domain using a direct solver. The scattering and absorption efficiencies were calculated by integrating relative normal Poynting vectors around the SL boundaries (scattering) and power loss in the SL volume (absorption) normalized by the illumination power density and physical cross-section of the SLs.

Synchrotron Extinction Measurements. SL samples were dispersed in water and drop-casted on double-side-polished <100> silicon substrates (University Wafer) and dried under vacuum. The samples were placed on an FTIR microscope equipped with a Mercury-Cadmium-Telluride (MCT) detector (Nicolet, Thermo Fisher) in the far-field infrared beamline (1.4) at the Advanced Light Source, National Lawrence Berkeley Laboratory. Synchrotron infrared radiation was directed through a Cassegrain objective lens with 36× magnification and focused into diffraction limited spot sizes. Blank measurements were collected from clean regions of the Si substrate, and the sample measurements were collected with the beam focused on the SLs of interest. Transmission (T) was measured by averaging 256 scans for each sample, and extinction was calculated by 1-T.

Determination of complex effective parameters of Au nanocube SLs. The real and imaginary parts of effective permittivity and permeability were calculated with a modified Nicholson-Ross-Weir (NRW) method and extrapolated to the bulk limits. First, we consider infinite 2D slabs of Au nanocube SLs with $a = 60$ nm, $g = 2$ nm, and thickness varying from 1 to 5 layers. With the S-parameters obtained from FEM, we retrieve the real and imaginary parts of the permittivity (Figs. 3-9a,b) and permeability (Figs. 3-9c,d). We only show values for wavelengths longer than the

positions of the first FP modes (FP$_0$) to eliminate artifacts associated with a phase-inversion (see Fig. 9e for the phase-corrected permittivity curve for 5 layers). The plots in Fig. 3-9a-d show that all curves converge to single values, indicating that the optical constants away from the FP modes do not depend on the number of layers. Upon closer inspection of the tail regions (insets of Figs. 3-9a and c), we find that the asymptote values slightly decrease as more layers are added but approach the bulk limits obtained by analytical modeling. We thus adopt these bulk values in all subsequent analyses. For the imaginary parts, we estimate the bulk limits by extrapolating to infinity the values obtained for several finite thicknesses, using the multiplication factor obtained from the real part. Specifically,

$$imag(\infty) = imag(2) - [imag(2) - imag(5)] * \frac{real(2) - real(\infty)}{real(2) - real(5)}$$

where imag(m) and real(m) are the imaginary and real parts of the optical constants, respectively, for an m layer slab of Au nanocubes.

This calculation was repeated for *g* values from 2 to 10 nm, and the long-wavelength values of the real and imaginary parts of effective parameters obtained at 12.4 mm are plotted in Fig. 2b of the main text. We assume that the effective parameters are wavelength-independent in the 2-15 mm wavelength range because this is within a non-dispersive quasi-static regime for Au nanocubes of the sizes used in this study.
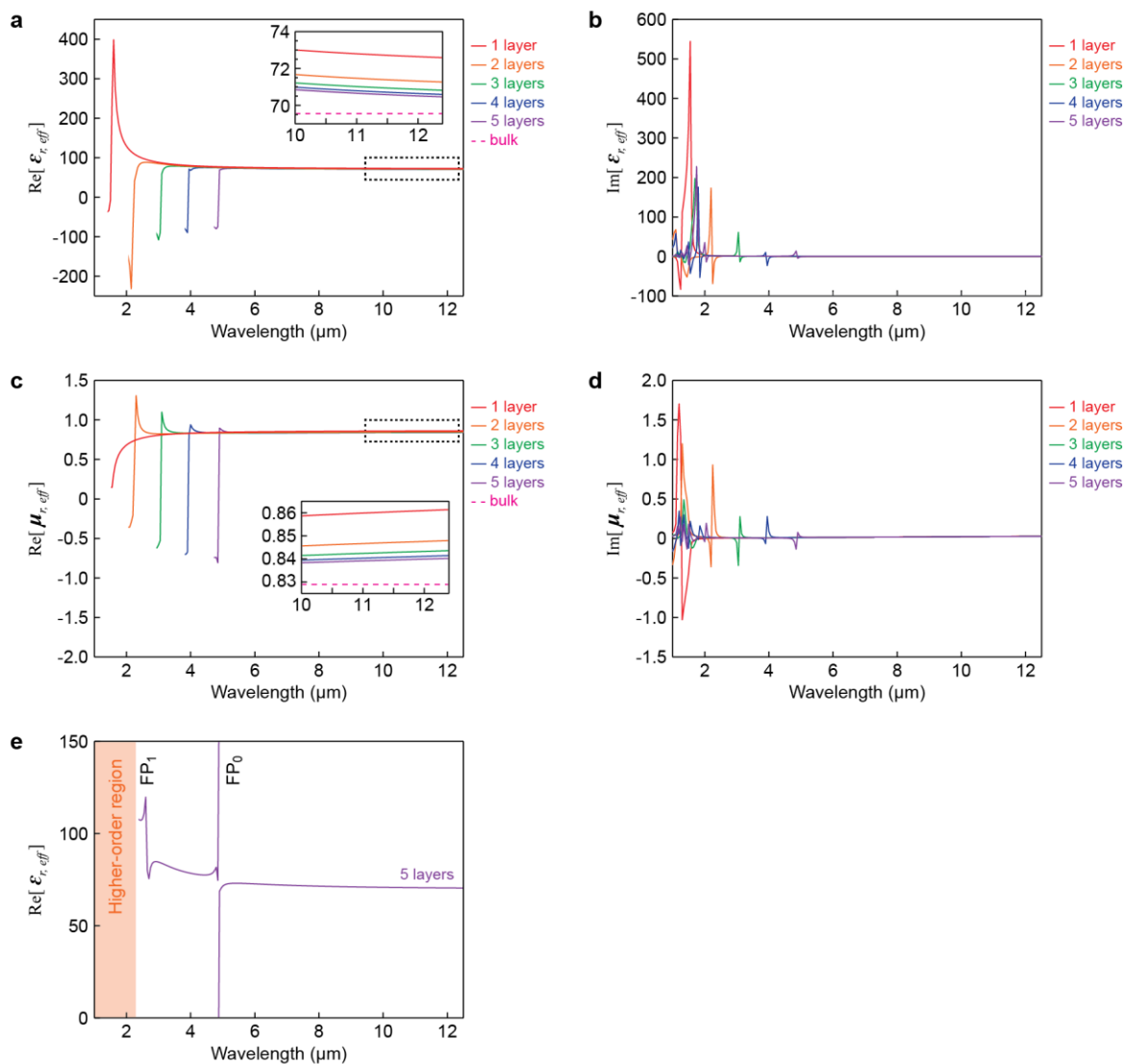
Figure 3-9. Effective optical constants of nanocube SL slabs of varying thicknesses. a-d) Real (a, c) and imaginary (b, d) parts of the retrieved effective permittivity (a, b) and permeability (c, d) of nanocube SL slabs with $a = 60$ nm, $g = 2$ nm, and varying number of layers from 1 to 5. Insets in panels a and c are magnified views of the boxed regions. Bulk values in the insets are from an analytical model.[1] e) Real part of the effective permittivity for 5 layers with phase corrected before and after the first FP mode (FP_0).
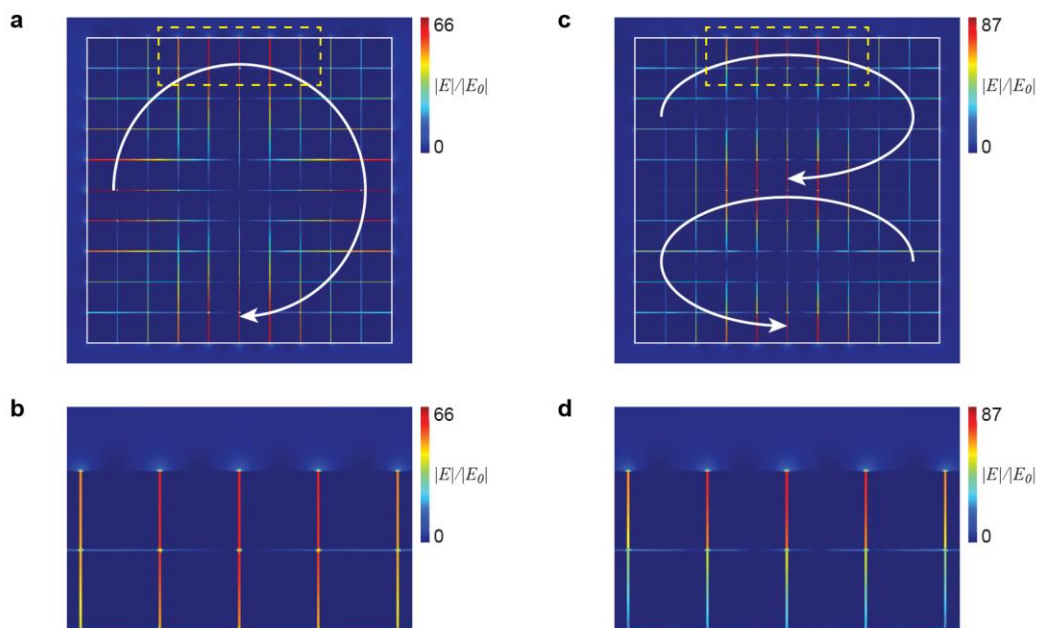
Figure 3-10. Electric field enhancement patterns of TE_{01} (a-b) and TE_{11} (c-d) modes from Fig. 2f-g. Panels b and d are magnified views of the boxed regions in panels a and c, respectively.
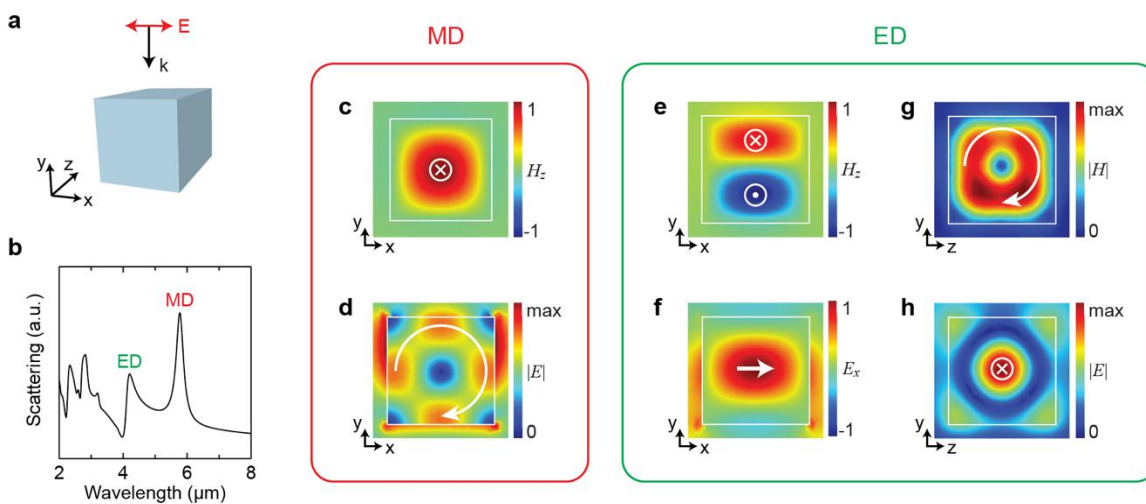
Figure 3-11. Field patterns of the MD and ED resonances in 3D metacrystals. a) Illumination geometry for a metacrystal. b) Calculated scattering spectrum of an effective metacrystal corresponding to $a = 60$ nm, $g = 2$ nm, $N_x = N_y = N_z = 10$. c-h) Magnetic (top) and electric (bottom) field patterns of MD (c-d) and ED (e-h) for different plane projections.
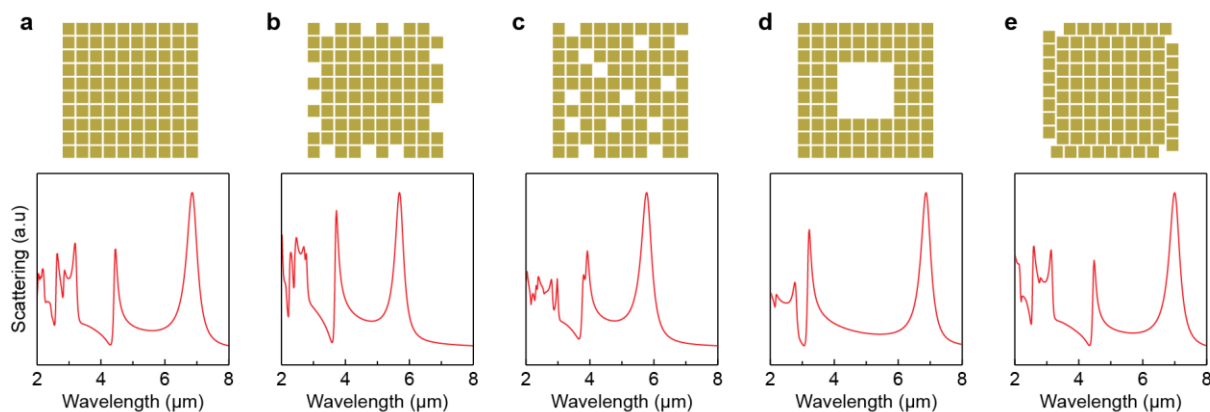
Figure 3.12. Effect of various defects. Simulation geometries (top) and calculated scattering spectra (bottom) of metacrystals with $a = 60$ nm, $g = 2$ nm, and $N = 10$ with no defects (a), missing particles on the surface (b), random vacancies (c), a hollow core (d), and a misaligned outermost shell (e). The main spectral features are preserved in all cases, albeit with minor shifts in peak positions.
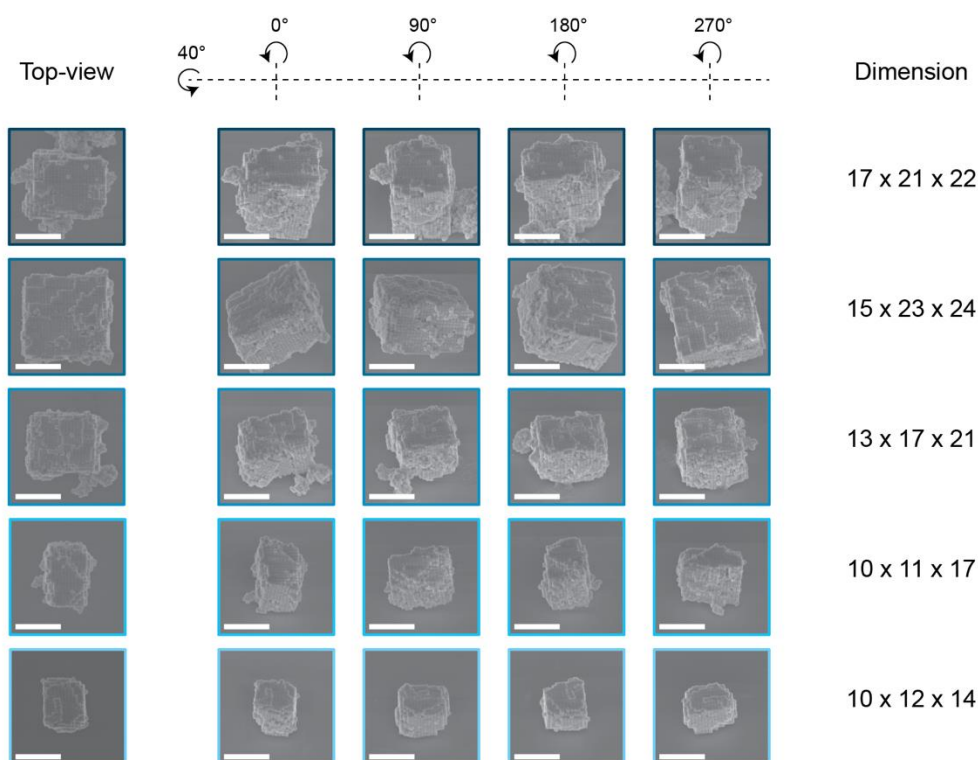
Figure 3-13. Size analysis of SLs used for measurements shown in Fig. 4. Top-view SEM images (left), tilted images at a 40° angle and various azimuthal angles (middle), and dimensions (x × y × z) of each SL in terms of the number of nanocubes (right). All scale bars, 1 mm.
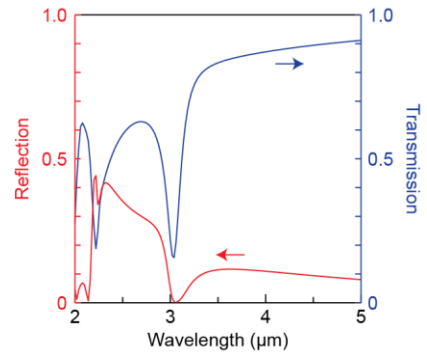
Figure 3-14. Calculated reflection and transmission spectra of the array of metacrystals shown in Fig. 5.

CHAPTER 4

Low Density 2D Superlattices Assembled via Directional DNA Bonding

This chapter is based on published work:

Z. Miao*, **C.Y. Zheng***, G.C. Schatz, B. Lee, C.A. Mirkin, et al., "Low Density 2D Superlattices Assembled via Directional DNA Bonding" *Angewandte Chemie Int. Ed.* **2021**, *60*, 19035. (*indicates equal contribution).

4.1. Background

Colloidal nanoparticle (NP) superlattices (SLs) can behave as metamaterials with unique optical,[55,146] electrical,[147,148] and magnetic[149] properties based on the structure-dependent interactions between the particles that comprise them. As such, researchers have devoted significant effort towards developing methods to prepare ordered assemblies of colloidal NPs with control over various structural parameters.[55,149–152] Colloidal crystal engineering with DNA, which utilizes DNA-grafted NPs as "programmable atom equivalents" (PAEs), has arisen as a versatile method to fabricate SLs with remarkable control over lattice symmetry and spacing independent of the size, shape, and composition of the NP core.[54,77,86] Indeed, this method has been used to prepare SLs in solution with over 50 distinct symmetries, some displaying interesting optical properties, including birefringence,[91] unnaturally high refractive indices,[146] and directional emission.[140] Furthermore, thin-films of spherical PAEs have been assembled on substrates with control over crystal thickness and orientation,[153,154] opening the door to the measurement of their optical[155] and mechanical properties[156] as well as their integration into devices.[157] Although the feasibility of this surface-bound growth technique has been demonstrated using spherical PAEs, anisotropic PAEs have not yet been explored in this context, and these particles offer an additional degree of structural control in assembly due to shape-induced directional bonding.[55,158,159] In addition, films of anisotropic plasmonic NPs may find even greater applicability in optical devices

compared to their spherical counterparts due to the strong shape- and size-dependent scattering of the individual NPs[160,161] and the extreme electric field confinement between neighbouring NPs.[155,162,163]

In this work, we investigate the assembly of complementary systems of Au PAEs with three polyhedral cores – cubes, octahedra, and rhombic dodecahedra (RD) – into thin-films on DNA-functionalized substrates. We predicted that, in accordance with previous studies and the complementary contact model (CCM)[54] involving the DNA-mediated assembly of polyhedral PAEs in solution, these PAEs would thermally reorganize into SL films with symmetries that maximize the face-to-face interactions between particles.[123] Moreover, we expected the bottom-most layer of NPs to orient with their facets parallel to the flat substrate in order to maximize DNA binding, as predicted by the CCM.[54] Because SL orientations resulting from large NP facets parallel to the substrate do not necessarily expose the closest-packed planes of a specific system, we hypothesized that this approach could allow for the assembly of open 2D lattices.

4.2. Results and Discussion

Indeed, although we found that cubic PAEs form close-packed films, we saw that RD PAEs, which form face centered-cubic (FCC) lattices in solution with {111} closest-packed planes, rearrange into 2D films on surfaces with a rhombic symmetry (corresponding to the open {110} planes of an FCC lattice). Furthermore, octahedral PAEs, which form body-centered cubic (BCC) lattices in solution with {110} closest-packed planes, rearrange into 2D films on surfaces with a honeycomb symmetry, corresponding to the open {111} planes of a BCC lattice. Neither of these unusual 2D lattices have been obtained by conventional entropy-driven NP crystallization, in which the formation of close-packed arrangements is favored.[151,164] Open structures are desirable in applications, spanning sensing to nanophotonics.[152,165] Taken together, our results

provide fundamental insight into the growth of PAE SLs on substrates and demonstrate the capability of colloidal crystal engineering with DNA for preparing optical metamaterials with unusual, but potentially useful properties and functions.
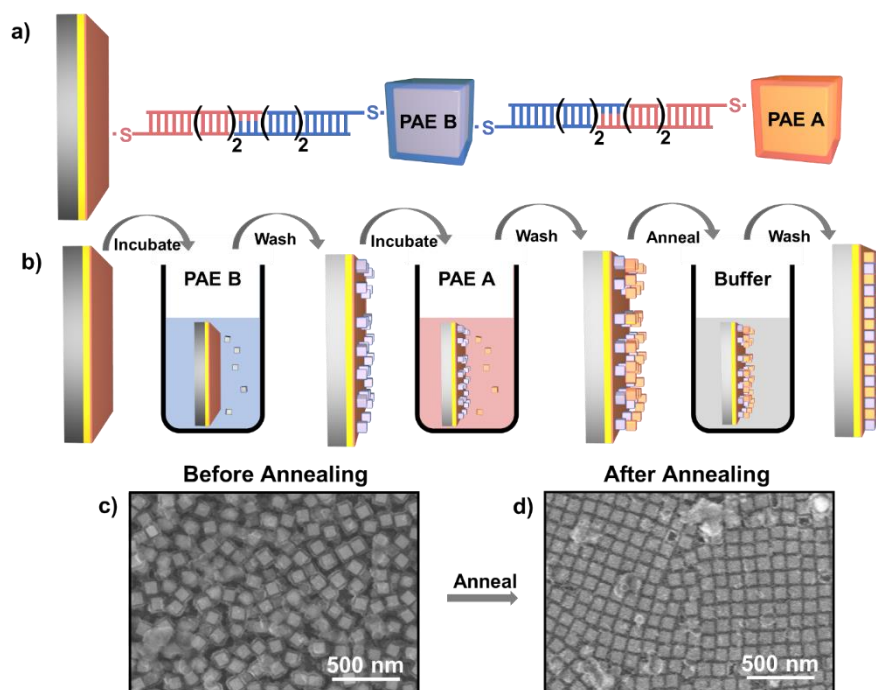
Figure 4-1. a) Schematic of the DNA design. A hetero-complementary DNA system is used. PAE A and the substrate are functionalized with A-type DNA (red), while particle B is functionalized with B-type DNA (blue). The stacked configuration is observed prior to annealing. b) Schematic of the assembly process. c) SEM image of an unannealed two-layer assembly. d) SEM image of the thermally annealed crystalline PAE monolayer thin-film.

To assemble films with controlled thicknesses, we utilized a binary system of "A" and "B"-type polyhedral PAEs, where DNA A and B are comprised of complementary "sticky ends" (Figure 4-1a). First, we grew two-layer amorphous films by functionalizing a Au-coated wafer with A-type DNA and then assembling B-type PAEs followed by A-type PAEs (Figure 4-1b,c). Next, the film was annealed just below the melting temperature of aggregates of PAE A and PAE B (T_m), allowing for its rearrangement into an ordered 2D, single-layer SL (Figure 4-1d). Finally, the samples were transferred into the solid state by embedding them in a silica matrix,[166] and

scanning electron microscopy (SEM) and grazing-incidence small-angle X-ray scattering (GISAXS) were performed. Large-area SEM images show that these films were grown in high uniformity over macroscopic areas (Figure 4-26). Importantly, although the resulting annealed films appear as monolayers in top-down SEM images, depending on the system, the A and B-type particles could be situated at different heights due to their distinct shape-driven bonding characteristics.

Films were formed with the three different-shaped PAEs mentioned above (Figure 2). We first examined a system consisting of cubic PAEs, which forms a simple cubic (SC) lattice with {100} closest-packed planes in solution.[24] Because cubic NPs are bound by {100} facets, when assembled on DNA-functionalized substrates, they should orient with the <100> direction perpendicular to the surface to maximize particle-substrate face-to-face binding. Indeed, SEM images of an assembly of 80-nm cubic NPs revealed a 2D square lattice with individual NPs oriented in the <100> direction (Figure 4-2a). This film is equivalent to the {100} planes of a SC lattice. Because we utilized a binary system of cubic PAEs, where B-type PAEs are able to hybridize with the DNA on the substrate, and where A-type PAEs are not, we predicted that neighboring A- and B-type PAEs would be situated at different heights in these structures. However, SEM images at 30º and 90º tilt angles (Figures 4-2c) as well as GISAXS scattering patterns (Figure 2d) suggest that both A- and B-type cubic PAEs lie within the same plane, post-annealing. This indicates that interparticle face-to-face hybridization interactions overcome the repulsive interactions between the NP and substrate, which are functionalized with the same DNA. As a result, the binary cubic system forms a *high density* film that exposes its closest-packed (100) plane even though only B-type PAEs form DNA bonds with the substrate that is functionalized

with A-type DNA. SEM images (Table 4-2) and a fit of GISAXS data (Figure 4-9) confirm that the films indeed adopt a 2D square symmetry with a lattice constant of 126 nm.

Next, we studied a binary octahedral system using NPs with edge lengths of 80 nm. The assembly of octahedral PAEs and their spherical counterparts can be directly compared, since in solution both systems form BCC SLs with RD Wulff shapes that expose their {110} closest-packed planes.[25,28] Among the low-index planes in a BCC lattice, the packing density goes as {110} > {100} > {111}.[167] When assembled onto a DNA-functionalized substrate, a binary system of spherical PAEs forms a film oriented in the <100> direction.[153] Importantly, this system adopts a non-close-packed orientation to maximize complementary NP-substrate bonds. However, unlike with the spherical system, octahedral PAEs reorganize into buckled honeycomb structures on substrates after assembly and annealing. This buckled honeycomb structure is equivalent to the {111} plane of a BCC lattice, as evidenced by SEM and GISAXS (Figure 4-2i-k, Table S2). Specifically, the GISAXS diffraction pattern can be assigned to a 2D hexagonal structure with two NPs per lattice point (Figure 4-20b), together comprising a honeycomb structure with a lattice constant of 165 nm. In this structure, each octahedral NP core is oriented in the <111> direction, and the resultant film exposes the {111} plane of a BCC SL. Notably, although 2D colloidal honeycomb SLs have been assembled using sub-10-nm NPs sub-10-nm NPs[150,168] and micron-sized particles,[31] this is the first time they have been prepared using NPs in the ~100-nm size range, which is most relevant for plasmonics and metamaterials. In fact, lithographically patterned honeycomb SLs at this length scale behave as the photonic counterpart of graphene, exhibiting extraordinary phenomena including Dirac-like plasmons[32–34] and complete photonic bandgaps.[35,36]
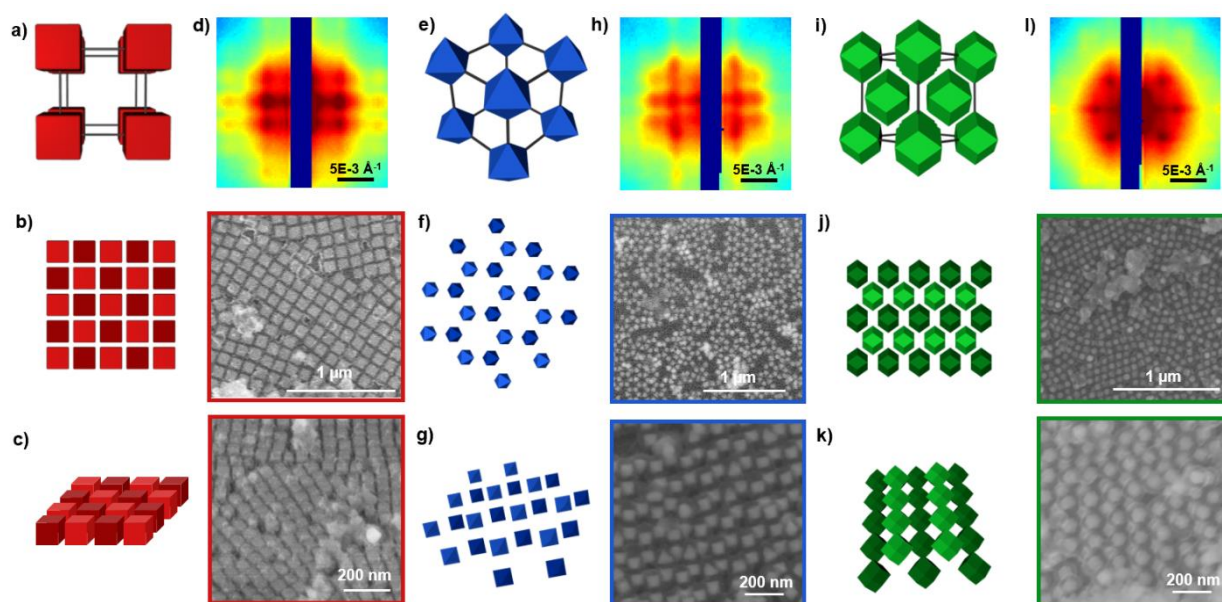
Figure 4-2. NP films. a,e,i) Schematics of the unit cells of cubic, octahedral, and RD PAE SLs rotated to match the orientation of the resulting 2D films. b,f,j) Schematics and corresponding SEM images of the resulting 2D films. Square, honeycomb, and rhombic symmetries were observed in films consisting of cubic, octahedral, and RD PAEs, respectively. c,g,k) Schematics and corresponding SEM images taken at a 30º tilt angle showing the height difference between A and B-type PAEs in each structure. d,h,l) GISAXS scattering patterns from the samples in b,f, and j, respectively.

Furthermore, this result elucidates the effect of shape-induced directionality on thin-film orientation. The drive of the system to maximize face-to-face interactions in polyhedral PAE systems affects the resulting SL orientation. Our observations are explained by a simple surface energy model, which demonstrates that when face-to-face NP-substrate interactions are present, the surface energy of the open {111} plane becomes lower than that of the closest-packed {110} plane (see Experimental Details). We also attempted to assemble films of octahedral PAEs with more than two layers, but interestingly, the resulting SLs were mostly amorphous (Figure 4-19). SEM images taken at a 90º tilt angle, post-annealing, (Figure 4-21b) revealed that A-type octahedral PAEs were situated at heights ~25% higher than expected based on a measurement of the bulk BCC system (Table 4-2). This result is likely due to the repulsion of the A-type octahedral

PAEs with the A-type substrate-bound DNA. This distortion of the 3D lattice likely explains why multi-layer crystalline films did not form.
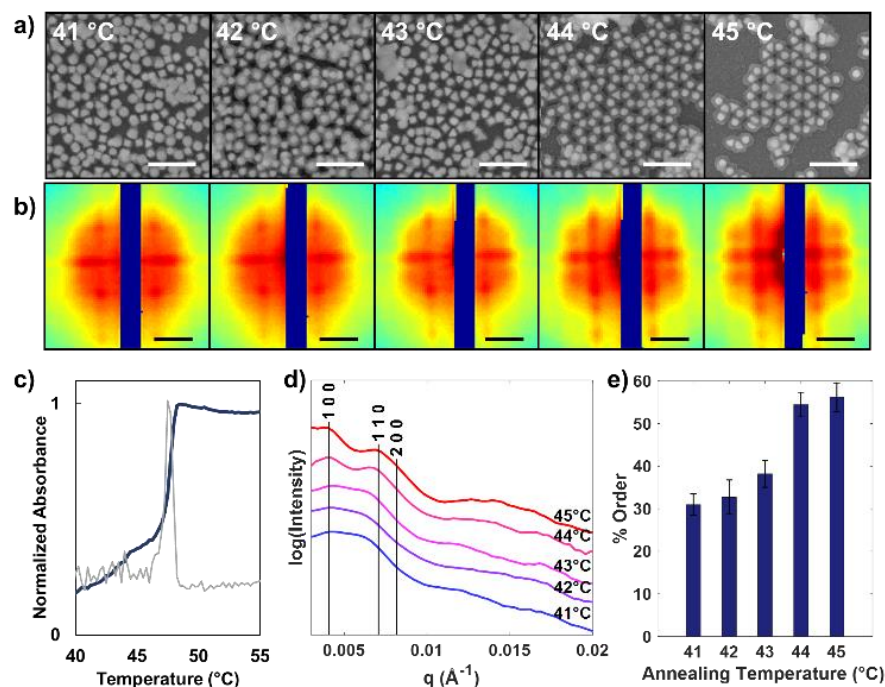
Figure 4-3. Assemblies of octahedral PAEs as a function of annealing temperature. a) SEM images of the assemblies at temperatures between 41 and 45°C. Scale bars are 500 nm. b) Corresponding 2D GISAXS diffraction spectra for the films in a). Scale bars are 5E-3 Å^{-1}. c) UV-vis spectroscopy of octahedra PAE aggregates in solution as it is heated. The sharp increase in absorbance at 47 °C indicates that the melting temperature (T_m) has been reached. The first derivative of the absorbance data is plotted in gray and is used to accurately determine T_m. d) 1D linecuts of the GISAXS spectra in b) taken at $q_z = 0$. e) Percent order as a function of annealing temperature.

The role of particle shape was further investigated using RD PAEs with edge lengths of 51 nm, which assemble into an FCC lattice with {111} closest-packed planes in solution.[123] A 2D rhombic SL with a lattice constant of 113 nm resulted from the assembly and annealing of these particles onto a DNA-functionalized substrate, as determined by GISAXS. This architecture can be matched with the {110} planes of an FCC lattice (Figure 4-2k). Furthermore, SEM images taken at a 90° tilt angle revealed that the height difference between the A- and B-type PAEs matches closely with that of an ideal FCC lattice (Table 4-2). Similar to the octahedral and cubic systems, individual

RD PAEs are oriented with a facet parallel to the surface, in the <110> direction in this case. As was seen with the octahedral films, this structure is derived from the least dense of the three low-index planes of the corresponding 3D lattice.

To better understand the reorganization process that occurs in these systems, we studied assembly using various annealing temperatures. For example, we annealed two-layer octahedral PAE films for 4 hours at multiple temperatures below the T_m of the aggregates of octahedral PAEs A and B (determined to be 47 °C, Figure 4-5) and characterized the resulting films using SEM and GISAXS (Figure 4-3). The SEM images indicate that the octahedral PAEs form mostly amorphous films at temperatures far below T_m but gradually develop a honeycomb structure with increasing crystallinity as the annealing temperature increases toward T_m. At temperatures just below T_m (44 °C), the films are comprised of a honeycomb structure with nearly 100% purity, but with lower surface coverage due to the significant melting of the PAEs from the substrate (Figures 4-3a, 4-4). Large-area SEM images (Figure 4-4) show that highly ordered films can be grown, while maintaining high surface coverage, by annealing at 44 °C, three degrees below T_m, for 4 hours. In addition, qualitatively similar results can be obtained by annealing at 45 °C for 2 hours. 2D GISAXS patterns further elucidate this trend; the diffraction spots sharpen as the temperature increases up to T_m (Figure 4-3b). 1D linecuts taken horizontally at $q_z = 0$ show the appearance of additional resolved peaks, indexed to a honeycomb structure (Figure 4-14b), indicating the emergence of long-range order (Figure 4-3d). Furthermore, SEM images were quantitatively analyzed using a homebuilt MATLAB script, and it was confirmed that, as temperature increases, percent order increases (Figure 4-3c). Similar trends were observed for cubic (Figures 4-16) and RD (Figures 4-17, 4-18) films, indicating that selecting an annealing temperature near T_m results in the highest quality films with both optimized percent order and substrate coverage.

The orientation of thin-films grown using DNA-mediated assembly can be altered by modifying the substrate-bound DNA,[153] a property unique to this system. In addition to substrates functionalized with A-DNA, we also studied the assembly of PAE films on bi-functionalized substrates with a 1:1 ratio of A:B DNA. In the spherical BCC system, films with <100> orientation and the closest-packed <110> orientation are obtained when mono-functionalized and bi-functionalized substrates are utilized, respectively.[153] However, for polyhedral PAEs, both SEM and GISAXS characterization indicate that the symmetries and orientations of the films assembled on bi-functionalized substrates are the same as those assembled on mono-functionalized ones (cubic PAEs form a square lattice, RD PAEs form a rhombic lattice, and octahedral PAEs form a honeycomb lattice, Figure 4-11), again demonstrating the influence of directional binding. Both octahedral and RD films exhibited slight distortions in lattice constants and bond angles, as the second layer of A-PAEs can also form DNA bonds with the bi-functionalized substrate (Figure 4-12).

4.3. Conclusion

In conclusion, we have utilized DNA to assemble crystalline thin-films comprised of polyhedral NPs and studied their reorganization as a function of NP core shape, annealing conditions, and substrate functionalization. In contrast with spherical PAEs, polyhedral PAEs form directional bonds that maximize NP-NP and NP-substrate face-to-face interactions, resulting, in certain cases, in more open crystallographic planes. The results demonstrate the importance of PAE shape on the formation of SLs on substrates and provide guidelines on how to predictably prepare desired structures by judicious choice of NP core and substrate functionalization. This additional level of control over PAE thin-film growth and the ability to access higher energy, open

crystallographic planes, could aid the discovery of emerging properties from the collective optical, electrical, and magnetic responses of NPs.
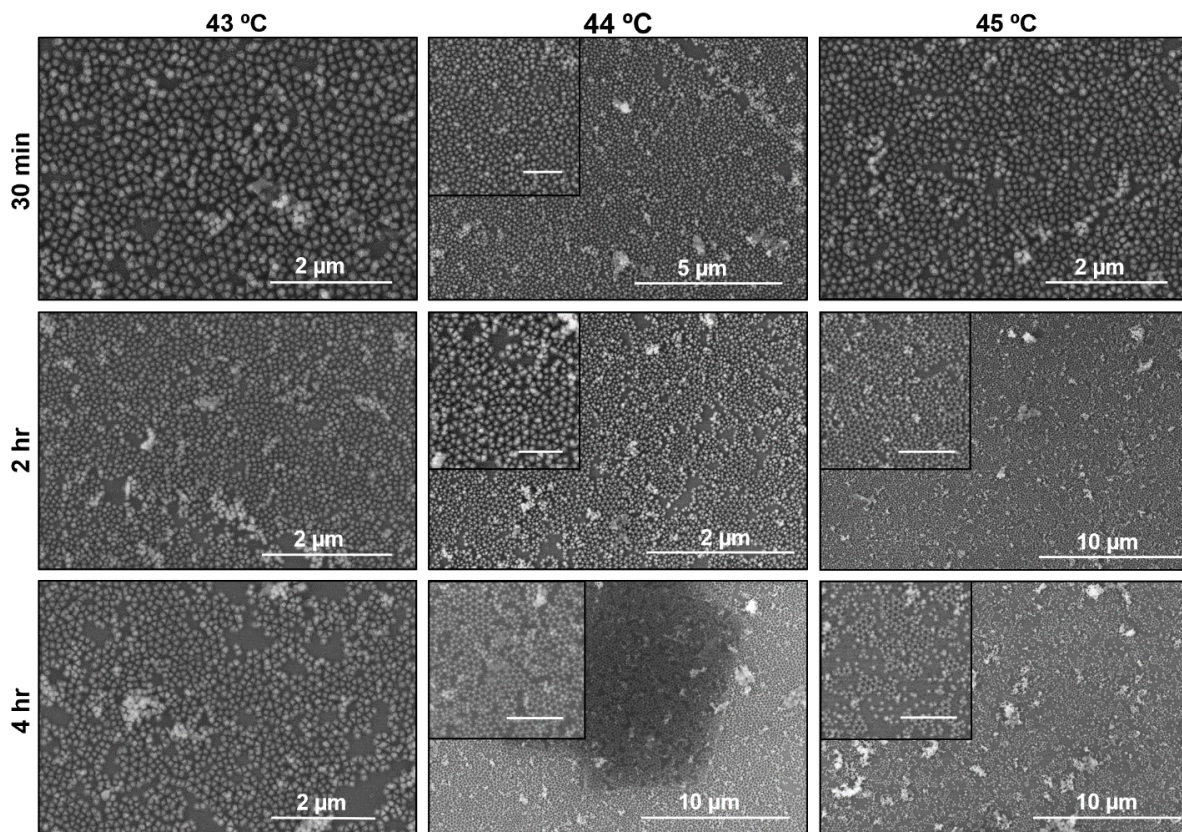
Figure 4-4. Large-area SEM images of two-layer octahedral PAE films grown on mono-functionalized substrates annealed at 43 ℃, 44 ℃, and 45 ℃ for 30 min, 2 hr, or 4 hr as indicated. Films annealed at 44 ℃ for 4 hr exhibit both high order and high coverage. Substrate annealing at 45 ℃ for 2 hr produces qualitatively similar results, while annealing at 45 ℃ for 4 hr results in films with high percent order, but lower coverage. Scale bars in insets are 2 μm.

4.4. Experimental Details

Nanoparticle Synthesis. All precursors were purchased from Sigma-Aldrich and used without further purification. Single-crystalline gold anisotropic nanoparticles (NPs) were synthesized via a seed-mediated method described in detail by O'Brien et al.[63] Briefly, uniform, single crystalline spherical gold NPs were synthesized via an iterative chemical growth and etching process. These NPs were then used as "seeds" for the growth of anisotropic NPs, including the cubes, octahedra, and rhombic dodecahedra used in this work. Importantly, this synthetic procedure results in uniform anisotropic NPs in high yield ($<$ 5 % coefficient of variation (CV), $>$ 90 % yield), which makes them ideal for the assembly of crystalline superlattices (SLs) with long-range order. The NPs were imaged by scanning transmission electron microscopy (STEM, Hitachi HD-2300 STEM).

Substrate Preparation. Gold-coated Si wafers were prepared via e-beam evaporation. Specifically, a Si wafer pre-diced into 5 x 5 mm squares was purchased from Ted Pella. The diced wafer was cleaned via an O_2 plasma at 50 W for 5 min. Following plasma cleaning, e-beam evaporation (Kurt J. Lesker Company) was used to deposit a 2-nm Cr adhesion layer at 0.2 Å/s, followed by an 8-nm Au layer at 0.5 Å/s onto the Si substrate.

NP and Surface DNA Functionalization. The DNA sequences used in this work are taken from the literature (Table S1).[2] Briefly, we functionalized the particles and substrates with 3' thiolated anchor DNA sequences, A and/or B depending on the experiment. Then, the appropriate corresponding complementary linker DNA strands were hybridized to the strands on the particle surfaces or the substrates. Each linker strand included a six-base single-stranded region designed

to link the particles A and B to each other (second layer) or to link the B-coated particles to the A-coated substrates (first layer) through complementary DNA hybridization events.

Table 4-1. Sequences Utilized in this Work. Note that "sp18" refers to a hexaethylene glycol spacer unit manufactured by Glen Research.

Description	DNA Sequence (5' to 3')
'A' anchor DNA	TCA ACT ATT CCT ACC TAC (sp18)$_2$ SH
'B' anchor DNA	TCC ACT CAT ACT CAG CAA (sp18)$_2$ SH
'A' linker DNA	GTA GGT AGG AAT AGT TGA A TTT AGT CAC GAC GAG TCA TT A TTT AGT CAC GAC GAG TCA TT A TTCCTT
'B' linker DNA	TTG CTG AGT ATG AGT GGA A TTT AGT CAC GAC GAG TCA TT A TTT AGT CAC GAC GAG TCA TT A AAGGAA
Duplexer	AAT GAC TCG TCG TGA CTA AA

The NPs were functionalized using a procedure modified from that described by Jones et al.[125] and O'Brien et al.[123] Briefly, 3' alkylthiol-modified oligonucleotides were first treated with a 100 mM solution of dithiothreitol (DTT) in 170 mM sodium phosphate buffer (pH = 7.4) and then purified on a Nap-10 size exclusion column (GE Life Sciences) to remove excess DTT. Next, the NPs were washed twice to remove excess ligands. Specifically, the NP solutions containing the as-synthesized particles were centrifuged for 8 min at 3,800 rpm, the supernatant was removed, and the pelleted NPs were resuspended in water. The NPs were then centrifuged a second time for 8 min at 3,800 rpm, the supernatant was removed, and then the solution of purified DNA was added to the pellet immediately. Five µmol of thiolated DNA was added per 1 OD of particles. The particle solution was then brought to 0.01 M sodium phosphate buffer (pH = 7.4) and 0.01 wt. % sodium dodecyl sulfate (SDS) in water. Stepwise addition of 2 M NaCl was then carried out

every 30 min, such that the NaCl concentration was increased to 0.05 M, 0.1 M, 0.2 M, 0.3 M, 0.4 M, and 0.5 M in turn. Following this process, the NPs were placed on a shaker at 700 rpm and left overnight to ensure a dense loading of oligonucleotides. After functionalization, the NP solutions were centrifuged three times to remove excess DNA. After each of the first two rounds of centrifugation, the NPs were resuspended in 0.01 wt. % SDS, and after the last centrifugation step, the particles were resuspended in 0.5 M PBS (0.5 M NaCl, 0.01 M sodium phosphate buffer (pH = 7.4), and 0.01 wt. % SDS). To form linker-duplexer complexes, the 20-base duplexer strands were mixed with the linkers in a 2:1 ratio in a 0.5 M PBS solution. This solution was heated at 55 ℃ for 30 min and then cooled to room temperature. The duplexers hybridize with the complementary single-strand regions of the linker strands to create a rigid DNA structure. Next, 5 nmol of the hybridized linker-duplexer complexes were added for each 10 OD of anchor DNA-functionalized NPs in solution. The solution was again heated at 55 ℃ for 30 min, and then cooled to room temperature to allow the linker-duplexer complexes to fully hybridize to the anchor strands.

The procedure for the DNA functionalization of the substrate was similar to that for the NPs as described above. Specifically, 1 µmol of DTT-cleaved DNA (A and/or B) in water was added to each substrate. However, instead of stepwise addition of NaCl, the substrates were brought to 0.5 M NaCl in one addition to a total volume of 500 µL per substrate, and then shook overnight at 700 rpm. The substrates were then rinsed three times with water and placed in a PBS solution. After functionalization with the anchor DNA strands, the substrates were incubated in a 0.5 M PBS solution containing 0.5 µM linker, pre-hybridized with duplexer, subsequently heated to 55 ℃ for 30 min, then allowed to slowly cool to room temperature to ensure full hybridization between anchor and linker DNA sequences.

Determination of PAE Melting Temperature. The melting temperatures (T_m) of each complementary NP system were measured using temperature-dependent UV-vis spectroscopy. First, A- and B-type PAEs were hybridized with the respective linker-duplexer complexes and then mixed in a 1:1 ratio in 0.5 M PBS. The formation of visible aggregates could be observed within a few seconds after mixing. Next, the solution was transferred to a quartz cuvette with a magnetic stir bar and loaded into a UV-vis spectrometer.
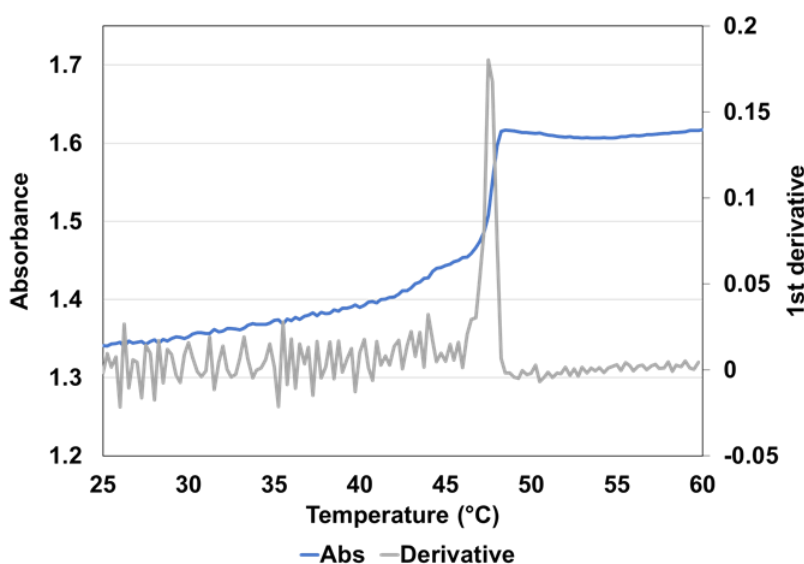
Figure 4-5. A temperature-dependent UV-vis trace used to determine the melting temperature of octahedral PAE assemblies. The sharp increase in absorbance indicates a cooperative melting event. The melting temperature (47 °C) is determined from the peak of the first derivative of the absorbance vs. temperature curve.

The sample was heated from 25 °C to 60 °C at a rate of 0.25 °C/min while stirring, and the absorbance at 260 nm (the absorbance maximum of the DNA) was recorded. The observed sharp increase in absorbance is representative of the cooperative melting behavior of the DNA bonds between PAEs. Finally, T_m was determined by finding the maximum of the first derivative of the absorbance trace (Figure 4-1).

NP Assembly. NP films were assembled layer-by-layer on gold-coated substrates. Since the mono-functionalized substrates were functionalized with A-type DNA, the complementary B-type

particles were assembled as the first layer. Specifically, the substrate was soaked in a 4 OD solution of B-type particles in 0.5 M PBS and shaken for 4 hours at room temperature at 700 rpm. Next, the substrate was removed from the B-particle solution and vortexed in clean 0.5 M PBS to remove excess particles not bound through DNA hybridization. Then, the substrate was transferred to a 4 OD solution of A-type particles in 0.5 M PBS and left on a shaker for 4 hours at room temperature at 700 rpm. Finally, the substrate was transferred to a 2-mL tube with 500 µL of 0.5 M PBS for annealing. The samples were annealed for 4 hours at various temperatures on a thermal shaker (that was not shaking). This process resulted in a two-layer amorphous film (Figure 4-c), where a single particle layer was added after each deposition cycle, because a given PAE does not bind with another one functionalized with the same DNA in this system.

Silica Embedding. The NP films were encapsulated in silica according to literature precedent.[5] This method mostly preserves the crystal symmetry and lattice parameters of the lattice in the solid state. The samples were transferred to a 2-mL Eppendorf tube and suspended in 1 mL of 0.5 M PBS solution. To this solution, 2 µL of the quaternary silane salt, N, trimethoxysilylpropyl-N,N,N-trimethylammonium chloride (TMSPA), was added, and the tube was agitated at room temperature on a thermomixer (Eppendorf) at a rate of 700 rpm for 30 min. Next, 5 µL of triethoxysilane (TES) was added to the solution, and a silica network formed around the entire lattice. The mixture was left on the thermomixer at 700 rpm for 2 hours. Finally, the sample was removed from solution, rinsed with water, and blown dry using a stream of N_2.

Grazing Incidence Small Angle X-Ray Scattering (GISAXS). All GISAXS experiments were conducted at the 12ID-B station at the Advanced Photon Source (APS) at Argonne National Laboratory. The samples were probed using 13.3 keV (0.932 Å) x-rays, and the sample-to-detector

distance was calibrated from a silver behenate standard. The beam was collimated using two sets of slits, and a pinhole was used to remove parasitic scattering. The beamwidth was approximately 200 – 300 µm horizontally and 20 µm vertically. The samples were aligned to the beam using the half-cut technique on a sample positioning stage that allowed for movement in the x, y, and z directions (where x is parallel to the beam and z is normal to the substrate), in addition to tilt (rotated about the y-axis) and rotation (rotated about the z-axis). Data was collected at incident angles, α_i, ranging from 0.3 – 0.4°. Scattered radiation was detected using a Pilatus2M detector. Analysis of GISAXS data, including 2D fits and horizontal and vertical linecuts, was performed using a homebuilt MATLAB package.

One- and Two-Layer Assemblies. The incubation times for the assembly of the first of PAEs were varied to find the minimum time necessary to achieve a saturated particle density. The substrates were incubated in 4 OD solutions of octahedra and rhombic dodecahedra PAEs for times ranging from 30 minutes to 24 hours. The substrates were then embedded in silica and imaged. To quantify surface loading, the particle density was also counted using ImageJ following the same procedure as was used to collect the data shown in Figure S2. The result for octahedra is shown in Figures 4-6 below.
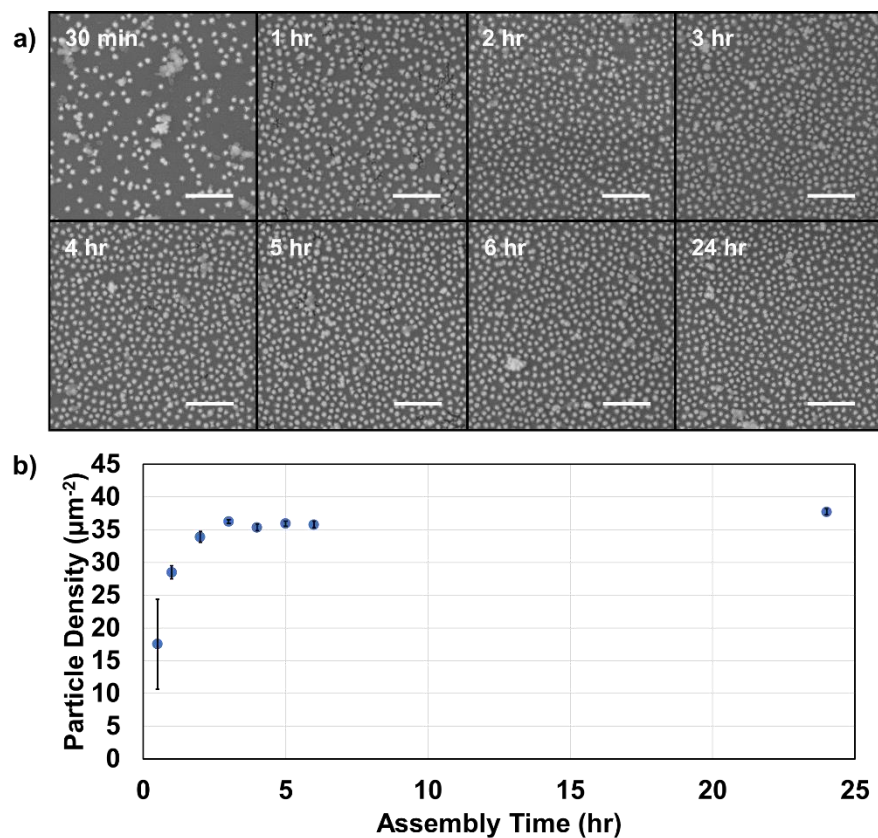
Figure 4-6. The density of octahedra PAEs after assembly of the first layer using different incubation times. a) Representative SEM images. Particle density increased quickly at early times and plateaued at longer incubation times. Scale bars are 1 µm. b) Quantified particle densities at each time point tested. The density plateaued after approximately 3 hours.
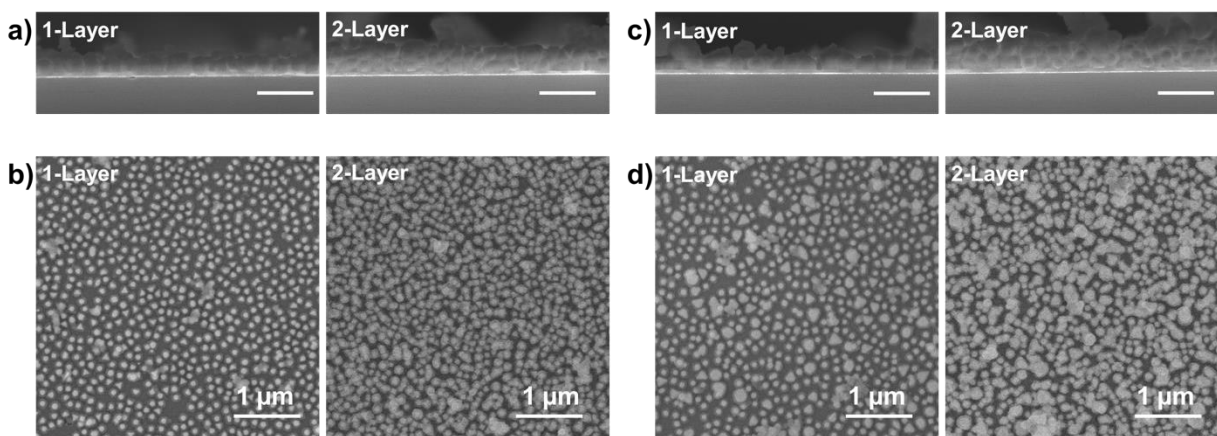
Figure 4-7. SEM images comparing one-layer and two-layer assemblies prior to annealing. a) Cross-sections of one- and two-layer octahedra assemblies. b) Top-down images of one- and two-layer octahedra assemblies. c) Cross-sections of one- and two--layer RD assemblies. d) Top-down images of one- and two-

layer RD assemblies. For both octahedra and RD, the two-layer assemblies contain more than a monolayer of particles and contain more particles per unit area compared to one-layer assemblies.
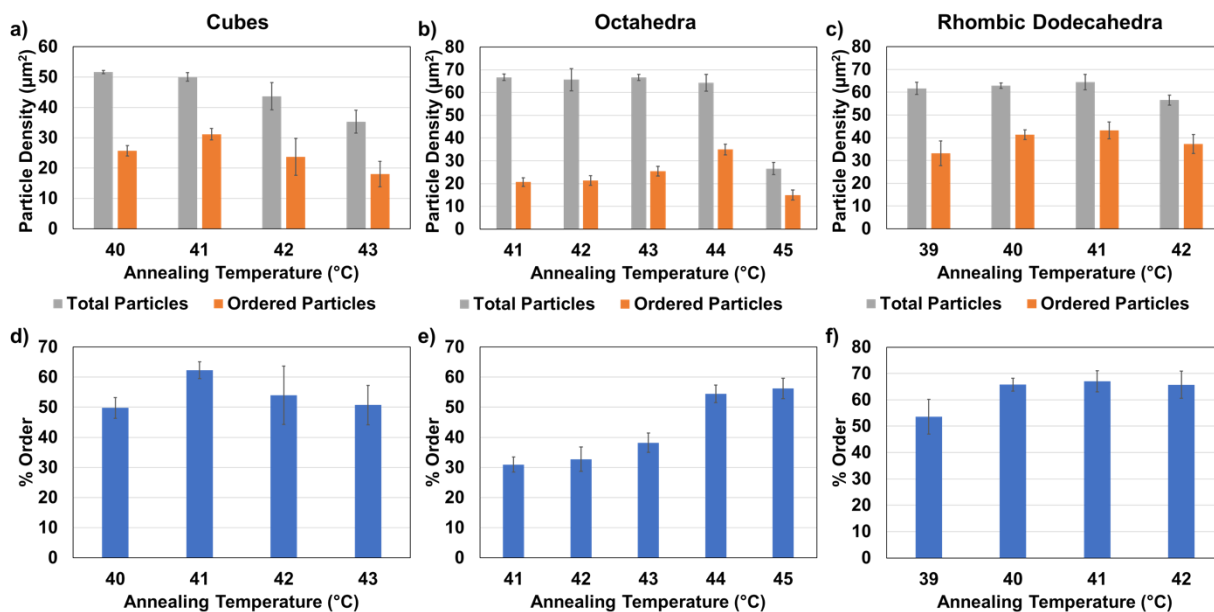
Figure 4-8. Results of MATLAB image analysis. a-c) Total and ordered particle densities for cubic, octahedral, and RD PAE assemblies. d-f) Percent order of samples in a-c, respectively, at different annealing temperatures.

Additional GISAXS Data
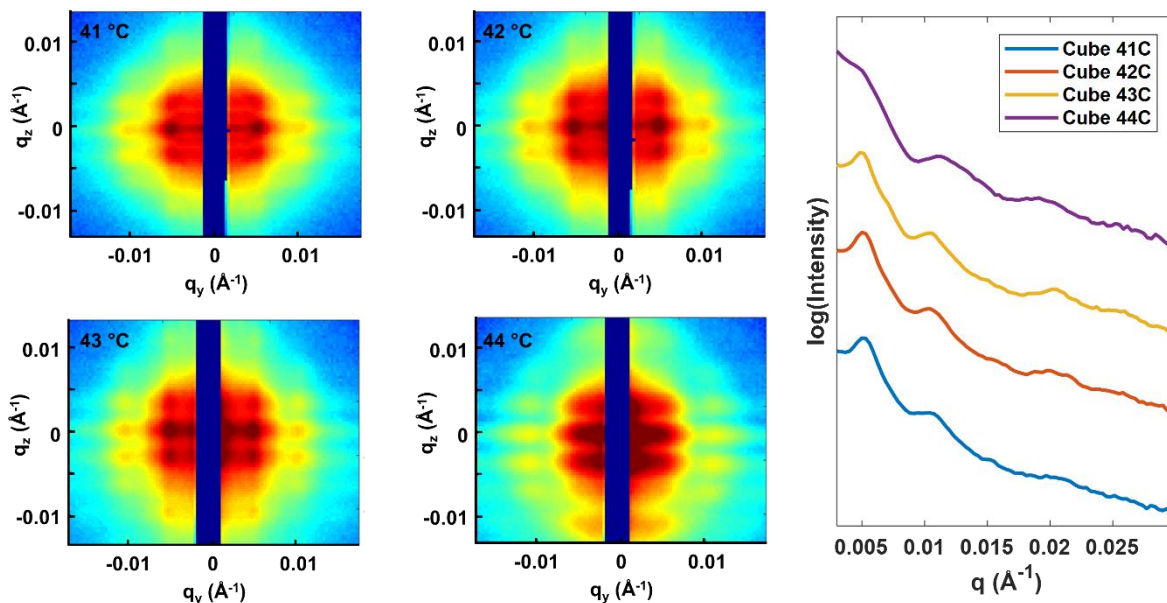
Figure 4-9. GISAXS scattering patterns of two-layer cube films annealed at 41 ℃, 42 ℃, 43 ℃, and 44 ℃. The diffraction spots become sharper as the temperature increases from 41 to 43 ℃. At 44 ℃, the individual spots are broader, and the pattern is dominated by the Kiessig fringes, indicative of a loss of ordering as the temperature approaches T_m. The 1D linecuts more clearly demonstrate peak sharpening from 41 to 43 ℃ and peak broadening at 44 ℃.
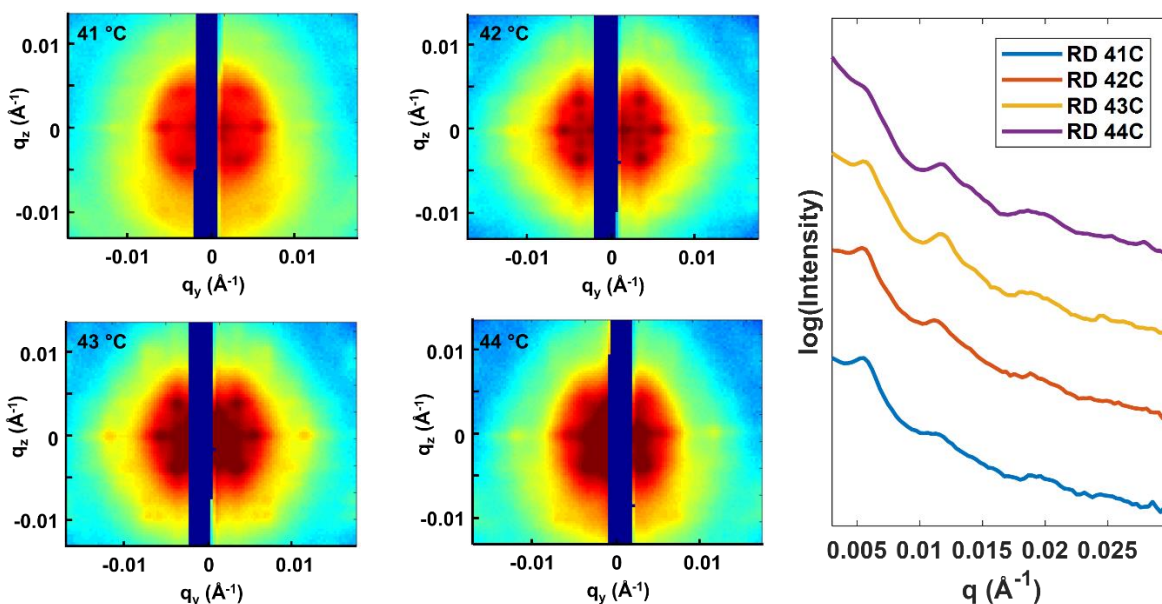
Figure 4-10. GISAXS scattering patterns of two-layer RD films annealed at 41 ℃, 42 ℃, 43 ℃, and 44 ℃. As with the cube films, at 44 ℃, the diffraction spots again become broader, indicative of a loss in ordering. The 1D linecuts also show peak sharpening from 41 to 43 ℃ and peak broadening at 44 ℃.

Effect of Substrate Functionalization. To prepare substrates functionalized with both A- and B-type DNA, we mixed a 1:1 molar ratio of DTT-cleaved A- and B-type anchor strands in 0.5 M PBS solution. Next, we immersed the Au-coated substrate into a 500 µL solution of 0.5 M PBS and 1 µmol of the anchor strand mixture and placed the sample on a shaker overnight at room temperature and 700 rpm. After the functionalization of the substrate with the anchor DNA strands, the linker/duplexer strands were hybridized by incubating these substrates in a solution containing 0.5 µL of a 1:1 mixture of A- and B-type linker DNA (pre-hybridized with duplexer) and subsequently heating them to 55 ℃ for 30 min. Then, the system was slowly cooled to room temperature to ensure full hybridization between the anchor and linker DNA strands.
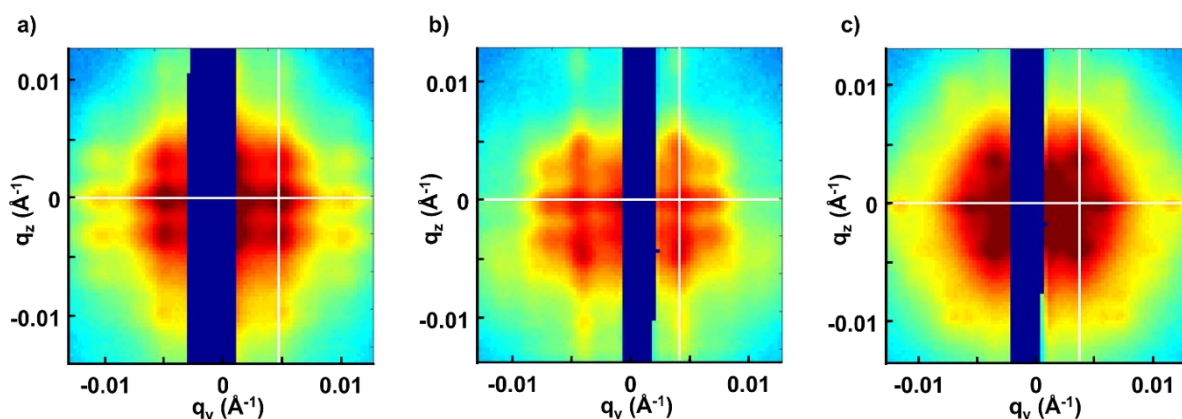
Figure 4-11. GISAXS scattering patterns indicating the positions (white lines) of horizontal and vertical linecuts for a) cube, b) octahedra, and c) RD films.

To analyze subtle differences between the GISAXS diffraction patterns of two-layer films assembled on mono- and bi-functionalized substrates, we took horizontal linecuts though $q_z = 0$, and vertical linecuts through the set of diffraction spots closest to $q_{x,y} = 0$ (Figure 4-17). The horizontal linecuts provide in-plane structural information, while the vertical cuts provide the out-of-plane spacing. In the case of the octahedral PAE system, a comparison of horizontal and vertical linecuts of GISAXS scattering patterns reveals a ~6.8 % expansion in the x-y lattice parameter and

a ~2.9 % contraction in the z-direction when a bi-functionalized substrate is used as compared to when a mono-functionalized one is used (Figure 4-18 b,e). The observed vertical compression and accompanying horizontal expansion can be attributed to a flattening of the lattice when the second layer of A-PAEs can also form DNA bonds with the substrate. In fact, unlike octahedral films grown on a mono-functionalized substrate, those grown on bi-functionalized substrates exhibited lattice constants closely matched with those of an ideal BCC (111) film (Table 4-2). RD films grown on a bi-functionalized substrate exhibited a similar degree of contraction (~7.2 %) in the z-direction as compared to RD films grown on a mono-functionalized substrate due to DNA-binding between second-layer RD A-PAEs and the substrate functionalized with DNA B. Interestingly, this contraction was not accompanied by a significant expansion in the x-y plane (Figure 4-18c,f). On the other hand, lattice distortions were not observed in the cubic PAE system (Table 4-2). Distortion is not expected in this system because the resulting structure in both cases is a square monolayer, where both A- and B-type PAEs form face-to-face contacts with the substrate (Figures 4-18a,d).

Form Factor Simulation. To determine the orientation of individual NPs within a SL, we performed form factor simulations for individual NPs (Figure 4-19). The form factor scattering formula of octahedron and RD are found in previous publications. To demonstrate that the Bragg streak occurs normal to the nanoparticle facet and thus it is possible to determine the nanoparticle orientation, we calculated the form factor scattering for two representative orientations of the superlattice for each particle type; <100> and <111> for octahedron and <100> and <110> for RD. In the particle models, the vertical and horizontal directions are the z and y axes, respectively. In the calculated 2D scattering images, vertical and horizontal directions are q_z and q_y axes, respectively, which is identical to the measurement geometry.
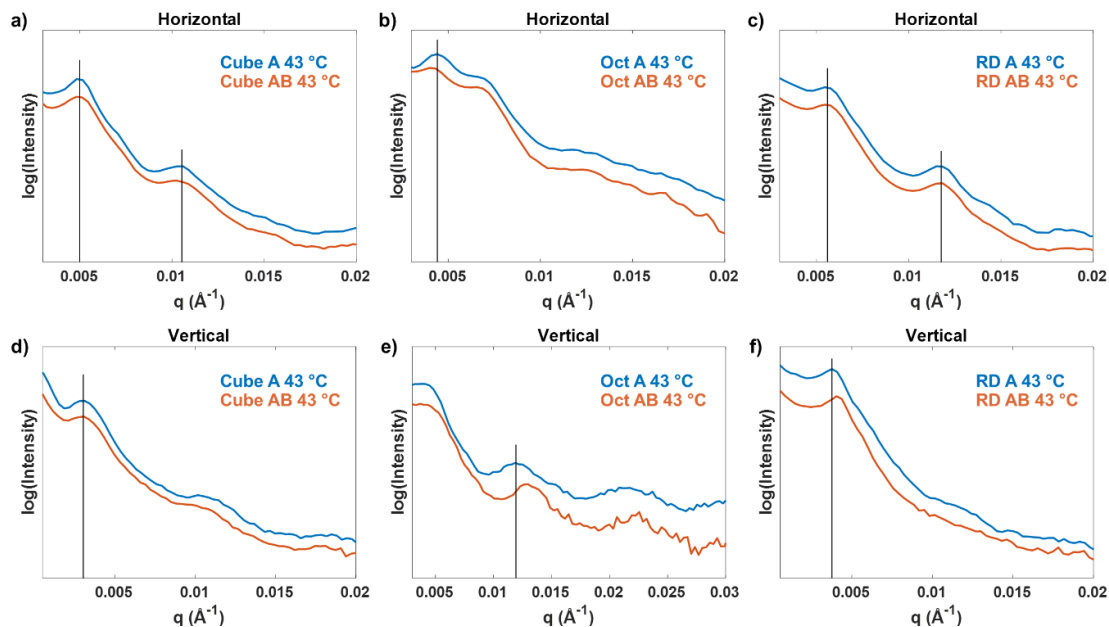
Figure 4-12. Comparison of two-layer films assembled on substrates functionalized with A-type DNA and those with both A and B-type DNA. a-c) Horizontal and d-f) vertical linecuts of the GISAXS patterns resulting from cubic, octahedral, and RD PAE films, respectively.

As expected, strong streaks are observed along the normal to the facet directions. A gold NP octahedron is surrounded only by the {111} planes of atoms. On the other hand, a RD is covered by the {110} planes of atoms. Therefore, the only observable streaks for octahedron and RD are along <111> and <110>, respectively. The direction will rotate as the particles rotate.

By comparing simulated form factors and measured diffraction patterns, we concluded that individual octahedral NPs in the honeycomb lattice were oriented with their <111> direction normal to the substrate (Figure S15a), while individual RD NPs in the rhombic lattice were oriented with their <110> direction normal to the substrate (Figure 4-19d). This analysis was not performed for cubic NPs, for which SEM images clearly showed NPs oriented with {100} facets parallel to the substrate. Importantly, all three PAEs are oriented with a NP facet parallel to the substrate to maximize face-to-face DNA binding.
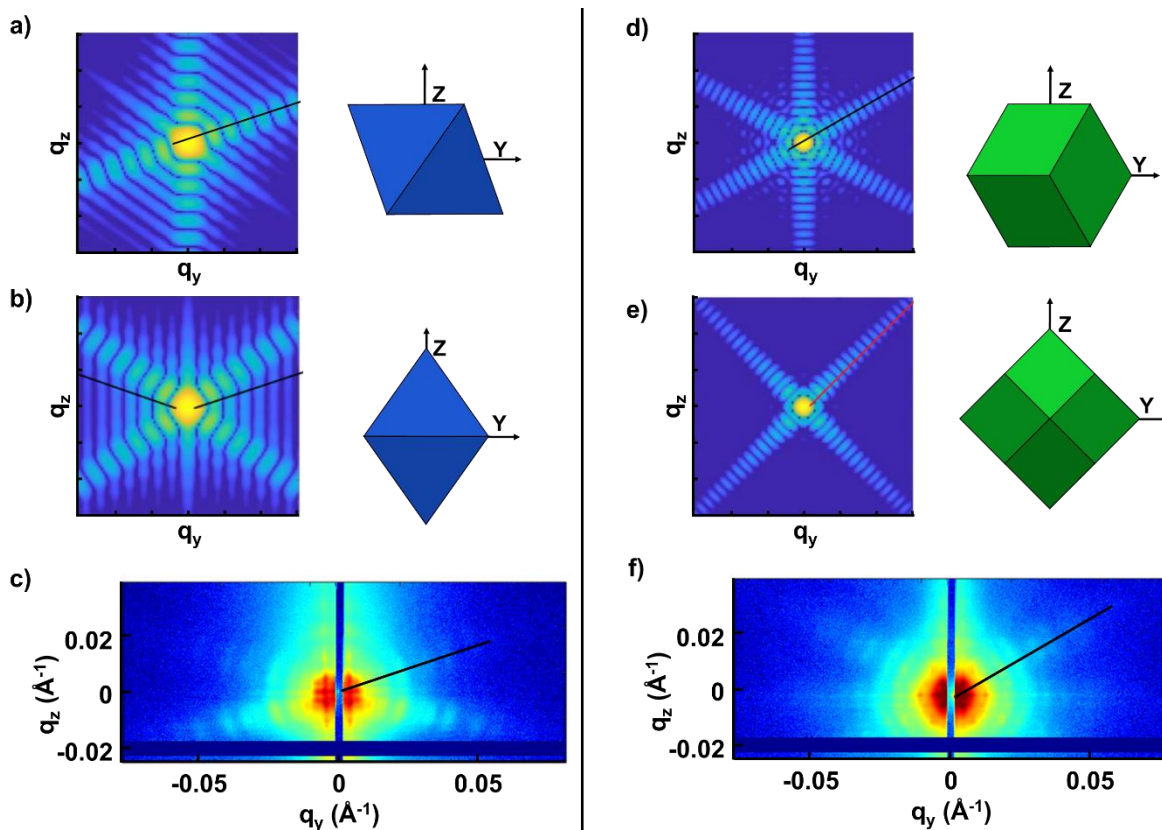
Figure 4-13. Form factors of octahedral and RD NPs. a-b) Simulated form factor of an octahedral NP oriented in the <111> and <100> directions, respectively, as shown in the diagrams on the right. c) GISAXS scattering pattern from a two-layer octahedral PAE assembly. d,e) Simulated form factor of RD NPs oriented in the <110> and <100> directions respectively, as shown in the diagrams on the right. f) GISAXS scattering pattern from a two-layer RD PAE assembly.

Surface Energy Model. To understand the effect of the DNA-functionalized substrate on total film energy, we developed a model to estimate the relative energies of each orientation, using the octahedral system as a proof-of-concept. Our model uses a dangling bond analysis that calculates the energy required to break a bulk crystal along a given plane based on the number of unsatisfied bonds in the exposed surface. The analysis was performed for SL surfaces both with and without binding to a DNA-functionalized substrate. This analysis helps rationalize the formation of the open honeycomb SLs.

A few assumptions were made to simplify the analysis. First, the PAE shapes, including the DNA shell on their surfaces, were assumed to be perfect octahedra, with perfectly sharp edges and vertices. However, in an experiment, a small degree of corner- and edge-truncation always exists. Second, we assumed that the DNA density on all NP and substrate surfaces was uniform and the same. This assumption allowed us to make the binding energy proportional to the overlap area between surfaces. Finally, we accounted only for attractive DNA interactions and ignored the effect of repulsion, which could be present in PAE systems.

Due to the orientation of individual octahedral NPs in a BCC SL, any bond between two PAEs occurs between two equilateral triangular facets that are oriented 180° from each other, forming a hexagonal contact area. This contact area is equal to 2/3 of the total triangular facet area (Figure S16a). For simplicity, this bond is defined to have a bond strength of ε. When a particle is bound to the substrate, the entire triangular facet can interact with the substrate, resulting in a 1.5x larger bond strength (1.5ε) compared to an interparticle bond.
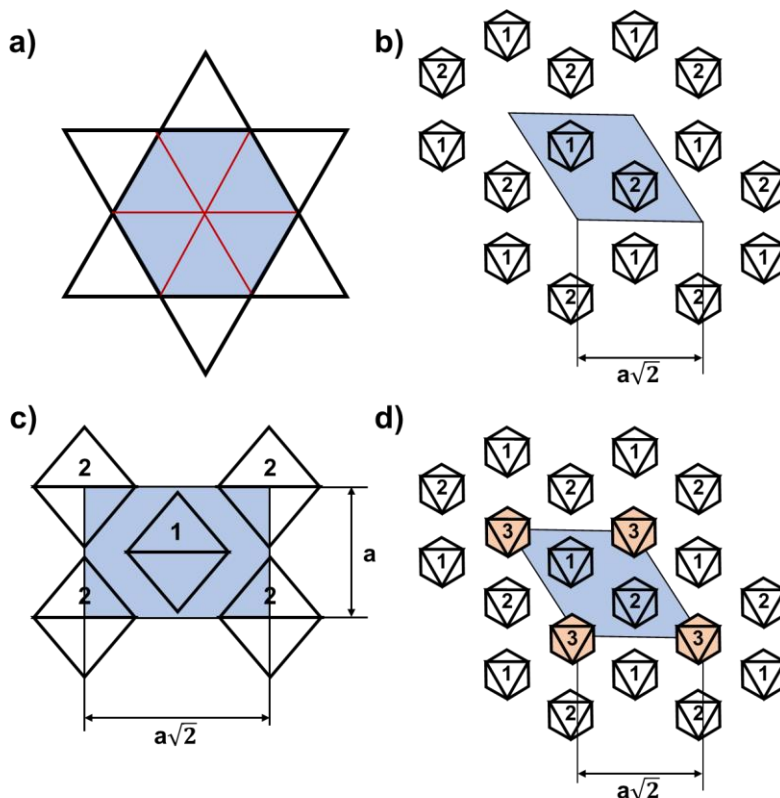
Figure 4-14. Surface energy calculations for the octahedral PAE system. a) Schematic illustrating the binding area between two complementary octahedral PAEs. The two triangular faces form a hexagonal overlap region that is 2/3 the area of the triangle. b) Arrangement of octahedral NPs in a BCC (111) slab with two layers. The shaded blue area indicates a 2D hexagonal unit cell. The numbering indicates that the NPs are situated in different layers, where 1 is the bottom layer, and 2 is the top layer. c) Arrangement of octahedra in the BCC (110) plane. The shaded blue area indicates a rectangular unit cell. The numbers indicate the locations of the two complementary PAEa, which are situated at the same height. d) Arrangement of octahedral NPs in a BCC (111) slab with three layers. The orange shading indicates NPs that can bind to a DNA-functionalized substrate placed above the slab.

In a BCC crystal, the {111} facet has 6 dangling bonds per $\sqrt{3}a^2$, where a is the lattice parameter of the BCC unit cell (Figure 4-20b). Dividing the bond energy by the area results in a surface energy of $3.46\,\varepsilon/a^2$. The {110} facet has 4 dangling bonds per $\sqrt{2}a^2$, resulting in a surface energy of $2.83\,\varepsilon/a^2$ (Figure 4-20c). Based on these calculations, without the presence of a DNA-functionalized substrate, the {110} plane of an octahedron BCC crystal should have the

lowest surface energy, resulting in the observed RD Wulff-shape in solution-assembled SLs of octahedral PAEs.

With the addition of a DNA-functionalized substrate, dangling bonds on the surface in contact with the substrate could potentially be eliminated. In the BCC (111) surface, individual octahedrons are oriented such that their entire facet can form DNA-bonds with the substrate if the substrate and first-layer PAEs are functionalized with complementary DNA. As a result of this favourable interaction, the energy of this surface is significantly reduced. Specifically, binding with the substrate results in a 1.5ε reduction in surface energy for each PAE in contact with the substrate. Applying this surface energy reduction to the $6\ \varepsilon$ dangling bond energy per $\sqrt{3}a^2$ area would result in $4.5\ \varepsilon$ per $\sqrt{3}a^2$ area. The result is a new surface energy of $2.60\ \varepsilon/a^2$. In contrast, individual octahedra in the (110) plane are oriented such that their edges are in contact with the substrate. Because we assumed that the PAEs have perfectly sharp corners and edges, a reduction in surface energy does not occur when the (110) surface is in contact with the substrate. It is important to note that in actual experiments, corner- and edge-rounding allows the PAEs to form a small number of favorable DNA bonds with the substrate. However, since the number of DNA strands on the edge of a PAE is far fewer than that on a facet, we treat the NP edge-to-substrate interaction as negligible in our model. As such, the energy of the (110) surface remains $2.83\ \varepsilon/a^2$ with the addition of a DNA-functionalized substrate. Accordingly, the addition of the DNA-functionalized substrate lowers the energy of the (111) surface below that of the (110) surface. The reversal in the order of surface energies agrees with experimental observations, in which the (111)-oriented film is the predominatant stucture in a two-layer octahedron film assembled on a mono-functionalized substrate.

Structural Analysis using SEM Imaging. To aid interpretation of GISAXS data and gain a more complete structural picture of the PAE films, we imaged the samples used for GISAXS measurements with SEM. First, in-plane interparticle distances were measured using top-down SEM images. We compared this spacing to the in-plane spacing derived from a fit of the horizontal linecut through $q_z = 0$ of the corresponding GISAXS scattering patterns. Next, the samples were sectioned and imaged at a 90° tilt angle to obtain the height difference between the first and second layers in each SL as well as the total film thickness. These values were compared to structural information obtained from fits of the vertical linecuts of the corresponding GISAXS scattering patterns. Representative cross-sectional images for the three NP films are shown in Figure 4-21, and a summary of the measurements obtained from SEM images and GISAXS patterns are shown in Table S2. SEM images of the cube samples used for this analysis revealed a mixture of one- and two-layer regions. The average film thickness from measurements at many random locations (204 nm) matched well with the values obtained from GISAXS (208 nm). The agreement between the values obtained from these two methods supports the hypothesis that the vertical oscillations in GISAXS data represents an average total film thickness rather than the out-of-plane d-spacing.

As with the cube films, the total thickness of the octahedron films measured via SEM matched the out-of-plane periodicity observed in GISAXS. The measured height difference between the two layers of NPs in the AB-substrates also matched well with the calculated height difference of an ideal BCC (111) film (Table 4-2). There is a slight discrepancy for the theoretical and measured height difference for the A-substrates (Table 4-2). Although the standard deviation is large enough that it could be interpreted as insignificant, it is the measurement with the largest deviation compared to other measurements. One possible physical explanation is that there is repulsion between the surface and the second layer of particles. Because the DNA on the substrate

and the DNA on the particles comprising the second layer cannot hybridize, it is possible that the small height difference causes their DNA shells to repel each other, leading to a slightly larger height difference.

The RD samples contained domains that are many layers in thickness. This is visible in Figure S17c as pyramidal grains. The height differences between layers measured in SEM matched well with those determined from GISAXS.
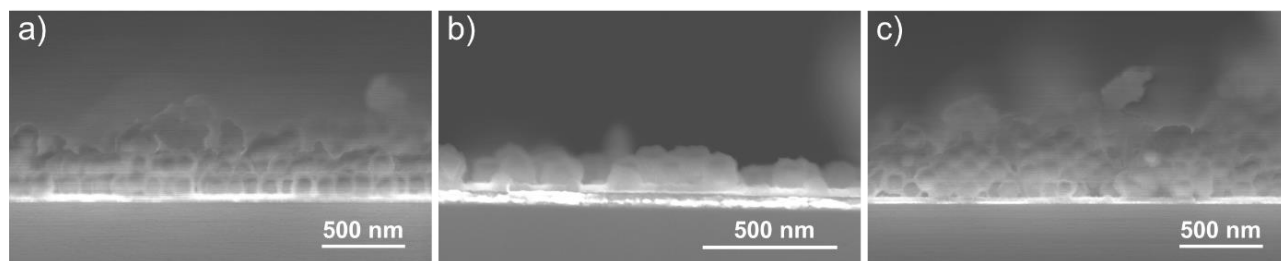
Figure 4-15. Cross-sectional SEM images of silica-embedded samples of a) cubes, b) octahedra, and c) RD.

Table 4-2. Comparison of Distance Measurements Between SEM and GISAXS.

PAE Shape	Symmetry	SEM Measurement A (nm)	SEM Total Thickness A (nm)	SEM Height Difference A (nm)	SEM Measurement AB (nm)	SEM Total Thickness AB (nm)	SEM Height Difference AB (nm)
Cube	Square	122.2 ± 6.9	204.2 ± 57.8	N/A	122.2 ± 6.3	207.7 ± 70.7	N/A
Octahedra	Hexagonal	163 ± 7.9	143.1 ± 6.3	42.2 ± 10.3	172.7 ± 11.3	140.4 ± 11.0	39.3 ± 10.8
RD	Rhombic	117.1 ± 7.2	N/A	64.7 ± 6.9	110.2 ± 5.9	N/A	63.8 ± 8.1
PAE Shape	Symmetry	GISAXS Horizontal Fit A (nm)	GISAXS Vertical Fit A (nm)	Derived Height Difference A (nm)	GISAXS Horizontal Fit AB (nm)	GISAXS Vertical Fit AB (nm)	Derived Height Difference AB (nm)
Cube	Square	126.4	208.8	0	126.9	205.1	0
Octahedra	Hexagonal	164.5	149.8	33.6	175.7	145.4	35.9
RD	Rhombic	113	166.8	65.2	112.8	154.8	65.1

Additional SEM Images
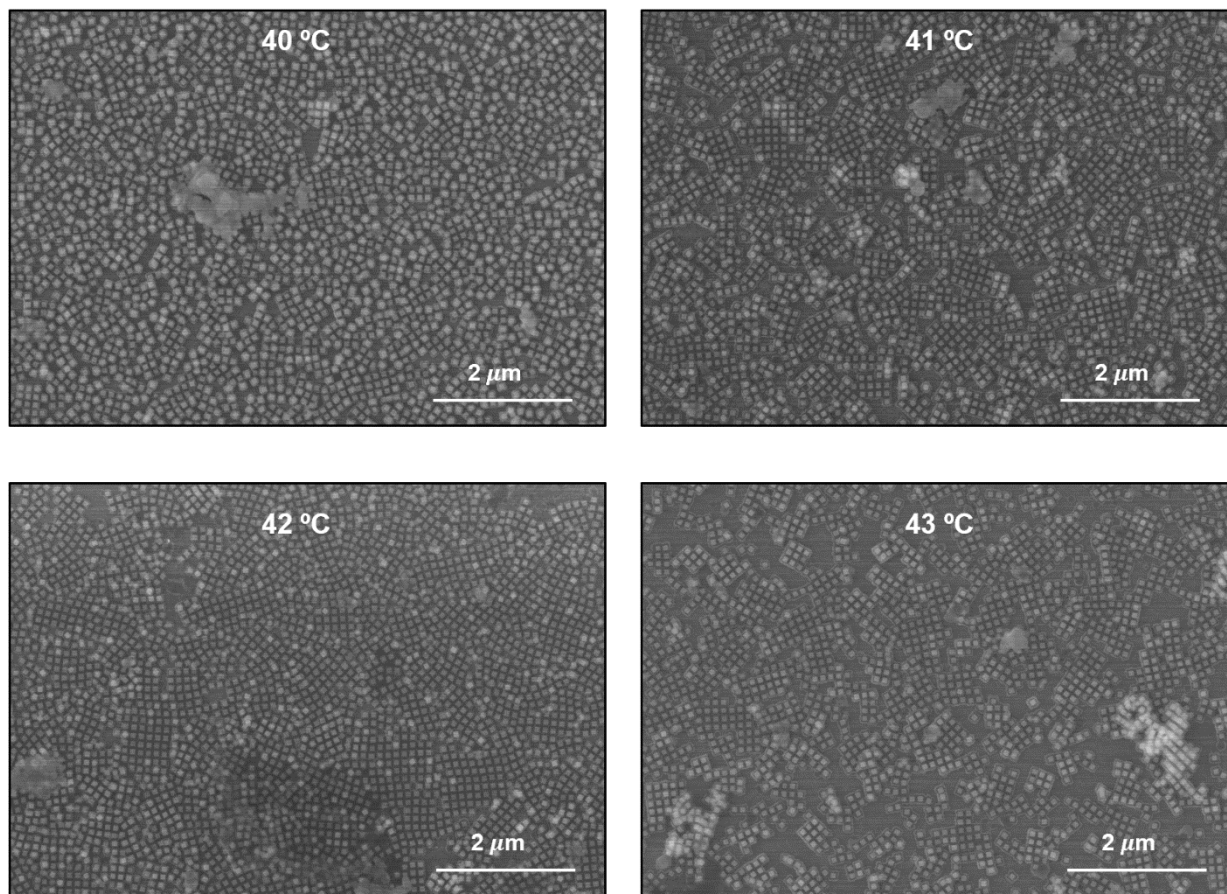
Figure 4-16. Large-area SEM images of cubic PAE SLs annealed for 4 hours at 40 °C, 41 °C, 42 °C, and 43 °C. Interestingly, when annealed at lower temperatures, the cubic PAE system forms two-layer films, where the second layer is comprised of isolated A-PAEs bound to the top facet of underlying B-PAEs. However, as the annealing temperature increases, the top PAEs melt off, resulting in the observed square monolayer. PAEs in the second layer are less strongly bound than those in the first layer because they are bound only to one other NP rather than four.
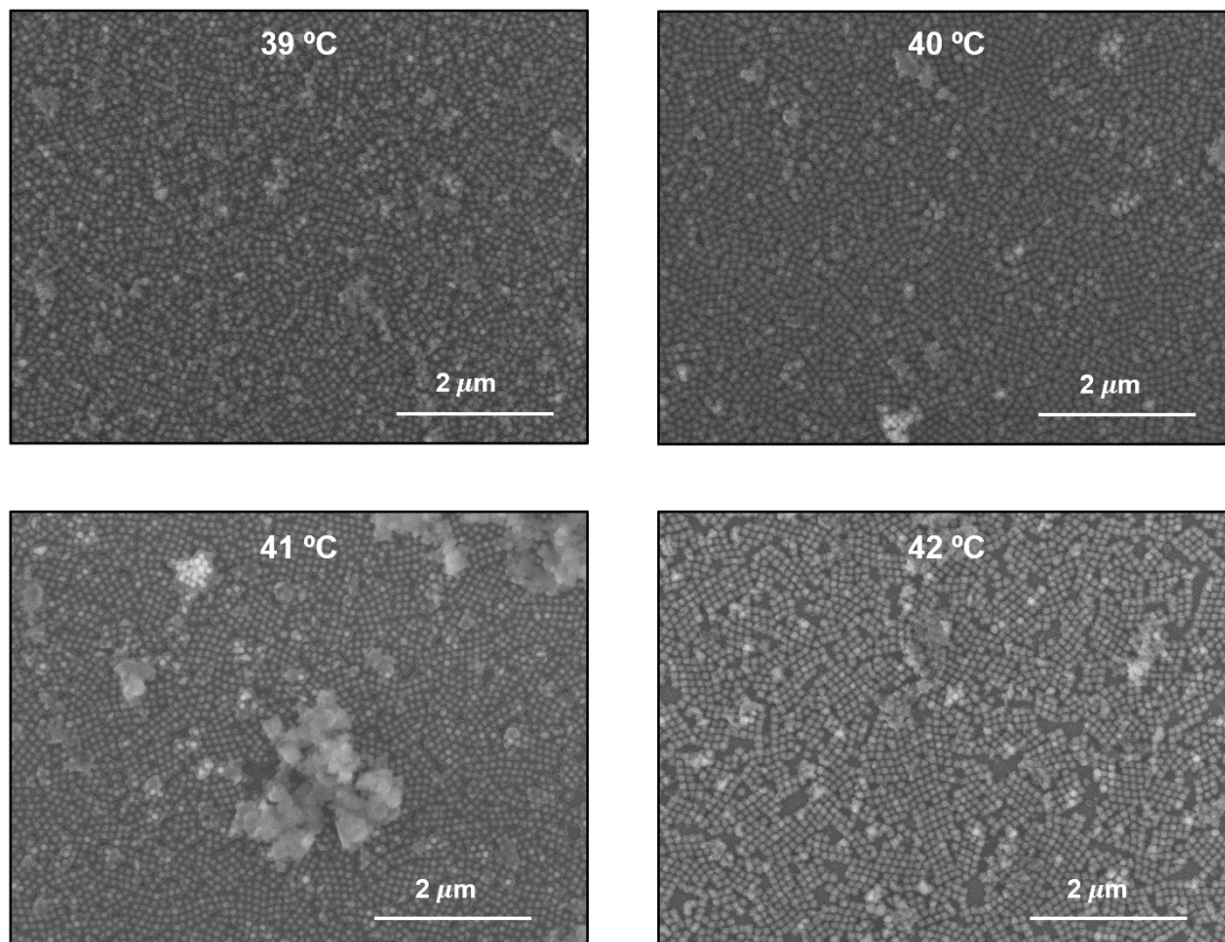
Figure 4-17. Large-area SEM images of RD PAE SLs annealed for 4 hours at 39 °C, 40 °C, 41 °C, and 42 °C.

(111) Films Formed at the Edges of RD PAE Films

Interestingly, at the four edges of the substrate, RD PAEs exclusively form films oriented in the close-packed {111} plane (Figure 4-24). Because excess PAEs move toward the edge of the substrate as the system anneals into a low-density film, the edges have a higher concentration of PAEs. It is likely that the higher local concentration of PAEs causes the film to adopt a close-packed structure to maximize the number of PAEs, and therefore the total number of DNA binding interactions, within the film.
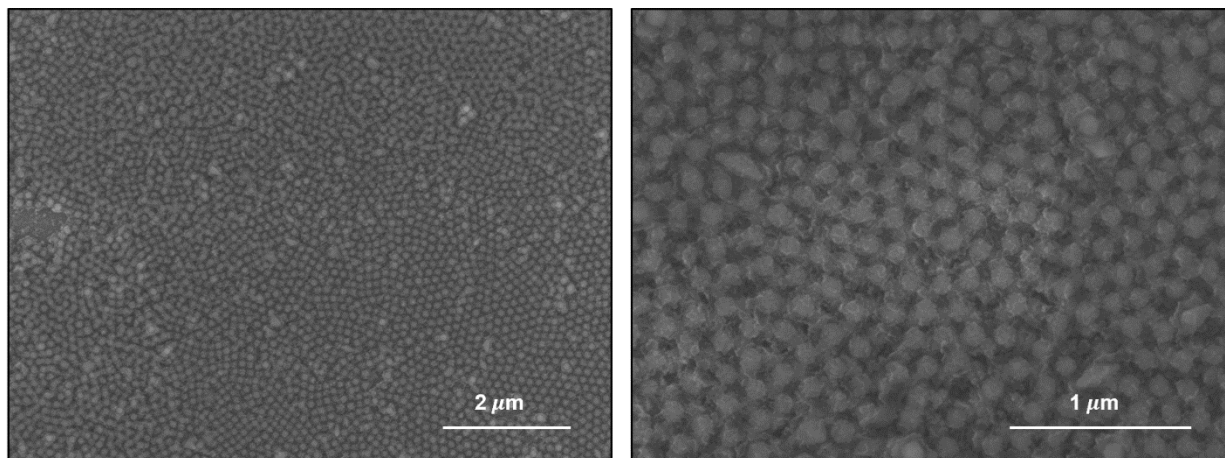
Figure 4-18. SEM image of the edge of a representative RD PAE film showing the interface between (110) and (111) textures (left). A close-up image of the closest-packed FCC (111) texture in a RD SL.
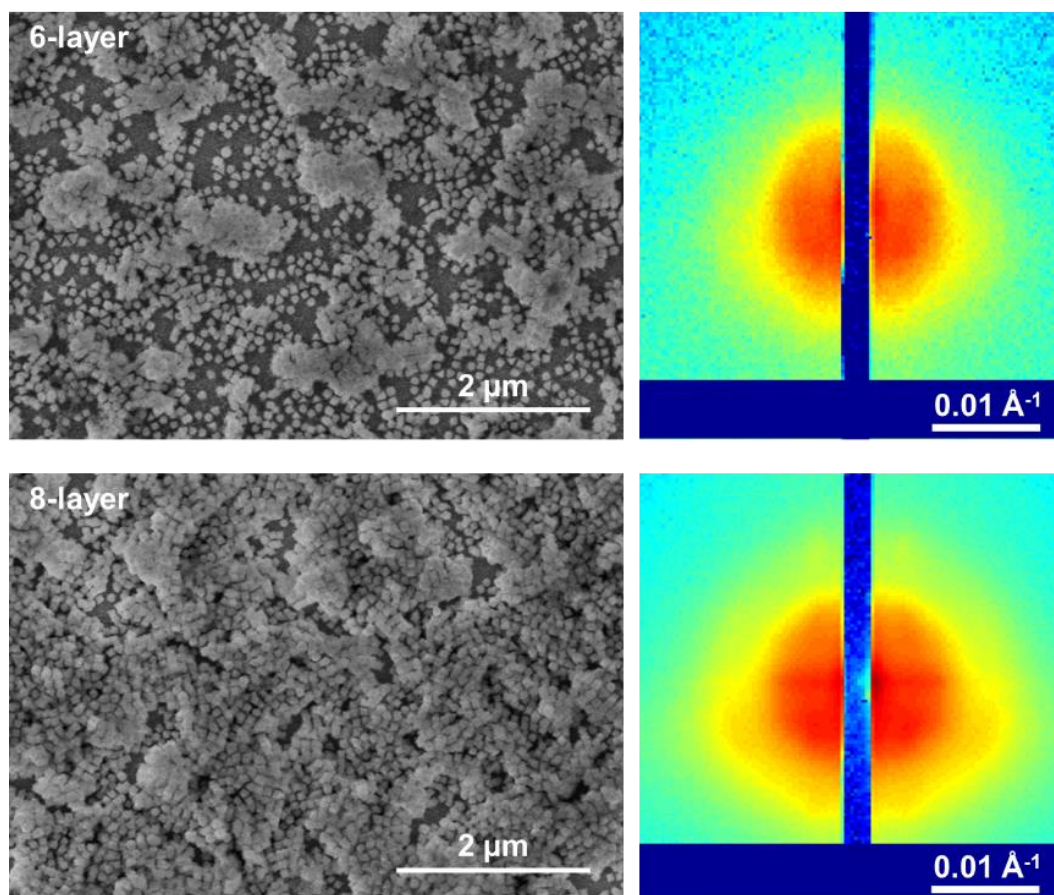
Figure 4-19. SEM images and GISAXS scattering patterns of 6- (top) and 8-layer (bottom) octahedral PAE films after annealing at 42 ℃. Both SEM and GISAXS indicate that the films are mostly disordered, with little alignment to the substrate.

CHAPTER 5

Large-Area, Highly Crystalline DNA-Assembled Metasurfaces Exhibiting Widely Tunable Epsilon-Near-Zero Behavior

This chapter is based on published work:

C.Y. Zheng*, W. Hadibrata*, S. Kim, G.C. Schatz, K. Aydin, C.A. Mirkin, et al., "Large-Area, Highly Crystalline DNA-Assembled Metasurfaces Exhibiting Widely Tunable Epsilon-Near-Zero Behavior" *ACS Nano*, **2021**, accepted.

5.1. Background

Optical metasurfaces,[2,9] comprised of subwavelength nanoparticle (NP) building blocks, provide a means to alter the spatial and temporal propagation of electromagnetic fields, enabling the rational design of structures that exhibit properties which do not exist in nature. To date, the lithographic patterning of ultrathin 2D metasurfaces has enabled the development of novel structures that exhibit unusual electromagnetic properties such as negative refraction,[20,175] optical magnetism,[19] and giant chiral optical response.[176] However, the high resolution required for lithographic patterning of nanoscale features renders this technique extremely time-consuming and unpractical for large-area fabrication. On the other hand, bottom-up assembly of colloidal NPs into two- and three-dimensional superlattices (SLs) has proven effective for the large-area fabrication of metamaterials in an efficient and scalable manner.[177,178] Towards this end, colloidal crystal engineering with DNA, which uses DNA-functionalized NPs as programmable atom equivalents (PAEs), has emerged as an exceptionally versatile platform for preparing 3D NP SLs.[54,79,81] This technique allows one to judiciously select NP shape, size, and composition independently of SL symmetry and interparticle distance,[80] offering precise control over the various structural parameters that dictate optical response. In addition, 2D PAE SL metasurfaces can be grown by

performing the assembly on a DNA-functionalized substrate,[153] and unlike other 2D colloidal assembly methods,[151,177,178] this technique allows SLs to be grown with chemical attachment to the substrate. Furthermore, stabilization procedures[166] could enable these materials to be used in the solid state and under a variety of harsh conditions, permitting their applicability in practical devices.[147,179,180]

Previously, PAE SL films were grown *via* layer-by-layer deposition of a binary system of complementary PAEs at room temperature, followed by post-deposition thermal annealing to prepare a crystalline film.[153] This process allows one to control the number of layers in the film *via* the number of deposition cycles. Indeed, thin film SLs assembled from spherical plasmonic PAEs demonstrated promise for engineering optical responses in the visible regime, exhibiting properties including optically metallic scattering and epsilon-near-zero (ENZ) response.[93] SLs assembled from large, anisotropic NPs, however, could exhibit further enhanced optical responses due to the extreme corner-to-corner[162] or face-to-face[178] electric field (E-field) coupling between neighboring NPs. In particular, when plasmonic NPs are closely packed and arranged such that their facets are parallel, a strong gap capacitance arises.[1,6] This capacitive coupling, which increases with decreasing gap distance, results in metamaterials with unnaturally high refractive indices, $\tilde{n}_{eff}$.[146,177]

In this work, we develop an isothermal, high-temperature growth method to prepare crystalline metasurfaces consisting of closely packed Au nanocubes functionalized with DNA. We demonstrate that these metasurfaces behave as effective dielectric media with unnaturally high refractive indices in the near-IR. In addition, when coupled with an underlying Au thin film, the effective medium behavior of these SLs drastically changes to that of a transparent conductor, exhibiting an ENZ condition. Importantly, the unique ability to control DNA length to sub-nm

precision[54,68] makes this platform ideal for the assembly of high index metamaterials because gap capacitance is highly sensitive to small changes in interparticle distance. Indeed, we demonstrate that the resonant wavelength of the metasurfaces is tunable throughout the near-IR regime by tuning DNA length and Au film thickness. This assembly route to highly-uniform, surface-bound colloidal metamaterials could enable fabrication of two- and three-dimensional crystalline metamaterials exhibiting a broad range of engineered optical responses, when combined with well-defined molds.
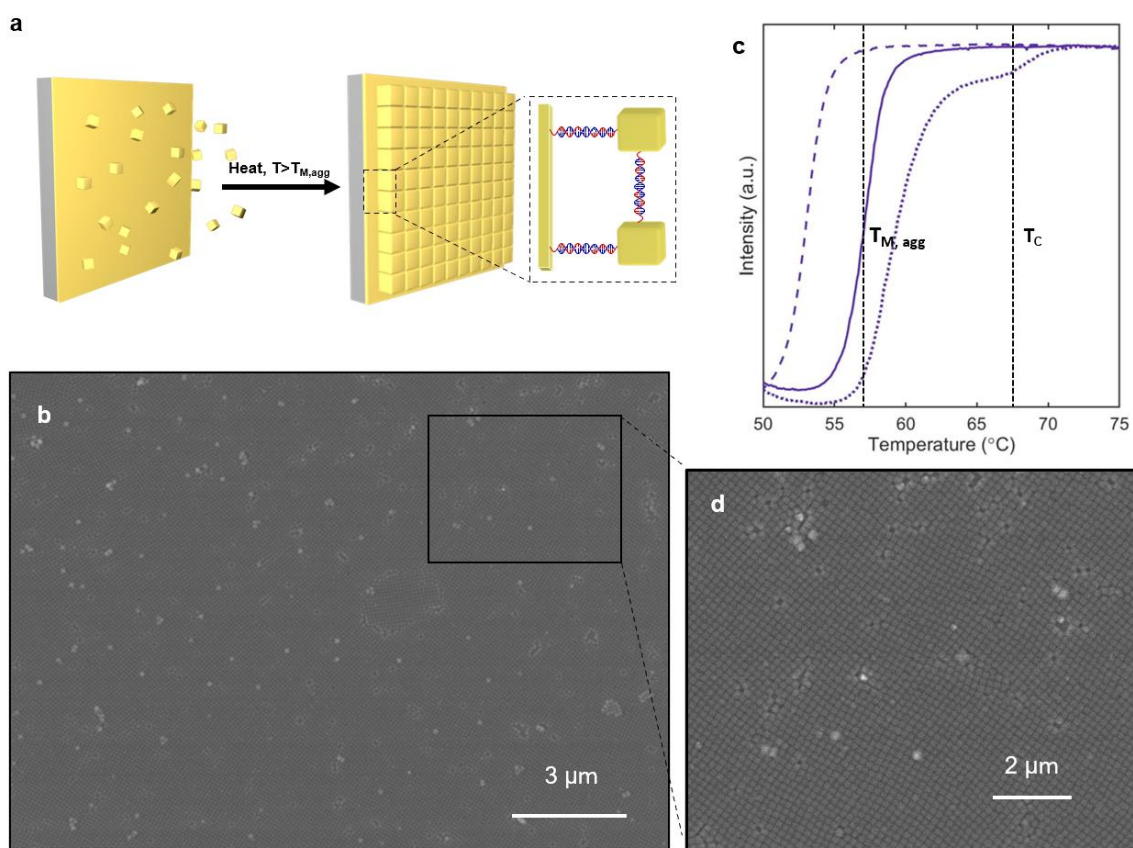
Figure 5-3. (a) Metasurface assembly scheme. PAE monomers are heated above the melting temperature of their assembled aggregates for several hours, forming 2D crystalline SLs. (b) Large-area SEM image of the PAE films, exhibiting long-range order and high uniformity. (c) Temperature-dependent UV-vis melting curves measured at λ=550 nm. The solid curve is the melting curve of the aggregates, the dashed curve is crystallization of dispersed particles, and the dotted curve is the melting of the crystal. (d) Zoomed-in area of (b).

5.2. Results and Discussion

We developed a one-step growth procedure to assemble crystalline polyhedral NP monolayers (Figure 5-1a). Unlike the layer-by-layer method[153] (which is performed with a binary system of PAEs), this procedure is performed using a solution of self-complementary anisotropic PAEs (*i.e.*, PAEs functionalized with DNA terminated with a self-complementary single-stranded binding region). In a typical experiment, we densely functionalize a 0.7 cm x 0.7 cm Au-coated Si wafer with thiolated anchor DNA by immersing the substrate in a DNA solution overnight. We then prepared cube PAEs by functionalizing uniform 80 nm colloidal Au nanocubes (Figures 5-6, 5-7) with the same thiolated anchor DNA that was used to functionalize the substrate. Next, we immersed the DNA-functionalized substrate in a solution of PAEs and 0.3 M NaCl in a 2-mL Eppendorf tube and placed the sample on a heated shaker. In contrast to the layer-by-layer method,[153] crystallization is facilitated above the melting temperature (T_M) of the PAE aggregates ($T_{M, agg}$) by utilizing the difference in T_M between the crystalline SLs and the amorphous aggregates (Figure 5-1c). Specifically, DNA-functionalized nanocubes rapidly aggregate upon being mixed with self-complementary linkers. These aggregates consist of nanocubes with random orientations, bound together with only a few DNA bonds and therefore are unstable and melt at a relatively low temperature. On the other hand, crystalline SLs consist of nanocubes bound with face-to-face interactions, held together by hundreds of DNA bonds,[181] resulting in a much higher T_M. For 80 nm self-complementary cube PAEs, $T_{M,agg}$ was determined to be ~57 ℃ by UV-visible spectroscopy (Figure 5-1c, solid curve), while the crystalline SLs exhibit a melting curve with two transitions at 60 ℃ and 68 ℃ (Figure 5-1c, dotted curve). Therefore, crystallization was facilitated at $T_C = 68$ ℃, at which an equilibrium exists between crystalline SLs and the melt. In addition, a smaller undercooling is required for heterogeneous growth compared to homogeneous growth,[182] a general phenomenon in crystal growth which has been shown to hold true for PAE systems.[183]

As such, growth on the substrate occurs at temperatures too high for homogeneous nucleation of crystalline SLs in solution, resulting in the observed substrate-bound films. After growth, the samples were cooled to room temperature and transferred to the solid state by embedding in an amorphous silica matrix.[166] Next, the embedded SLs were characterized by scanning electron microscopy (SEM) and small-angle X-ray scattering (SAXS).
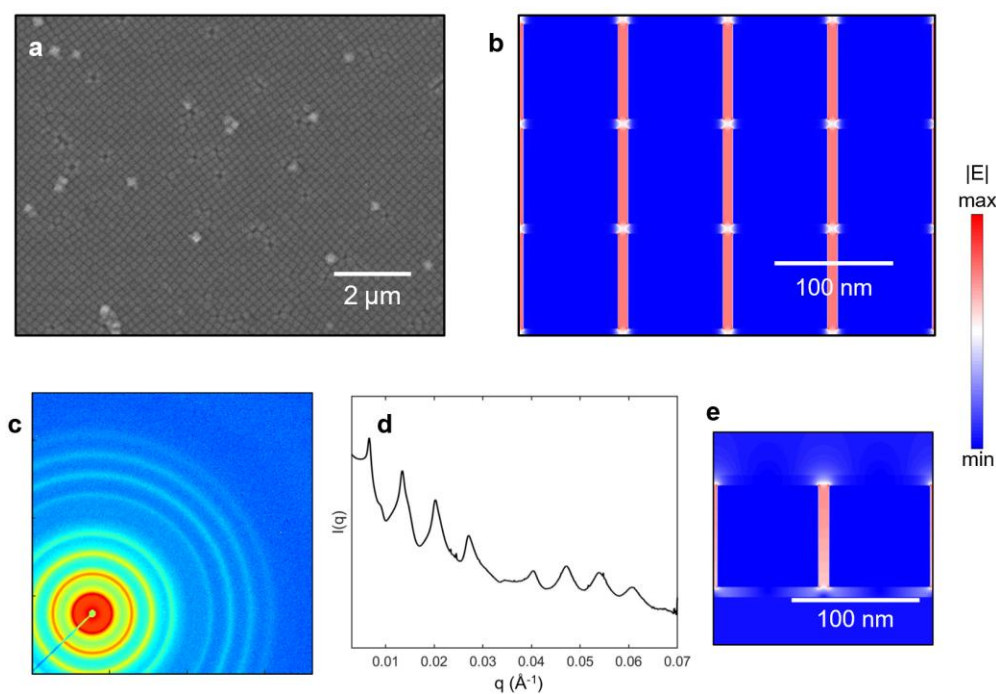
Figure 5-4. (a) Zoomed-in region of Figure 1b, showing a nanocube PAE film. (b) 2D and (c) 1D integrated SAXS pattern of the sample in (a). Calculated E-field intensity distribution in a (d) in-plane and (e) out-of-plane cut of a cube SL.

Large-area SEM images (Figure 5-1b and 5-19) show crystalline thin films with large domain size and extremely high crystallinity, resulting from the equilibrium process involved in this crystallization method. Close inspection of Figure 1b reveals that the entire 15 µm field of view consists mainly of a single crystalline domain. In addition, the SLs consist solely of monolayer films with the exception of sparse adsorbed NPs, which appear as bright spots. The 2D SAXS pattern (Figure 5-2b), which exhibits over eight diffraction orders, further confirms the high

crystallinity of these SLs. Notably, the high-quality diffraction is unlike that observed in previous works involving large, polyhedral NPs assembled with short DNA, which only give rise to a few broad peaks in SAXS.[184] In addition, attempts to crystallize a binary, complementary system of cube PAEs with the same core size and DNA length using the layer-by-layer method resulted in films with much smaller domain sizes as well as regions with multilayers, rather than the desired monolayer films (Figure 5-8).

To explore the generalizability of this method, we assembled both cube and octahedron PAE films and characterized them using SEM and SAXS. According to the complementary contact model (CCM),[185] PAEs should assemble into films that maximize DNA hybridization both between neighboring NPs and between NPs and the underlying DNA-functionalized film. We found that cube PAEs formed films with a simple cubic geometry, as evident from both SEM (Figure 5-2a) and SAXS (Figure 5-2b,c) characterization. In this structure, NPs form face-to-face bonds with neighboring NPs and the underlying Au film. Octahedron PAEs, on the other hand, formed films with hexagonally close packed symmetry as evidenced from SEM (Figure 5-3a) and SAXS characterization (Figure 5-3b). In this structure, each octahedron NP forms a face-to-face bond with the underlying Au film. However, unlike cube PAEs, the octahedron PAEs do not form perfect face-to-face contacts with neighboring NPs. To understand how the difference in facet registry affects coupling between NPs, we used finite-difference time-domain (FDTD) simulations to calculate the E-field patterns inside the SLs. In both cases, E-field hotspots are concentrated within the interparticle gaps (Figure 5-2d,e and 5-3c,d). However, neighboring NPs in the cube PAE film exhibit stronger E-field hotspots in three dimensions due to the larger capacitive coupling between its large, parallel facets. Indeed, a recent manuscript reports that although both close-packed cube and octahedron NP films behave as high refractive index metamaterials, cube
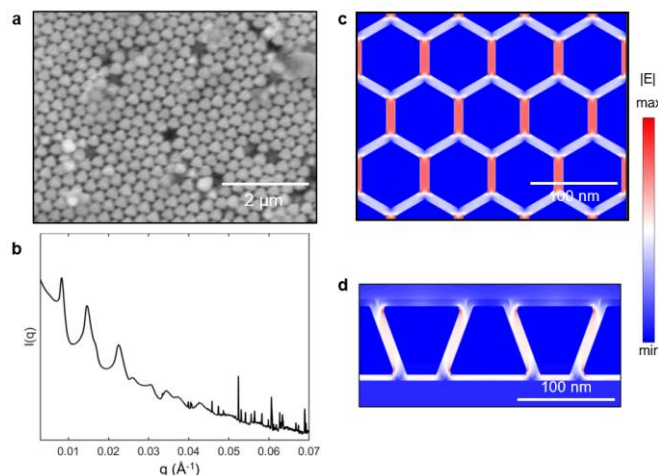
Figure 5-3. (a) SEM image of a PAE film prepared using octahedral NPs. (b) 1D SAXS pattern of the sample in (a). Calculated E-field intensity distribution in a (c) in-plane and (d) out-of-plane cut an octahedral SL.

NP films exhibit larger $\tilde{n}_{eff}$ compared to their octahedron counterparts.[177] Hence, we focus on cube PAE films for the remainder of the discussion.

To understand the meta-optical properties of the metasurfaces, we calculated their effective parameters using FDTD simulations. Importantly, because periodicities are deep subwavelength ($<\lambda/5$) compared to the visible and IR regimes, an effective medium treatment is appropriate.[10] We modeled the unit cell as a 80 nm Au cube embedded in a dielectric matrix atop a 8 nm Au film. Next, we repeated the unit cell in a 2D square grid using periodic boundary conditions to simulate the crystalline SL film. The period of the structure is set to the sum of the cube size and interparticle distance, or DNA length. The gap between the NPs and underlying Au layer is taken to be the same as the interparticle distance (Figure S6).

First, we calculated the effective index of the SL monolayers without an underlying Au film and found that they behave as effective dielectrics (Figure 5-9, 5-10). Furthermore, we found that for typical interparticle spacings ranging from 4 nm to 24 nm, effective refractive indices can be tuned from 1.5 to 4 by means of DNA length as well as embedding material (Figure 5-11). Next, we studied the effect of an underlying 8 nm Au film on the overall effective optical behavior.
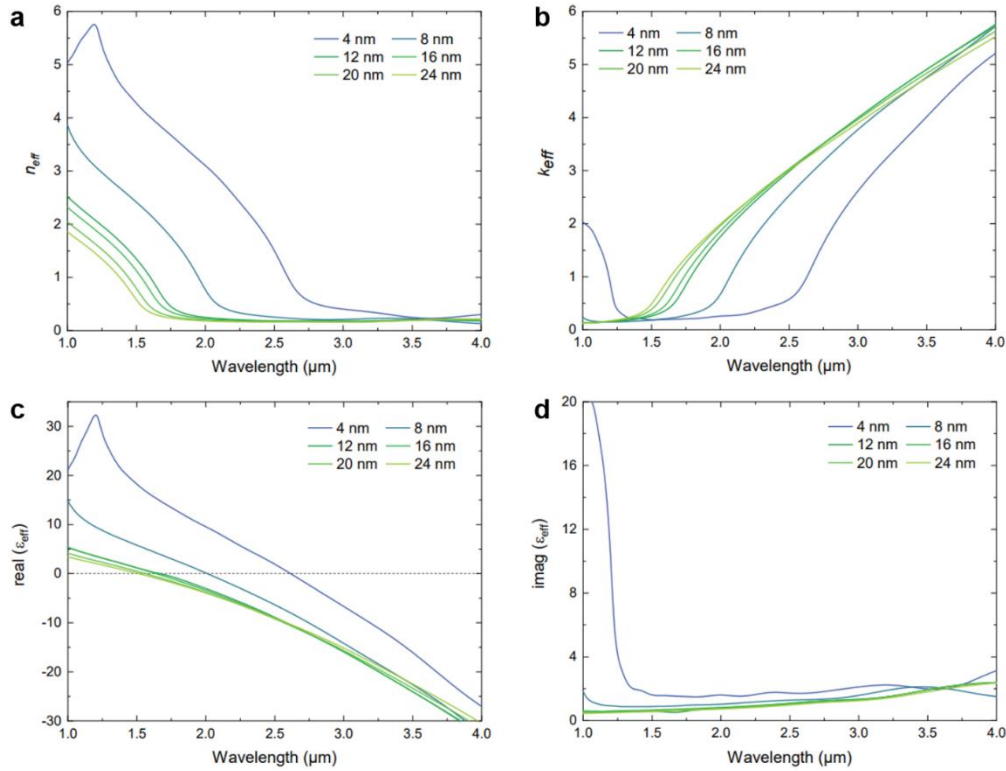
Figure 5-4. Calculated effective parameters of nanocube metasurfaces with DNA length varying from 4 to 24 nm, above a gold film 8 nm thick. (a) n_{eff}. (b) k_{eff}. (c) real(ε_{eff}). (d) imag(ε_{eff}).

Interestingly, we discover that the presence of a very thin Au film drastically alters the effective materials behavior from that of a dielectric to that of a metal (Figure 5-4). Specifically, the real part of the refractive index (n_{eff}) is high for lower wavelengths and decreases to nearly zero towards higher wavelengths, accompanied by an increase in k_{eff}, the imaginary part of the refractive index, as wavelength increases (Figure 5-4a,b). Next, we calculated the effective permittivity (Figure 5-4c,d) of the SL monolayer-Au film structure. The plot shows that the real part of the permittivity, real(ε_{eff}) is positive in the near-IR and decreases with increasing wavelength, eventually becoming negative. Because the structure is comprised of an effective dielectric and a metal, its behavior is a mixture, dielectric below a certain wavelength and metallic above that. Wavelengths at or near the crossover point are known as the ENZ condition. ENZ materials, such as highly doped semiconductors like indium tin oxide (ITO), exhibit large optical

nonlinearities and therefore are promising for applications ranging from all-optical data processing to microscopy.[186] The calculations show that the zero-permittivity wavelength can be easily tuned *via* interparticle spacing, which tunes n_{eff} of the SL layer. For example, at a 24 nm interparticle spacing, the ENZ condition occurs at around 1.5 µm, but when spacing is decreased to 4 nm, it shifts to 2.6 µm. Thus, the ENZ condition can be tuned over a broad spectral range throughout the telecom wavelengths by simply tuning the SL lattice constants. Previously reported methods to actively tune the operational wavelengths of conventional ENZ materials include doping,[187,188] electrical tuning,[189,190] introducing defects,[191] and irradiating with a laser pulse.[192] Of these, laser irradiation has the largest tuning window of ~1 µm. The calculations show that DNA-assembled metasurfaces can be tuned across a comparable window by simply tuning DNA length.

Because the addition of a Au film drastically alters the resulting effective materials parameters, we predicted that the optical response of the metasurfaces could further be tuned *via* the Au film thickness. We calculated the permittivity of cube SLs with underlying Au films between 8 and 50 nm thick for an intermediate interparticle spacing of 16 nm (Figure 5-12). Indeed, we found that the ENZ wavelength blue shifts from 1.5 to 1.0 µm, further expanding spectral tunability to shorter wavelengths in the near-IR. Next, we calculated the reflection and transmission spectra of the metasurfaces. Figure 5a shows calculated reflection spectra for metasurfaces with varying gap spacings. The spectra exhibit deep dips in reflection at the resonance wavelength and near unity reflection at other wavelengths. This dip can be attributed to localization of the E-field inside the interparticle gaps, which can be seen in near-field simulations (Figure 5-2d,e). This in-plane field localization in the IR is complementary to the out-of-plane E-field localization between the cube and underlying Au layer, which results in a resonance in the visible regime.[155] Previously, we have shown that this out-of-plane "gap mode" is tunable

throughout the visible spectrum *via* DNA length and can be used to selectively enhance emission of embedded fluorophores.[155] Here, however, because in-plane field localization occurs at IR wavelengths, such resonances could potentially couple with molecular vibrations, and hence find application in sensing.[193]

To experimentally characterize the tunable optical response of the colloidal metasurfaces, ~80 nm Au cubes were assembled into monolayer PAE films on a transparent glass slide coated with a 2 nm Cr adhesion layer, followed by an 8 nm Au film. A transparent substrate was required to measure both the transmission and reflection of the metasurfaces for better comparison with simulations. Interestingly, the films appear uniform and bright green in color (Figure 5-16), in contrast to the pink color of Au nanocubes in solution[194] or red color of individual Au nanocubes coupled with an underlying Au film.[100] This further elucidates the effect of in-plane coupling on the resultant optical properties. In addition to its specificity, another advantage of using DNA as a ligand is that it is responsive to a variety of chemical and physical stimuli including pH,[99] light,[98] and solvent polarity.[97] In particular, it has been shown that adding increasing amounts of ethanol to an aqueous buffer results in a gradual contraction of SL lattice parameters until up to 20 % of their original values.[97] In this work, we utilize this effect to prepare metasurfaces with smaller interparticle distances. Specifically, after growth, we transfer the metasurfaces to solutions containing varying ethanol percentages (from 0 to 80 %). Remarkably, they could be cycled between 0 and 80 % ethanol, causing their color to change from bright green to yellow and back, without visible degradation (Figure 5-16). Indeed, it has been shown that DNA can store high amounts of strain upon lattice compression due to its flexibility,[195] rendering these materials viable for use in tunable architectures. Notably, the ability to tune the interparticle gaps of DNA-assembled metasurfaces enables the tunability of in-plane gap modes. Silica embedding locks the

SLs in the contracted state, resulting in solid-state metasurfaces with smaller gap distances (Figure 5-5c). As expected, lattice shrinkage was accompanied by a decrease in domain size when the samples released strain upon being transferred to the solid state.

Reflection and transmission measurements were carried out using an FTIR setup coupled to a microscope. The measurement spot size was approximately 50 x 50 μm^2, which is a sufficiently large area to obtain representative averages of the sample. Measured reflection spectra are shown in Figure 5-5b. For 60% ethanol, the reflection dip occurs near 2.3 μm, which approximately matches the simulated reflection for metasurfaces with 8 nm gaps (Figure 5-5a). At lower ethanol concentrations, the reflection dip shifts towards smaller wavelengths. For 0% ethanol, the reflection spectrum exhibits a dip at around 1.5 μm. The dips occur near the location of the ENZ condition (Figure 5-4c) where the E-field is highly localized between neighboring Au NPs (Figure 5-2d,e). This is accompanied by increased transmission (Figure 5-14) when n_{eff} matches that of the glass substrate underneath. Finally, we extracted n_{eff} (Figure 5-5d) and ε_{eff} (Figure 5e) from the measured reflection spectra and found that the extracted curves exhibit tunable ENZ conditions, in agreement with those from simulations (Figure 5-4, details in Experimental Details). From these results, we experimentally show that the metasurfaces give rise to widely tunable reflections and ENZ wavelengths in the near-IR.

5.3. Conclusion

In summary, we have developed a high-temperature growth method to assemble crystalline NP SL-based metasurfaces using DNA. The extraordinary crystallinity, scalability and generalizability offered by this technique could enable design of large-area metasurfaces with optical properties not found in nature. As a proof of concept, we assembled high volume-fraction nanocube-based SLs and designed them to behave as ENZ materials, with resonant wavelengths

in the near-IR. Furthermore, owing to the incredible flexibility of DNA, the ENZ wavelength was tuned through a ~1 µm window in the near-IR, comparable to the literature record, by simply changing solvent. Growing uniform monolayer SLs over macroscopic areas allows for facile optical characterization as well as potential device integration. As a result, the metasurfaces could find use in catalysis, telecommunications, and quantum computing.
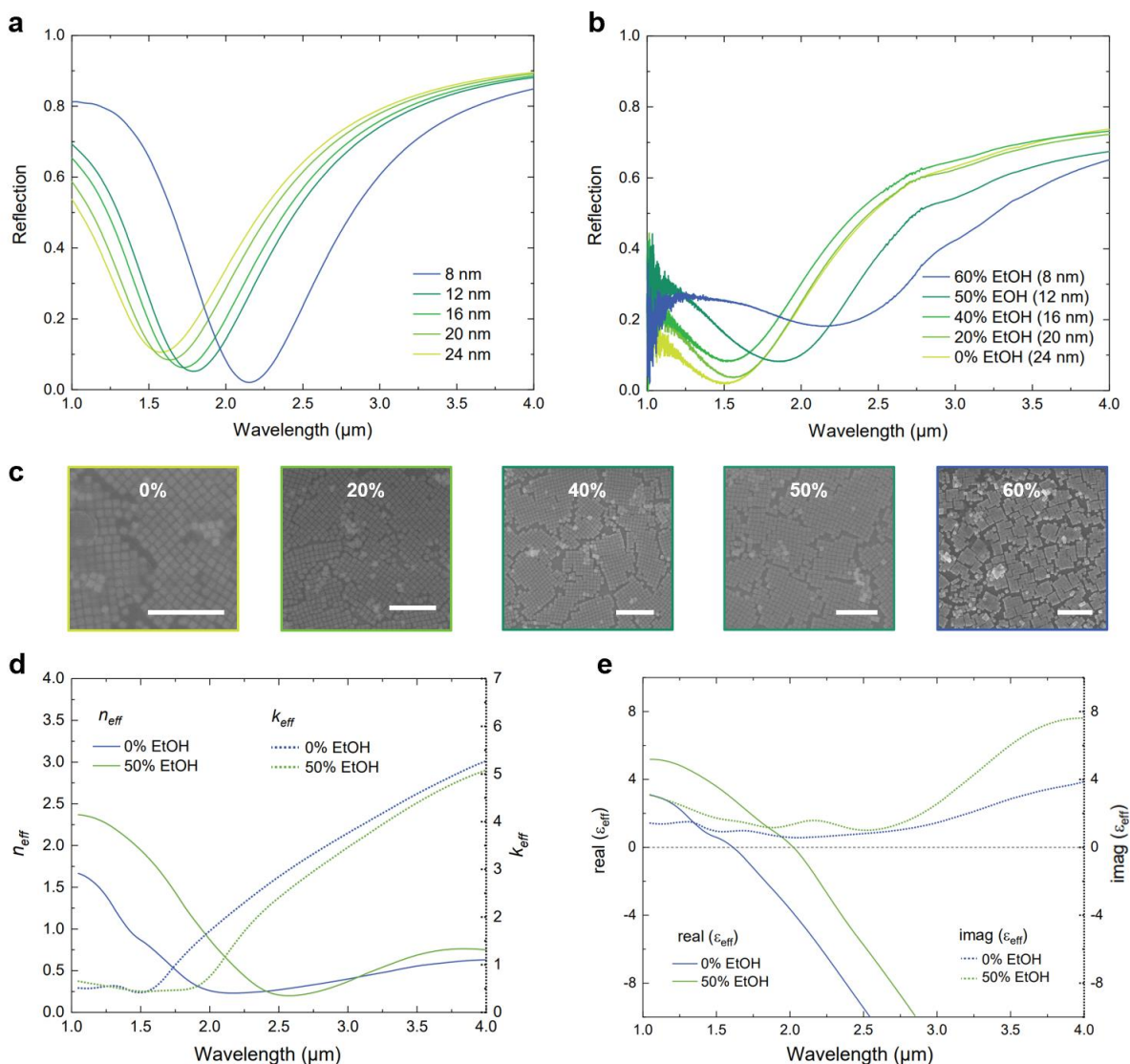
Figure 5-5. (a) Simulated reflection spectra for metasurfaces with varying interparticle spacings. (b) Experimental reflection spectra of metasurfaces as a function of ethanol concentration; samples were prepared in a solution with the designated ethanol content and then embedded in silica. (c) SEM images of the metasurfaces measured in (b). Scale bars: 1 µm. (d) n_{eff} and (e) ε_{eff} extracted from experimental reflection spectra, showing reasonable agreement with simulations in Figure 4.

5.4 Additional Information

Materials and Methods

Nanoparticle Synthesis. All precursors were purchased from Sigma-Aldrich and used without further purification. Gold nanoparticles (NPs) were synthesized via a seed-mediated method described in detail by O'Brien et al.[63] Briefly, uniform, single crystalline spherical gold NPs were synthesized via an iterative chemical growth and etching process. These NPs were then used as "seeds" for the growth of anisotropic NPs, including the cubes and octahedra used in this work. Importantly, this synthetic procedure results in uniform anisotropic NPs in high yield ($<$ 5 % coefficient of variation (CV), $>$ 90 % yield), which makes them ideal for the assembly of crystalline superlattices (SLs) with long-range order. The NPs were imaged by scanning transmission electron microscopy (STEM, Hitachi HD-2300 STEM).

Substrate Preparation. Gold-coated glass slides were prepared via e-beam evaporation. Specifically, glass microscope slides were diced into 5 x 5 mm squares. The diced wafers were cleaned via an O_2 plasma at 50 W for 2 min. Following plasma cleaning, e-beam evaporation (Kurt J. Lesker Company) was used to deposit a 2-nm Cr adhesion layer at 0.2 Å/s, followed by an 8-nm Au layer at 0.5 Å/s onto the glass substrate.

NP and Surface DNA Functionalization. The DNA sequences used in this work are taken from the literature (Table S1).[2] Briefly, we functionalized the particles and substrates with 3' thiolated anchor DNA sequences. Then, the corresponding complementary linker strands were hybridized to the anchor strands on the NPs or substrates. Each linker strand included a self-complementary, four-base single-stranded region designed to link the particles to each other and to the substrate through DNA hybridization.

Table 5-1. Sequences Utilized in this Work. Note that "sp18" refers to a hexaethylene glycol spacer unit manufactured by Glen Research.

Description	DNA Sequence (5' to 3')
Anchor DNA	TCA ACT ATT CCT ACC TAC (sp18)$_2$ SH
Self-complementary linker DNA	GTA GGT AGG AAT AGT TGA (sp18) GCGC

NPs were functionalized using a procedure modified from that described by Jones et al.[125] and O'Brien et al.[123] Briefly, 3' alkylthiol-modified oligonucleotides were first treated with a 100 mM solution of dithiothreitol (DTT) in 170 mM sodium phosphate buffer (pH = 7.4) and then purified on a Nap-10 size exclusion column (GE Life Sciences) to remove excess DTT. Next, the NPs were washed twice to remove excess ligands. Specifically, the NP solutions containing the as-synthesized particles were centrifuged for 8 min at 3,200 rpm, the supernatant was removed, and the pelleted NPs were resuspended in water. The NPs were then centrifuged a second time for 8 min at 3,200 rpm, the supernatant was removed, and then the solution of purified DNA was added to the pellet immediately. Five µmol of thiolated DNA was added per 1 OD of particles. The particle solution was then brought to 0.01 M sodium phosphate buffer (pH = 7.4) and 0.01 wt. % sodium dodecyl sulfate (SDS) in water. Stepwise addition of 2 M NaCl was then carried out every 30 min, such that the NaCl concentration was increased to 0.05 M, 0.1 M, 0.2 M, 0.3 M, 0.4 M, 0.5 M in turn. Following this process, the NPs were placed on a shaker at 700 rpm and left overnight to ensure a dense loading of oligonucleotides. After functionalization, the NP solutions were centrifuged three times to remove excess DNA. After each of the first two rounds of centrifugation, the NPs were resuspended in 0.01 wt. % SDS, and after the last centrifugation step, the particles were resuspended in 0.5 M PBS (0.5 M NaCl, 0.01 M sodium phosphate buffer (pH = 7.4), and 0.01 wt. % SDS).

The procedure for DNA functionalization of the substrate was similar to that for the NPs as described above. Specifically, 1 µmol of DTT-cleaved anchor DNA in water was added to each substrate. However, instead of stepwise addition of NaCl, the substrates were brought to 0.5 M NaCl in one addition, and then shook overnight at 700 rpm. The substrates were then rinsed three times with water and placed in PBS.

NP Assembly. NP films were assembled with a one-step high temperature crystallization procedure. A DNA-functionalized substrate was placed inside a 5 mL Eppendorf tube containing 4 OD PAEs in 0.3 M PBS. 20 µL of 40 OD linker DNA was added to the PAE solution, in slight excess of the anchor DNA, immediately causing the solution color to change from pink to purple-blue and eventually to grey, indicating the formation of aggregates. Next, the tube was placed on a 5 mL shaker at 70 ℃ and 700 rpm, at which the aggregates quickly melted, resulting in again in a pink solution. The PAEs and DNA-functionalized substrate were left to react for 4-8 hours during which SL monolayers formed on the substrates.

Silica Embedding. The NP films were encapsulated in silica according to literature precedent.[174] This method mostly preserves the crystal symmetry and lattice parameters of the lattice in the solid state. The samples were transferred to a 2-mL Eppendorf tube and suspended in 1 mL of 0.5 M PBS solution. To this solution, 2 µL of the quaternary silane salt, N, trimethoxysilylpropyl-N,N,N-trimethylammonium chloride (TMSPA), was added and the tube was agitated at room temperature on a thermomixer (Eppendorf) at a rate of 700 rpm for 30 min. Next, 5 µL of triethoxysilane (TES) was added to the solution, and a silica network formed around the entire lattice. The mixture was left on the thermomixer at 700 rpm for 2 hours. Finally, the sample was removed from solution and blown dry using a stream of N_2. To prepare metasurfaces with smaller interparticle distances, the samples are transferred from buffer

solution to a mixture of ethanol and buffer. The reagents are then added sequentially to the

mixture of buffer and ethanol, locking the superlattices in their contracted state. The

correspondence between ethanol concentration and interparticle spacing, as measured from SEM

images, is as follows: 0% ethanol: 24 nm. 20% ethanol: 20 nm. 40% ethanol: 16 nm. 50%

ethanol: 12 nm. 60% ethanol: 8 nm.

Electron Microscopy. Scanning electron microscopy (SEM) images were taken with a Hitachi

SU-8030 field emission SEM with an acceleration voltage 30 kV and a current of 20 μA.

Scanning transmission electron microscopy (STEM) images were taken with a Hitachi HD-2300

STEM.
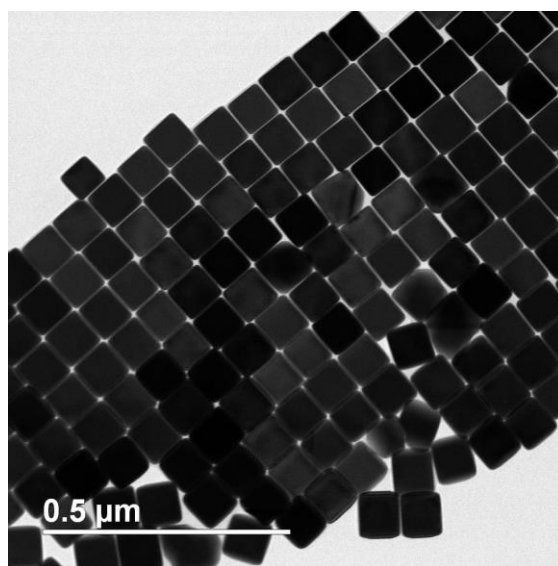
Figure 5-6. STEM images of a typical batch of nanocubes used to assemble metasurfaces in this work.
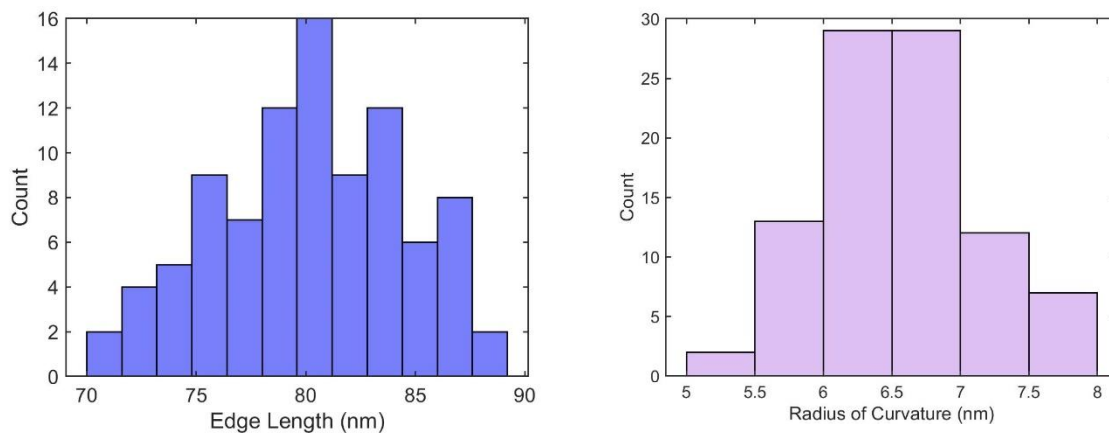
Figure 5-7. Histograms of edge lengths (80 ± 4 nm) and radius of curvatures (6 ± 1 nm) measured from 100 nanocubes.

Cubic PAE films formed via layer-by-layer deposition followed by thermal annealing
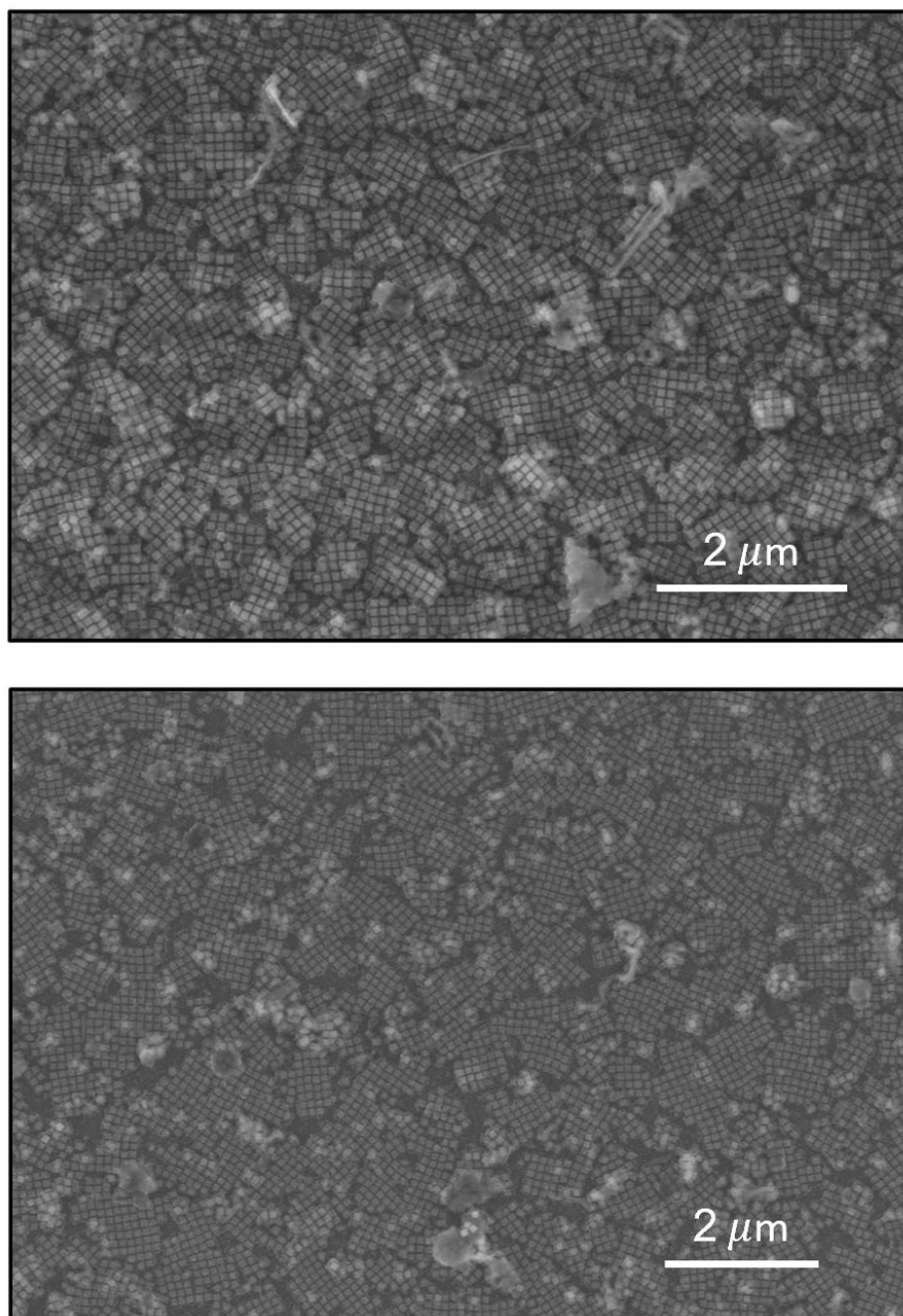
Figure 5-8. SEM images of cubic PAE films formed by layer-by-layer assembly of a binary PAE system followed by thermal annealing below the aggregate melting temperature. Domain sizes are significantly smaller than those in films formed through the high-temperature growth method due to limited diffusion on the substrate. The top image shows the presence of multilayer regions which can be found throughout the sample.

Calculation of Effective Optical Parameters

Effective index retrieval via S-parameters calculations. We employed a retrieval method to calculate effective indices. In brief, we first set up FDTD simulations to calculate the reflection and transmission spectra of the SL structures. Next, we retrieved complex S-parameters from the simulated reflection and transmission spectra. Finally, the effective indices were calculated from the retrieved S-parameters.

For structures symmetric along the direction of light propagation, effective refractive indices can be calculated using the formula derived by Smith et al.[10]

$$n_{eff} = \frac{1}{kd}\cos^{-1}\left(\frac{1 - S_{11}^{2} + S_{21}^{2}}{2S_{21}}\right)$$

where k is the wavevector and d corresponds to the effective length of the structure.

For non-symmetric structures, the abovementioned formula is slightly modified to:

$$\cos(nkd) = \frac{1}{S_{21}}(1 - S_{11}S_{22} + S_{21}^{2})$$

Both equations above result in non-trivial solutions and require careful consideration when selecting the physically relevant roots.

For FDTD simulations, we placed two monitors at opposite sides of the structure along the direction of light propagation. We placed a plane-wave source far from the structure in either the forward or backward direction and utilized periodic boundary conditions in the x-y direction and perfectly-matched-layers (PML) in the z-direction. The period of the unit cell was set to the sum of the NP size and gap distance (DNA length). Note that for calculation of S-parameters, we

assume that the effective structure is suspended in air without any underlying substrate besides an 8 nm Au film, for the SL-on-film structure.

Effective High Index Dielectric - Nanocube SL. The refractive index of Au was obtained from Johnson and Christy.[196] We find that colloidal Au NPs, arranged in a periodic square lattice, behave as effective dielectric materials with low, nondispersive n_{eff} and near-zero k_{eff} throughout the wavelengths of interest. Figure S4 shows the calculated effective index for a film comprised of 80 nm Au NPs with gaps of 20 nm and surrounded by air.
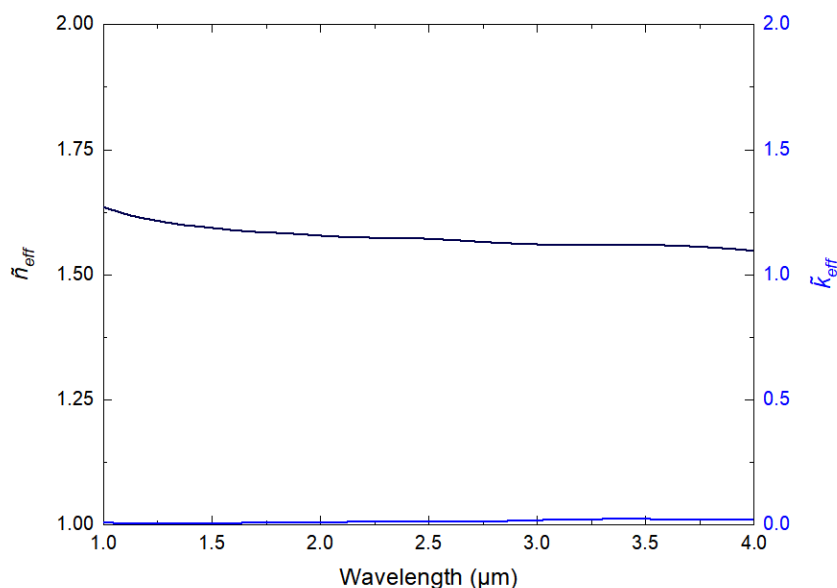
Figure 5-9. Extracted refractive index of a SL monolayer comprised of 80 nm Au cubes separated by 20 nm gap distances, surrounded by air.

Effective High Index Dielectric - Nanocube SL embedded in Silica. When the same SL is embedded in silica, which itself is a dielectric material with $n \sim 1.45$, the SL still behaves as an

effective dielectric throughout the near-IR regime, but with a significantly higher real part (Figure

S5). This is because overall effective index increases with a higher host refractive index.
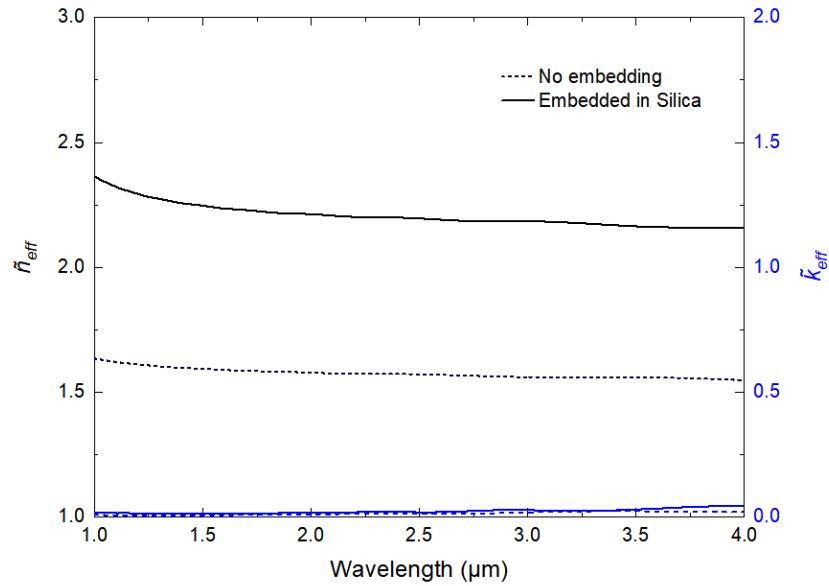
Figure 5-10. Extracted refractive index of a SL monolayer comprised of 80 nm Au nanocubes separated by 20 nm gap distances, embedded in silica.

Effective High Index Dielectrics – Discussion
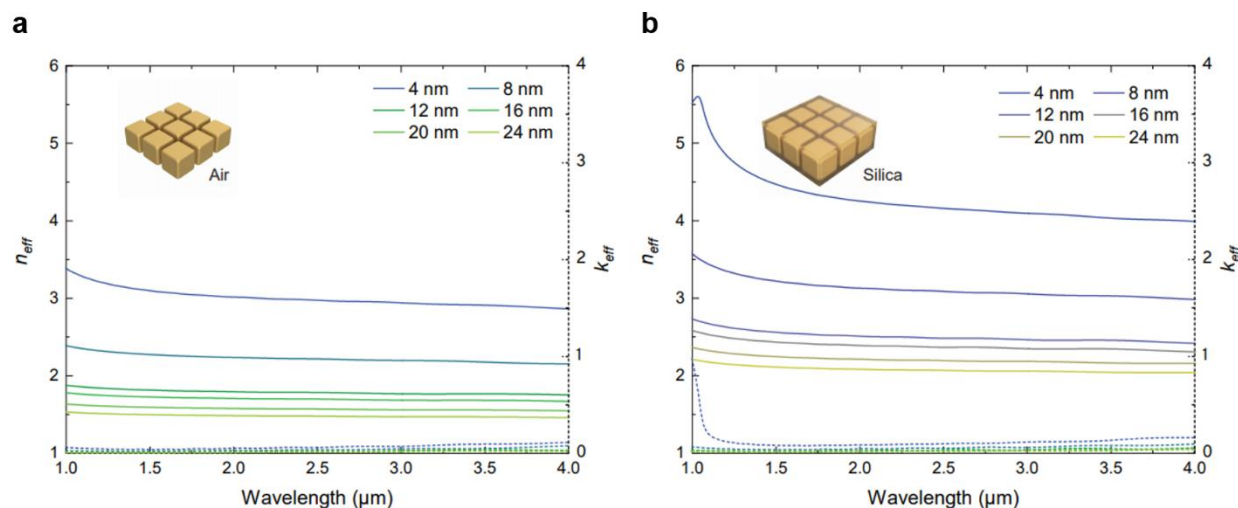
Figure 5-11. Calculated refractive indices of cube PAE metasurfaces with varying gap distances embedded in (a) an air matrix and (b) an amorphous silica matrix. Insets are cartoons of the simulated geometry.

We also studied the effect of varying gap distance between NPs. We observed that $\tilde{n}_{eff}$ increases with decreasing NP spacing, diverging for very small spacings, due to the inverse dependence of capacitance on interparticle distance. Specifically, for a moderate interparticle spacing of 16 nm, the off resonance n_{eff} is ~1.71, which is higher than that of common dielectric materials such as SiO_2. Additionally, when interparticle spacing is decreased to 4 nm, n_{eff} increases to ~3.01 (Figure S6a). Embedding in a dielectric matrix can be used to further increase n_{eff}. Specifically, for a moderate interparticle spacing of 16 nm, n_{eff} is ~2.38 at 2 μm (Figure S6b), which is significantly higher than that of an equivalent SL in air ($n_{eff} \approx 1.71$). At a further decreased spacing of 4 nm, the off-resonant effective index n_{eff} increases to ~4.25, which is comparable high index materials in nature (Si and Ge). Theoretically, DNA length can be further decreased down to 2 nm to achieve even higher n_{eff}.

Embedded PAE on thin Au layer
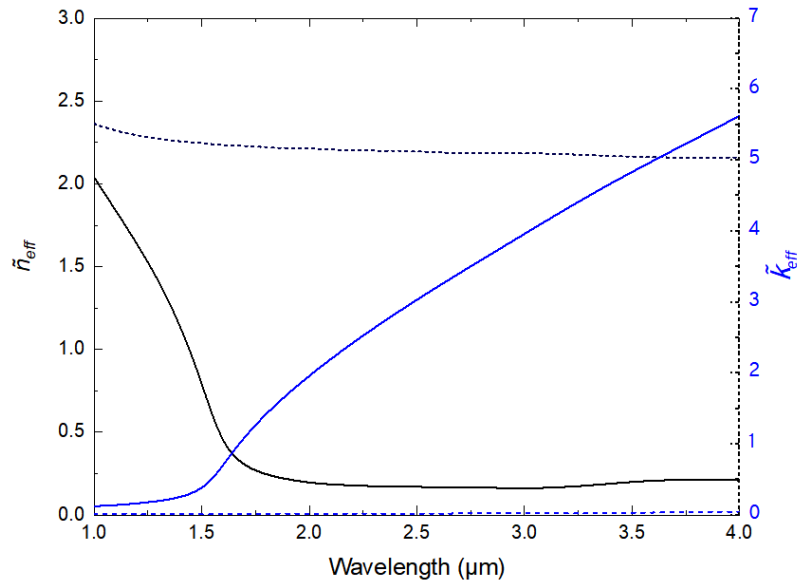
Figure 5-12. Extracted refractive index for a metasurface comprised of 80 nm nanocubes separated by 20 nm gaps, coupled to an underlying 8 nm Au film, separated by the gap distance.

Placing the silica-embedded SL on top of a thin gold film changes the effective medium behavior drastically. The presence of the thin Au film brings metal-like behavior with an increasing imaginary part of the effective index as shown in Figure S7. Meanwhile, the real part of the effective index decreases to slightly below unity. The wavelength at which the imaginary part of the effective index increases rapidly approximately coincides with the IR resonance of the structure. We observed that by placing the SL on a thin Au layer, it possesses both dielectric- and metal-like behavior, with dielectric behavior below the resonance wavelength, and metallic behavior beyond that.

Calculation of Transmission and Reflection. For the calculation of reflection and transmission spectra, we place SL monolayers on top of a glass substrate. Similar to the S-parameter calculation, a plane wave is launched in the negative z-direction in which the boundary condition is set to be

PML. The boundary conditions in the x- and y-directions are set to be periodic. Two monitors are places at opposite ends of the simulation region for recording reflection and transmission. The calculated reflection spectra are shown in Figure 4a.

Validation of the Effective Refractive Index. To verify the validity of the effective medium calculation, we compare reflection spectra calculated using the effective index to that calculated from the full structure. We perform the calculation for SL composed of 80 nm Au cubes with 20 nm gap on top of an 8 nm Au film. The entire metasurfaces is placed on top of transparent glass substrate. Similarly, a slab with the same thickness as the effective metasurface with refractive indices obtained from the parameter extraction is placed on top of a glass substrate. Figure S8 shows a comparison of the simulated reflection spectra for both structures. We observe a reasonably good agreement between the reflection from the full structure and the that from the retrieved effective index. The slight discrepancy could arise from minor discrepancies in the simulation setup, such as the refractive index fitting step in the FDTD simulation.

FTIR Measurements. Reflection and transmission measurements were performed using an FTIR setup (Hyperion Vertex 70) coupled to an optical microscope. A spot side of $\sim$ 50x50 μm^2 was used to excite the sample. Reflection from an optically thick Au film was used as a reference for reflection measurements.
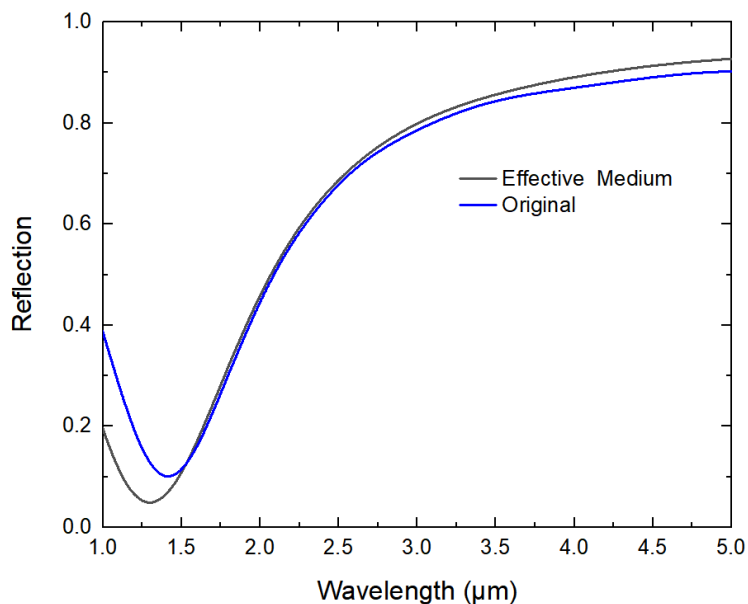
Figure 5-13. Comparison of reflection from metasurfaces calculated with the full structure (blue) and the effective medium (black), indicating reasonably good agreement.

Transmission Simulation and Experiment
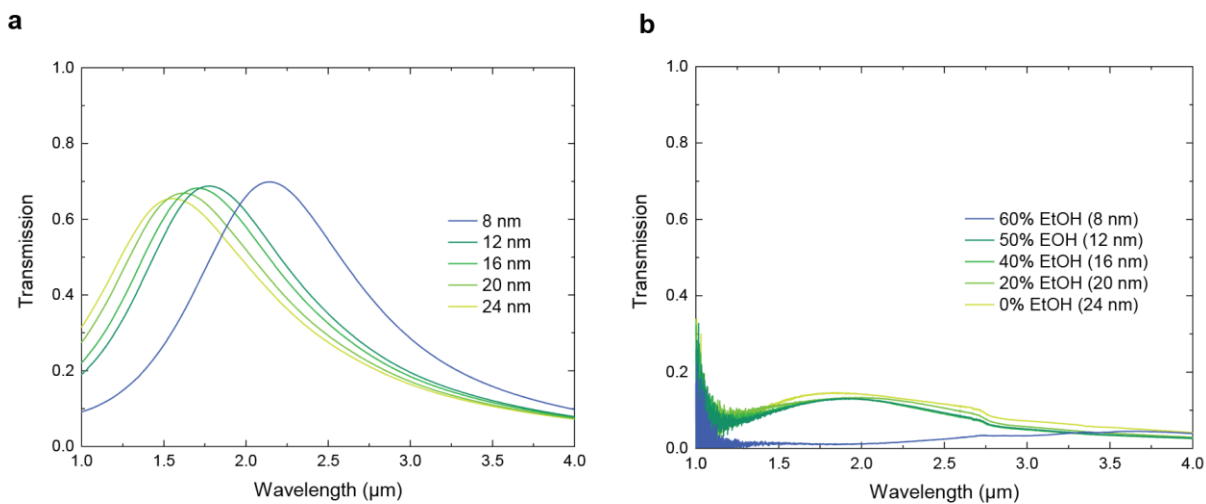
Figure 5-14. a) Simulated transmission spectra for metasurfaces with varying interparticle spacings. b) Experimental transmission spectra as a function of ethanol concentration. Samples were prepared in a solution with the designated ethanol content and then embedded in silica.

Effect of Au Film Thickness
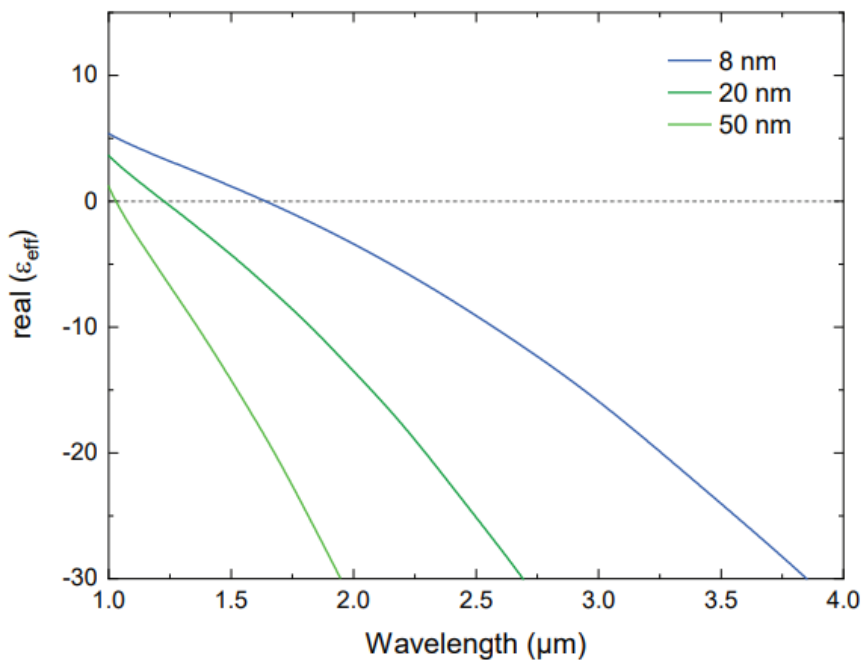
Figure 5-15. Calculated real part of the effective permittivity as a function of underlying Au film thickness. The ENZ condition wavelength can be further tuned to the red by increasing the thickness of the underlying Au film.

Optical Images and Experimental Reflection Spectra of Metasurfaces
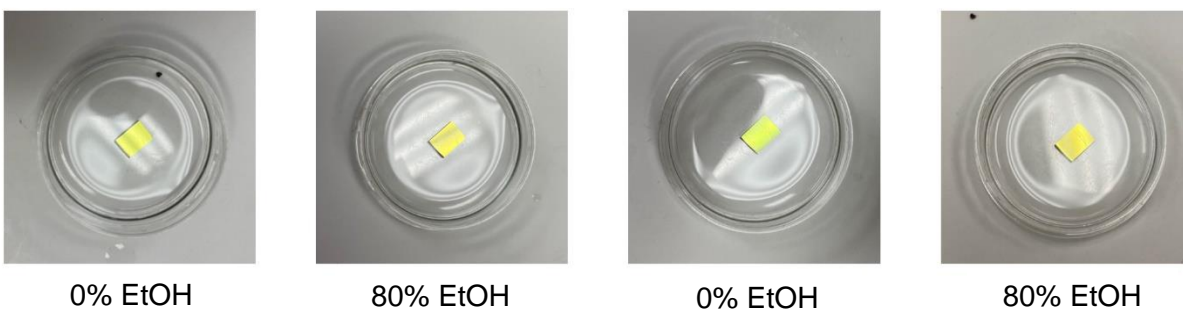
Figure 5-16. Optical images of metasurfaces assembled on glass cover slides coated with 8 nm Au. The color changes from green to yellow when changing the submerging liquid from aqueous buffer to 80% EtOH buffer. Cycling between 0% and 80% EtOH does not result in noticeable sample degradation, indicating reversibility.
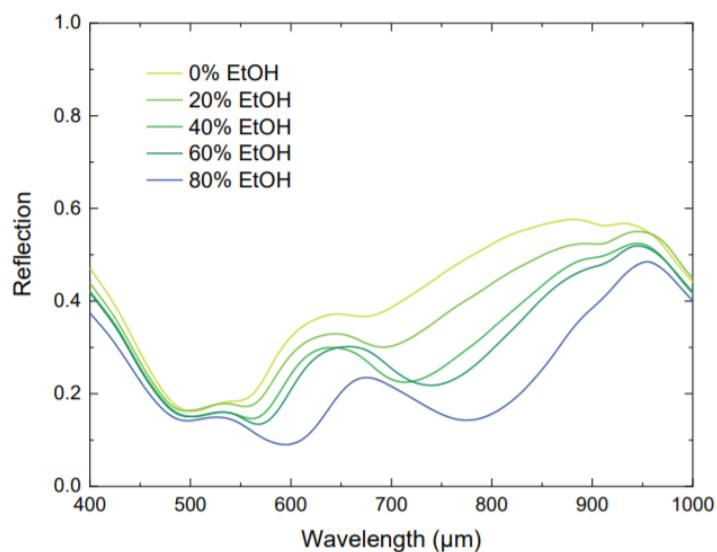
Figure 5-17. Visible range reflection measurements of metasurfaces assembled on glass cover slides coated with 8 nm Au, immersed in buffer with various ethanol concentrations from 0 to 80%. Two dips can be seen in this range and both red-shift as a function of increasing ethanol concentration (decreasing gap distance).
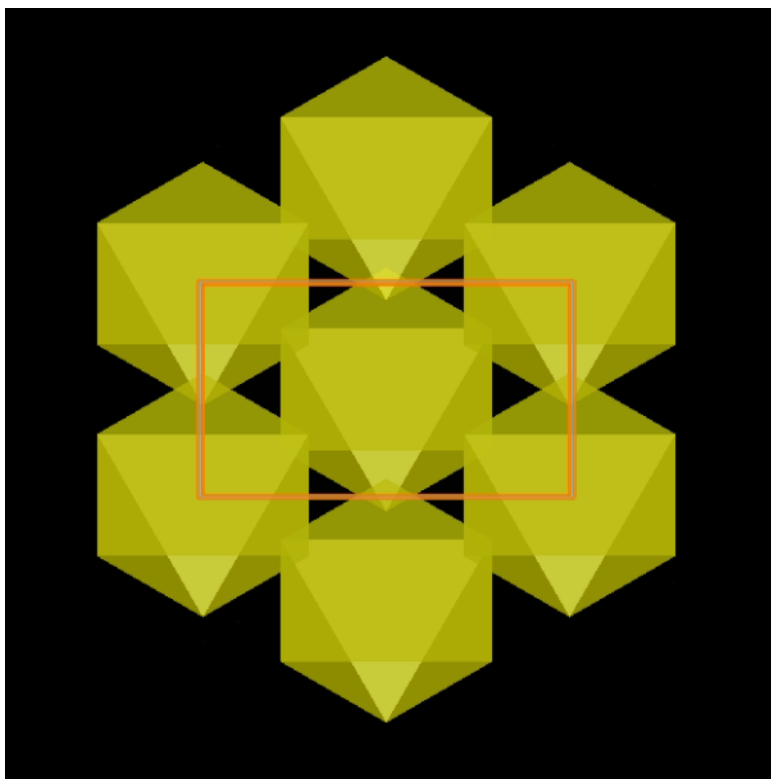
Figure 5-18. Projection of the octahedron film simulation geometry. The orange box indicates the repeated unit cell.

Additional SEM Images
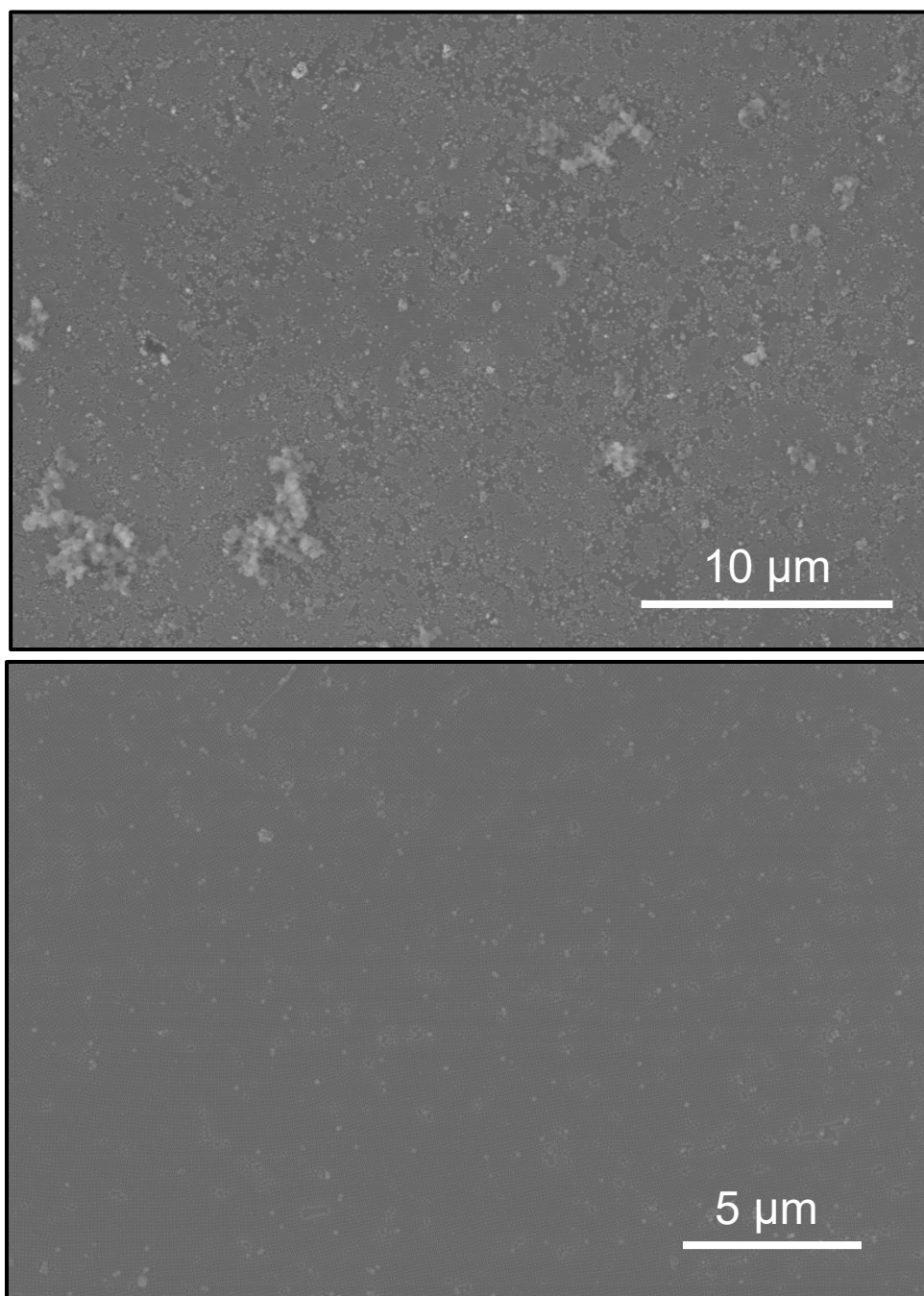
Figure 5-19. Large-area SEM images elucidating the growth process of the SL films. In the top image, single-crystalline 2D SL islands can be seen. Cube monomers attach to the substrate in the spaces between the islands, likely joining the islands through surface migration. Finally, as the islands merge, they sometimes rotate to align with each other (bottom). Because the growth temperature is well above the aggregate melting temperature, unstable regions will remelt into solution, explaining the high crystallinity of the films.

CHAPTER 6

Scalable Assembly of Three-Dimensional Metamaterials

This chapter is based on unpublished work.

Collaborators include Junjing Deng, Yudong Yao, Seonke Seinfert, Alexa Wong, Liban Jibril, Wisnu Hadibrata, Seokhyoung Kim, Koray Aydin, Byeongdu Lee, Chad Mirkin, and George Schatz.

6.1 Introduction

Confinement in nano- or micro-scale pores can have an enormous effect on the outcome of crystallization[197] for a wide range of materials including block copolymers,[198–201] organic molecules,[202–204] and nanoparticles (NPs).[205–207] Various works have shown the successful application of 2D lateral confinement to control the morphologies and sizes,[203,208] orientations,[201,209] crystal structures,[204] and chirality of assemblies on substrates.[202] In these studies, templates are constructed such that their side walls and/or the bottom substrate surface exhibit attractive or repulsive interactions with the material undergoing crystallization. Alternatively, the template can simply act as a hard barrier, confining growth inside a small volume.[5] Additionally, assembly of materials into lithographically patterned trenches on substrates offers a route towards fabricating devices with subwavelength feature sizes and controlled morphologies.[210]

DNA-assembled NP superlattices (SLs)[54,81] represent a promising class of materials for achieving unusual optical,[79,146] electrical, and mechanical responses[156] due to the immense library of structures which can be obtained[114,185] and the active tunability afforded by the stimuli-responsiveness of DNA.[98,99,155] In addition, DNA-functionalized NPs serve as a model system to study crystal growth, behaving as programmable atom equivalents (PAEs), due to their similarity to atoms in atomic crystals.[90] In this work, we study the crystallization of PAEs SLs under lateral

confinement by assembling cube PAEs inside lithographically patterned microscale trenches on DNA-functionalized substrates. We hypothesize that growth in trenches would result in single crystalline SLs with controlled sizes and orientations as individual crystallites are forced to merge inside a trench. Small-angle X-ray scattering (SAXS) and scanning electron microscopy (SEM) characterization were employed to visualize the growth pathways and resulting SL structures. Indeed, we discover that single crystalline, square-prism shaped SLs with lateral dimensions ranging from 1-3 µm can be formed inside square trenches of those same dimensions. Microfocus SAXS measurements elucidate the distribution of orientations within an array, revealing that SLs preferentially align with their {100} facets parallel to the trench walls, with better aligned SLs in smaller trenches.

In addition, the unique ability to prepare ensembles of SLs with controlled sizes allows us to study the variation of the SLs' defect structure with size. X-ray ptychography[211] is a high resolution coherent diffractive imaging technique capable of imaging the internal structure of microscale colloidal crystals due to the high penetrative depth of X-rays.[212] SEM and ptychography were used to study the surface and internal defect structure of the SLs, respectively. We found that SLs grown in 1 µm trenches were typically single crystals with very few defects, those grown in 2 µm trenches were generally single crystals with dislocations, and those grown in 3 µm trenches consisted of several connected grains. Next, *ex situ* SEM experiments conducted on samples quenched at various growth stages suggest that SLs grow *via* nucleation and growth, followed by coalescence of neighboring domains, elucidating how trench size dictates the observed defect structures. Taken together, our results reveal the effect of lateral confinement on the crystallization of PAE SLs on substrates and provides a general understanding of defects in DNA-assembled colloidal crystals.

Upon successfully utilizing confined SL growth to prepare crystals with control over size, shape, position, and orientation on a substrate, we studied their behavior as optical metamaterials. Specifically, we prepared arrays of metacrystals with various sizes and measured their optical responses. First, synchrotron FTIR with a ~8 μm beam diameter was used to measure the extinction from single SLs within an array, revealing uniformity in optical response within an array. Next, ensemble measurements across an array were collected using tabletop FTIR with a large beam. We find that the tabletop FTIR measurements can resolve multiple resonance peaks in the mid-IR, suggesting that this platform is promising for the scalable preparation of uniform, 3-dimensional metacrystals. Finally, we use the spacing between metacrystals in an array as an additional design parameter to engineer optical response, introducing another degree of hierarchy in functional DNA-assembled metamaterials.

6.2 Results and Discussion – Structural Characterization
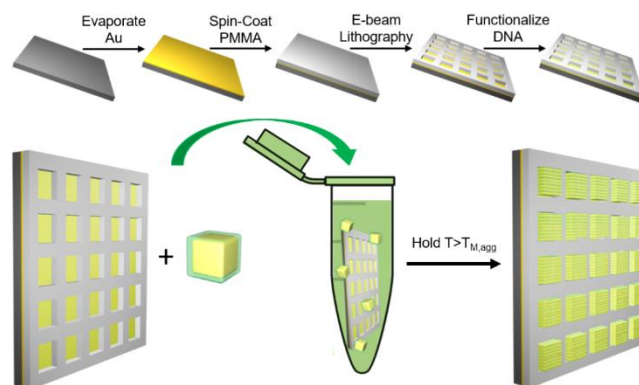
Scheme 6-1. (top) Trench array fabrication process. (bottom) SL assembly scheme.

To prepare templates for subsequent PAE crystallization, we used electron beam lithography (EBL) to pattern square trenches into a polymer resist (Scheme 6-1, top). Specifically, we spin-coated an ~600 nm thick layer of PMMA resist on a Au-coated Si wafer and used EBL to pattern microscale square pores of varying sizes, exposing the underlying Au film. Next, we functionalized the exposed Au regions with thiolated anchor DNA. Cube PAEs were prepared by

functionalizing ~ 80 nm Au nanocubes with the same thiolated anchor DNA as that on the substrate and performing a salt aging procedure to maximize DNA loading. The reaction solution was prepared by mixing the PAE solution, patterned substrate, and linker DNA in a 5 mL Eppendorf tube and bringing the solution to 0.3 M NaCl. The linker strands were designed to be complementary to the anchor strands, for the exception of a four base self-complementary "sticky end" region used to bind to other PAEs. To determine optimal reaction conditions, we measured the melting temperature of the system by collecting temperature-dependent UV-Vis data. We chose a growth temperature of 68ºC, well above the melting temperature of PAE aggregates (58ºC), but within the crystal-melt coexistence regime. To crystallize PAEs inside the templates, we placed the Eppendorf tube on a shaker at 68ºC for 60 hrs, during which SLs formed inside the pores (Scheme 1, bottom). Finally, we embedded the samples in an amorphous silica matrix for subsequent characterization.
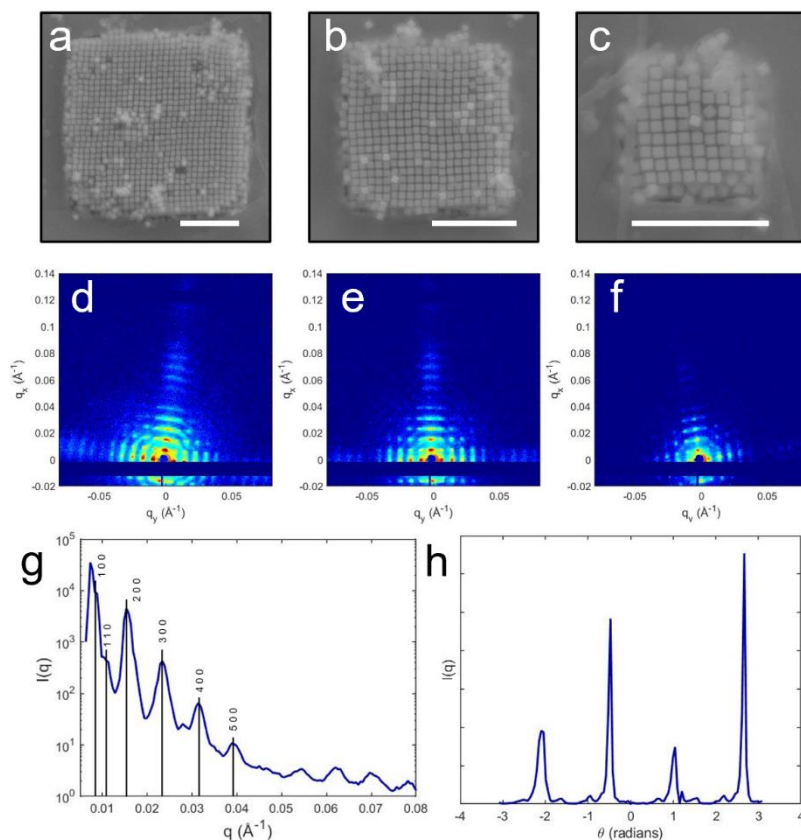
Figure 6-5. Assembly results. SEM images of typical SLs grown in (a) 3, (b) 2, and (c) 1 µm trenches. 2D microfocus SAXS patterns from SLs grown in (d) 3, (e) 2, and (f) 1 µm trenches. (g) Azimuthally averaged 1D SAXS profile from a 3 µm SL, with simple cubic indexing. Scale bars: 1 µm.

Figure 6-1a-c shows typical SEM images of SLs grown in 3, 2, and 1 µm square trenches, respectively, on the same substrate. PAEs fill the entire trench volume, forming square prism crystal habits. SAXS patterns were collected using a 5 x 10 µm focused X-ray beam. The discrete spots in the 2D SAXS patterns (Figure 6-1d-f) indicate that SLs of all three sizes contain one dominant domain, suggesting that this technique can be used to prepare high quality single crystals of varying sizes. 1D plots of the SAXS patterns averaged azimuthally (Figure 6-1g and S8) indicate that the SLs have a simple cubic symmetry with periodicity of ~98 nm, regardless of size of the trench they were grown in. This result suggests that the lateral confinement has little to no effect on the SLs' nanoscale crystal structure, which is commensurate with the square shape of the

trenches. As seen in the SEM images, individual nanocubes assemble with a facet parallel to the substrate, resulting in a (100) out-of-plane orientation, consistent with previous studies of polyhedral PAE thin film assembly, where NPs assemble with face-to-face interactions with a DNA-functionalized substrate to maximize hybridization.[213] The four-fold symmetry evident in the diffraction pattern mirrors the four-fold in-plane symmetry of the simple cubic {100} planes. Azimuthally plotting the SAXS patterns along the {200} reflections reveals that although the peaks are generally very sharp, there are small amounts of intensity at other in-plane orientations (Figure 6-1h and S8), which is also seen from the streaking around the diffraction spots in the 2D SAXS patterns (Figure 6-1d-f).

To measure the in-plane distribution of SL orientations within an array, we collected 2D maps of SAXS patterns using a microfocused beam (Figure S2). Importantly, each SL could potentially contain multiple domains with different orientations, some of which may not be visible in the top-down SEM images. In contrast to the surface structure provided by SEM, SAXS measurements also give information about the interior of the SLs, revealing a true distribution of orientations. Specifically, the beam was raster scanned across the array area and SAXS data was collected at 5 µm intervals in both the x and y directions. For this experiment, the beam diameter was ~ 15 µm, while the spacing between SLs in the array was 5 µm, so each SAXS pattern likely represented signal from several neighboring SLs. Nevertheless, this measurement provides information on the homogeneity and distribution of orientations within an array. To determine in-plane orientations from SAXS patterns, we azimuthally plotted each diffraction pattern along the {200} reflections, as in Figure 1h. Next, we created 2D maps of the intensities at selected azimuthal angles varying from 15 to 90 ° (Figure 6-2a,b). Finally, we integrated the intensities within each 2D map to create a bar graph of the total intensity of each orientation (Figure 6-2c-e). The bar
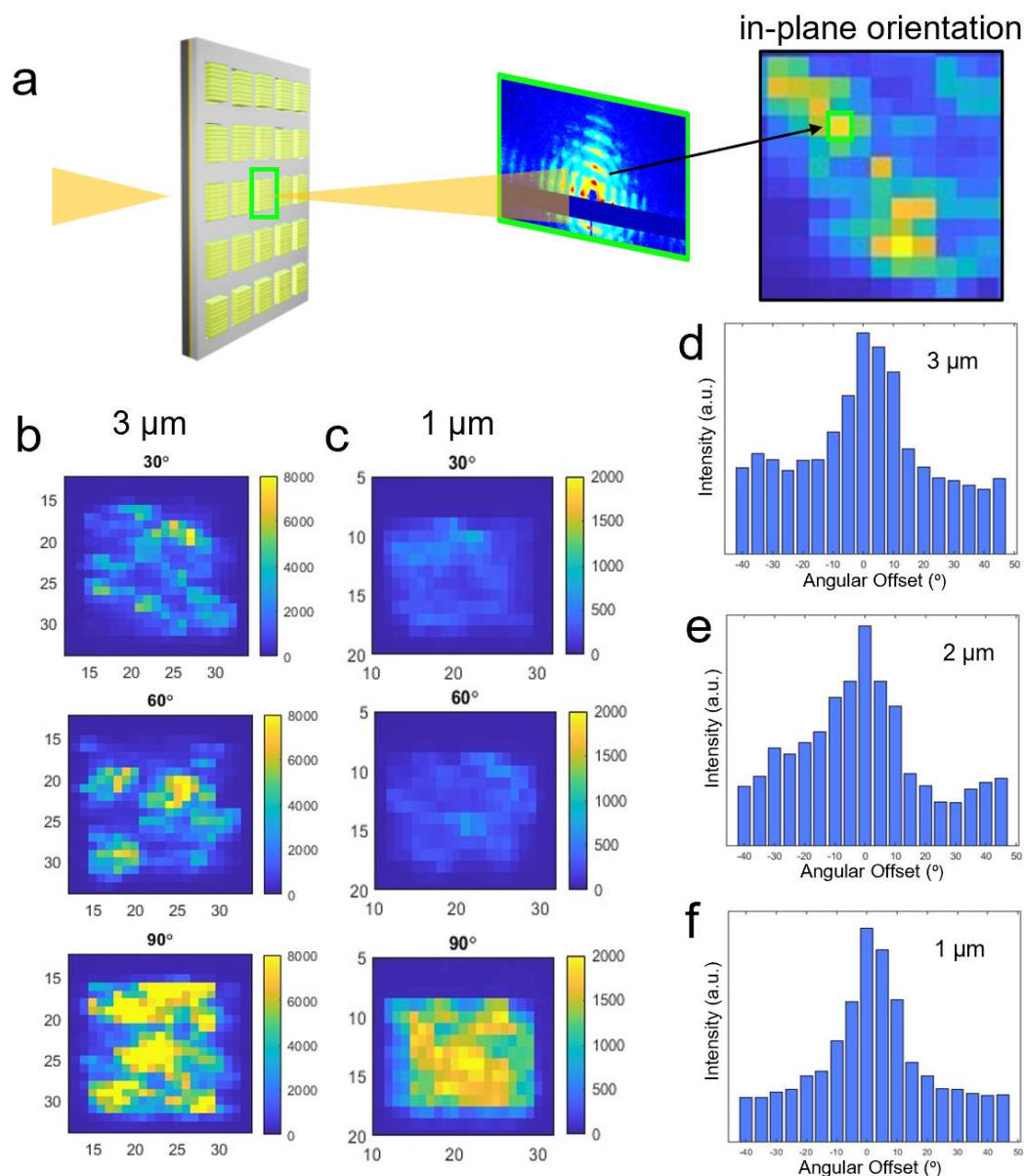
Figure 6-6. Statistics of in-plane orientation. (a) Schematic of microfocus SAXS experiment and orientation analysis. A focused X-ray beam is used to collect signal from a small area (green box) of the sample. The in-plane orientation of the SL is then determined from the SAXS pattern and plotted as a single pixel in the orientation map. (b-c) Intensity at various orientations along the {200} reflections in microfocus SAXS patterns for (b) 3 µm and (c) 1 µm SLs. Bar graphs of the total intensity of each orientation integrated over all SAXS patterns for arrays of (d) 3, (e) 2, and (f) 1 µm SLs. Standard deviations are 22.5, 21.7, and 20.1 °, respectively.

graphs are plotted as offset from 90 °, taking into account the four-fold symmetry of the diffraction

patterns. For all three trench sizes, the results indicate that there is a symmetric distribution of

orientations, peaking at 0 °, at which the SL (100) direction is aligned with the trench walls (Figure

6-2c-e). The strong bias for the 0 ° orientation is likely because in this orientation, the sides of the

SLs expose their most energetically favorable {100} facets. Furthermore, the widths of the bar graphs increase as a function of trench size, suggesting that smaller trenches better control the SLs' in-plane orientation. Previous work showed that the in-plane orientation of PAE SLs can be controlled by lithographically defining Au posts, which act as the first layer of PAEs for subsequent thin film growth.[195] In this technique, patterning of nanoscale features is required. On the other hand, we show here how microscale features can be used to control the orientation of nanoscale PAEs, significantly reducing the cost of patterning.
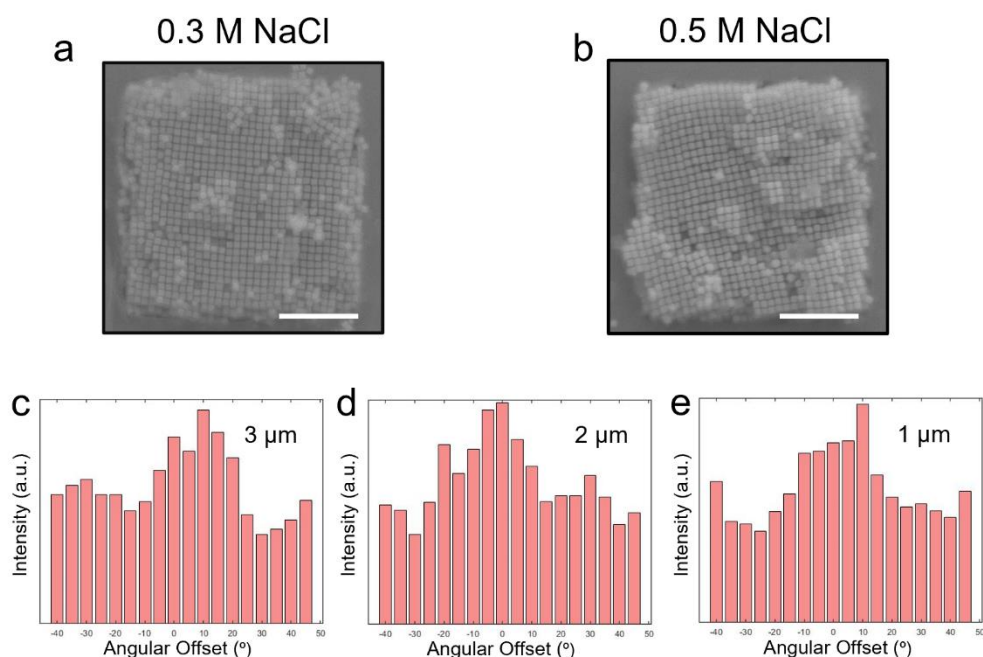
Figure 6-7. Effect of growth rate on the distribution of SL orientations. Exemplary SEM images of 3 µm SLs grown in (a) 0.3 M NaCl and (b) 0.5 M NaCl. In-plane orientation distributions of SL arrays grown in 0.5 M NaCl for (c) 3, (b) 2, and (e) 1 µm SLs. Standard deviations are 24.4, 23.8, and 24.5 °, respectively. Scale bars: 1 µm.

Statistical analyses were also performed on large-area SEM images, where the image resolution was sufficiently high to determine the orientations of individual SLs. As seen from the histograms in Figures S6 and S7, SL orientations measured from SEM images are more narrowly distributed than those determined from SAXS. This discrepancy arises because SLs contain

domains which are not visible in SEM images. In fact, histograms generated from SEM analysis suggest that 3 µm SLs have a narrower distribution of orientations than 2 µm SLs. This indicates that although 3 µm SLs are more likely to appear aligned from the surface, they have more misaligned subsurface grains, highlighting the importance of SAXS measurements. Similarly, 1 µm SLs have the highest degree of alignment because each trench likely contains a single crystallite.

In all crystallization processes, the quality of the resulting crystals depends largely on growth conditions, especially the growth rate. Specifically, growing crystals at fast rates usually results in the formation of crystals with a high density of defects, while higher quality crystals are typically grown by slowing the crystallization rate.[214] Here, we synthesized SLs with varying degrees of crystallinity by using solution ionic strength as a lever for controlling the rate of NP assembly. Previously, it has been shown that increasing salt concentration in PAE assembly results in quicker DNA association rates, and therefore faster assembly, due to the additional charge screening which minimizes repulsion between the negatively charged DNA strands.[78] Indeed, crystallization in 0.5 M NaCl (and otherwise identical conditions) occurs in ~20 hours, which is much faster than crystallization in 0.3 M NaCl which takes ~60 hours to complete. SEM images show that SLs grown in 0.5 M NaCl (Figure 6-3b) contain more surface defects compared to the nearly perfect crystals grown in 0.3 M NaCl (Figure 6-3a). In addition, statistical analyses performed on microfocus SAXS data show that the distribution of orientations is wider in crystals grown in 0.5 M NaCl (Figure 3c-e) compared to those grown in 0.3 M NaCl (Figure 6-2c-e). This indicates that faster crystallization largely compromises the confinement effect provided by the trench.
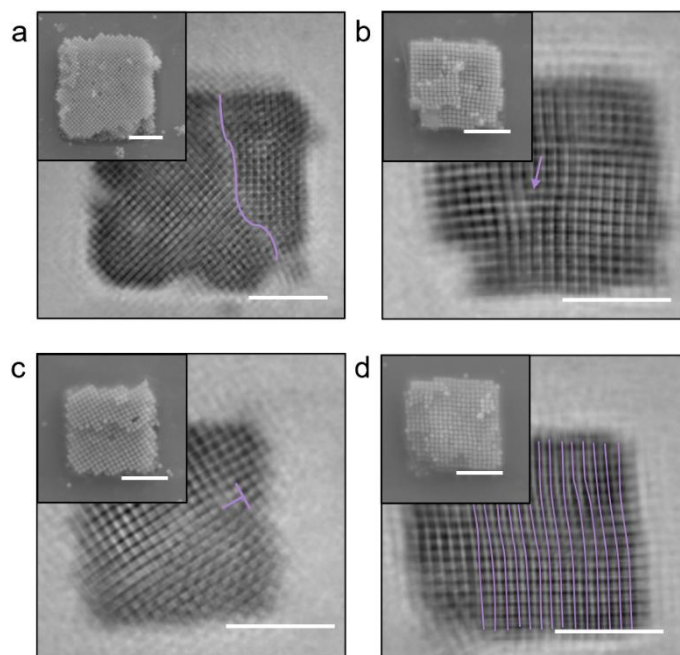
Figure 6-8. (a-d) Ptychographic reconstructions of SLs grown in trenches showing typical defect structures.

We found that larger trench sizes resulted in SLs with worse crystallinity and alignment, suggesting that the SLs' internal defect structures differed by size. Although previous reports have shown that DNA-assembled colloidal crystals exhibit analogous defects to those in atomic crystals (e.g., vacancies, antisites, dislocations, twinning, etc.),[166] their internal structures have not been directly visualized and imaging of defects has been limited to SL surfaces. Furthermore, growth in confinement could lead to different defect structures than otherwise present in solution- or substrate-grown SLs because individual crystallites are forced to merge within a trench during growth. Here, X-ray ptychography was used to image the SLs' internal structure, confirming whether SLs which appear as single crystals in SEM indeed contain multiple subsurface domains. We grew SL arrays in 0.5 M NaCl in order to generate a considerable number of defects and fully visualize the spectrum that typically occur in the samples.

Figure 4 shows ptychography reconstructions of selected SLs portraying typically observed defects. These include edge (Figure 6-4c) and screw dislocations (Figure 6-4b), tilt (Figure 6-4a,c)

and twist (Figure 6-4a,c) grain boundaries, as well as curved rows of NPs (Figure 6-4d). As predicted, subsurface grain boundaries were commonly observed in SLs that appear as single crystals in SEM images (Figure 6-4a,c and S11). For this to occur, in-plane tilt boundaries must be accompanied by interlayer twist boundaries, a unique feature which was observed in many of the 3 µm crystals (Figures 6-4a,c). Out of over 200 imaged SLs (Figure S9 and S10 show representative ones), none exhibited an interlayer twist boundary without the presence of an in-plane tilt boundary, suggesting that twist boundaries are relatively unstable. We hypothesize that interlayer twist boundaries form when a new layer grows on top of two grains meeting at a tilt boundary. As the new layer grows laterally from one domain over to the surface of the tilted neighbor domain, new adparticles assemble to form face-to-face registry with in-plane neighbors rather than the underlying particles, which may be due to the higher coordination number in-plane than out-of-plane, 4-vs-2 in this cube system.

Fast Fourier transform (FFT) analysis on ptychography reconstructions of 3 µm SLs (Figure 6-5d and S11) typically exhibit multiple independent sets of diffraction spots, suggesting that they generally contain several highly misaligned grains. On the other hand, FFT of ptychography reconstructions on 2 µm SLs typically have one set of diffraction spots with some streaking (Figure 6-5h, S10), indicating that they are generally single crystals with possible edge dislocations but no grain boundaries. Finally, the single sets of sharp diffraction spots in FFT of ptychography reconstructions on 1 µm SLs indicate that they are largely defect-free (Figure S9). The ptychography reconstructions were color-coded by orientation to highlight the different domains (Figures 6-5c,g, S10, and S11). Disparate colors are seen across grain boundaries, while subtle color differences are observed near dislocations. In atomic crystals, the interfaces between two crystallites are categorized by low-angle (LAGBs, typically less than 10 °) and high-angle
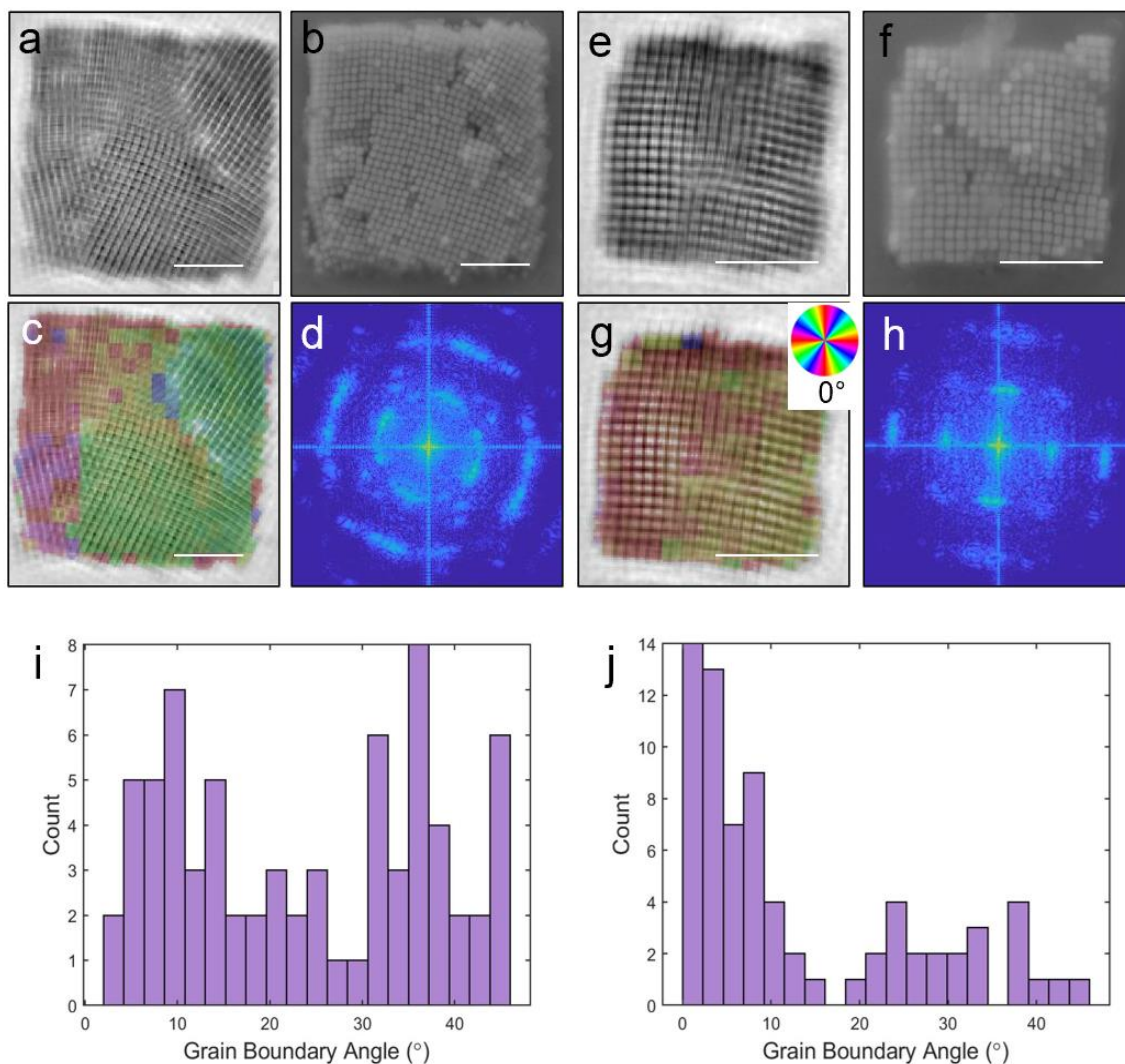
Figure 6-9. Ptychography reconstructions of a (a) 3 and (e) 2 µm SL and (b,f) corresponding SEM images. (c,g) The reconstruction in (a,e) with color code to indicate domain orientations (see color wheel). (d,h) FFT of (a,e). Histogram of grain boundary angles in (i) 2 and (j) 3 µm SLs.

grain boundaries (HAGBs, greater than 10 °). The interfacial energy of LAGBs increases roughly linearly with misorientation angle while that of HAGBs are high except near ideal configurations where the two lattices have a large degree of overlap, for example a twin boundary, resulting in a stable configuration.[215] To study the distribution of misorientation angles in the SLs, we measured over 50 grain boundaries for both 2 and 3 µm SLs. For 3 µm SLs, we found a random distribution of misorientation angles (Figure 6-5j), indicating that grain boundaries emerge through

coalescence of independently formed grains which do not undergo reorientation or restructuring once formed. In contrast, for 2 µm SLs, the number of boundaries with a certain misorientation angle decreases as the angle increases up to ~10 °, beyond which the proportion is low (Figure 6-5i). In addition, close inspection of the reconstructed images reveals that LAGBs are filled with edge dislocations which form to connect two merging grains. These results suggest that in 2 µm trenches, a small number of domains nucleate preferentially at the edge of the trench. In contrast, in 3 µm trenches, some nuclei form away from the trench edge and thus without any confinement effect. Interestingly, many interfaces with both small and large misorientations remain continuous (i.e., it is not possible to pinpoint the start of a new domain) by connecting through curved rows of NPs (Figure S12), in contrast with the sharp HAGBs of many crystal systems.[216] The gradual change in orientation can also be visualized by the presence of intermediate colors near a grain boundary in the color-coded reconstructions (Figure 6-5c,g). The bending of domains is possible because DNA length can vary locally due to its flexibility.[195] Overall, the ptychography experiment elucidates how defect structure depends on the area of the confining region. Such understanding can enable defect engineering to control light-matter interactions in photonic crystals.[217,218]

Finally, we conducted an *ex situ* SEM study of SL growth to rationalize the formation of the unusual defect structures (Figure 6-6). Specifically, we performed SL crystallization in 0.5 M NaCl, quenched the samples at various stages (4, 8, 10, 14, and 24 hours) of the crystallization process, and imaged them using SEM. The images show that samples grown in 1 µm trenches typically contain one or two nuclei at 4 hours, grow into full single-crystalline layers at 8 hours, and subsequently epitaxially grow more layers as PAEs fill the trench. This growth pathway explains why the 1 µm SLs are mostly single crystalline with very few defects. On the other hand, 4-5 nuclei can typically be seen after 4 hours in 2 µm trenches. From 8 to 14 hours, these nuclei
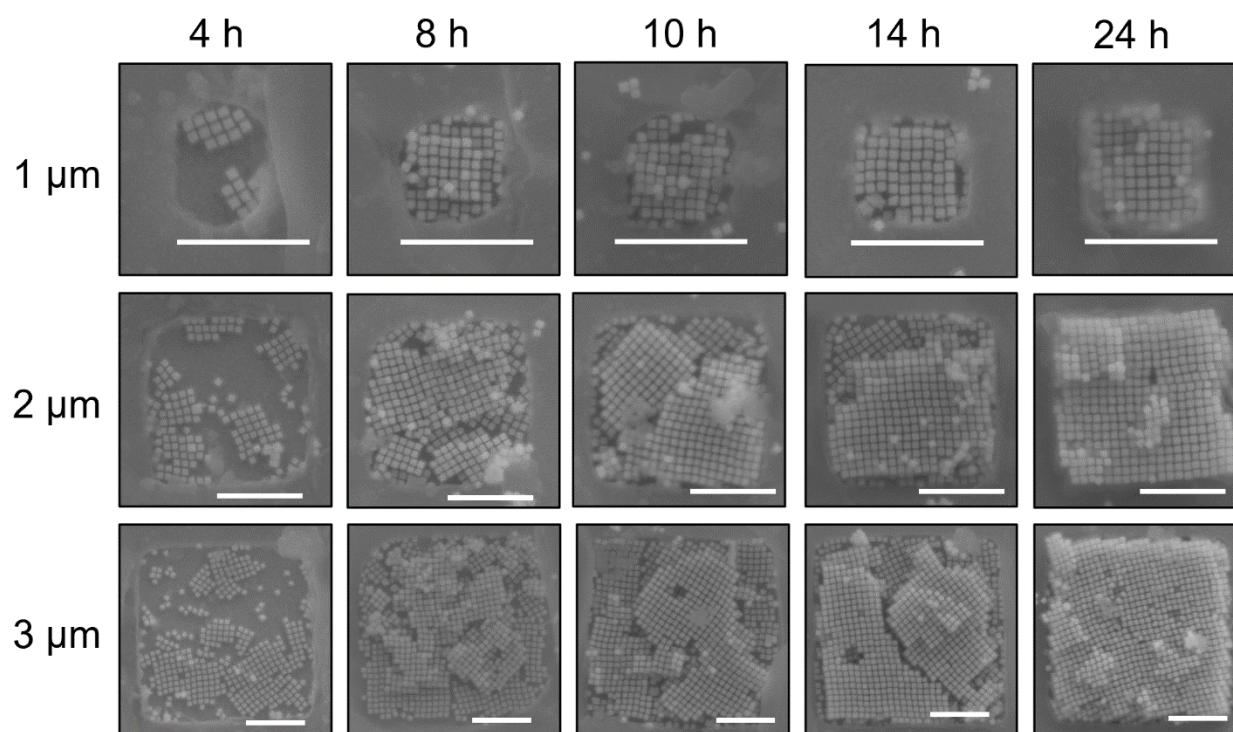
Figure 10-6. SEM images of SLs assembled in trenches and quenched at various stages of the growth process. Scale bars: 1 µm.

appear to grow and eventually collide. When the domains collide, the more aligned (i.e., {100} facet parallel to trench wall) domains continue to grow while the smaller, unaligned ones rotate to combine with them. The growth of aligned grains at the expense of less favorably oriented ones has been observed in the confined growth of block copolymers where collisions with the trench walls halt the growth of unaligned grains.[219] Because smaller crystallites are less stable, they rotate to join the larger domains. Finally, at 24 hours, the images show the formation of single crystals. However, it is evident from the 14-hour time point, that subsurface layers can have different orientations than the surface layer, as observed in the ptychography images. This observation supports our hypothesis that coherent in-plane growth of layers occurs faster than reorientation of subsurface grains. Growth in the 3 µm trenches occurs via a similar pathway, but more nuclei are present at early time points due to the larger trench size. As such, the resulting 3 µm SLs typically contain a higher number of grains and HAGBs, as observed in the ptychographic reconstructions.

Comparison of the SL growth pathways in the three trench sizes also reveals that the natural grain size of SLs is ~ 1 µm, so SLs grown in larger trenches tend to have ~1 µm crystallites connected through defects and grain boundaries.

The growth mechanism can be categorized into layer-by-layer (Frank-van der Merwe) growth. A notable difference from atomic systems, however, is that growth here starts with the formation of islands randomly oriented with respect to one another when nucleation is faster than growth during crystallization. When the islands collide, a continuous adlayer grows on top of several misoriented islands. NPs in the adlayer form bonds with the subsurface layer, but with an orientation defined by their in-plane neighbors rather than the ones underneath. This is largely due to the particles' cube shapes that results in a higher in-plane coordination number than out-of-plane. Therefore, in some sense, the observed growth is opposite to the Stranski-Krastanov (SK) mode, where a film grows layer-by-layer until it reaches a critical thickness. Beyond this thickness, island formation begins because a continuous film is no longer stable due to strain energy from lattice mismatch. Thus, instead of decreasing packing density on higher layers (as in SK growth), the packing density of the PAE films is highest on the top layers.

6.3 Results and Discussion – Behavior as Optical Metamaterials

As described above, assembling SLs in trenches could provide a viable method to scalably fabricate 3-dimensional metamaterials on substrates with control over placement, orientation, shape, and size (Figure 6-7). Here, we explore engineering the optical properties of these metamaterials using both nanoscale materials parameters and mesoscale crystal habit design. Several design parameters exist for tuning the effective optical parameters of DNA-assembled colloidal metamaterials. These include nanoparticle shape, size, and composition (which dictate individual NP resonances) as well as interparticle spacing and superlattice symmetry (which are
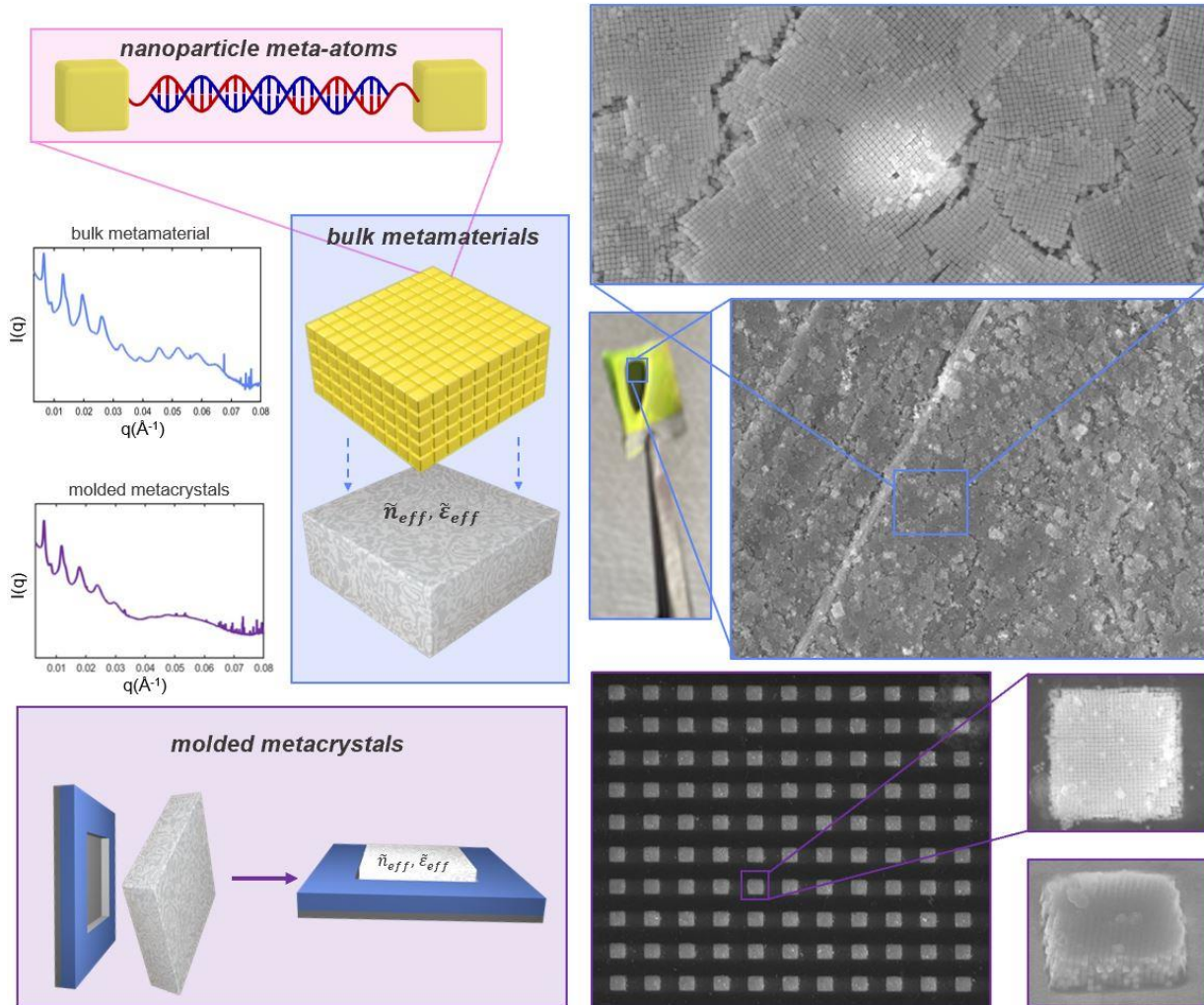
Figure 11-7. Using trench confinement to engineer the optical properties of 3-dimensional metamaterials. Three-dimensional metamaterials can be grown over macroscopic areas on substrates using a recently developed crystallization technique. Trench confinement molds these crystals into discrete faceted metacrystals with controlled size, position, and orientation.

defined by DNA design and determine coupling between NPs).[94,140,220] Indeed, microscale crystals with over 50 distinct symmetries and numerous lattice parameters have been synthesized, opening a vast design space for metamaterials with diverse optical properties.[54] Here, we explore one possible class of DNA-assembled metamaterials, effective dielectric media made from capacitively coupled nanocubes arranged in a simple cubic SL.[8,146] We use an effective parameter retrieval method to extract effective optical parameters from finite-difference time-domain (FDTD) simulations of metamaterials with various structural parameters. The results show that

effective refractive index can be tuned using both nanocube size and interparticle spacing (Figure 6-8). Specifically, decreasing nanoparticle size (from 90 to 60 nm) while keeping interparticle spacing at 20 nm results in smaller refractive indices (from ~3 to ~ 2.6). On the other hand,
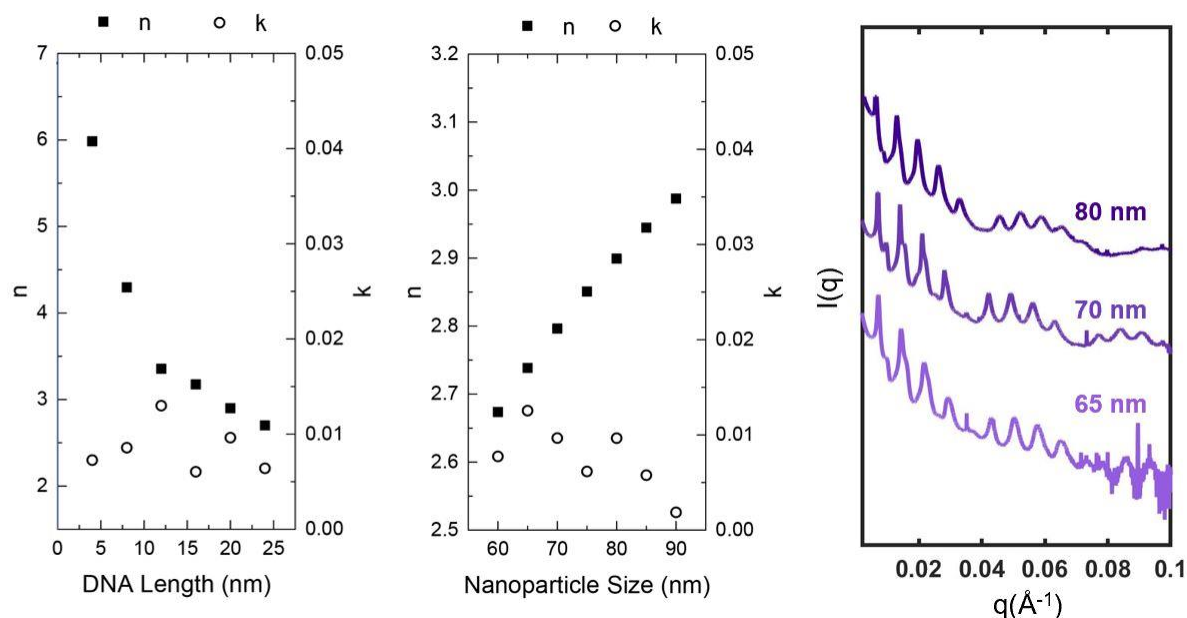
Figure 12-8. (left and middle) Extracted refractive indices from DNA-assembled metasurfaces. Ways to tune the effective optical parameters of DNA-assembled metasurfaces include nanocube edge length and DNA length. (right) SAXS patterns from 3D metasurfaces assembled with different nanoparticle edge lengths, showing extremely high crystallinity in all cases.

decreasing interparticle spacing (from 24 to 4 nm) results in larger refractive indices (from ~2.6 to ~6). Experimentally, we assembled metasurfaces from nanocubes with edge lengths varying from 65 to 80 nm. Small-angle X-ray scattering characterization shows extremely sharp peaks with many diffraction orders for all three cube sizes, indicating that the SLs are highly crystalline.

As an example of using trenches to template the assembly of optically-active metacrystals, we patterned a 12 x 12 array of identical square trenches of 3 µm edge lengths and used them to direct the assembly of 80 nm cube PAEs (Figure 6-7). A large-area SEM image shows that SLs grew inside each of the trenches, while the zoomed-in SEM image in shows that the PAEs filled the trench, forming a square-prism mesoscale habit. Furthermore, an image taken at a 40° tilt angle

shows that a typical metacrystal in the array consists of around six PAE layers. To characterize the crystallinity of the metacrystal arrays, a large-area small angle X-ray scattering (SAXS) pattern was collected on the entire array. Indexing the 1D integration of the SAXS pattern indicates that the SLs are highly crystalline, with simple-cubic symmetry and a lattice constant of ~100 nm. As a control, we also grew SLs from cube PAEs of similar size and identical DNA design on a bare Au wafer (Figure 1). The 1D SAXS pattern from this sample (Figure 2c) shows similar symmetry and lattice constant to that from the SL array, indicating that SLs inside the template grew according to their bulk crystal structure, as previously revealed in the structural study.
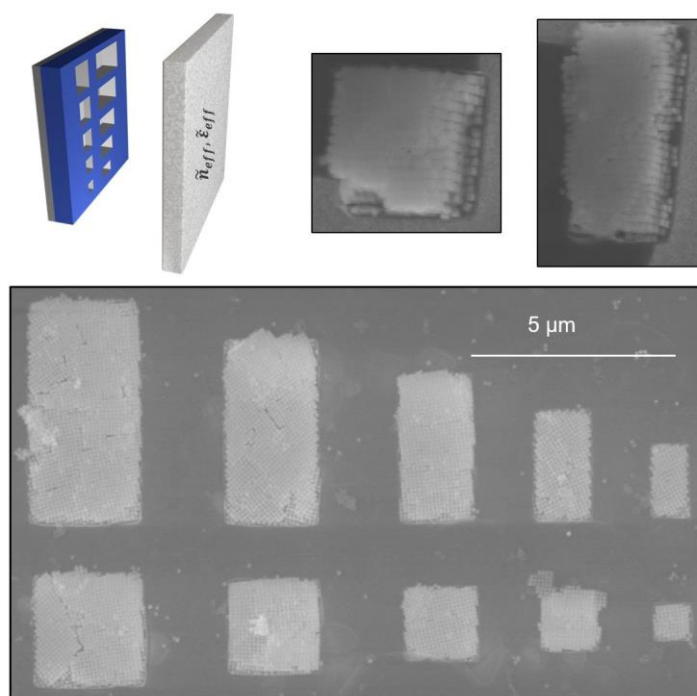
Figure 13-9. Shaping 3D metamaterials into habited metacrystals with controlled, tunable sizes and aspect ratios.

In a previous work, we discovered that metacrystals of identical materials parameters (cube size and DNA length) can be engineered to exhibit tunable Mie resonances by virtue of habit size.[146] Specifically, we found that larger metacrystals give rise to resonances at longer wavelengths, analogous to Mie resonances in dielectric NPs. In addition, changing the aspect ratio of metacrystals could allow tuning of their Mie resonances. Here, we use the in-plane size and

aspect ratio of templates to control the morphology of the resultant metacrystals. Specifically, we patterned onto the sample substrate, square templates of sizes ranging from 1-3 µm and rectangular templates with 2:1 aspect ratios and short edge length varying from 1-3 µm. Next, crystallization of nanocube PAEs into the templates was facilitated under the abovementioned conditions. SEM images (Figure 6-8) reveal that the resultant metacrystals are well-confined within the

Figure 14-10. Synchrotron FTIR mreasurements of individual metacrystals growth in square trenches of varying edge lengths from 1-3 µm.

template trenches and, as a result, their in-plane sizes and aspect ratios are dictated by those of the trenches. In addition, although the 3 µm crystals contain a few grain boundaries, single crystals could be grown on the same substrate for sizes varying from 1-2.5 µm. SEM images taken at a 40° tilt angle show that the metacrystals are 3-dimensional in nature and contain, on average, 6 layers of PAEs. Importantly, SLs with non-unity aspect ratios, including these rod-like SLs, cannot be obtained using solution-grown methods, which produce Wulff-shaped crystal habits (cubic PAEs form cube-shaped habits). As such, template-directed assembly enables researchers to access new crystal habits, including these elongated ones, which could give rise to polarization-dependent scattering.[221]

To optically characterize metacrystals of varying sizes, we utilized a synchrotron source to perform far-field Fourier-transform infrared (FTIR) extinction measurements on individual metacrystals grown in square trenches of edge length varying from 1 to 3 µm. The beam spot size

was ~8 µm, while the spacing between metacrystals was 15 µm, so each spectrum represented

signal from a single metacrystal. We found that metacrystals of all sizes gave rise to multiple Mie

resonance peaks, which red-shifted as a function of increasing trench size. For a metacrystal grown

inside a 1 µm x 1 µm template, the first-order Mie resonance occurred at ~3.8 µm, while it occurred

at ~7.2 µm for a 3 µm metacrystal (Figure 6-9).
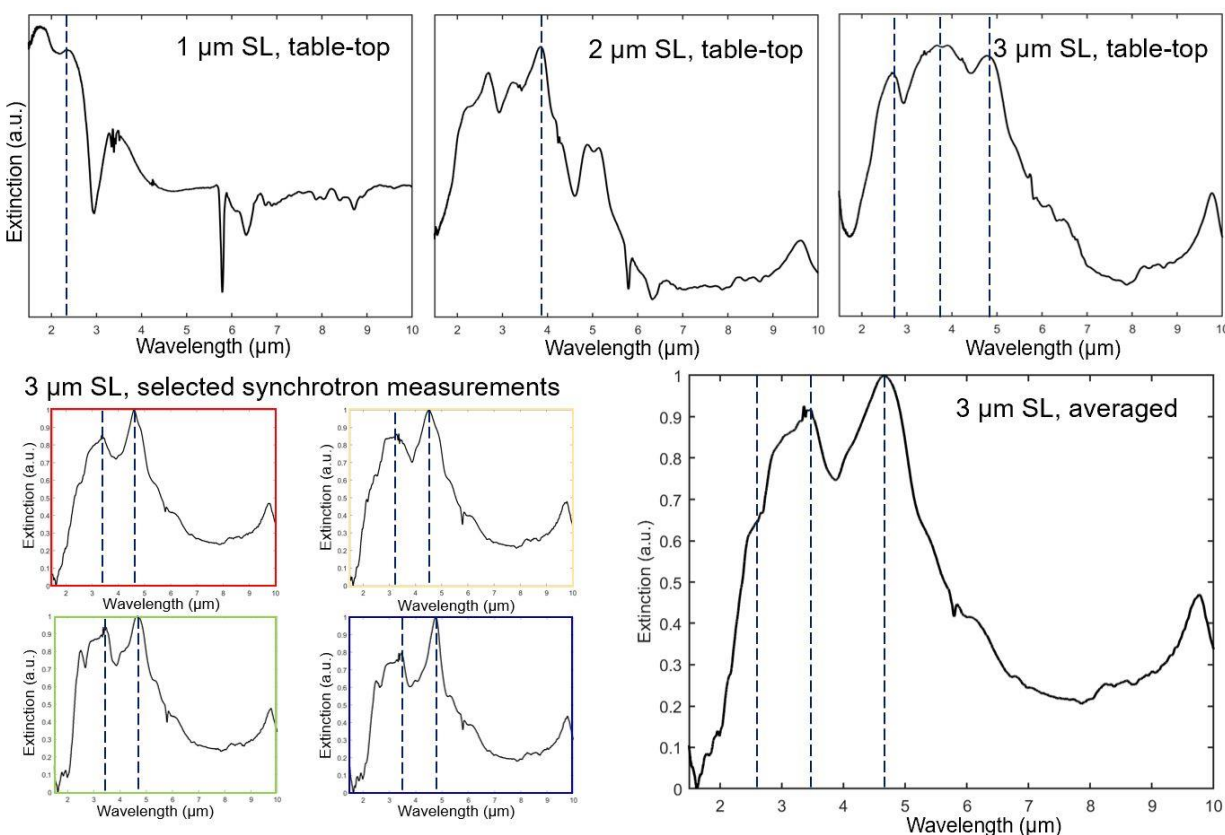
Figure 15-11. Tabletop FTIR measurements performed on arrays of metacrystals. Selected synchrotron FTIR measurements with 8 µm spot size are collected at various locations within the array, showing uniformity in optical response.

In addition to the size-control offered by SL assembly in templates, a major advantage of

this synthetic platform over those performed in solution is that uniform arrays of metacrystals can

be grown, enabling ensemble measurements of their optical properties. We patterned arrays of at

least 12 x 12 metacrystals and measured their optical response using a tabletop FTIR spectrometer.

Specifically, we performed far-field reflection measurements on arrays of 1, 2, and 3 µm
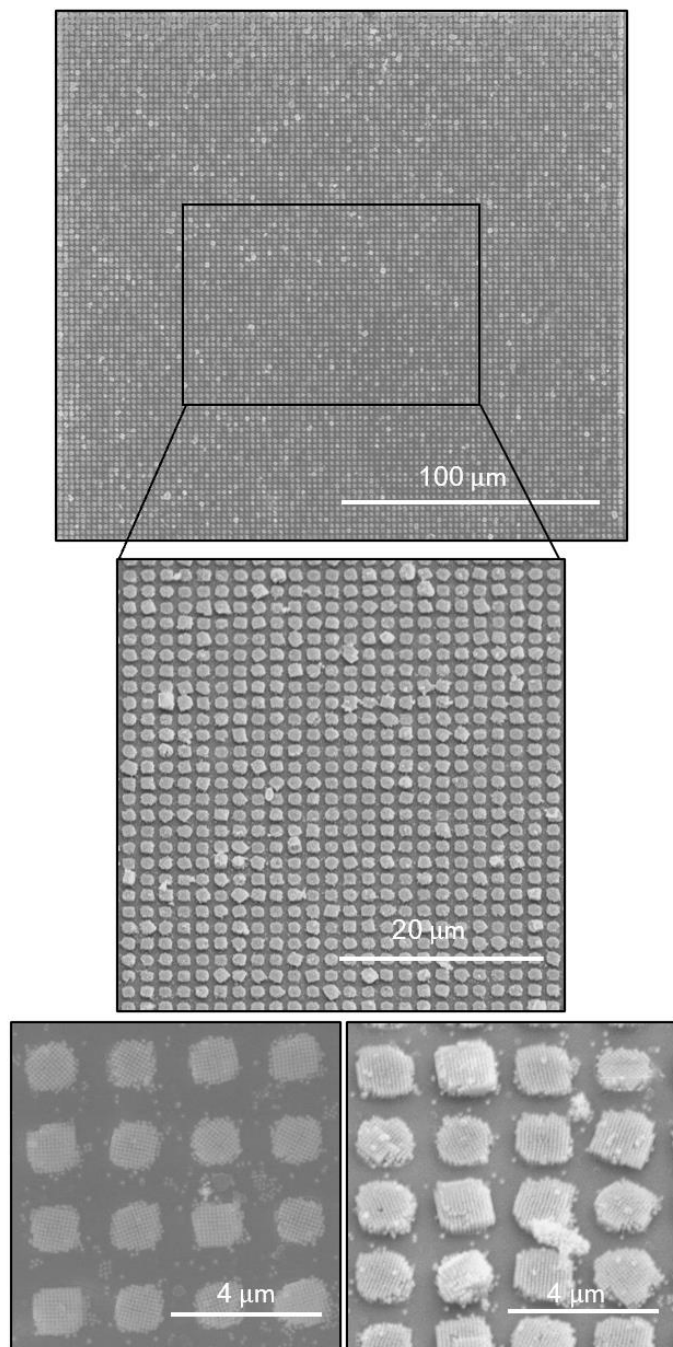
Figure 16-12. Large-area patterning of metacrystals.

metacrystals, spaced by 5 µm (Figure 6-10). Indeed, the spectra show that tabletop FTIR can resolve multiple Mie resonance peaks for each array, with resonances at longer wavelengths for larger metacrystals. Next, we performed synchrotron FTIR measurements on each array to confirm the uniformity of metacrystals within an array. For the 3 µm array, a 10 x 10 grid of measurements were taken at 8 µm spacings, for a total of 100 measurements. Importantly, because the beam spot size (8 µm) was larger than the spacing between metacrystals (5 µm), each measurement could include signal from up to four metacrystals. Four representative spectra from various spots within the sample are plotted in Figure 5g. Although the exact peak positions vary for different spots, the spectra all show two main peaks at ~4.7 µm and ~3.4 µm, respectively, indicating high uniformity. Furthermore, the average of all 100 spectra is shown in

Figure 6-10, showing reasonable agreement with that measured using tabletop FTIR. Indeed, the spectral locations of all three main peaks match, as indicated with dotted lines.

To demonstrate that this method can be scaled up for large-scale fabrication of metacrystals, we used EBL to pattern a 100 x 100 array of metacrystals in 1.2 μm x 1.2 μm square trenches (Figure 6). Close-up SEM images shows that every trench contains a metacrystal comprised, on average, of ~11 x 11 x 4 nanocube PAEs arranged in simple cubic lattices. Notably, although we utilized EBL as a proof of concept, any lithographic technique that can produce microscale features into a polymer resist should be compatible with this assembly method. Scalable fabrication of 3D optical metamaterials is a major challenge in the metamaterials community[2] and our platform provides a viable solution.
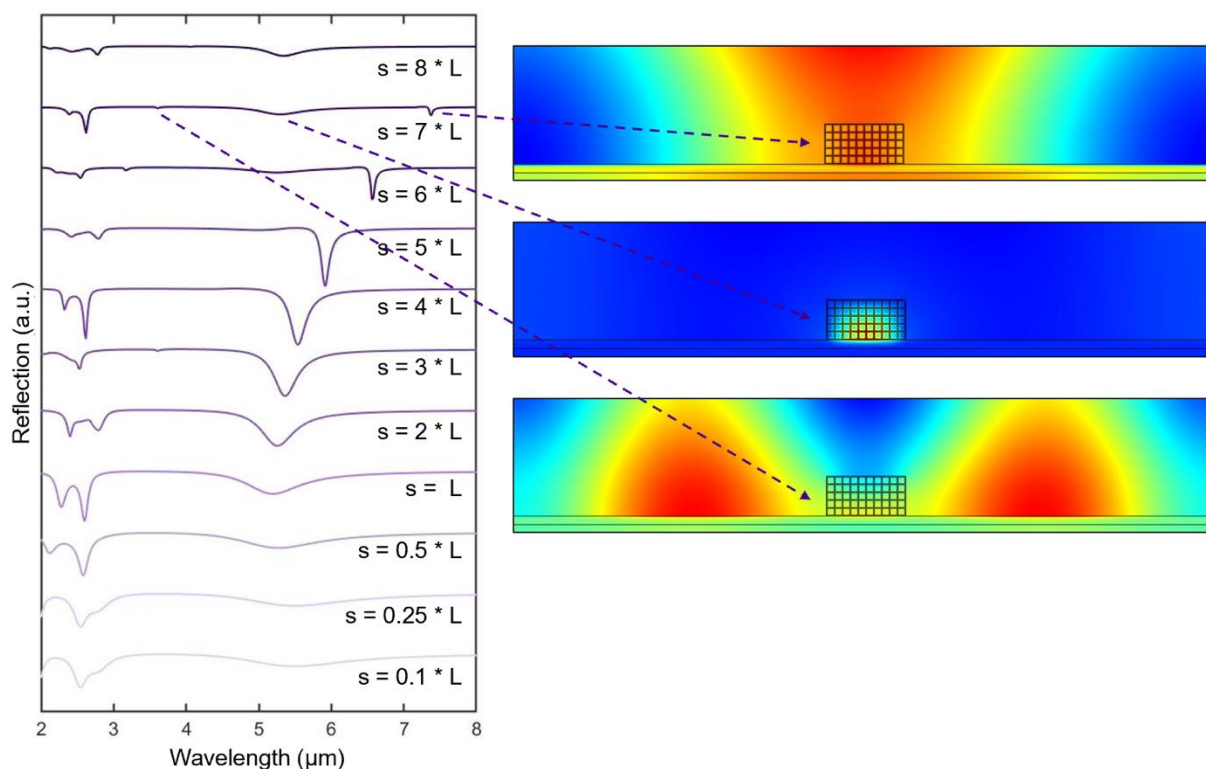
Figure 17-13. (left) Simulated reflection of metacrystal arrays with varying periodicities. L is the edge length of an individual metacrystal (900 nm), and s is the spacing between metacrystals. (right) Calculated magnetic field profile at various wavelengths including the first-order lattice mode, isolated Mie resonance, and second-order lattice mode.

Finally, we used electromagnetic simulations to explore using the spacing between metacrystals within an array as an additional degree of hierarchy to engineer optical properties. Specifically, we performed 2D simulations, modeling the SLs as an array of gold rods, infinitely extended in the z direction. The left panel of Figure 6-12 shows calculated reflection spectra of metacrystal arrays with varying periodicity. The figure shows the clear appearance of a dispersive lattice mode arising from the diffractive coupling between metacrystals, which shifts as a function of periodicity. For example, for a spacing, s, of 7*L, where L is the edge length of an individual metacrystal, the first-order lattice mode occurs at ~7.5 μm. This mode assignment is further supported by the magnetic field profile which shows a single node in magnetic field between metacrystals. The broad dip at ~5.5 μm is the isolated Mie resonance, where magnetic field is concentrated inside the metacrystals. A second-order lattice mode occurs at ~3.8 μm. Importantly, when the lattice mode is spectrally close to the isolated Mie resonance, they couple, as indicated by the sharpening of the resonance.

6.4 Conclusions

In conclusion, we studied the DNA-mediated crystallization of nanocubes under lateral confinement on substrates. We discovered that the combined use of DNA-functionalized substrates and microscale trenches enabled simultaneous control over in-plane and out-of-plane SL orientations as well as habit size, offering unprecedented architectural control in DNA-assembled SLs. In addition, ptychographic imaging of SLs revealed that the defect structure depends largely on trench size due to the nucleation, growth, and coalescence mechanism by which the SLs form. This work serves as a proof-of-concept demonstrating the use of lateral confinement in PAE systems and opens the door to further studies such as accessing low-symmetry crystals using incommensurate trench shapes or studies of size-dependent physical properties. Finally, we

showed that arrays of trench-grown SLs exhibit uniform mid-IR Mie resonances, which can be measured using tabletop FTIR.

6.5 Experimental Details
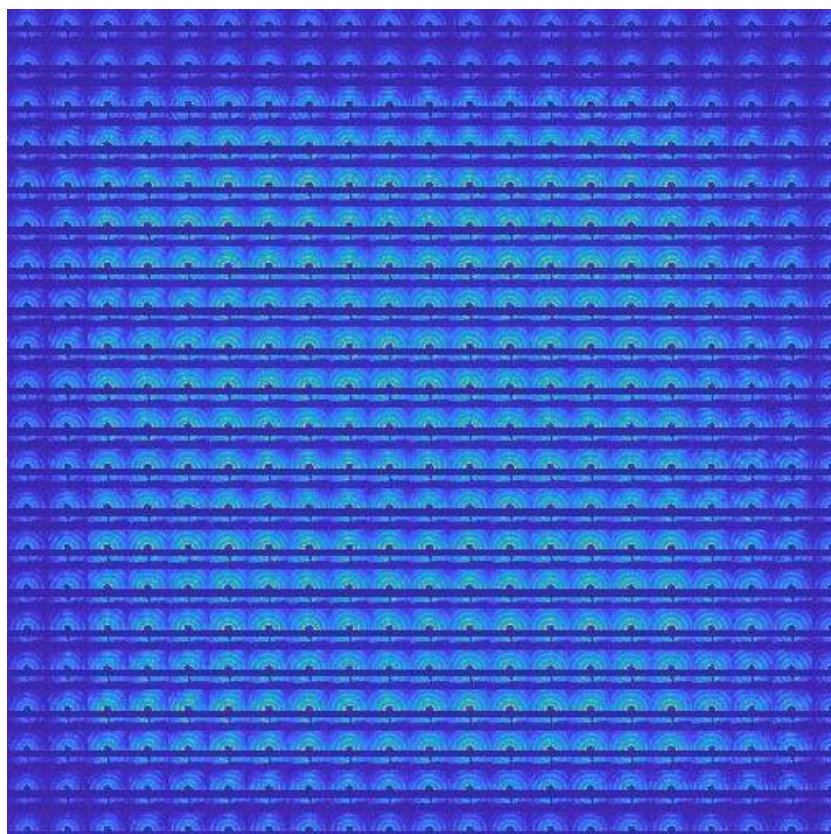
Figure 6-14. Stitched 2D SAXS patterns from a typical microfocus SAXS experiment. Each SAXS pattern is from a unique sample spot.
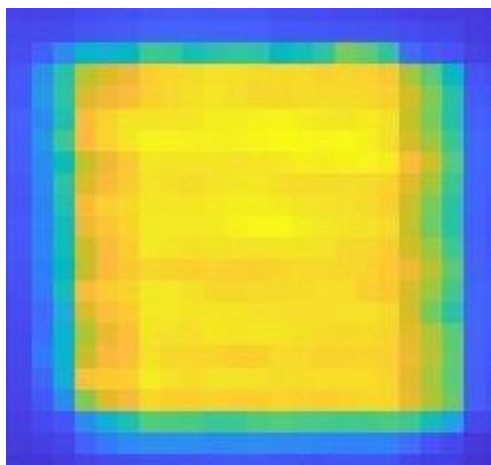
Figure 6-15. Integrated intensity map. Each pixel represents the integrated intensity over all pixels in a 2D SAXS pattern in Figure S2. The high intensity region (yellow) reflects strong diffraction from the sample area, while the weak intensity region (blue) is the background.

Large Area SEM Images
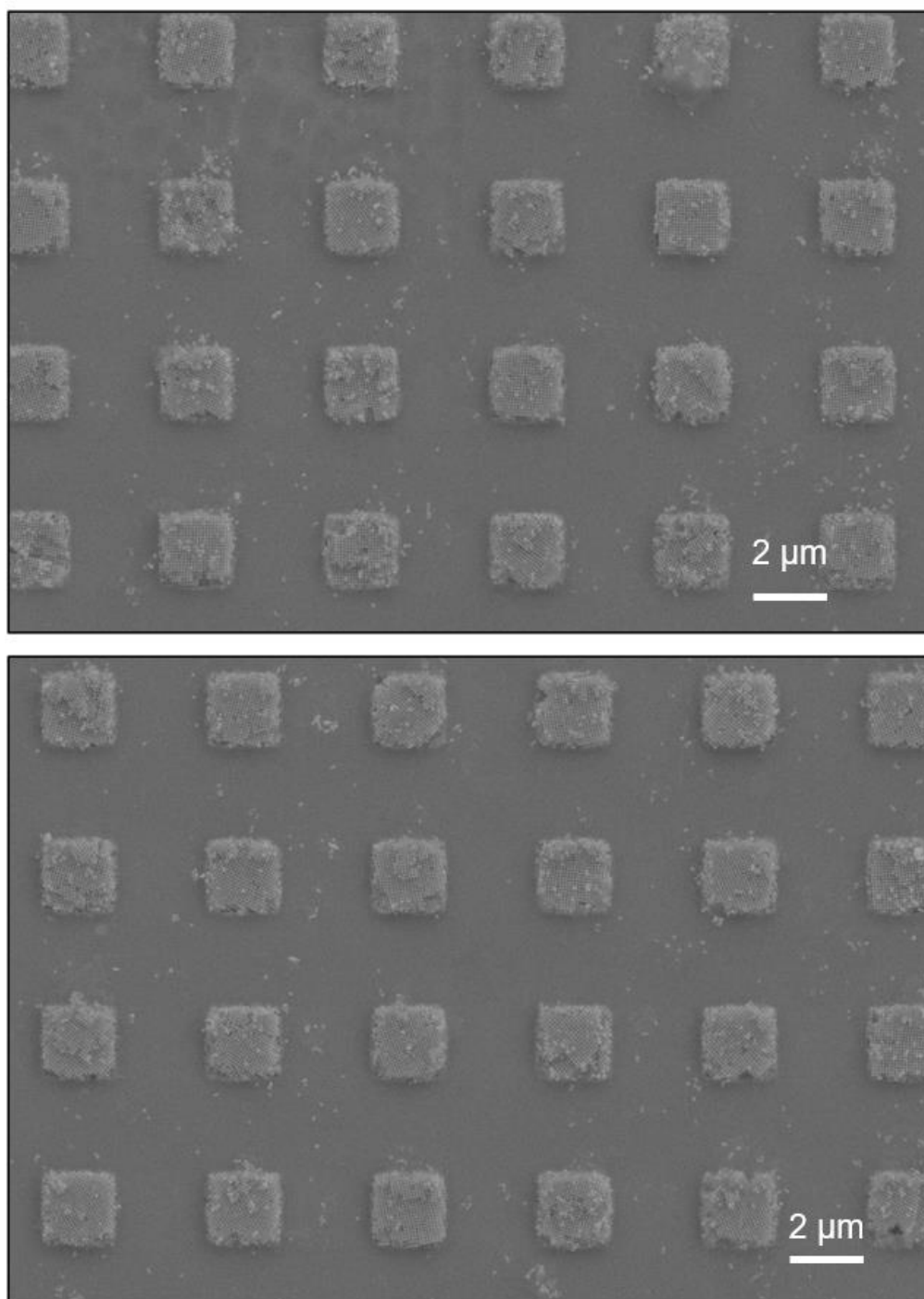
Figure 6-16. SEM images of arrays of 2 μm SLs grown in 0.3 M NaCl.
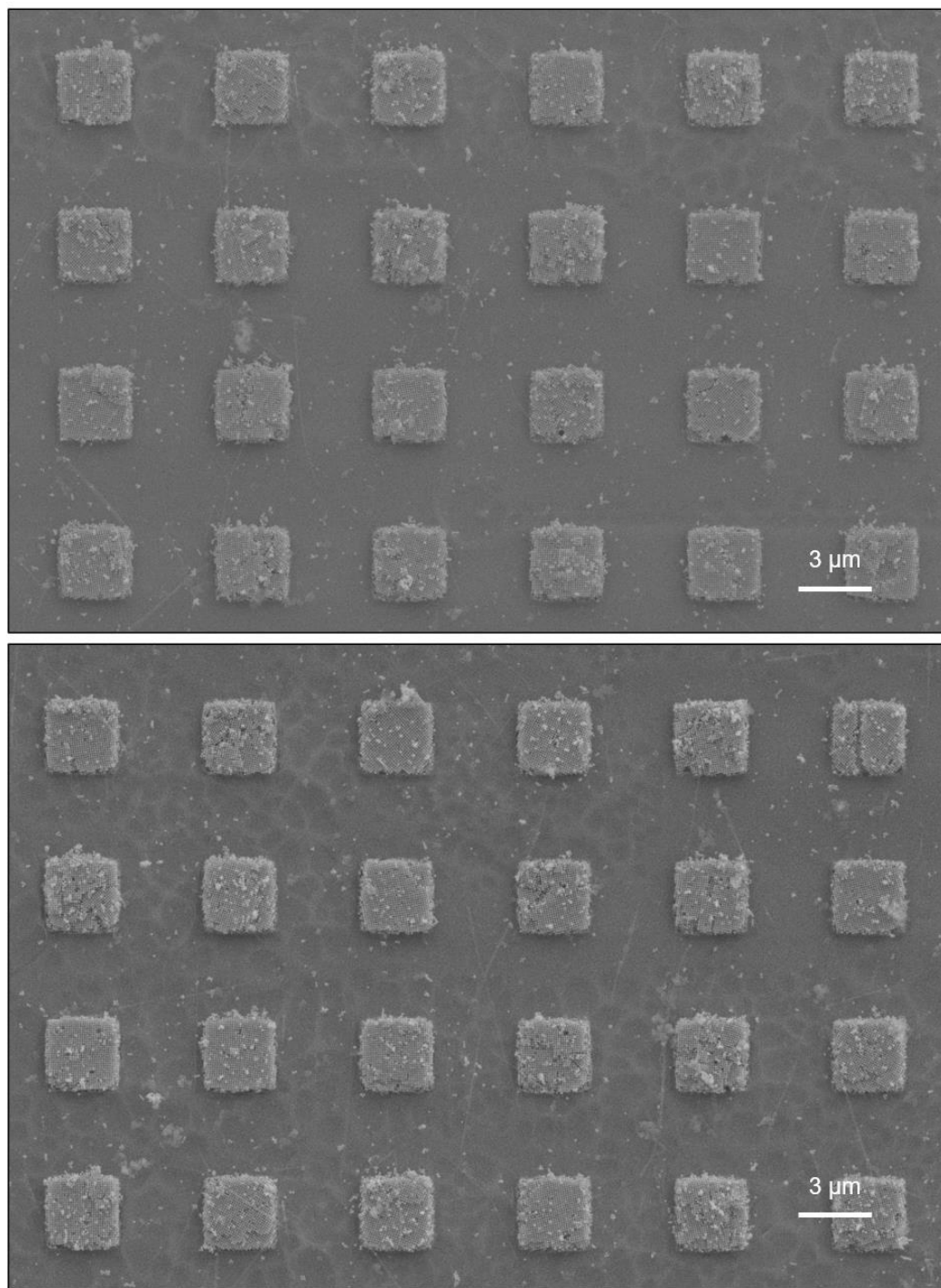
Figure 6-17. SEM images of arrays of 3 μm SLs grown in 0.3 M NaCl.
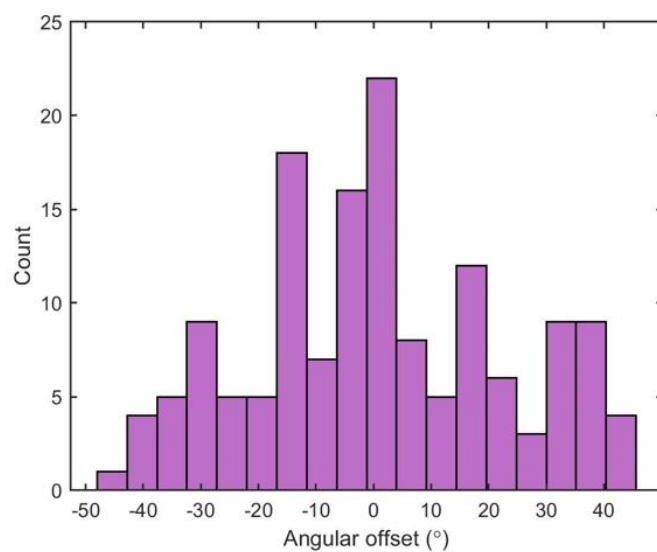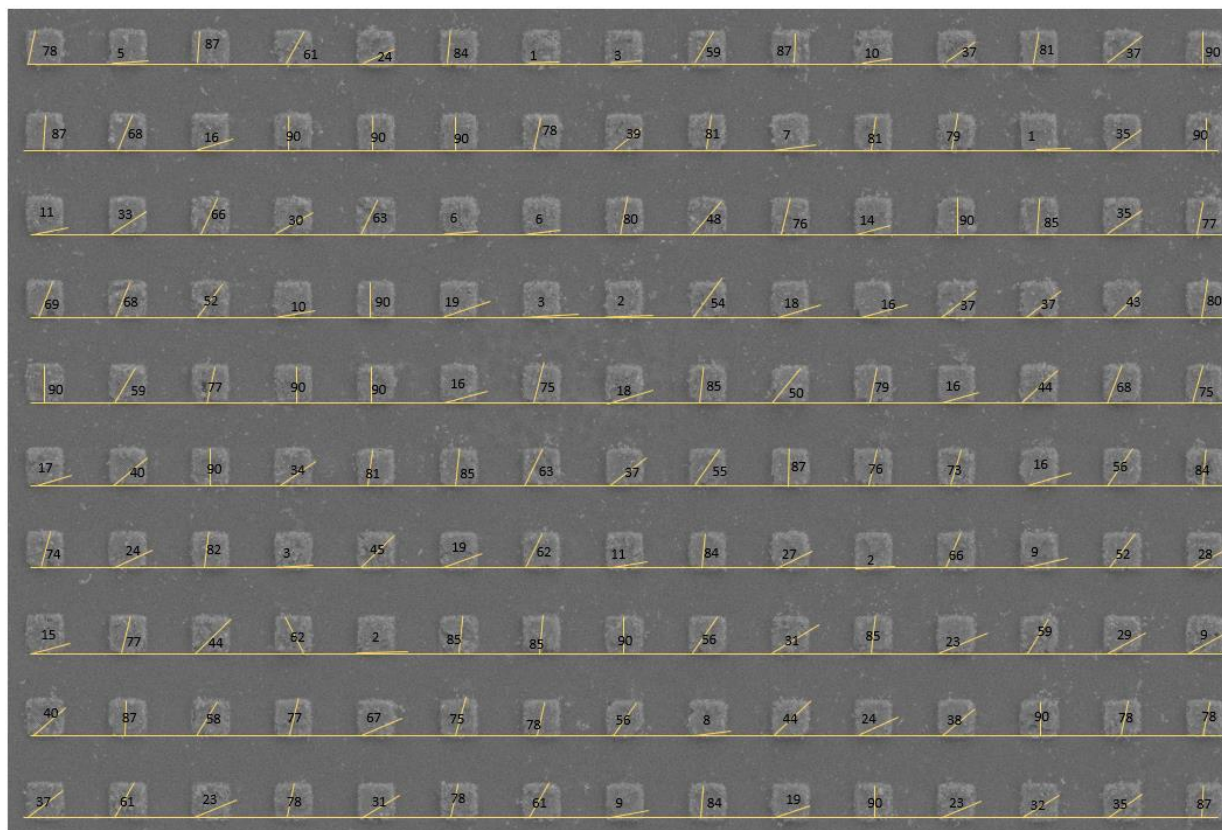
Figure 6-18. Orientation distribution of 2 μm SLs growin in 0.3 M NaCl, determined from SEM images. (top) SEM image of the measured sample area with lines drawn to show the superlattice orientation. (bottom) Histrogram of orientations (offset from 0°, representing {100} facets parallel to trench walls. Standard deviation: 22.79°.
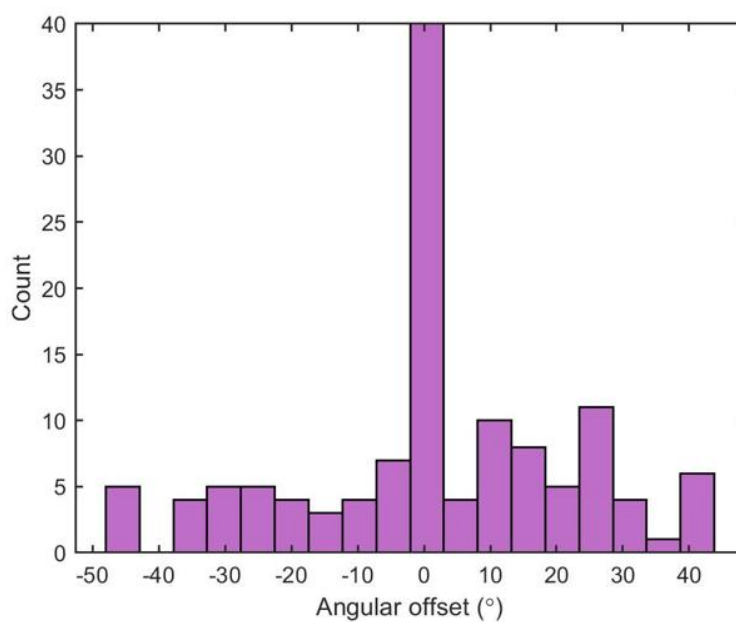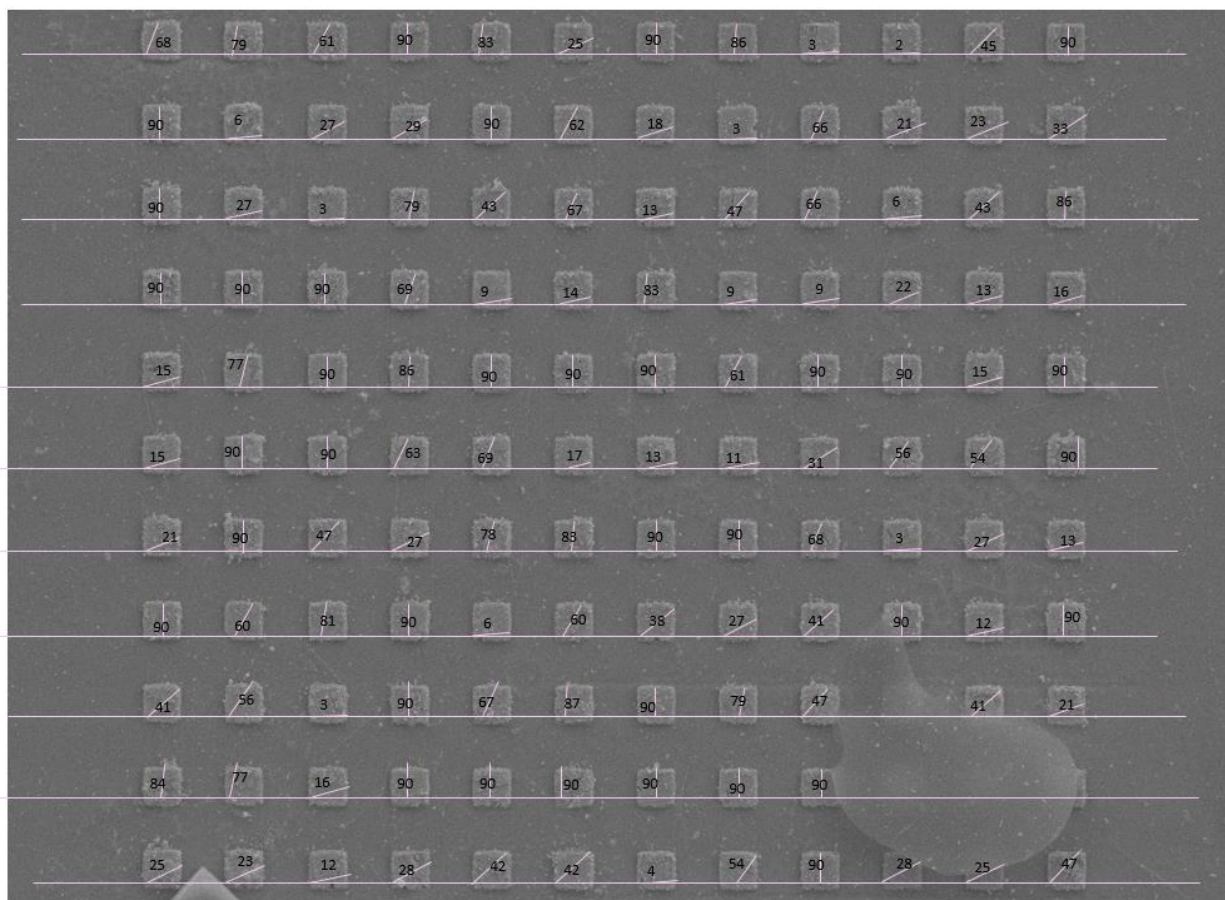
Figure 6-19. Orientation distribution of 3 μm SLs growin in 0.3 M NaCl, determined from SEM images. (top) SEM image of the measured sample area with lines drawn to show the superlattice orientation. (bottom) Histrogram of orientations (offset from 0°, representing {100} facets parallel to trench walls. Standard deviation: 20.77°.
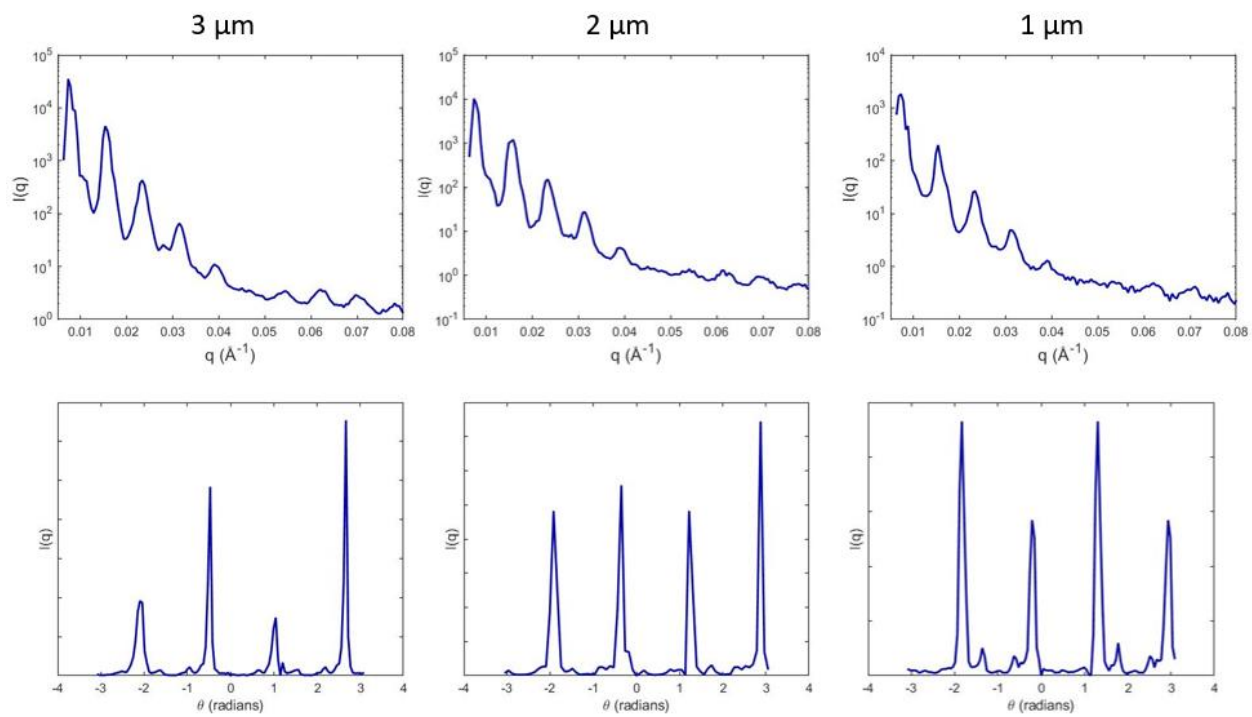
Figure 6-20. Azimuthal average and linecut.
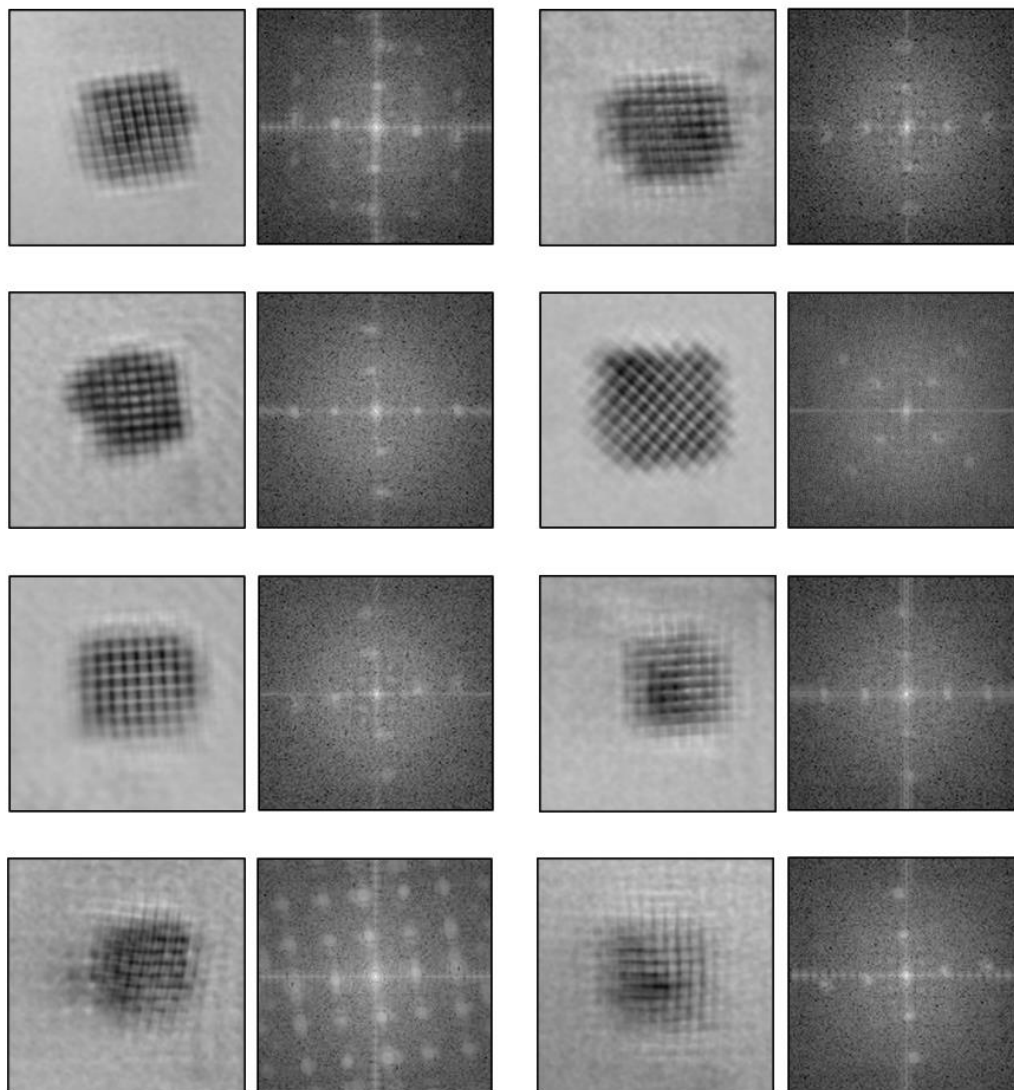
Figure 6-21. Side-by-side layout of ptychography reconstructions and their FFT patterns from typical SLs grown in 1 μm trenches.
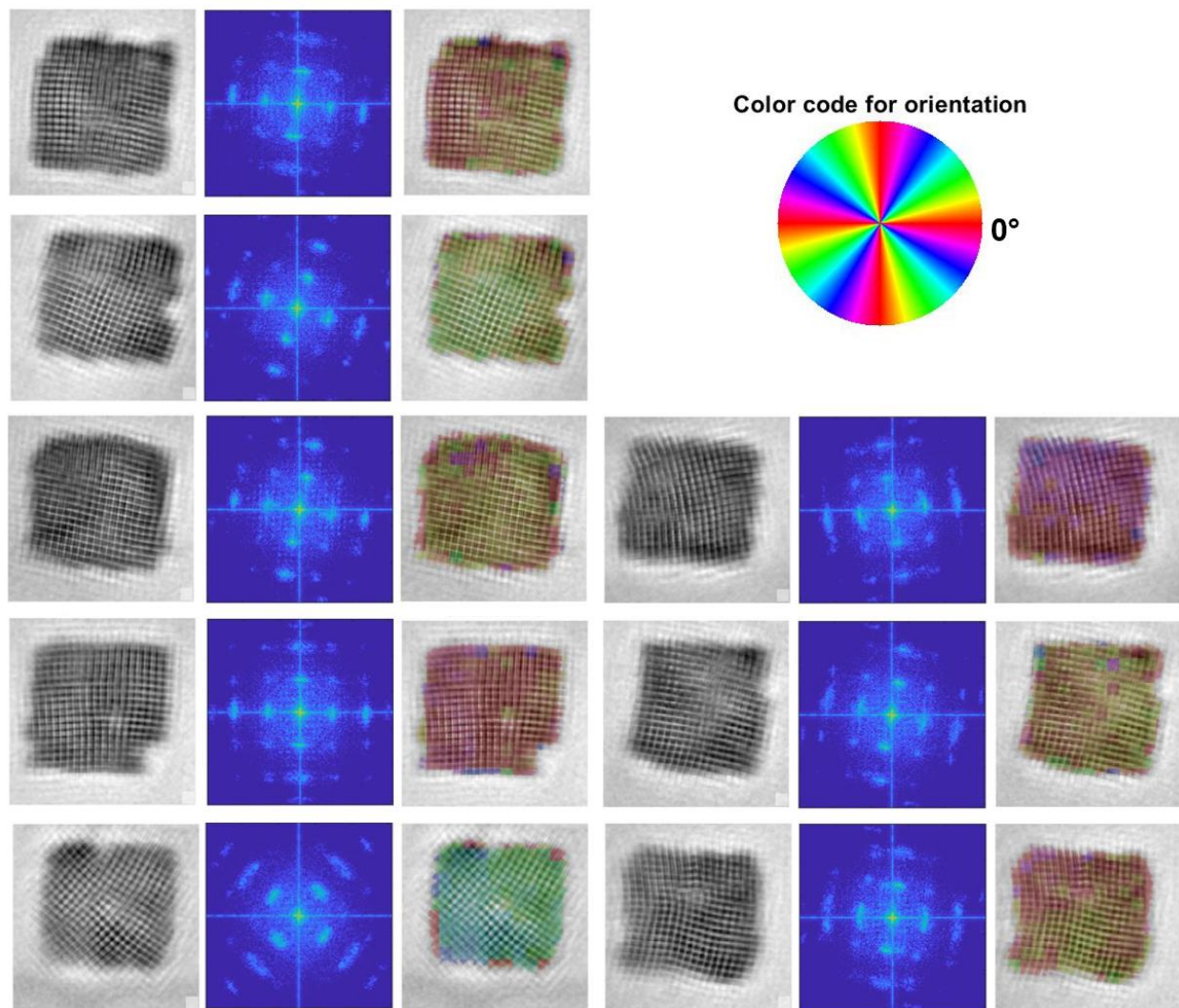
Figure 6-22. Ptychography data from typical SLs grown in 2 μm trenches. For each set, the ptychography reconstruction is on the left, FFT of ptychography reconstruction is in the middle, and orientation-based color overlay is on the right.
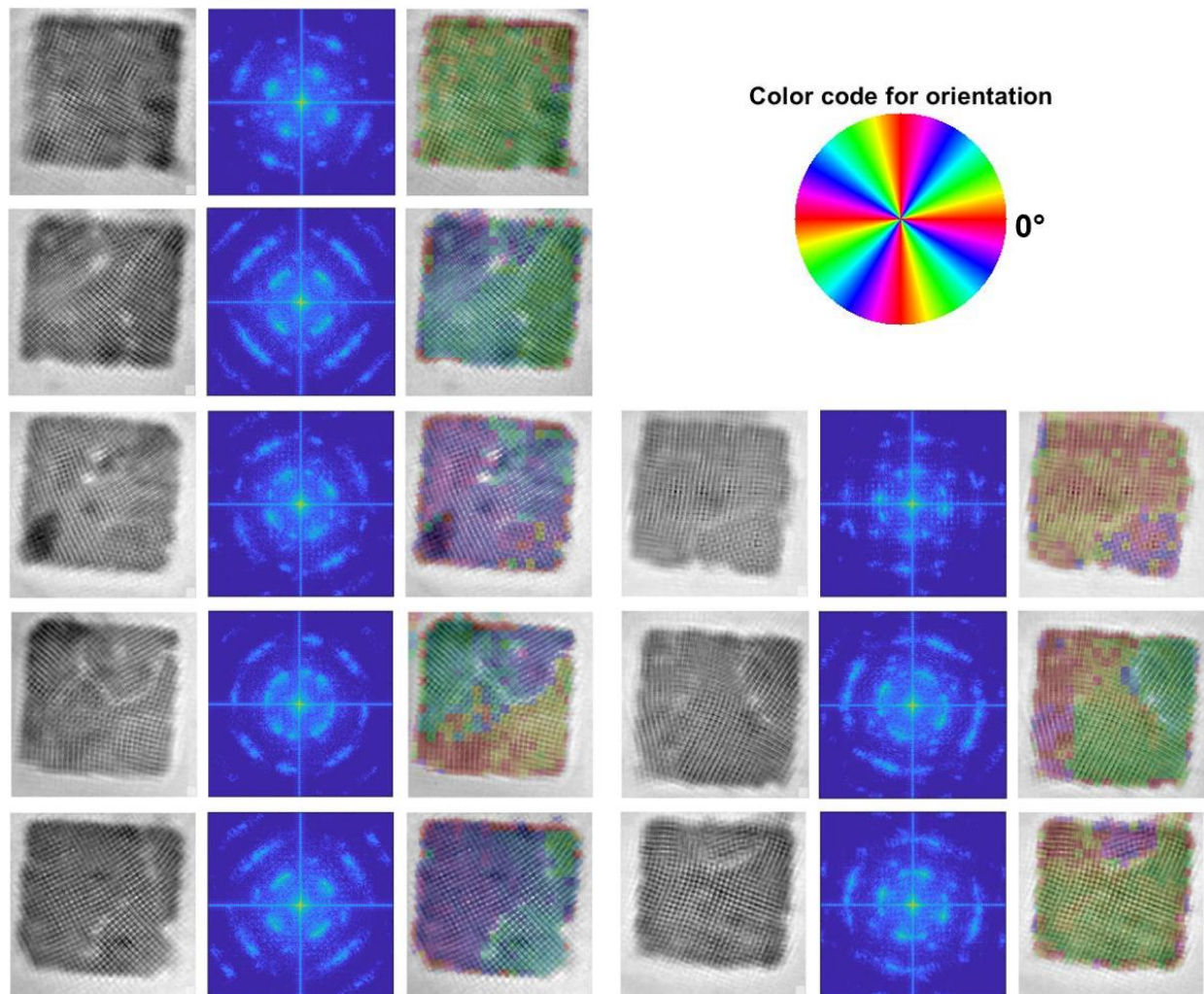
Figure 6-23. Ptychography data from typical SLs grown in 3 μm trenches. For each set, the ptychography reconstruction is on the left, FFT of ptychography reconstruction is in the middle, and orientation-based color overlay is on the right.
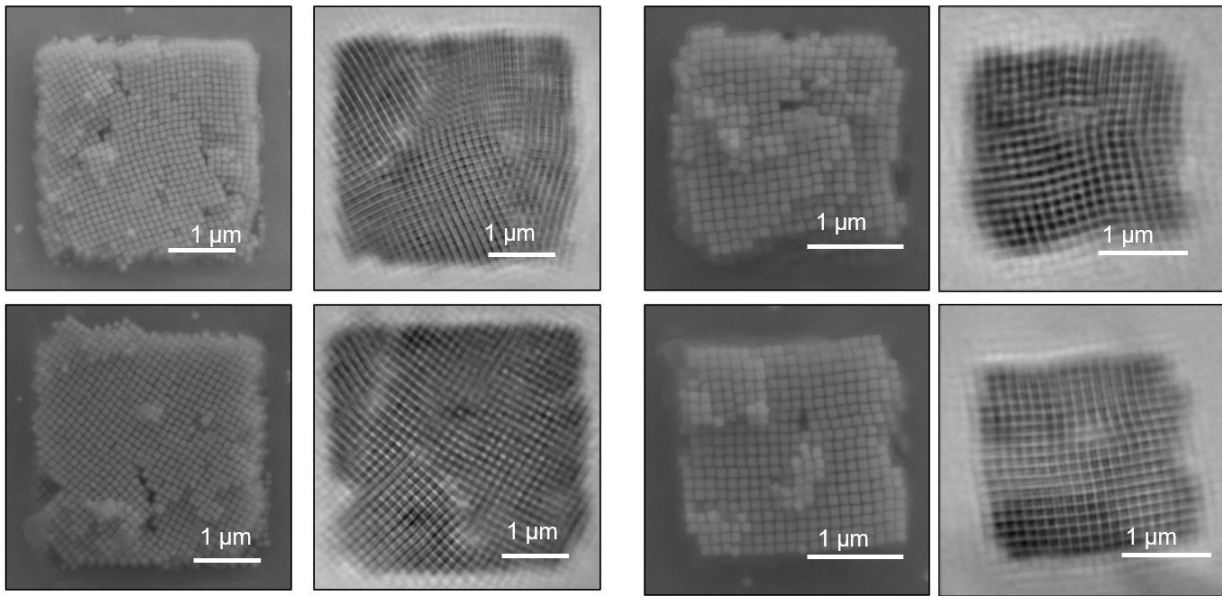
Figure 6-24. Examples of SLs exhibiting curved PAE rows which connect neighboring grains across a grain boundary, making it difficult to determine the precise locations of grain boundaries.

CHAPTER 7

Conclusions and Future Remarks

The scalable fabrication of 3-dimensional (3D) optical metamaterials is a major challenge preventing metamaterials from progressing towards commercial applications. Towards this end, colloidal crystal engineering with DNA represents a versatile method to scalably fabricate 3D, crystalline metamaterials with emergent optical properties, as detailed in this thesis. Although many unique and structurally sophisticated materials have been assembled using this technique, some of which have been shown to be optically active, advances in the targeted synthesis of superlattices with desired optical properties are few. Indeed, most of the previous studies of optically-active colloidal crystals involve uncovering the optical response of already available materials, mainly due to their ease of synthesis.

In my thesis work, I sought to advance to colloidal metamaterials assembled with DNA by taking a materials-by-design approach. Specifically, I developed new synthetic approaches to assemble previously unattainable structures which are designed using electromagnetics simulations and theory to exhibit targeted metamaterials responses. Notably, most of the work in this thesis (Chapters 2, 3, 5, 6) centered on metamaterials made from capacitively-coupled anisotropic nanoparticles which exhibit extreme field confinements and ultrahigh refractive indices. Within this thesis, studies of these capacitively-coupled nanostructures across three dimensionalities were discussed. First, arrays of isolated nanocube-on-mirror cavities were used to enhance the emission from embedded dye molecules. Next, a new synthetic method to assemble highly crystalline, 2-dimensional arrays of nanocubes on a metallic film were discussed. These films were designed to behave as epsilon-near-zero (ENZ) metasurfaces, with ENZ conditions tunable throughout the near-IR regime. Finally, novel methods to assemble densely packed 3D

nanocube superlattices with high crystallinity and uniformity were developed. Using electromagnetics simulations and FTIR measurement, we discovered that the superlattices behaved as high-refractive index dielectrics, which gave rise to tunable Mie resonances when confined in cube-shaped microscale habits. Furthermore, the 3D metamaterials could be grown over macroscopic areas and shaped, using lithographically-patterned trenches, into discrete microscale superlattices. Notably, this technique enabled arrays of high refractive index superlattices to be synthesized, introducing another degree of hierarchy to the design of colloidal metamaterials. Taken together, the work in this thesis lays the framework for scalably fabricating metamaterials using colloidal nanoparticles and proposes several potential applications based on their emergent optical properties.

Moving forward, arrays of metacrystals could be designed to exhibit hierarchical optical properties. For example, in Chapter 6 of this thesis, we predicted that arrays of metacrystals could give rise to diffractive lattice modes, which can couple with Mie-resonances to produce near-perfect absorption. Additionally, in Chapter 3, we proposed a negative refractive index material made from arrays of cuboid-shaped metacrystals.

Beyond this thesis work, the versatility of DNA-mediated assembly could enable the design and assembly of a virtually endless number of novel metamaterials with targeted optical responses. For example, the nanoparticle core can be changed to those of other shapes, sizes, or compositions. In addition, "alloys" of multiple nanoparticle cores could introduce more complex coupling in plasmonic superlattices. Dielectric nanoparticles, such as those made from SiO_2 or TiO_2 which sustain magnetic resonances, could act as magnetic meta-atoms. When these are assembled together with plasmonic nanoparticles with electric resonances, the resultant superlattices could exhibit negative refractive indices in the visible regime.

In another application, discrete 2- and 3D superlattices could be assembled together on a patterned substrate into an integrated photonic microcircuit. In such a circuit, each individual superlattice structure performs its own optical function, acting for example as a laser, waveguide, amplifier, or detector. Together, these components can be designed to perform tasks using the transmission of light signals, which could become a much faster and lower power alternative to electronic circuits.

Finally, to aid the commercialization of devices made from colloidal metamaterials, future research should center around methods to incorporate earth-abundant plasmonic nanoparticles into DNA-assembled superlattices. For example, methods to synthesize aluminum nanoparticles with spherical and polyhedral shapes are currently being developed by Naomi Halas et al. The group found that aluminum nanoparticles are passivated with a thin oxide layer, rendering them stable against oxidation. The passivated particles retain the intense plasmonic properties of aluminum, making them promising building blocks for colloidal metamaterials. Future research will focus on synthesizing aluminum nanoparticles in high yield and with control over size and shape as well as developing methods to functionalize their oxide-passivated surfaces with DNA ligands.

References

(1) Chung, K.; Kim, R.; Chang, T.; Shin, J. Optical Effective Media with Independent Control of Permittivity and Permeability Based on Conductive Particles. *Appl. Phys. Lett.* **2016**, *109* (2), 21114. https://doi.org/10.1063/1.4958987.

(2) Soukoulis, C. M.; Wegener, M. Past Achievements and Future Challenges in the Development of Three-Dimensional Photonic Metamaterials. *Nat. Photonics* **2011**, *5* (9), 523–530. https://doi.org/10.1038/nphoton.2011.154.

(3) West, P. R.; Ishii, S.; Naik, G. V.; Emani, N. K.; Shalaev, V. M.; Boltasseva, A. Searching for Better Plasmonic Materials. *Laser Photonics Rev.* **2010**, *4* (6), 795–808. https://doi.org/10.1002/lpor.200900055.

(4) Wu, C.; Arju, N.; Kelp, G.; Fan, J. A.; Dominguez, J.; Gonzales, E.; Tutuc, E.; Brener, I.; Shvets, G. Spectrally Selective Chiral Silicon Metasurfaces Based on Infrared Fano Resonances. *Nat. Commun.* **2014**, *5* (May), 1–9. https://doi.org/10.1038/ncomms4892.

(5) Hanske, C.; Tebbe, M.; Kuttner, C.; Bieber, V.; Tsukruk, V. V.; Chanana, M.; König, T. A. F.; Fery, A. Strongly Coupled Plasmonic Modes on Macroscopic Areas via Template-Assisted Colloidal Self-Assembly. *Nano Lett.* **2014**, *14* (12), 6863–6871. https://doi.org/10.1021/nl502776s.

(6) Liu, N.; Giessen, H. Coupling Effects in Optical Metamaterials. *Angew. Chemie - Int. Ed.* **2010**, *49* (51), 9838–9852. https://doi.org/10.1002/anie.200906211.

(7) Vassant, S.; Hugonin, J.-P.; Marquier, F.; Greffet, J.-J. Berreman Mode and Epsilon near Zero Mode. *Opt. Express* **2012**, *20* (21), 23971–23977. https://doi.org/10.1364/OE.20.023971.

(8) Huh, J. H.; Kim, K.; Im, E.; Lee, J.; Cho, Y. D.; Lee, S. Exploiting Colloidal Metamaterials for Achieving Unnatural Optical Refractions. *Adv. Mater.* **2020**, *32* (51), 1–23. https://doi.org/10.1002/adma.202001806.

(9) Meinzer, N.; Barnes, W. L.; Hooper, I. R. Plasmonic Meta-Atoms and Metasurfaces. *Nat. Photonics* **2014**, *8* (12), 889–898. https://doi.org/10.1038/nphoton.2014.247.

(10) Smith, D. R.; Vier, D. C.; Koschny, T.; Soukoulis, C. M. Electromagnetic Parameter Retrieval from Inhomogeneous Metamaterials. *Phys. Rev. E* **2005**, *71* (3), 36617. https://doi.org/10.1103/PhysRevE.71.036617.

(11) Chen, H. T.; Padilla, W. J.; Zide, J. M. O.; Gossard, A. C.; Taylor, A. J.; Averitt, R. D. Active Terahertz Metamaterial Devices. *Nature* **2006**, *444* (7119), 597–600. https://doi.org/10.1038/nature05343.

(12) Tao, H.; Bingham, C. M.; Pilon, D.; Fan, K.; Strikwerda, A. C.; Shrekenhamer, D.; Padilla, W. J.; Zhang, X.; Averitt, R. D. A Dual Band Terahertz Metamaterial Absorber. *J. Phys. D. Appl. Phys.* **2010**, *43* (22). https://doi.org/10.1088/0022-3727/43/22/225102.

(13) Zhu, J.; Ma, Z.; Sun, W.; Ding, F.; He, Q.; Zhou, L.; Ma, Y. Ultra-Broadband Terahertz Metamaterial Absorber. *Appl. Phys. Lett.* **2014**, *105* (2). https://doi.org/10.1063/1.4890521.

(14) Tao, H.; Bingham, C. M.; Strikwerda, A. C.; Pilon, D.; Shrekenhamer, D.; Landy, N. I.; Fan, K.; Zhang, X.; Padilla, W. J.; Averitt, R. D. Highly Flexible Wide Angle of Incidence Terahertz

Metamaterial Absorber: Design, Fabrication, and Characterization. *Phys. Rev. B - Condens. Matter Mater. Phys.* **2008**, *78* (24), 2–5. https://doi.org/10.1103/PhysRevB.78.241103.

(15)   Choi, M.; Lee, S. H.; Kim, Y.; Kang, S. B.; Shin, J.; Kwak, M. H.; Kang, K. Y.; Lee, Y. H.; Park, N.; Min, B. A Terahertz Metamaterial with Unnaturally High Refractive Index. *Nature* **2011**, *470* (7334), 369–373. https://doi.org/10.1038/nature09776.

(16)   Alici, K. B.; Ozbay, E. Electrically Small Split Ring Resonator Antennas. *J. Appl. Phys.* **2007**, *101* (8), 1–5. https://doi.org/10.1063/1.2722232.

(17)   Martín, F.; Bonache, J.; Falcone, F.; Sorolla, M.; Marqués, R. Split Ring Resonator-Based Left-Handed Coplanar Waveguide. *Appl. Phys. Lett.* **2003**, *83* (22), 4652–4654. https://doi.org/10.1063/1.1631392.

(18)   Rockstuhl, C.; Zentgraf, T.; Guo, H.; Liu, N.; Etrich, C.; Loa, I.; Syassen, K.; Kuhl, J.; Lederer, F.; Giessen, H. Resonances of Split-Ring Resonator Metamaterials in the near Infrared. *Appl. Phys. B Lasers Opt.* **2006**, *84* (1–2), 219–227. https://doi.org/10.1007/s00340-006-2205-2.

(19)   Enkrich, C.; Wegener, M.; Linden, S.; Burger, S.; Zschiedrich, L.; Schmidt, F.; Zhou, J. F.; Koschny, T.; Soukoulis, C. M. Magnetic Metamaterials at Telecommunication and Visible Frequencies. *Phys. Rev. Lett.* **2005**, *95* (20), 5–8. https://doi.org/10.1103/PhysRevLett.95.203901.

(20)   Burgos, S. P.; De Waele, R.; Polman, A.; Atwater, H. A. A Single-Layer Wide-Angle Negative-Index Metamaterial at Visible Frequencies. *Nat. Mater.* **2010**, *9* (5), 407–412. https://doi.org/10.1038/nmat2747.

(21)   Smith, D. R.; Pendry, J. B.; Wiltshire, M. C. K. Metamaterials and Negative Refractive Index. *Science (80-.).* **2004**, *305* (5685), 788–792. https://doi.org/10.1126/science.1096796.

(22)   Wuestner, S.; Pusch, A.; Tsakmakidis, K. L.; Hamm, J. M.; Hess, O. Overcoming Losses with Gain in a Negative Refractive Index Metamaterial. *Phys. Rev. Lett.* **2010**, *105* (12), 1–4. https://doi.org/10.1103/PhysRevLett.105.127401.

(23)   Shelby, R. A.; Smith, D. R.; Schultz, S. Experimental Verification of a Negative Index of Refraction. *Science (80-.).* **2001**, *292* (5514), 77–79. https://doi.org/10.1126/science.1058847.

(24)   Hasan, R. M. M.; Luo, X. Promising Lithography Techniques for Next-Generation Logic Devices. *Nanomanufacturing Metrol.* **2018**, *1* (2), 67–81. https://doi.org/10.1007/s41871-018-0016-9.

(25)   Manouras, T.; Argitis, P. High Sensitivity Resists for EUV Lithography: A Review of Material Design Strategies and Performance Results. *Nanomaterials* **2020**, *10* (8), 1–24. https://doi.org/10.3390/nano10081593.

(26)   Monti, A.; Bilotti, F.; Toscano, A. Optical Cloaking of Cylindrical Objects by Using Covers Made of Core–Shell Nanoparticles. *Opt. Lett.* **2011**, *36* (23), 4479. https://doi.org/10.1364/ol.36.004479.

(27)   Smolyaninov, I. I.; Smolyaninova, V. N.; Kildishev, A. V.; Shalaev, V. M. Anisotropic Metamaterials Emulated by Tapered Waveguides: Application to Optical Cloaking. *Phys. Rev. Lett.* **2009**, *102* (21), 1–4. https://doi.org/10.1103/PhysRevLett.102.213901.

(28)   Cai, W.; Chettiar, U. K.; Kildishev, A. V.; Shalaev, V. M. Designs for Optical Cloaking with High-Order Transformations. *Opt. Express* **2008**, *16* (8), 5444. https://doi.org/10.1364/oe.16.005444.

(29)   Nie, G.; Shi, Q.; Zhu, Z.; Shi, J. Selective Coherent Perfect Absorption in Metamaterials. *Appl. Phys. Lett.* **2014**, *105* (20). https://doi.org/10.1063/1.4902330.

(30)   Duan, G.; Schalch, J.; Zhao, X.; Zhang, J.; Averitt, R. D.; Zhang, X. Identifying the Perfect Absorption of Metamaterial Absorbers. *Phys. Rev. B* **2018**, *97* (3), 4–10. https://doi.org/10.1103/PhysRevB.97.035128.

(31)   Wang, X.; Luo, X.; Zhao, H.; Huang, Z. Acoustic Perfect Absorption and Broadband Insulation Achieved by Double-Zero Metamaterials. *Appl. Phys. Lett.* **2018**, *112* (2). https://doi.org/10.1063/1.5018180.

(32)   Qin, J.; Deng, L.; Kang, T.; Nie, L.; Feng, H.; Wang, H.; Yang, R.; Liang, X.; Tang, T.; Shen, J.; Li, C.; Wang, H.; Luo, Y.; Armelles, G.; Bi, L. Switching the Optical Chirality in Magnetoplasmonic Metasurfaces Using Applied Magnetic Fields. *ACS Nano* **2020**, *14* (3), 2808–2816. https://doi.org/10.1021/acsnano.9b05062.

(33)   Gorkunov, M. V.; Antonov, A. A.; Kivshar, Y. S. Metasurfaces with Maximum Chirality Empowered by Bound States in the Continuum. *Phys. Rev. Lett.* **2020**, *125* (9), 93903. https://doi.org/10.1103/PhysRevLett.125.093903.

(34)   Fang, N.; Lee, H.; Sun, C.; Zhang, X. Sub-Diffraction-Limited Optical Imaging with a Silver Superlens. *Science* **2005**, *308* (5721), 534–537. https://doi.org/10.1126/science.1108759.

(35)   Xiao, S.; Wang, T.; Liu, T.; Zhou, C.; Jiang, X.; Zhang, J. Active Metamaterials and Metadevices: A Review. *J. Phys. D. Appl. Phys.* **2020**, *53* (50). https://doi.org/10.1088/1361-6463/abaced.

(36)   Zheludev, N. I.; Kivshar, Y. S. From Metamaterials to Metadevices. *Nat. Mater.* **2012**, *11* (11), 917–924. https://doi.org/10.1038/nmat3431.

(37)   Zhu, J.; Han, J.; Tian, Z.; Gu, J.; Chen, Z.; Zhang, W. Thermal Broadband Tunable Terahertz Metamaterials. *Opt. Commun.* **2011**, *284* (12), 3129–3133. https://doi.org/10.1016/j.optcom.2011.02.038.

(38)   Pitchappa, P.; Manjappa, M.; Krishnamoorthy, H. N. S.; Chang, Y.; Lee, C.; Singh, R. Bidirectional Reconfiguration and Thermal Tuning of Microcantilever Metamaterial Device Operating from 77 K to 400 K. *Appl. Phys. Lett.* **2017**, *111* (26). https://doi.org/10.1063/1.5006836.

(39)   Arbabi, E.; Arbabi, A.; Kamali, S. M.; Horie, Y.; Faraji-Dana, M. S.; Faraon, A. MEMS-Tunable Dielectric Metasurface Lens. *Nat. Commun.* **2018**, *9* (1). https://doi.org/10.1038/s41467-018-03155-6.

(40)   Roy, T.; Zhang, S.; Jung, I. W.; Troccoli, M.; Capasso, F.; Lopez, D. Dynamic Metasurface Lens Based on MEMS Technology. *APL Photonics* **2018**, *3* (2). https://doi.org/10.1063/1.5018865.

(41)   Manjappa, M.; Pitchappa, P.; Singh, N.; Wang, N.; Zheludev, N. I.; Lee, C.; Singh, R. Reconfigurable MEMS Fano Metasurfaces with Multiple-Input–Output States for Logic Operations at Terahertz Frequencies. *Nat. Commun.* **2018**, *9* (1), 1–10. https://doi.org/10.1038/s41467-018-06360-5.

(42)   Fan, K.; Padilla, W. J. Dynamic Electromagnetic Metamaterials. *Mater. Today* **2015**, *18* (1), 39–50. https://doi.org/10.1016/j.mattod.2014.07.010.

(43)   Markel, V. A. Introduction to the Maxwell Garnett Approximation: Tutorial. *J. Opt. Soc. Am. A*

2016, *33* (7), 1244. https://doi.org/10.1364/josaa.33.001244.

(44) Paula, A. L. de; Rezende, M. C.; Barroso, J. J. Modified Nicolson-Ross-Weir (NRW) Method to Retrieve the Constitutive Parameters of Low-Loss Materials. In *2011 SBMO/IEEE MTT-S International Microwave and Optoelectronics Conference (IMOC 2011)*; 2011; pp 488–492. https://doi.org/10.1109/IMOC.2011.6169293.

(45) Shalaev, V. M. Optical Negative-Index Metamaterials. *6*, 41–48.

(46) Zhou, J.; Koschny, T.; Kafesaki, M.; Economou, E. N.; Pendry, J. B.; Soukoulis, C. M. Saturation of the Magnetic Response of Split-Ring Resonators at Optical Frequencies. *Phys. Rev. Lett.* **2005**, *95* (22). https://doi.org/10.1103/PhysRevLett.95.223902.

(47) Landy, N. I.; Bingham, C. M.; Tyler, T.; Jokerst, N.; Smith, D. R.; Padilla, W. J. Design, Theory, and Measurement of a Polarization-Insensitive Absorber for Terahertz Imaging. *Phys. Rev. B - Condens. Matter Mater. Phys.* **2009**, *79* (12), 1–6. https://doi.org/10.1103/PhysRevB.79.125104.

(48) Dolling, G.; Enrich, C.; Wegener, M.; Soukoulis, C. M.; Linden, S. Low-Loss Negative-Index Metamaterial at Telecommunication Wavelengths. *Opt. Lett.* **2006**, *31* (12), 1800. https://doi.org/10.1364/ol.31.001800.

(49) Moitra, P.; Yang, Y.; Anderson, Z.; Kravchenko, I. I.; Briggs, D. P.; Valentine, J. Realization of an All-Dielectric Zero-Index Optical Metamaterial. *Nat. Photonics* **2013**, *7* (10), 791–795. https://doi.org/10.1038/nphoton.2013.214.

(50) Arai, N.; Watanabe, S.; Miyahara, M. T. On the Convective Self-Assembly of Colloidal Particles in Nanofluid Based on in Situ Measurements of Interaction Forces. *Langmuir* **2019**, *35* (35), 11533–11541. https://doi.org/10.1021/acs.langmuir.9b00811.

(51) Young, K. L.; Jones, M. R.; Zhang, J.; Macfarlane, R. J.; Esquivel-Sirvent, R.; Nap, R. J.; Wu, J.; Schatz, G. C.; Lee, B.; Mirkin, C. A. Assembly of Reconfigurable One-Dimensional Colloidal Superlattices Due to a Synergy of Fundamental Nanoscale Forces. *Proc. Natl. Acad. Sci. U. S. A.* **2012**, *109* (7), 2240–2245. https://doi.org/10.1073/pnas.1119301109.

(52) Liu, M.; Zheng, X.; Grebe, V.; Pine, D. J.; Weck, M. Tunable Assembly of Hybrid Colloids Induced by Regioselective Depletion. *Nat. Mater.* **2020**, *19* (12), 1354–1361. https://doi.org/10.1038/s41563-020-0744-2.

(53) Baranov, D.; Fiore, A.; Van Huis, M.; Giannini, C.; Falqui, A.; Lafont, U.; Zandbergen, H.; Zanella, M.; Cingolani, R.; Manna, L. Assembly of Colloidal Semiconductor Nanorods in Solution by Depletion Attraction. *Nano Lett.* **2010**, *10* (2), 743–749. https://doi.org/10.1021/nl903946n.

(54) Laramy, C. R.; O'Brien, M. N.; Mirkin, C. A. Crystal Engineering with DNA. *Nat. Rev. Mater.* **2019**, *4* (3), 201–224. https://doi.org/10.1038/s41578-019-0087-2.

(55) Tao, A.; Sinsermsuksakul, P.; Yang, P. Tunable Plasmonic Lattices of Silver Nanocrystals. *Nat. Nanotechnol.* **2007**, *2* (7), 435–440. https://doi.org/10.1038/nnano.2007.189.

(56) Wuithschick, M.; Birnbaum, A.; Witte, S.; Sztucki, M.; Vainio, U.; Pinna, N.; Rademann, K.; Emmerling, F.; Kraehnert, R.; Polte, J. Turkevich in New Robes: Key Questions Answered for the Most Common Gold Nanoparticle Synthesis. *ACS Nano* **2015**, *9* (7), 7052–7071. https://doi.org/10.1021/acsnano.5b01579.

(57) Zhao, P.; Li, N.; Astruc, D. State of the Art in Gold Nanoparticle Synthesis. *Coord. Chem. Rev.*

2013, *257* (3–4), 638–665. https://doi.org/10.1016/j.ccr.2012.09.002.

(58)   Grieve, K.; Mulvaney, P.; Grieser, F. Synthesis and Electronic Properties of Semiconductor Nanoparticles/Quantum Dots. *Curr. Opin. Colloid Interface Sci.* **2000**, *5* (1–2), 168–172. https://doi.org/10.1016/S1359-0294(00)00050-9.

(59)   Cobley, C. M.; Skrabalak, S. E.; Campbell, D. J.; Xia, Y. Shape-Controlled Synthesis of Silver Nanoparticles for Plasmonic and Sensing Applications. *Plasmonics* **2009**, *4* (2), 171–179. https://doi.org/10.1007/s11468-009-9088-0.

(60)   Herricks, T.; Chen, J.; Xia, Y. Polyol Synthesis of Platinum Nanoparticles: Control of Morphology with Sodium Nitrate. *Nano Lett.* **2004**, *4* (12), 2367–2371. https://doi.org/10.1021/nl048570a.

(61)   Gole, A.; Murphy, C. J. Seed-Mediated Synthesis of Gold Nanorods: Role of the Size and Nature of the Seed. *Chem. Mater.* **2004**, *16* (19), 3633–3640. https://doi.org/10.1021/cm0492336.

(62)   Jana, N. R.; Gearheart, L.; Murphy, C. J. Evidence for Seed-Mediated Nucleation in the Chemical Reduction of Gold Salts to Gold Nanoparticles. *Chem. Mater.* **2001**, *13* (7), 2313–2322. https://doi.org/10.1021/cm000662n.

(63)   O'Brien, M. N.; Jones, M. R.; Brown, K. A.; Mirkin, C. A. Universal Noble Metal Nanoparticle Seeds Realized through Iterative Reductive Growth and Oxidative Dissolution Reactions. *J. Am. Chem. Soc.* **2014**, *136* (21), 7603–7606. https://doi.org/10.1021/ja503509k.

(64)   Willets, K. A.; Van Duyne, R. P. Localized Surface Plasmon Resonance Spectroscopy and Sensing. *Annu. Rev. Phys. Chem.* **2006**, *58* (1), 267–297. https://doi.org/10.1146/annurev.physchem.58.032806.104607.

(65)   Nehl, C. L.; Hafner, J. H. Shape-Dependent Plasmon Resonances of Gold Nanoparticles. *J. Mater. Chem.* **2008**, *18* (21), 2415–2419. https://doi.org/10.1039/b714950f.

(66)   Grzelczak, M.; Pérez-Juste, J.; Mulvaney, P.; Liz-Marzán, L. M. Shape Control in Gold Nanoparticle Synthesis. *Chem. Soc. Rev.* **2008**, *37* (9), 1783–1791. https://doi.org/10.1039/b711490g.

(67)   Halas, N. J.; Lal, S.; Chang, W. S.; Link, S.; Nordlander, P. Plasmons in Strongly Coupled Metallic Nanostructures. *Chem. Rev.* **2011**, *111* (6), 3913–3961. https://doi.org/10.1021/cr200061k.

(68)   Ren, S.; Wang, J.; Song, C.; Li, Q.; Yang, Y.; Teng, N.; Su, S.; Zhu, D.; Huang, W.; Chao, J.; Wang, L.; Fan, C. Single-Step Organization of Plasmonic Gold Metamaterials with Self-Assembled DNA Nanostructures. *Research* **2019**, *2019*, 7403580. https://doi.org/10.34133/2019/7403580.

(69)   Luk'Yanchuk, B.; Zheludev, N. I.; Maier, S. A.; Halas, N. J.; Nordlander, P.; Giessen, H.; Chong, C. T. The Fano Resonance in Plasmonic Nanostructures and Metamaterials. *Nat. Mater.* **2010**, *9* (9), 707–715. https://doi.org/10.1038/nmat2810.

(70)   Fu, Y.; Zhang, J.; Lakowicz, J. R. Plasmon-Enhanced Fluorescence from Single Fluorophores End-Linked to Gold Nanorods. *J. Am. Chem. Soc.* **2010**, *132* (16), 5540–5541. https://doi.org/10.1021/ja9096237.

(71)   Nepal, D.; Drummy, L. F.; Biswas, S.; Park, K.; Vaia, R. A. Large Scale Solution Assembly of Quantum Dot-Gold Nanorod Architectures with Plasmon Enhanced Fluorescence. *ACS Nano*

2013, *7* (10), 9064–9074. https://doi.org/10.1021/nn403671q.

(72)   Li, J. F.; Li, C. Y.; Aroca, R. F. Plasmon-Enhanced Fluorescence Spectroscopy. *Chem. Soc. Rev.* **2017**, *46* (13), 3962–3979. https://doi.org/10.1039/c7cs00169j.

(73)   Anger, P.; Bharadwaj, P.; Novotny, L. Enhancement and Quenching of Single-Molecule Fluorescence. *Phys. Rev. Lett.* **2006**, *96* (11), 3–6. https://doi.org/10.1103/PhysRevLett.96.113002.

(74)   Zhou, W.; Dridi, M.; Suh, J. Y.; Kim, C. H.; Co, D. T.; Wasielewski, M. R.; Schatz, G. C.; Odom, T. W. Lasing Action in Strongly Coupled Plasmonic Nanocavity Arrays. *Nat. Nanotechnol.* **2013**, *8* (7), 506–511. https://doi.org/10.1038/nnano.2013.99.

(75)   Zhou, W.; Odom, T. W. Tunable Subradiant Lattice Plasmons by Out-of-Plane Dipolar Interactions. *Nat. Nanotechnol.* **2011**, *6* (7), 423–427. https://doi.org/10.1038/nnano.2011.72.

(76)   Marinakos, S. M.; Chen, S.; Chilkoti, A. Plasmonic Detection of a Model Analyte in Serum by a Gold Nanorod Sensor. *Anal. Chem.* **2007**, *79* (14), 5278–5283. https://doi.org/10.1021/ac0706527.

(77)   Mirkin, C. A.; Letsinger, R. L.; Mucic, R. C.; Storhoff, J. J. A DNA-Based Method for Rationally Assembling Nanoparticles into Macroscopic Materials*. *Nature* **1996**, *382* (August), 3–11. https://doi.org/10.4324/9780429200151-2.

(78)   Macfarlane, R. J.; Thaner, R. V.; Brown, K. A.; Zhang, J.; Lee, B.; Nguyen, S. B. T.; Mirkin, C. A. Importance of the DNA "Bond" in Programmable Nanoparticle Crystallization. *Proc. Natl. Acad. Sci. U. S. A.* **2014**, *111* (42), 14995–15000. https://doi.org/10.1073/pnas.1416489111.

(79)   Zhang, Y.; Lu, F.; Yager, K. G.; Lelie, D. Van Der; Gang, O. A General Strategy for the DNA-Mediated Self-Assembly of Functional Nanoparticles into Heterogeneous Systems. *Nat. Nanotechnol.* **2013**, *8* (11), 865–872. https://doi.org/10.1038/nnano.2013.209.

(80)   Zhang, C.; Macfarlane, R. J.; Young, K. L.; Choi, C. H. J.; Hao, L.; Auyeung, E.; Liu, G.; Zhou, X.; Mirkin, C. A. A General Approach to DNA-Programmable Atom Equivalents. *Nat. Mater.* **2013**, *12* (8), 741–746. https://doi.org/10.1038/nmat3647.

(81)   Nykypanchuk, D.; Maye, M. M.; Lelie, D. Van Der; Gang, O. DNA-Guided Crystallization of Colloidal Nanoparticles. *Nature* **2008**, *451* (January), 549–552. https://doi.org/10.1038/nature06560.

(82)   Urbach, Z. J.; Park, S. S.; Weigand, S. L.; Rix, J. E.; Lee, B.; Mirkin, C. A. Probing the Consequences of Cubic Particle Shape and Applied Field on Colloidal Crystal Engineering with DNA. *Angew. Chemie - Int. Ed.* **2021**, *60* (8), 4065–4069. https://doi.org/10.1002/anie.202012907.

(83)   Sun, D.; Gang, O. Binary Heterogeneous Superlattices Assembled from Quantum Dots and Gold Nanoparticles with DNA. *J. Am. Chem. Soc.* **2011**, *133* (14), 5252–5254. https://doi.org/10.1021/ja111542t.

(84)   Wang, Y.; Wang, Y.; Zheng, X.; Ducrot, É.; Yodh, J. S.; Weck, M.; Pine, D. J. Crystallization of DNA-Coated Colloids. *Nat. Commun.* **2015**, *6*. https://doi.org/10.1038/ncomms8253.

(85)   Hurst, S. J.; Lytton-Jean, A. K. R.; Mirkin, C. A. Maximizing DNA Loading on a Range of Gold Nanoparticle Sizes. *Anal. Chem.* **2006**, *78* (24), 8313–8318. https://doi.org/10.1021/ac0613582.

(86)   Park, S. Y.; Lytton-Jean, A. K. R.; Lee, B.; Weigand, S.; Schatz, G. C.; Mirkin, C. A. DNA-Programmable Nanoparticle Crystallization. *Nature* **2008**, *451* (7178), 553–556.

https://doi.org/10.1038/nature06508.

(87)   Macfarlane, R. J.; Lee, B.; Jones, M. R.; Harris, N.; Schatz, G. C.; Mirkin, C. A. Nanoparticle Superlattice Engineering with DNA. *Science (80-.).* **2011**, *334* (6053), 204–208. https://doi.org/10.1126/science.1210493.

(88)   Wang, M. X.; Brodin, J. D.; Millan, J. A.; Seo, S. E.; Girard, M.; Olvera De La Cruz, M.; Lee, B.; Mirkin, C. A. Altering DNA-Programmable Colloidal Crystallization Paths by Modulating Particle Repulsion. *Nano Lett.* **2017**, *17* (8), 5126–5132. https://doi.org/10.1021/acs.nanolett.7b02502.

(89)   Thaner, R. V.; Kim, Y.; Li, T. I. N. G.; Macfarlane, R. J.; Nguyen, S. T.; Olvera De La Cruz, M.; Mirkin, C. A. Entropy-Driven Crystallization Behavior in DNA-Mediated Nanoparticle Assembly. *Nano Lett.* **2015**, *15* (8), 5545–5551. https://doi.org/10.1021/acs.nanolett.5b02129.

(90)   Auyueng, E.; Li, T. I. N. G.; Senisi, A. J.; Schmucker, A. L.; Pals, B. C.; Olvera de la Cruz, M.; Mirkin, C. A. DNA-Mediated Nanoparticle Crystallization into Wulff Polyhedra. *Nature* **2013**, *505* (7481), 73–77. https://doi.org/10.1038/nature12739.

(91)   Ross, M. B.; Blaber, M. G.; Schatz, G. C. Using Nanoscale and Mesoscale Anisotropy to Engineer the Optical Response of Three-Dimensional Plasmonic Metamaterials. *Nat. Commun.* **2014**, *5* (May), 1–11. https://doi.org/10.1038/ncomms5090.

(92)   Sun, L.; Lin, H.; Park, D. J.; Bourgeois, M. R.; Ross, M. B.; Ku, J. C.; Schatz, G. C.; Mirkin, C. A. Polarization-Dependent Optical Response in Anisotropic Nanoparticle-DNA Superlattices. *Nano Lett.* **2017**, *17* (4), 2313–2318. https://doi.org/10.1021/acs.nanolett.6b05101.

(93)   Young, K. L.; Ross, M. B.; Blaber, M. G.; Rycenga, M.; Jones, M. R.; Zhang, C.; Senesi, A. J.; Lee, B.; Schatz, G. C.; Mirkin, C. A. Using DNA to Design Plasmonic Metamaterials with Tunable Optical Properties. *Adv. Mater.* **2014**, *26* (4), 653–659. https://doi.org/https://doi.org/10.1002/adma.201302938.

(94)   Ross, M. B.; Ku, J. C.; Vaccarezza, V. M.; Schatz, G. C.; Mirkin, C. A. Nanoscale Form Dictates Mesoscale Function in Plasmonic DNA-Nanoparticle Superlattices. *Nat. Nanotechnol.* **2015**, *10* (5), 453–458. https://doi.org/10.1038/nnano.2015.68.

(95)   Park, D. J.; Zhang, C.; Ku, J. C.; Zhou, Y.; Schatz, G. C.; Mirkin, C. A. Plasmonic Photonic Crystals Realized through DNA-Programmable Assembly. *Proc. Natl. Acad. Sci. U. S. A.* **2015**, *112* (4), 977–981. https://doi.org/10.1073/pnas.1422649112.

(96)   Park, D. J.; Ku, J. C.; Sun, L.; Lethiec, C. M.; Stern, N. P.; Schatz, G. C.; Mirkin, C. A. Directional Emission from Dye-Functionalized Plasmonic DNA Superlattice Microcavities. *Proc. Natl. Acad. Sci. U. S. A.* **2017**, *114* (3), 457–461. https://doi.org/10.1073/pnas.1619802114.

(97)   Mason, J. A.; Laramy, C. R.; Lai, C.-T.; O'Brien, M. N.; Lin, Q.-Y.; Dravid, V. P.; Schatz, G. C.; Mirkin, C. A. Contraction and Expansion of Stimuli-Responsive DNA Bonds in Flexible Colloidal Crystals. *J. Am. Chem. Soc.* **2016**, *138* (28), 8722–8725. https://doi.org/10.1021/jacs.6b05430.

(98)   Yan, Y.; Wang, X.; Chen, J. I. L.; Ginger, D. S. Depends on Local Sequence. **2013**.

(99)   Jin, K. S.; Shin, S. R.; Ahn, B.; Rho, Y.; Kim, S. J.; Ree, M. PH-Dependent Structures of an i-Motif DNA in Solution. *J. Phys. Chem. B* **2009**, *113* (7), 1852–1856. https://doi.org/10.1021/jp808186z.

(100) Lin, Q.-Y.; Mason, J. A.; Li, Z.; Zhou, W.; O'Brien, M. N.; Brown, K. A.; Jones, M. R.; Butun, S.;

Lee, B.; Dravid, V. P.; Aydin, K.; Mirkin, C. A. Building Superlattices from Individual Nanoparticles via Template-Confined DNA-Mediated Assembly. *Science (80-.).* **2018**, *359* (6376), 669–672. https://doi.org/10.1126/science.aaq0591.

(101) Kelly, K. L.; Coronado, E.; Zhao, L. L.; Schatz, G. C. The Optical Properties of Metal Nanoparticles: The Influence of Size, Shape, and Dielectric Environment. *J. Phys. Chem. B* **2003**, *107* (3), 668–677. https://doi.org/10.1021/jp026731y.

(102) Pompa, P. P.; Martiradonna, L.; Della Torre, A.; Della Sala, F.; Manna, L.; de Vittorio, M.; Calabi, F.; Cinagolani, R.; Rinaldi, R. Metal-Enhanced Fluorescence of Colloidal Nanocrystals with Nanoscale Control. *Nat. Nanotechnol.* **2006**, *1* (2), 126–130. https://doi.org/10.1038/nnano.2006.93.

(103) Lakowicz, J. R.; Fu, Y. Modification of Single Molecule Fluorescence near Metallic Nanostructures. *Laser Photonics Rev.* **2009**, *3* (1–2), 221–232. https://doi.org/10.1002/lpor.200810035.

(104) Oulton, R. F.; Sorger, V. J.; Zentgraf, T.; Ma, R. M.; Gladden, C.; Dai, L.; Bartal, G.; Zhang, X. Plasmon Lasers at Deep Subwavelength Scale. *Nature* **2009**, *461* (7264), 629–632. https://doi.org/10.1038/nature08364.

(105) Akimov, A. V.; Mukherjee, A.; Yu, C. L.; Chang, D. E.; Zibrov, A. S.; Hemmer, P. R.; Park, H.; Lukin, M. D. Generation of Single Optical Plasmons in Metallic Nanowires Coupled to Quantum Dots. *Nature* **2007**, *450* (7168), 402–406. https://doi.org/10.1038/nature06230.

(106) Kinkhabwala, A.; Yu, Z.; Fan, S.; Avlasevich, Y.; Mullen, K.; Moerner, W. E. Large Single-Molecule Fluorescence Enhancements Produced by a Bowtie Nanoantenna. *Nat. Photonics* **2009**, *3* (11), 654–657. https://doi.org/10.1038/nphoton.2009.187.

(107) Kosako, T.; Kadoya, Y.; Hofmann, H. F. Directional Emission of Light from a Nano-Optical Yagi-Uda Antenna. *Nat. Photonics* **2010**, *4* (5), 312–315. https://doi.org/10.1038/nphoton.2010.34.

(108) Moreau, A.; Ciraci, C.; Mock, J. J.; Hill, R. T.; Wiley, B. J.; Chilkoti, A.; Smith, D. R. Controlled-Reflectance Surfaces with Film-Coupled Colloidal Nanoantennas. *Nature* **2012**, *492* (7427), 86–89. https://doi.org/10.1038/nature11615.

(109) Hoang, T. B.; Akselrod, G. M.; Argyropoulos, C.; Huang, J.; Smith, D. R.; Mikkelsen, M. H. Ultrafast Spontaneous Emission Source Using Plasmonic Nanoantennas. *Nat. Commun.* **2015**, *6*, 1–7. https://doi.org/10.1038/ncomms8788.

(110) Akselrod, G. M.; Argyropoulos, C.; Hoang, T. B.; Ciraci, C.; Fang, C.; Huang, J.; Smith, D. R.; Mikkelsen, M. H. Probing the Mechanisms of Large Purcell Enhancement in Plasmonic Nanoantennas. *Nat. Photonics* **2014**, *8* (11), 835–840. https://doi.org/10.1038/nphoton.2014.228.

(111) Zou, S.; Janel, N.; Schatz, G. C. Silver Nanoparticle Array Structures That Produce Remarkably Narrow Plasmon Lineshapes. *J. Chem. Phys.* **2004**, *120* (23), 10871–10875. https://doi.org/10.1063/1.1760740.

(112) Kravets, V. G.; Kabashin, A. V.; Barnes, W. L.; Grigorenko, A. N. Plasmonic Surface Lattice Resonances: A Review of Properties and Applications. *Chem. Rev.* **2018**, *118* (12), 5912–5951. https://doi.org/10.1021/acs.chemrev.8b00243.

(113) Gutha, R. R.; Sadeghi, S. M.; Sharp, C.; Wing, W. J. Biological Sensing Using Hybridization Phase of Plasmonic Resonances with Photonic Lattice Modes in Arrays of Gold Nanoantennas. *Nanotechnology* **2017**, *28* (35), 355504–3555511. https://doi.org/10.1088/1361-6528/aa7bb5.

(114) Liu, W.; Tagawa, M.; Xin, H. L.; Wang, T.; Emamy, H.; Li, H.; Yager, K. G.; Starr, F. W.; Tkachenko, A. V; Gang, O. Diamond Family of Nanoparticle Superlattices. *Science (80-.).* **2016**, *351* (6273), 582–587.

(115) Zhou, W.; Lin, Q. Y.; Mason, J. A.; Dravid, V. P.; Mirkin, C. A. Design Rules for Template-Confined DNA-Mediated Nanoparticle Assembly. *Small* **2018**, *14* (44), 1–7. https://doi.org/10.1002/smll.201802742.

(116) Lin, Q.-Y.; Li, Z.; Brown, K. A.; O'Brien, M. N.; Ross, M. B.; Zhou, Y.; Butun, S.; Chen, P.-C.; Schatz, G. C.; Dravid, V. P.; Aydin, K.; Mirkin, C. A. Strong Coupling between Plasmonic Gap Modes and Photonic Lattice Modes in DNA-Assembled Gold Nanocube Arrays. *Nano Lett.* **2015**, *15* (7), 4699–4703. https://doi.org/10.1021/acs.nanolett.5b01548.

(117) Frederiksen, M. U.; Rudd, M. T.; Lenges, C. P.; Brookhart, M.; Brookhart, M.; Schley, N. D.; Crabtree, R. H. Reports 20. **2012**, *6630* (506), 506–511.

(118) Cormier, S.; Ding, T.; Turek, V.; Baumberg, J. J. Actuating Single Nano-Oscillators with Light. *Adv. Opt. Mater.* **2018**, *6* (6), 1–5. https://doi.org/10.1002/adom.201701281.

(119) Huang, J.; Traverso, A. J.; Yang, G.; Mikkelsen, M. H. Real-Time Tunable Strong Coupling: From Individual Nanocavities to Metasurfaces. *ACS Photonics* **2019**, *6* (4), 838–843. https://doi.org/10.1021/acsphotonics.8b01743.

(120) Chikkaraddy, R.; De Nijs, B.; Benz, F.; Barrow, S. J.; Scherman, O. A.; Rosta, E.; Demetriadou, A.; Fox, P.; Hess, O.; Baumberg, J. J. Single-Molecule Strong Coupling at Room Temperature in Plasmonic Nanocavities. *Nature* **2016**, *535* (7610), 127–130. https://doi.org/10.1038/nature17974.

(121) Chikkaraddy, R.; Turek, V. A.; Kongsuwan, N.; Benz, F.; Carnegie, C.; Van De Goor, T.; De Nijs, B.; Demetriadou, A.; Hess, O.; Keyser, U. F.; Baumberg, J. J. Mapping Nanoscale Hotspots with Single-Molecule Emitters Assembled into Plasmonic Nanocavities Using DNA Origami. *Nano Lett.* **2018**, *18* (1), 405–411. https://doi.org/10.1021/acs.nanolett.7b04283.

(122) Wang, S.; Scarabelli, D.; Du, L.; Kuznetsova, Y. Y.; Pfeiffer, L. N.; West, K. W.; Gardner, G. C.; Manfra, M. J.; Pellegrini, V.; Wind, S. J.; Pinczuk, A. Observation of Dirac Bands in Artificial Graphene in Small-Period Nanopatterned GaAs Quantum Wells. *Nat. Nanotechnol.* **2018**, *13* (1), 29–33. https://doi.org/10.1038/s41565-017-0006-x.

(123) O'Brien, M. N.; Lin, H. X.; Girard, M.; Olvera De La Cruz, M.; Mirkin, C. A. Programming Colloidal Crystal Habit with Anisotropic Nanoparticle Building Blocks and DNA Bonds. *J. Am. Chem. Soc.* **2016**, *138* (44), 14562–14565. https://doi.org/10.1021/jacs.6b09704.

(124) Jones, M. R.; Macfarlane, R. J.; Lee, B.; Zhang, J.; Young, K. L.; Senise, A. J.; Mirkin, C. A. DNA-Nanoparticle Superlattices Formed from Anisotropic Building Blocks. *Nat. Mater.* **2010**, *9* (11), 913–917. https://doi.org/10.1038/nmat2870.

(125) O'Brien, M. N.; Jones, M. R.; Lee, B.; Mirkin, C. A. Anisotropic Nanoparticle Complementarity in DNA-Mediated Co-Crystallization. *Nat. Mater.* **2015**, *14* (8), 833–839. https://doi.org/10.1038/nmat4293.

(126) Kuzyk, A.; Schreiber, R.; Zhang, H.; Govorov, A. O.; Liedl, T.; Liu, N. Reconfigurable 3D Plasmonic Metamolecules. *Nat. Mater.* **2014**, *13* (9), 862–866. https://doi.org/10.1038/nmat4031.

(127) A., F. J.; Chihhui, W.; Kui, B.; Jiming, B.; Rizia, B.; J., H. N.; N., M. V.; Peter, N.; Gennady, S.; Federico, C. Self-Assembled Plasmonic Nanoparticle Clusters. *Science (80-.).* **2010**, *328* (5982), 1135–1138. https://doi.org/10.1126/science.1187949.

(128) Liberal, I.; Engheta, N. Near-Zero Refractive Index Photonics. *Nat. Photonics* **2017**, *11* (3), 149–158. https://doi.org/10.1038/nphoton.2017.13.

(129) A., S. R.; R., S. D.; S., S. Experimental Verification of a Negative Index of Refraction. *Science (80-.).* **2001**, *292* (5514), 77–79. https://doi.org/10.1126/science.1058847.

(130) Engheta, N. Circuits with Light at Nanoscales: Optical Nanocircuits Inspired by Metamaterials. *Science (80-.).* **2007**, *317* (5845), 1698–1702. https://doi.org/10.1126/science.1133268.

(131) Grigorenko, A. N.; Geim, A. K.; Gleeson, H. F.; Zhang, Y.; Firsov, A. A.; Khrushchev, I. Y.; Petrovic, J. Nanofabricated Media with Negative Permeability at Visible Frequencies. *Nature* **2005**, *438* (7066), 335–338. https://doi.org/10.1038/nature04242.

(132) Yang, Y.; Kravchenko, I. I.; Briggs, D. P.; Valentine, J. All-Dielectric Metasurface Analogue of Electromagnetically Induced Transparency. *Nat. Commun.* **2014**, *5*, 1–7. https://doi.org/10.1038/ncomms6753.

(133) Engheta, N.; Salandrino, A.; Alù, A. Circuit Elements at Optical Frequencies: Nanoinductors, Nanocapacitors, and Nanoresistors. *Phys. Rev. Lett.* **2005**, *95* (9), 1–4. https://doi.org/10.1103/PhysRevLett.95.095504.

(134) Chen, W. T.; Zhu, A. Y.; Sanjeev, V.; Khorasaninejad, M.; Shi, Z.; Lee, E.; Capasso, F. A Broadband Achromatic Metalens for Focusing and Imaging in the Visible. *Nat. Nanotechnol.* **2018**, *13* (3), 220–226. https://doi.org/10.1038/s41565-017-0034-6.

(135) Shin, J.; Shen, J. T.; Fan, S. Three-Dimensional Metamaterials with an Ultrahigh Effective Refractive Index over a Broad Bandwidth. *Phys. Rev. Lett.* **2009**, *102* (9), 1–4. https://doi.org/10.1103/PhysRevLett.102.093903.

(136) Kuznetsov, A. I.; Miroshnichenko, A. E.; Brongersma, M. L.; Kivshar, Y. S.; Luk'yanchuk, B. Optically Resonant Dielectric Nanostructures. *Science* **2016**, *354* (6314). https://doi.org/10.1126/science.aag2472.

(137) Rockstuhl, C.; Lederer, F.; Etrich, C.; Pertsch, T.; Scharf, T. Design of an Artificial Three-Dimensional Composite Metamaterial with Magnetic Resonances in the Visible Range of the Electromagnetic Spectrum. *Phys. Rev. Lett.* **2007**, *99* (1), 1–4. https://doi.org/10.1103/PhysRevLett.99.017401.

(138) Lee, S.; Zheng, C. Y.; Bujold, K. E.; Mirkin, C. A. A Cross-Linking Approach to Stabilizing Stimuli-Responsive Colloidal Crystals Engineered with DNA. *J. Am. Chem. Soc.* **2019**, *141* (30), 11827–11831. https://doi.org/10.1021/jacs.9b06106.

(139) Kivshar, Y.; Miroshnichenko, A. Meta- Optics with Mie Resonances. **2017**, No. January, 24–31.

(140) Park, D. J.; Ku, J. C.; Sun, L.; Lethiec, C. M.; Stern, N. P.; Schatz, G. C.; Mirkin, C. A. Directional Emission from Dye-Functionalized Plasmonic DNA Superlattice Microcavities. *Proc. Natl. Acad. Sci.* **2017**, *114* (3), 457–461. https://doi.org/10.1073/pnas.1619802114.

(141) Senesi, A. J.; Eichelsdoerfer, D. J.; Brown, K. A.; Lee, B.; Auyeung, E.; Choi, C. H. J.; Macfarlane, R. J.; Young, K. L.; Mirkin, C. A. Oligonucleotide Flexibility Dictates Crystal Quality in DNA-Programmable Nanoparticle Superlattices. *Adv. Mater.* **2014**, *26* (42), 7235–7240. https://doi.org/https://doi.org/10.1002/adma.201402548.

(142) Neubrech, F.; Huck, C.; Weber, K.; Pucci, A.; Giessen, H. Surface-Enhanced Infrared Spectroscopy Using Resonant Nanoantennas. *Chem. Rev.* **2017**, *117* (7), 5110–5145. https://doi.org/10.1021/acs.chemrev.6b00743.

(143) Auyeung, E.; Morris, W.; Mondloch, J. E.; Hupp, J. T.; Farha, O. K.; Mirkin, C. A. Controlling Structure and Porosity in Catalytic Nanoparticle Superlattices with DNA. *J. Am. Chem. Soc.* **2015**, *137* (4), 1658–1662. https://doi.org/10.1021/ja512116p.

(144) Rybin, M. V.; Koshelev, K. L.; Sadrieva, Z. F.; Samusev, K. B.; Bogdanov, A. A.; Limonov, M. F.; Kivshar, Y. S. High- Q Supercavity Modes in Subwavelength Dielectric Resonators. *Phys. Rev. Lett.* **2017**, *119* (24), 1–5. https://doi.org/10.1103/PhysRevLett.119.243901.

(145) Staude, I.; Miroshnichenko, A. E.; Decker, M.; Fofang, N. T.; Liu, S.; Gonzales, E.; Dominguez, J.; Luk, T. S.; Neshev, D. N.; Brener, I.; Kivshar, Y. Tailoring Directional Scattering through Magnetic and Electric Resonances in Subwavelength Silicon Nanodisks. *ACS Nano* **2013**, *7* (9), 7824–7832. https://doi.org/10.1021/nn402736f.

(146) Kim, S.; Zheng, C. Y.; Schatz, G. C.; Aydin, K.; Kim, K. H.; Mirkin, C. A. Mie-Resonant Three-Dimensional Metacrystals. *Nano Lett.* **2020**, *22*, 1–6. https://doi.org/10.1021/acs.nanolett.0c03089.

(147) Kim, D. K.; Lai, Y.; Diroll, B. T.; Murray, C. B.; Kagan, C. R. Flexible and Low-Voltage Integrated Circuits Constructed from High-Performance Nanocrystal Transistors. *Nat. Commun.* **2012**, *3*, 1–6. https://doi.org/10.1038/ncomms2218.

(148) Cargnello, M.; Johnston-Peck, A. C.; Diroll, B. T.; Wong, E.; Datta, B.; Damodhar, D.; Doan-Nguyen, V. V. T.; Herzing, A. A.; Kagan, C. R.; Murray, C. B. Substitutional Doping in Nanocrystal Superlattices. *Nature* **2015**, *524* (7566), 450–453. https://doi.org/10.1038/nature14872.

(149) Cheon, J.; Park, J. Il; Choi, J. S.; Jun, Y. W.; Kim, S.; Kim, M. G.; Kim, Y. M.; Kim, Y. J. Magnetic Superlattices and Their Nanoscale Phase Transition Effects. *Proc. Natl. Acad. Sci. U. S. A.* **2006**, *103* (9), 3023–3027. https://doi.org/10.1073/pnas.0508877103.

(150) Wu, X.; Chen, J.; Xie, L.; Li, J.; Shi, J.; Luo, S.; Zhao, X.; Deng, K.; He, D.; He, J.; Luo, J.; Wang, Z.; Quan, Z. Directing Gold Nanoparticles into Free-Standing Honeycomb-Like Ordered Mesoporous Superstructures. *Small* **2019**, *15* (31), 1–7. https://doi.org/10.1002/smll.201901304.

(151) Shevchenko, E. V.; Talapin, D. V.; Kotov, N. A.; O'Brien, S.; Murray, C. B. Structural Diversity in Binary Nanoparticle Superlattices. *Nature* **2006**, *439* (7072), 55–59. https://doi.org/10.1038/nature04414.

(152) Udayabhaskararao, T.; Altantzis, T.; Houben, L.; Coronado-Puchau, M.; Langer, J.; Popovitz-Biro, R.; Liz-Marzán, L. M.; Vukovic, L.; Král, P.; Bals, S.; Klajn, R. Tunable Porous Nanoallotropes Prepared by Post-Assembly Etching of Binary Nanoparticle Superlattices. *Science (80-.).* **2017**, *358* (6362), 514–518. https://doi.org/10.1126/science.aan6046.

(153) Senesi, A. J.; Eichelsdoerfer, D. J.; Macfarlane, R. J.; Jones, M. R.; Auyeung, E.; Lee, B.; Mirkin, C. A. Stepwise Evolution of DNA-Programmable Nanoparticle Superlattices. *Angew. Chemie -*

Int. Ed. **2013**, *52* (26), 6624–6628. https://doi.org/10.1002/anie.201301936.

(154) Zornberg, L. Z.; Gabrys, P. A.; Macfarlane, R. J. Optical Processing of DNA-Programmed Nanoparticle Superlattices. *Nano Lett.* **2019**, *19* (11), 8074–8081. https://doi.org/10.1021/acs.nanolett.9b03258.

(155) Zheng, C. Y.; Palacios, E.; Zhou, W.; Hadibrata, W.; Sun, L.; Huang, Z.; Schatz, G. C.; Aydin, K.; Mirkin, C. A. Tunable Fluorescence from Dye-Modified DNA-Assembled Plasmonic Nanocube Arrays. *Adv. Mater.* **2019**, *31* (41), 1–6. https://doi.org/10.1002/adma.201904448.

(156) Lewis, D. J.; Carter, D. J. D.; Macfarlane, R. J. Using DNA to Control the Mechanical Response of Nanoparticle Superlattices. *J. Am. Chem. Soc.* **2020**. https://doi.org/10.1021/jacs.0c08790.

(157) Zhou, W.; Liu, Z.; Huang, Z.; Lin, H.; Samanta, D.; Lin, Q. Y.; Aydin, K.; Mirkin, C. A. Device-Quality, Reconfigurable Metamaterials from Shape-Directed Nanocrystal Assembly. *Proc. Natl. Acad. Sci. U. S. A.* **2020**, *117* (35), 21052–21057. https://doi.org/10.1073/pnas.2006797117.

(158) Liao, C. W.; Lin, Y. S.; Chanda, K.; Song, Y. F.; Huang, M. H. Formation of Diverse Supercrystals from Self-Assembly of a Variety of Polyhedral Gold Nanocrystals. *J. Am. Chem. Soc.* **2013**, *135* (7), 2684–2693. https://doi.org/10.1021/ja311008r.

(159) Jones, M. R.; MacFarlane, R. J.; Lee, B.; Zhang, J.; Young, K. L.; Senesi, A. J.; Mirkin, C. A. DNA-Nanoparticle Superlattices Formed from Anisotropic Building Blocks. *Nat. Mater.* **2010**, *9* (11), 913–917. https://doi.org/10.1038/nmat2870.

(160) Olson, J.; Dominguez-Medina, S.; Hoggard, A.; Wang, L. Y.; Chang, W. S.; Link, S. Optical Characterization of Single Plasmonic Nanoparticles. *Chem. Soc. Rev.* **2015**, *44* (1), 40–57. https://doi.org/10.1039/c4cs00131a.

(161) Zhang, Z.; Chen, Z.; Qu, C.; Chen, L. Highly Sensitive Visual Detection of Copper Ions Based on the Shape-Dependent LSPR Spectroscopy of Gold Nanorods. *Langmuir* **2014**, *30* (12), 3625–3630. https://doi.org/10.1021/la500106a.

(162) Gao, B.; Arya, G.; Tao, A. R. Self-Orienting Nanocubes for the Assembly of Plasmonic Nanojunctions. *Nat. Nanotechnol.* **2012**, *7* (7), 433–437. https://doi.org/10.1038/nnano.2012.83.

(163) Hatab, N. A.; Hsueh, C. H.; Gaddis, A. L.; Retterer, S. T.; Li, J. H.; Eres, G.; Zhang, Z.; Gu, B. Free-Standing Optical Gold Bowtie Nanoantenna with Variable Gap Size for Enhanced Raman Spectroscopy. *Nano Lett.* **2010**, *10* (12), 4952–4955. https://doi.org/10.1021/nl102963g.

(164) Dong, A.; Ye, X.; Chen, J.; Murray, C. B. Two-Dimensional Binary and Ternary Nanocrystal Superlattices: The Case of Monolayers and Bilayers. *Nano Lett.* **2011**, *11* (4), 1804–1809. https://doi.org/10.1021/nl200468p.

(165) Plotnik, Y.; Rechtsman, M. C.; Song, D.; Heinrich, M.; Zeuner, J. M.; Nolte, S.; Lumer, Y.; Malkova, N.; Xu, J.; Szameit, A.; Chen, Z.; Segev, M. Observation of Unconventional Edge States in "Photonic Graphene." *Nat. Mater.* **2014**, *13* (1), 57–62. https://doi.org/10.1038/nmat3783.

(166) Auyeung, E.; MacFarlane, R. J.; Choi, C. H. J.; Cutler, J. I.; Mirkin, C. A. Transitioning DNA-Engineered Nanoparticle Superlattices from Solution to the Solid State. *Adv. Mater.* **2012**, *24* (38), 5181–5186. https://doi.org/10.1002/adma.201202069.

(167) Fan, Q. A New Method of Calculating Planar Density: The Position-Duplication-Number Method. *J. Appl. Crystallogr.* **2016**, *49* (5), 1454–1458. https://doi.org/10.1107/S1600576716010827.

(168) Boneschanscher, M. P.; Evers, W. H.; Geuchies, J. J.; Altantzis, T.; Goris, B.; Rabouw, F. T.; Van Rossum, S. A. P.; Van Der Zant, H. S. J.; Siebbeles, L. D. A.; Van Tendeloo, G.; Swart, I.; Hilhorst, J.; Petukhov, A. V.; Bals, S.; Vanmaekelbergh, D. Long-Range Orientation and Atomic Attachment of Nanocrystals in 2D Honeycomb Superlattices. *Science (80-.).* **2014**, *344* (6190), 1377–1380. https://doi.org/10.1126/science.1252642.

(169) Grillo, F.; Fernandez-Rodriguez, M. A.; Antonopoulou, M. N.; Gerber, D.; Isa, L. Self-Templating Assembly of Soft Microparticles into Complex Tessellations. *Nature* **2020**, *582* (7811), 219–224. https://doi.org/10.1038/s41586-020-2341-6.

(170) Weick, G.; Woollacott, C.; Barnes, W. L.; Hess, O.; Mariani, E. Dirac-like Plasmons in Honeycomb Lattices of Metallic Nanoparticles. *Phys. Rev. Lett.* **2013**, *110* (10), 1–6. https://doi.org/10.1103/PhysRevLett.110.106801.

(171) Han, D.; Lai, Y.; Zi, J.; Zhang, Z. Q.; Chan, C. T. Dirac Spectra and Edge States in Honeycomb Plasmonic Lattices. *Phys. Rev. Lett.* **2009**, *102* (12), 1–4. https://doi.org/10.1103/PhysRevLett.102.123904.

(172) Sinelnik, A. D.; Rybin, M. V.; Lukashenko, S. Y.; Limonov, M. F.; Samusev, K. B. Optical Properties of Honeycomb Photonic Structures. *Phys. Rev. A* **2017**, *95* (6), 1–10. https://doi.org/10.1103/PhysRevA.95.063837.

(173) Polini, M.; Guinea, F.; Lewenstein, M.; Manoharan, H. C.; Pellegrini, V. Artificial Honeycomb Lattices for Electrons, Atoms and Photons. *Nat. Nanotechnol.* **2013**, *8* (9), 625–633. https://doi.org/10.1038/nnano.2013.161.

(174) Auyueng, E.; MacFarlane, R. J.; Choi, C. J. J.; Cutler, J. I.; Mirkin, C. A. Transitioning DNA-Engineered Nanoparticle Superlattices from Solution to the Solid State. *Adv. Mater.* **2012**, *24*, 5181–5186.

(175) Chanda, D.; Shigeta, K.; Gupta, S.; Cain, T.; Carlson, A.; Mihi, A.; Baca, A. J.; Bogart, G. R.; Braun, P.; Rogers, J. A. Large-Area Flexible 3D Optical Negative Index Metamaterial Formed by Nanotransfer Printing. *Nat. Nanotechnol.* **2011**, *6* (7), 402–407. https://doi.org/10.1038/nnano.2011.82.

(176) Cui, Y.; Kang, L.; Lan, S.; Rodrigues, S.; Cai, W. Giant Chiral Optical Response from a Twisted-Arc Metamaterial. *Nano Lett.* **2014**, *14* (2), 1021–1025. https://doi.org/10.1021/nl404572u.

(177) Huh, J.-H.; Lee, J.; Lee, S. Soft Plasmonic Assemblies Exhibiting Unnaturally High Refractive Index. *Nano Lett.* **2020**, *20* (7), 4768–4774. https://doi.org/10.1021/acs.nanolett.0c00422.

(178) Rozin, M. J.; Rosen, D. A.; Dill, T. J.; Tao, A. R. Colloidal Metasurfaces Displaying Near-Ideal and Tunable Light Absorbance in the Infrared. *Nat. Commun.* **2015**, *6*, 1–7. https://doi.org/10.1038/ncomms8325.

(179) Choi, J.-H.; Wang, H.; Oh, S. J.; Paik, T.; Sung, P.; Sung, J.; Ye, X.; Zhao, T.; Diroll, B. T.; Murray, C. B.; Kagan, C. R. Exploiting the Colloidal Nanocrystal Library to Construct Electronic Devices. *Science (80-.).* **2016**, *352* (6282), 205 LP – 208. https://doi.org/10.1126/science.aad0371.

(180) Oh, S. J.; Wang, Z.; Berry, N. E.; Choi, J.-H.; Zhao, T.; Gaulding, E. A.; Paik, T.; Lai, Y.; Murray, C. B.; Kagan, C. R. Engineering Charge Injection and Charge Transport for High Performance PbSe Nanocrystal Thin Film Devices and Circuits. *Nano Lett.* **2014**, *14* (11), 6210–6216. https://doi.org/10.1021/nl502491d.

(181)   Jones, M. R.; Macfarlane, R. J.; Prigodich, A. E.; Patel, P. C.; Mirkin, C. A. Nanoparticle Shape Anisotropy Dictates the Collective Behavior of Surface-Bound Ligands. *J. Am. Chem. Soc.* **2011**, *133* (46), 18865–18869. https://doi.org/10.1021/ja206777k.

(182)   Markov, I. V. *Crystal Growth for Beginners*; WORLD SCIENTIFIC, 2003. https://doi.org/doi:10.1142/5172.

(183)   O'brien, M. N.; Brown, K. A.; Mirkin, C. A. Critical Undercooling in DNA-Mediated Nanoparticle Crystallization. *ACS Nano* **2016**, *10* (1), 1363–1368. https://doi.org/10.1021/acsnano.5b06770.

(184)   O'Brien, M. N.; Girard, M.; Lin, H. X.; Millan, J. A.; De La Cruz, M. O.; Lee, B.; Mirkin, C. A. Exploring the Zone of Anisotropy and Broken Symmetries in DNA-Mediated Nanoparticle Crystallization. *Proc. Natl. Acad. Sci. U. S. A.* **2016**, *113* (38), 10485–10490. https://doi.org/10.1073/pnas.1611808113.

(185)   Macfarlane, R. J.; Lee, B.; Jones, M. R.; Harris, N.; Schatz, G. C.; Mirkin, C. A. Nanoparticle Superlattice Engineering with DNA. *Science (80-.).* **2011**, *334* (6053), 204–208. https://doi.org/10.1126/science.1210493.

(186)   Alam, M. Z.; De Leon, I.; Boyd, R. W. Large Optical Nonlinearity of Indium Tin Oxide in Its Epsilon-near-Zero Region. *Science (80-.).* **2016**, *352* (6287), 795–797. https://doi.org/10.1126/science.aae0330.

(187)   Yoon, J.; Zhou, M.; Badsha, M. A.; Kim, T. Y.; Jun, Y. C.; Hwangbo, C. K. Broadband Epsilon-Near-Zero Perfect Absorption in the Near-Infrared. *Sci. Rep.* **2015**, *5* (1), 12788. https://doi.org/10.1038/srep12788.

(188)   Chen, C.; Wang, Z.; Wu, K.; Ye, H. Tunable Near-Infrared Epsilon-near-Zero and Plasmonic Properties of Ag-ITO Co-Sputtered Composite Films. *Sci. Technol. Adv. Mater.* **2018**, *19* (1), 174–184. https://doi.org/10.1080/14686996.2018.1432230.

(189)   Park, J.; Kang, J. H.; Liu, X.; Brongersma, M. L. Electrically Tunable Epsilon-Near-Zero (ENZ) Metafilm Absorbers. *Sci. Rep.* **2015**, *5*. https://doi.org/10.1038/srep15754.

(190)   Xie, Z. T.; Wu, J.; Fu, H. Y.; Li, Q. Tunable Electro- and All-Optical Switch Based on Epsilon-Near-Zero Metasurface. *IEEE Photonics J.* **2020**, *12* (4), 1–10. https://doi.org/10.1109/JPHOT.2020.3010284.

(191)   Lian, J.; Zhang, D.; Hong, R.; Qiu, P.; Lv, T.; Zhang, D. Defect-Induced Tunable Permittivity of Epsilon-near-Zero in Indium Tin Oxide Thin Films. *Nanomaterials* **2018**, *8* (11). https://doi.org/10.3390/nano8110922.

(192)   Hong, R.; Yan, T.; Tao, C.; Wang, Q.; Lin, H.; Zhang, D. Laser Induced the Tunable Permittivity of Epsilon-Near-Zero Induced in Indium Tin Oxide Thin Films. *Opt. Mater. (Amst).* **2020**, *107*. https://doi.org/10.1016/j.optmat.2020.110137.

(193)   Yoo, D.; de León-Pérez, F.; Pelton, M.; Lee, I. H.; Mohr, D. A.; Raschke, M. B.; Caldwell, J. D.; Martín-Moreno, L.; Oh, S. H. Ultrastrong Plasmon–Phonon Coupling via Epsilon-near-Zero Nanocavities. *Nat. Photonics* **2021**, *15* (2), 125–130. https://doi.org/10.1038/s41566-020-00731-5.

(194)   Jeon, H. Bin; Tsalu, P. V.; Ha, J. W. Shape Effect on the Refractive Index Sensitivity at Localized Surface Plasmon Resonance Inflection Points of Single Gold Nanocubes with Vertices. *Sci. Rep.*

2019, *9* (1), 1–8. https://doi.org/10.1038/s41598-019-50032-3.

(195) Gabrys, P. A.; Seo, S. E.; Wang, M. X.; Oh, E.; Macfarlane, R. J.; Mirkin, C. A. Lattice Mismatch in Crystalline Nanoparticle Thin Films. *Nano Lett.* **2018**, *18* (1), 579–585. https://doi.org/10.1021/acs.nanolett.7b04737.

(196) Johnson, P. B.; Christy, R. W. Optical Constants of the Noble Metals. *Phys. Rev. B* **1972**, *6* (12), 4370–4379. https://doi.org/10.1103/PhysRevB.6.4370.

(197) Jiang, Q.; Ward, M. D. Crystallization under Nanoscale Confinement. *Chem. Soc. Rev.* **2014**, *43* (7), 2066–2079. https://doi.org/10.1039/c3cs60234f.

(198) Bang, J.; Jeong, U.; Ryu, D. Y.; Russell, T. P.; J Hawker, C. Block Copolymer Nanolithography: Translation of Molecular Level Control to Nanoscale Patterns. *Adv. Mater.* **2009**, *21* (47), 4769–4792. https://doi.org/10.1002/adma.200803302.

(199) Jacobberger, R. M.; Thapar, V.; Wu, G. P.; Chang, T. H.; Saraswat, V.; Way, A. J.; Jinkins, K. R.; Ma, Z.; Nealey, P. F.; Hur, S. M.; Xiong, S.; Arnold, M. S. Boundary-Directed Epitaxy of Block Copolymers. *Nat. Commun.* **2020**, *11* (1), 1–10. https://doi.org/10.1038/s41467-020-17938-3.

(200) Ren, J.; Segal-Peretz, T.; Zhou, C.; Craig, G. S. W.; Nealey, P. F.; Nealey, P. F. Three-Dimensional Superlattice Engineering with Block Copolymer Epitaxy. *Sci. Adv.* **2020**, *6* (24), 1–7. https://doi.org/10.1126/sciadv.aaz0002.

(201) Tavakkoli K. G., A.; Nicaise, S. M.; Gadelrab, K. R.; Alexander-Katz, A.; Ross, C. A.; Berggren, K. K. Multilayer Block Copolymer Meshes by Orthogonal Self-Assembly. *Nat. Commun.* **2016**, *7*. https://doi.org/10.1038/ncomms10518.

(202) Seibel, J.; Verstraete, L.; Hirsch, B. E.; Braganca, A. M.; De Feyter, S. Biasing Enantiomorph Formation via Geometric Confinement: Nanocorrals for Chiral Induction at the Liquid-Solid Interface. *J. Am. Chem. Soc.* **2018**, *140* (37), 11565–11568. https://doi.org/10.1021/jacs.8b04992.

(203) Verstraete, L.; Greenwood, J.; Hirsch, B. E.; De Feyter, S. Self-Assembly under Confinement: Nanocorrals for Understanding Fundamentals of 2D Crystallization. *ACS Nano* **2016**, *10* (12), 10706–10715. https://doi.org/10.1021/acsnano.6b05954.

(204) Seibel, J.; Amabilino, D. B.; De Feyter, S. Preferred Formation of Minority Concomitant Polymorphs in 2D Self-Assembly under Lateral Nanoconfinement. *Angew. Chemie* **2019**, *131* (37), 13098–13102. https://doi.org/10.1002/ange.201908552.

(205) Lalander, C. H.; Zheng, Y.; Dhuey, S.; Cabrini, S.; Bach, U. DNA-Directed Self-Assembly of Gold Nanoparticles onto Nanopatterned Surfaces: Controlled Placement of Individual Nanoparticles into Regular Arrays. *ACS Nano* **2010**, *4* (10), 6153–6161. https://doi.org/10.1021/nn101431k.

(206) Grzelczak, M.; Vermant, J.; Furst, E. M.; Liz-marza, L. M. Directed Self-Assembly of Nanoparticles. **2010**, *4* (7), 3591–3605.

(207) Varghese, B.; Cheong, F. C.; Sindhu, S.; Yu, T.; Lim, C. T.; Valiyaveettil, S.; Sow, C. H. Size Selective Assembly of Colloidal Particles on a Template by Directed Self-Assembly Technique. *Langmuir* **2006**, *22* (19), 8248–8252. https://doi.org/10.1021/la060732q.

(208) Xu, J.; Park, S.; Wang, S.; Russell, T. P.; Ocko, B. M.; Checco, A. Directed Self-Assembly of Block Copolymers on Two-Dimensional Chemical Patterns Fabricated by Electro-Oxidation

Nanolithography. *Adv. Mater.* **2010**, *22* (20), 2268–2272.
https://doi.org/10.1002/adma.200903640.

(209)   Park, S.; Dong, H. L.; Xu, J.; Kim, B.; Sung, W. H.; Jeong, U.; Xu, T.; Russell, T. P. Macroscopic
10-Terabit-per-Square-Inch Arrays from Block Copolymers with Lateral Order. *Science (80-.).*
2009, *323* (5917), 1030–1033. https://doi.org/10.1126/science.1168108.

(210)   Pinto-Gómez, C.; Pérez-Murano, F.; Bausells, J.; Villanueva, L. G.; Fernández-Regúlez, M.
Directed Self-Assembly of Block Copolymers for the Fabrication of Functional Devices. *Polymers
(Basel).* **2020**, *12* (10), 1–20. https://doi.org/10.3390/polym12102432.

(211)   Pfeiffer, F. X-Ray Ptychography. *Nat. Photonics* **2018**, *12* (1), 9–17.
https://doi.org/10.1038/s41566-017-0072-5.

(212)   Lazarev, S.; Besedin, I.; Zozulya, A. V.; Meijer, J. M.; Dzhigaev, D.; Gorobtsov, O. Y.; Kurta, R.
P.; Rose, M.; Shabalin, A. G.; Sulyanova, E. A.; Zaluzhnyy, I.; Menushenkov, A. P.; Sprung, M.;
Petukhov, A. V.; Vartanyants, I. A. Ptychographic X-Ray Imaging of Colloidal Crystals. *Small*
2018, *14* (3), 1–8. https://doi.org/10.1002/smll.201702575.

(213)   Miao, Z.; Zheng, C. Y.; Schatz, G. C.; Lee, B.; Mirkin, C. A. Low-Density 2D Superlattices
Assembled via Directional DNA Bonding. *Angew. Chemie - Int. Ed.* **2021**, *60* (35), 19035–19040.
https://doi.org/10.1002/anie.202105796.

(214)   Pimpinelli, A.; Villain, J. *Physics of Crystal Growth*; 1999.

(215)   Grimmer, H.; Bollmann, W.; Warrington, D. ~H. Coincidence-Site Lattices and Complete Pattern-
Shift in Cubic Crystals. *Acta Crystallogr. Sect. A* **1974**, *30* (2), 197–207.
https://doi.org/10.1107/S056773947400043X.

(216)   Singer, A.; Boucheron, L.; Dietze, S. H.; Jensen, K. E.; Vine, D.; McNulty, I.; Dufresne, E. R.;
Prum, R. O.; Mochrie, S. G. J.; Shpyrko, O. G. Domain Morphology, Boundaries, and Topological
Defects in Biophotonic Gyroid Nanostructures of Butterfly Wing Scales. *Sci. Adv.* **2016**, *2* (6), 1–
6. https://doi.org/10.1126/sciadv.1600149.

(217)   Schwartz, T.; Bartal, G.; Fishman, S.; Segev, M. Transport and Anderson Localization in
Disordered Two-Dimensional Photonic Lattices. *Nature* **2007**, *446* (7131), 52–55.
https://doi.org/10.1038/nature05623.

(218)   Painter, O.; Vučković, J.; Scherer, A. Defect Modes of a Two-Dimensional Photonic Crystal in an
Optically Thin Dielectric Slab. *J. Opt. Soc. Am. B* **1999**, *16* (2), 275–285.
https://doi.org/10.1364/JOSAB.16.000275.

(219)   Sundrani, D.; Darling, S. B.; Sibener, S. J. Guiding Polymers to Perfection: Macroscopic
Alignment of Nanoscale Domains. *Nano Lett.* **2004**, *4* (2), 273–276.
https://doi.org/10.1021/nl035005j.

(220)   Ross, M. B.; Ku, J. C.; Lee, B.; Mirkin, C. A.; Schatz, G. C. Plasmonic Metallurgy Enabled by
DNA. *Adv. Mater.* **2016**, *28* (14), 2790–2794. https://doi.org/10.1002/adma.201505806.

(221)   Hiqin, Z. L. I.; Hen, Y. I. C.; Hu, X. U. Z.; Heng, M. E. Z.; Engliang, F.; Ong, D.; Hen, P. E. C.;
Ihua, L. X. U.; Hu, W. E. C.; Hen, K. E. C.; Uan, H. U. D. Polarization-Dependent Scattering
Properties of Single-Crystalline Silicon Nanocylindroids. **2018**, *8* (3), 503–510.